Novel scanning electron microscope (SEM) imaging approaches to study microstructural evolution of alloys at elevated temperatures.

Rhiannon Heard

Trinity College

University of Oxford

A thesis submitted to the Department of Engineering Science of the University of Oxford in fulfilment of the requirements for the Degree of Doctor of Philosophy.

May 2021

“There is freedom waiting for you,

On the breezes of the sky,

and you ask: What if I fall?

Oh, but my darling,

What if you fly?”

~ Enid Hanson

This quote has been on my wall since I started my DPhil,

and I’m happy to say, it looks like I flew.

However, I have a lot of people to thank for that, so here goes…

Acknowledgements

First, to my supervisors, Kalin Dragnevski and Clive Siviour, who inspired my passion for research, microscopy and all things experimental. Thank you for sticking by my out-of-the-box ideas with endless patience and enthusiasm – without you, this thesis would not have been possible. It has been a pleasure working with you both.

My gratitude also goes to The Engineering and Physical Sciences Research Council (EPSRC) and Deben UK Ltd for their financial support, with thanks to Gary Edwards and Ed Williamson-Brown for their technical assistance. Likewise, I'd like to thank all the staff and technicians in the Solid Mechanics and Material's Engineering group, University of Oxford, with particular thanks to Marzena Tkaczyk, Richard Duffin and Igor Dyson for their help with this project.

On a similar note, I am grateful to all the staff at Trinity College, University of Oxford, who've supported me on my academic journey and beyond. A special mention goes to Steve Sheard, from my undergraduate tutor to college mentor, colleague and friend. Your continued support is much appreciated.

Next, I'd like to say a big thank you to my lab-mates, housemates, and friends for keeping me sane during this rollercoaster of a lockdown write up year; you know who you are. To my best friends, thanks for sticking by me over the years and listening to my DPhil drama, you should know it was worth it and I can now graduate as a doctor from Oxford and move happily onto my next phase in life's journey.

Finally, to my family, who've been here from the beginning, I say, mission accomplished; I hope I've made you proud.

Abstract

This thesis presents an investigation into high-temperature imaging of metals and alloys using a novel heat stage for *in situ* scanning electron microscopy (SEM). The results demonstrate the advantages and challenges of SEM imaging at elevated temperatures using secondary electron (SE) and electron backscatter diffraction (EBSD) detectors. The data collected using the heat stage showed beam, vacuum and detector stability at high-temperatures, without the need for shielding or detector modification, owing to the optimally designed heat stage and specimen geometry.

The novel heat stage was used to conduct investigations, during the heat treatment of carbon steel, into the impact of surface effects on the surface and bulk microstructural evolution. Results highlighted a significant discrepancy between the surface and bulk grain growth of the specimens during heat treatment at temperatures of 850 °C and above. It was concluded that the combination of thermal etching and oxidation led to the retardation of grain growth on the surface of carbon steel, but that the bulk of the specimen's grain growth was unaffected. The mechanism that caused the grain retardation was found to be not dissimilar to Zener pinning, where in this case oxide particles pinned the newly exposed etched grain boundaries. However, it was found that for heat treatments of carbon steel conducted at 800 °C for less than 1 hour, the surface microstructural evolution was representative of the bulk, as there was a lack of oxidation present at this temperature. Usefully, though, the presence of oxidation at higher temperatures did allow for the tracking of the morphological evolution that occurred during the thermal oxidation of carbon steel.

Despite some of the challenges, the presence of thermal etching did enable *in situ* tracking of the microstructural evolution of carbon steel during the heat treatment. High-temperature SE imaging, combined with thermal etching, was used to study the grain and phase transformations during 1-hour heat treatments of carbon steel at 800 °C. The temperature and timescales were chosen to ensure the surface observations were representative of the bulk microstructure. The high-temperature SE data, supported by optical and high-temperature EBSD data, suggested that grain growth in the austenitic region could be described by linear, 'abnormal' grain growth. The real-time SE and EBSD data also enabled studies on the phase transformation into the austenitic region from starting structures of ferrite / pearlite and martensite. The results of these studies compared favourably to current phase-field models.

High-temperature SE and EBSD imaging of nickel and steel allowed for the investigation of one of the most notable, but rarely documented, limitations of high-temperature SEM. Namely, the impact of material properties on the specimen-beam interaction on EBSD imaging. Data showed high-temperature EBSD imaging was affected by both the evolution of surface roughness during heating and the material's magnetic properties. In particular, at temperatures close to the Curie temperature of nickel there was a loss of EBSD image quality, but quality was regained when temperatures were further increased. This was attributed to the influence of local magnetization on electron trajectories, likely resulting in a decrease in interaction volume and subsequent loss of EBSD image quality.

Overall, this thesis documents the development, testing, and use of a novel heat stage in the study of the high-temperature microstructural evolution of nickel and carbon steel. In particular, this project provides a unique scientific contribution to the understanding of microstructural changes during the heat treatment of carbon steel, as well as the development and application of a new high-temperature SEM imaging technique.

Publications & Conferences

The following papers have been produced based on this thesis:

- Heard, R., Siviour, C.R. & Dragnevski, K.I., 2020. *In situ* SEM analysis of surface oxidation mechanisms in carbon steel during vacuum heat treatment. Materials Today: Proceedings, DOI: 10.1016/j.matpr.2020.05.396.
- Heard, R., Huber, J.E., Siviour, C.R., Edwards, G. & Williamson-Brown, E., 2020. An investigation into experimental *in situ* SEM imaging at high temperature. Review of Scientific Instruments, DOI: 10.1063/1.5144981.
- Heard, R., Siviour, C.R. & Dragnevski, K.I., 2020. *In situ* SEM observation of grain growth in the austenitic region of Carbon Steel using thermal etching. Journal of Microscopy, DOI: 10.1111/jmi.12894.
- Heard, R., Siviour, C.R. & Dragnevski, K.I. In-depth evaluation of the effect of thermal etching on grain growth (in preparation).
- Heard, R., Siviour, C.R. & Dragnevski, K.I. *In situ* SEM observations of the microstructural evolution of phase changes in Steels (in preparation).

Three further papers were also published based on collaborative work or alternative projects that are not a direct result of this thesis:

- Dragnevski, K.I., Pellegrino, A., Heard, R., Siviour, C.R., Mullins, A.M. & Cochrane, R.F., 2019. Mechanical behaviour of rapidly solidified copper: effects of undercooling and strain rate. Materials Science and Technology, DOI: 10.1080/02670836.2019.1691354.
- Heard, R., Dragnevski, K.I. & Edwards, G., 2019. Applications of the Brazilian disk test to study mechanical properties of various materials observed *in situ* in an Environmental Scanning Electron Microscope (ESEM). Microscopy & Microanalysis, DOI: 10.1002/micro.2924/full.
- Heard, R., 2017. Cold chocolate under stress: An alternative approach to study high-rate behaviour in polymers. inFocus, Royal Microscopical Society, DOI: 10.22443/rms.inf.1.154.

During this DPhil, oral presentations were presented at the conferences listed below:

- International Virtual Early Career European Microscopy Congress 2020, Heard, R. (presenter), Siviour, C.R., Dragnevski, K.I., Investigations into high temperature *in situ* SEM imaging of metallic materials.
- International Microscience Microscopy Congress 2019, Manchester, Heard, R. (presenter), Dragnevski, K.I., Edwards, G., Williamson-Brown, E., Siviour, C.R, *In situ* SEM observation of abnormal grain growth in the austenitic region of Carbon Steel.
- Trinity College MCR Gaudy 2019, Oxford, Heard, R. (presenter & conference organiser), Novel microscopy imaging approach to facilitate study of Iron-based alloys at high temperatures.
- The Society of Electron Microscope Technology Meeting 2018, London, Heard, R. (presenter), Novel high temperature *in situ* SEM approaches reveal abnormal grain growth in Fe-based alloy.

In addition to the oral presentations, posters were also presented at:

- International Microscience Microscopy Congress 2019, Manchester, Heard, R. (presenter), Shentu, Y., Dragnevski, K.I., Edwards, G., Williamson-Brown, E., Siviour, C.R., A new *in situ* heating stage for SEM imaging at elevated temperature.
- Electron Microscopy and Analysis Group 2018: Applications of Electron Microscopy to Beam Sensitive Materials, Warwick, Heard, R. (presenter), Micromechanics of pharmaceutics – a novel *in situ* tensile test. Heard, R. (presenter), Cold chocolate under stress: an alternative approach to study high-rate behaviour in polymers.
- International Microscience Microscopy Congress 2017, Manchester, Heard, R. (presenter), Dragnevski, K.I., Sinka, C., Cocks, A., Micromechanics of pharmaceutics - a novel *in situ* ESEM approach.

Contents

List of Figures

List of Tables

Chapter 1

Introduction

1.1 Context

Understanding the microstructural evolution of alloys during dynamic processing (via the application of temperature and / or load) provides greater scope for modification of the processes used to produce microstructures, which facilitate preferential mechanical properties. The use of electron microscopy to capture the microstructural changes before and after processing is a well-established technique. However, what is now of interest is how the microstructural formation occurs. Hence, there is a necessity to develop technologies, and corresponding techniques, to track microstructural evolution of alloys while temperature and / or load is applied to further this understanding. At present, current *in situ* microscopy based studies focus on localised, individual grain changes via the use of a transmission electron microscope (TEM). Recently, there has been movement towards the development of these techniques within a scanning electron microscope (SEM), known as *in situ* SEM. Nonetheless, research is still required to develop *in situ* SEM techniques and technologies, that provide an easier and more reliable experimental set up, enable the study of longer dynamic process, can be combined with other detectors, and can capture a more statistically significant number of grains. Despite several commercially available stages, there are still a limited number of successful studies using these techniques due to the physical and technical difficulties of capturing a rapidly evolving microstructure.

One of the dynamic processes commonly applied to metals and alloys post-formation is heat treatment. Steel is one of the most widely used alloys owing to its high strength to cost ratio, and it is commonly used for infrastructure, tools, buildings, machines and weapons. The

specific use of steel is highly dependent on the carbon and alloy content and the material formation process (including post-formation heat treatments). The heat treatment of steel drastically modifies the microstructure, which in turn dictates the phases present, to produce significant changes in physical and mechanical properties, often focused on improving ductility and strength. As a result, gaining an improved understanding of the formation of the steel microstructure, and how it may be modified to produce favourable characteristics during heat treatment, is of great interest.

1.2 Aims & Strategies

The aim of this project is to facilitate the development of new techniques and technology and to subsequently capture the unique formations that occur during these dynamic processes; with an emphasis on the heat treatment of carbon steel. Studies have shown that there are both logistical and technical challenges when using SEM imaging at high-temperature. These challenges are attributed to the volatile environment created by heating within the SEM, combined with the limitations of surface imaging. Hence, this project focuses on developing techniques that ensure the surface data captured is representative of the bulk of the specimen, and that the *in situ* heat treatment environment produces a microstructure equivalent to conventional heat treatments. Current literature identifies these as the key elements for development in the *in situ* microscopy field.

As stated above, the main application of this project is to provide a contribution to scientific knowledge on the microstructural evolution during the heat treatment of carbon steel and develop robust new tools and methodologies with which to do so. Historically, microstructural evolution understanding has been derived from data collected using imaging methodologies conducted after the heat treatment has occurred. However, these data do not

capture the stage at which microstructural formation occurs, nor necessarily the process by which it occurs. Understanding the role that each stage of the heat treatment process plays in materials' microstructural evolution is necessary to modify heat treatments. Hence, there is a drive in the microscopy and materials fields to develop novel *in situ* techniques, which will capture changes in structure and composition while temperature and / or load is applied.

1.3 Thesis Scope

This thesis documents the development of new technology and techniques for use within SEM. The imaging and analysis methodologies enable the documentation of changes in microstructure during the heat treatment of carbon steel. As well as providing a contribution to scientific knowledge, the application studies also demonstrate the benefits and challenges of capturing the microstructural evolution of dynamic processes in real-time. The project is split into seven thesis chapters.

Chapters 2 & 3 – Literature Review

Chapter 2 provides an in-depth review of the literature relating to the material properties of industrially pure nickel and 0.4 wt.% carbon steel; the focus of this study. The chapter subsequently investigates literature documenting the microstructural evolutions observed during heat treatment including grain growth, thermal oxidation and phase transformations. Additionally, the literature review explores the latest *in situ* SEM studies on nickel and steel.

Chapter 3 is the second literature review chapter which examines the main techniques used within this thesis. The microscopy techniques include SEM, electron backscatter diffraction (EBSD), optical microscopy, and atomic force microscopy (AFM), as well as the current best practices for calculating grain size from microstructural images. The chapter also

evaluates the latest *in situ* SEM studies conducted, to document the current challenges and benefits of these techniques and to provide context to the developments achieved in this thesis.

Overall, the literature chapters provide the basis for developing new techniques and technology for *in situ* high-temperature SEM. Following on from this, the novel techniques developed have facilitated real-time capturing of the microstructural evolution during the heat treatment of carbon steel.

Chapter 4 – Investigative In Situ *High-Temperature SEM Imaging*

Chapter 4 presents the development and testing of a novel heat stage, which can be used for *in situ SEM* imaging without the need for shielding or consumable heaters. The chapter demonstrates the stage's capabilities and stability in the SEM environment, including its compatibility with secondary electron (SE) and EBSD detectors. Moreover, data are presented on the preliminary material studies conducted on nickel and carbon steel, highlighting the benefits of high-temperature imaging.

Chapter 5 – Surface Changes During In Situ *SEM Heat Treatment of Carbon Steel*

Chapter 5 investigates the surfaces effects that occur during the heat treatment of carbon steel *in situ*. The experimental results enable the optimisation of parameters for *in situ* SEM imaging to ensure that SE surface observations are representative of the bulk of the specimen. The chapter goes on to utilise these *in situ* SEM techniques to improve understanding of the grain growth and thermal surface oxidation formation that occurs during the heat treatment of carbon steel.

Chapter 6 – In Situ *Microstructural Evolution of Phase Changes in Carbon Steel*

Chapter 6 documents the exploratory work on using the newly developed *in situ* high-temperature SEM imaging techniques to capture carbon steel phase changes of ferrite / pearlite to austenite, and martensite to austenite. A combination of real-time, high-

temperature SE and EBSD imaging techniques are used to provide insight into the microstructural evolution during these phase changes. The qualitative and quantative data are subsequently compared to existing transformation models.

Chapter 7 – Conclusions & Future Work

Chapter 7 summarises the findings of this thesis and draws together the primary conclusions. The chapter also suggests appropriate points to extend this project, in the form of future work, relating both to industrially relevant development, and to scientifically significant material property investigations.

1.4 Research Novelty

The nature of a thesis is to provide a unique contribution to the field via research and experimentation leading to improvement of the knowledge and understanding within the scientific community. This project has focused on the following aspects to facilitate the development and application of novel, robust technology and techniques for microstructural analysis of dynamic processes in metals and alloys using *in situ* high-temperature SEM imaging.

Development of novel heat stage technology in collaboration with Deben UK Ltd.

The current literature observes that *in situ* high-temperature SEM is a powerful tool for capturing microstructural changes in metals and alloys. However, researchers acknowledge several key technical challenges that have impacted the development of these techniques, despite the presence of commercially available stages. The challenges include:

- The proximity of the detector to the sample, leading to the overheating of detectors and limiting the size of the stages used.

- The signal to noise ratio interfering with both beam-sample interactions and detector imaging.
- The loss of vacuum quality due to the high-temperature environment.
- The temperature gradient through the specimen during heating.
- The degradation of heaters.

Thus, extensive industry and academic collaboration was deemed necessary to develop a novel heat stage suitable for both SE and EBSD imaging.

Identification of the parameters under which* in situ *SEM surface observations are representative of the bulk of the specimen and of the* ex situ *dynamic processes.

The combination of *in situ* and *ex situ* microscopy techniques used to capture the heat treatment of carbon steel between 800 °C and 920 °C suggested that heat treatments at 800 °C longer than 1 hour, and those above 800 °C, for at least 1 hour, led to thermal oxidation within thermally etched grain boundaries. This phenomenon resulted in surface growth retardation, not dissimilar to the Zener pinning model, that was not representative of the bulk of the specimen. However, for heat treatments at 800 °C for less than 1 hour, the formation of thermal etching resulted in grain boundaries being visible under SE imaging at temperature. These grain boundaries were representative of the bulk of the specimen. Hence, the combined thermal etching SE imaging technique can be used to track a statistically significant number of grains in carbon steel and their corresponding evolution, while undergoing heat treatment at this temperature.

Focussed applications using the newly developed technologies and techniques to investigate the microstructural evolution during the heat treatment of carbon steel.

- **Grain Growth in the Austenitic Region:** *In situ* SE data at 800 °C facilitated the tracking of grain growth during the ferrite to austenite phase change into the austenitic region of carbon steel. The data indicated that abnormal linear grain growth occurs under these conditions.
- **Thermal Oxidation Formation:** During heat treatment of carbon steel between temperatures of 800 °C and 920 °C, thermal oxidation formation was captured by SE imaging at regular time intervals. Observations of the surface morphology during this time indicated that oxidation formation occurs by the agglomeration of surface nodules to form a wüstite layer.
- **Ferrite / Pearlite to Austenite Phase Transformation**: Real-time *in situ* SE and EBSD images capturing microstructural evolution during this phase change produced qualitative and quantative data supporting current nucleation and growth driven models. The data indicated that while nucleation initially occurs homogeneously within pearlite grains, soon after the austenite nuclei begin to grow in the pearlite, heterogeneous nucleation of austenite appears to form along the ferrite grain boundaries, eventually leading to growth and complete transformation.
- **Martensite to Austenite Phase Transformation:** Use of combined SE thermally etched *in situ* data captured the formation of austenite nuclei within the already present martensitic laths. Evolution appears to be rapid and homogeneous with little growth observed after formation. These data support the current models for martensite to austenite reversion.

Chapter 2

Literature Review of Materials' Behaviour at Elevated Temperatures

2.1 Introduction

When producing metals and alloys, an understanding of the three-way relationship between structure, properties, and processing is vital to ensure a material can operate within the intended environment [1]. The structure, particularly the microstructure, of a material greatly impacts its physical and mechanical properties and hence any application of the material. Microstructural development is influenced by processing, such as the heat and load treatments that the metal or alloy undergoes either during or after its formation. A common process for metals and alloys is the heat treatment at some elevated temperature below its melting point, post-formation [2]. This is executed to produce a desired change in microstructure and thus more favourable properties, such as increasing the hardness, ductility or strength [1].

This chapter focuses on the current understanding of microstructural evolution during heat treatments post-metal or alloy formation, with an emphasis on nickel and steel; the materials used within this thesis to develop *in situ* high-temperature scanning electron microscope (SEM) techniques. Nickel is commonly used within the SEM for the calibration of the electron backscatter diffraction (EBSD) detector [2], owing to nickel's high orientation and high topographic contrast post-polishing. The combination of these physical properties makes nickel ideal for EBSD imaging [3], and hence its use in this thesis for developing *in situ* high-temperature SEM imaging techniques. The application of these methodologies and

technologies to steel is credited to it undergoing an extensive range of heat treatments leading to multiple different microstructural formations and corresponding properties. Hence, increasing understanding of the heat treatments that contribute to these changes in microstructural evolution, via novel *in situ* SEM techniques, will provide a fundamental contribution to scientific knowledge, while also demonstrating the benefits of these new techniques. To identify the ideal areas of investigation, a review of the current literature on material behaviour at high-temperature is first necessary and follows in this chapter.

2.2 Metal & Alloy Structures

2.2.1 Overview of Metal & Alloy Structures

The structure and composition of metals and alloys greatly impacts their physical and mechanical properties. These properties, which dictate the materials' overall use, can be influenced by processing, such as heat and deformation treatments, which the material undergoes either during or after its formation. Thus, an understanding of the fundamentals of metal and alloy structures is required to develop processing parameters for producing favourable material properties.

Metallic material structures consist of atomic, crystallographic and grain structures, which dictate the overall material structure and its subsequently associated properties [4]. The atomic structure refers to the arrangement of electrons surrounding the nucleus of individual atoms, which can influence the bonding of atoms [1]. From these atomic bonds, most metals form crystal structures: a regular and ordered atomic arrangement of repeating units, known as unit cells. The four most common formations of metallic unit cells are simple cubic, body centred cubic (BCC), face centred cubic (FCC), and hexagonally close packed (HCP) [5]; see Figure 2.1. Multiple unit cells arranged in a single orientation make up a grain, which exists

on a microlevel; the microstructure of the material [6]. Individual grains are separated by grain boundaries, which consist of regions containing imperfections between different crystal orientations. The size and shape of these grains contributes to the material's behaviour and consequently its mechanical properties [1].

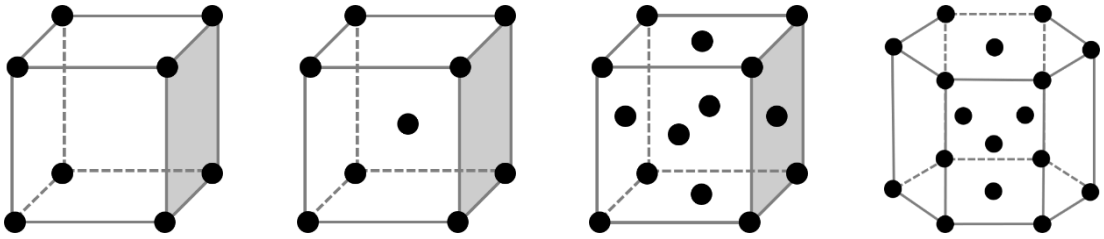

Figure 2.1: Unit Cells as (a) simple cubic, (b) body centred cubic (BCC), (c) face centred cubic (FCC), and (d) hexagonal close packed (HCP).

The combination of an atomic and crystallographic formation in metals and alloys often produces a distinctive grain structure with unique properties; this is referred to as a phase. The type, size, distribution, and percentage of a phase present within a structure dictates the resulting overall properties of the microstructure and the material [4]. Phases are characterised via phase diagrams, which were first derived by Roberts-Austen based on the Gibbs phase rule [7],

$$p + f = c + 2 \qquad \textit{Equation 2.1}$$

which, gives the relationship between the number of equilibrium phases (p) and the chemical components (c) in a given alloy under equilibrium conditions, based on the number of thermodynamic degrees of freedom in the system (f) [8]. However, if it is also assumed that the phase is formed under equilibrium conditions and constant pressure, the Gibbs phase rule is reduced by one degree of freedom to,

$$p + f = c + 1 \qquad \textit{Equation 2.2}$$

where *p, f* and *c* are as defined above [9]. Equation 2.2 is the most commonly used when dealing with phase transformations in metals and alloys where constant pressure can be assumed[1]. However, for multi-component alloys, such as high entropy alloys (HEAs), the number of phases observed is significantly less than predicted by the Gibbs phase rule due to the complexity of interactions between multiple components [10]. Although a significant area of interest for future studies in this field, this thesis focuses on the study of steel and nickel phases, which both obey the Gibbs phase rule. Further information concerning the kinetics and thermodynamics of phase formation and transformation is discussed in Section 2.4.

The presence of microstructural features, aside from ordered atoms, crystallographic unit cells, grains, and phases, can also impact the properties of the material. Alternative features within the microstructure include: twins, a pair of grains with identical crystal structure where the arrangement of one of the grains is generated from the other by reflection across a common plane [11]; precipitates, the formation of particles (often alloying components such as carbon) independent of the grain structure [6]; and dislocations, the deformed versions of the crystal lattice structure [12]. These features can modify the ease with which movement can occur within the system, and hence how, or whether, deformation or transformation transpires via mechanical or thermal loading [6]. This once again demonstrates the necessity of understanding the structure-property-composition relationship.

[1]All future phase transformations discussed in this thesis will be assumed under constant pressure unless stated to the contrary.

2.2.2 Microstructure of Nickel

Industrially pure nickel contains greater than 99% Ni, with small amounts of cobalt and impurities including iron, copper and manganese [13]. It has a uniform, FCC crystal structure, while the grain structure is dependent on the formation process and can vary in grain size from a few nano-meters to several hundred microns [14]. As well as being uniform, nickel's microstructure is also very thermodynamically stable, resulting in negligible grain evolution up to temperatures of 900 °C unless annealed for significant periods of time (>5 hours) [15]. The stability of pure nickel extends to its good corrosion resistance in oxidising, water, and alkaline environments [16]. Furthermore, pure nickel is able to alloy with most metals, and this, combined with its favourable properties, means it is often used as a base for alloys operating in high-temperature and pressure environments [17]. Nickel's microstructural stability is of great advantage during this research, as for the preliminary, high-temperature, technique development it minimises difficulty with imaging that may arise as a result of microstructural deformation or transformation, enabling identification of the impact of technical challenges, such as overexposure of the detectors to light and / or heat, on imaging.

2.2.3 Microstructure of Steel

Steel is an alloy of iron (generally > 97%), carbon (generally < 2%) and other alloying elements. The addition of carbon to iron distorts the iron crystal lattice increasing the overall strength; this provides a similar effect to work hardening [18]. However, the specific microstructure of steel is dependent on its manufacturing process, which includes heat and surface treatments (discussed in Section 2.3.2), initial formation, and deformation via mechanical loading, as well as the alloying elements and carbon content present. Due to the

complex nature of steel microstructures, the crystallography is thus categorised with respect to phases.

Steel's equilibrium phases are defined by the iron-carbon phase diagram based on iron's allotropes; BCC α-Fe, FCC γ-Fe and BCC δ-Fe. Small atoms of solid carbon dissolve interstitially in these allotropes to form three primary solid solutions of steel: alpha-ferrite (BCC), austenite (FCC), and delta-ferrite (BCC). These phases are often accompanied by the iron-carbide metallic compound Fe_3C, known as pearlite or cementite depending on its microstructure [19]. In general, these phases can be distinguished from one another based on four main features: composition, crystal structure, shape change, and carbon mobility.

Figure 2.2 presents a labelled iron-carbon phase diagram up to 6.7 wt.% carbon, as per standard convention [20]. The diagram shows the eutectoid point (A), which occurs at 723 °C for 0.8 wt.% C, where the maximum number of allowable solid phases are in equilibrium; in this case it is austenite, ferrite, and Fe_3C. These solid phases exist simultaneously at the eutectoid point. The eutectic point (B) on the iron-carbon phase diagram also has a maximum number of allowable phases; at this point, the liquid and solid phases remain in equilibrium [7]. The microstructure and properties of the different steel compounds that exist in equilibrium (often made up of multiple phases), as shown in Figure 2.2, are detailed in Table 2-1.

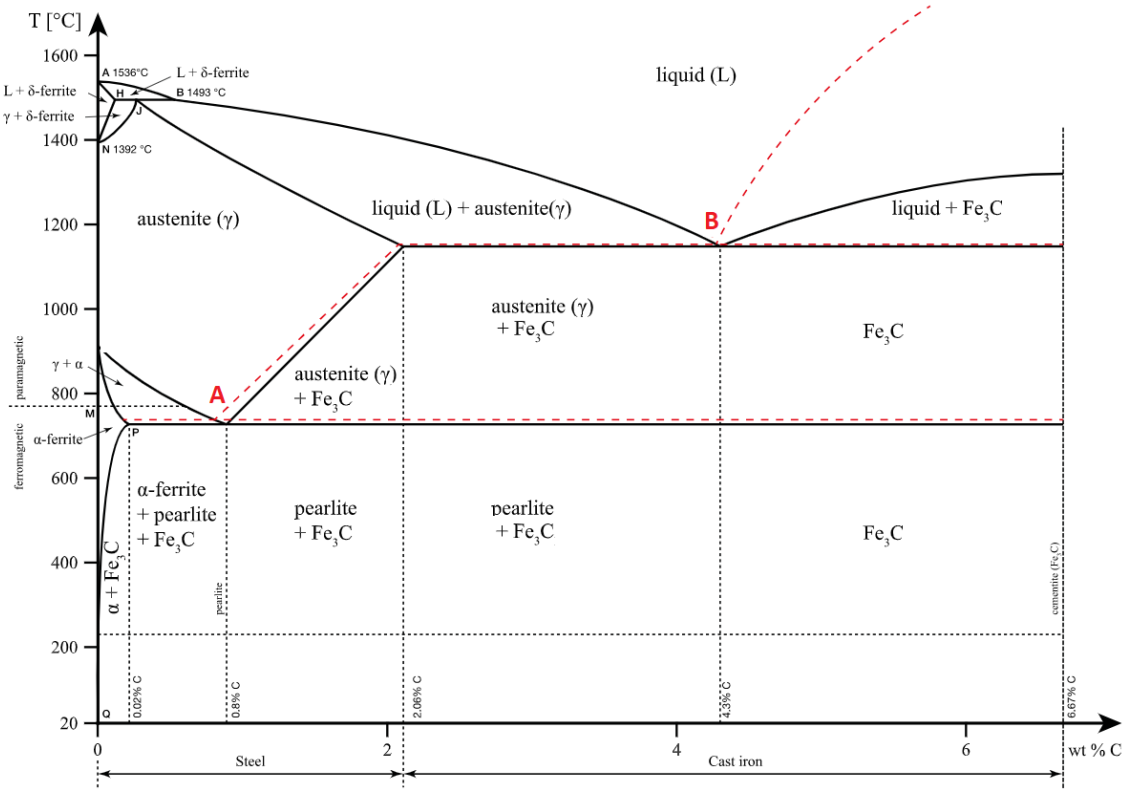

Figure 2.2: Iron-Carbon Phase Diagram [21]

At room temperature iron-carbon alloys are split into the following categories [19]:

- **Hypoeutectoid steels** have a carbon content of less than 0.83% and consist of alpha-ferrite and pearlite.
- **Eutectoid steels** have a carbon content of 0.83% and consist of pearlite only.
- **Hypereutectoid steels** have a carbon content of above 0.83% but less than 2.06% and consist of cementite and pearlite.
- **Cast irons** have a carbon content between 2.06% and 6.7% and consist of cementite and pearlite. It is noted that cast iron is an iron-carbon alloy and it is not classified as a steel.

Iron-carbon with a carbon content of above 6.7% at room temperature consists of pure cementite, as 6.7% is the maximum solubility of carbon in iron. These are not commonly used commercially, owing to the increasing brittleness of the alloy with increasing carbon [22].

	Phases	Symbol	Crystal	Optical Image	Properties
1)	alpha-ferrite	α	BCC	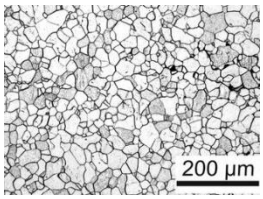	Single phase, limited solubility of C in Fe, maximum carbon content of 0.022%. Stable at room temperature, ferromagnetic.
2)	delta-ferrite	δ	BCC	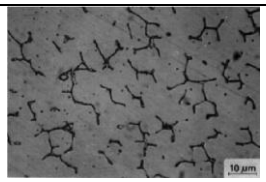 (shown delta ferrite in austenite matrix)	Similar structure to α-ferrite, but only exists at high-temperatures.
3)	austenite	γ	FCC	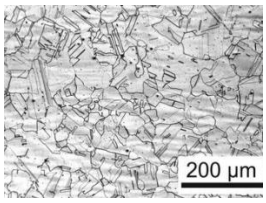	Single phase, high solubility of C in Fe, maximum carbon content of 2.14%, paramagnetic.
4)	cementite	Fe_3C	orthorhombic	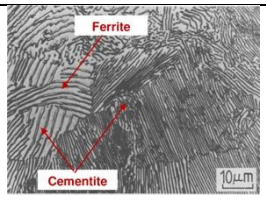 (shown cementite, pearlite, ferrite mix)	Iron-carbide of a fixed composition of carbon (~6.67 wt.% C). Very brittle.
5)	pearlite	α/Fe_3C (P)	composition	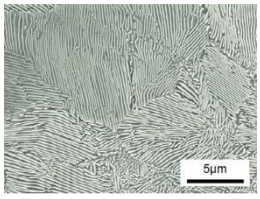	Eutectoid product when austenite transforms to a fine lamellar by growth of ferrite and cementite.
6)	liquid	L	liquid	n/a	Liquid iron-carbon compound.

Table 2-1: A summary of the different phases present, including diagram, crystallographic structure and properties [7]. *References for diagrams are: 1:* [23], *2:* [24], *3:* [23], *4:*[25] *and 5:* [26].

2.3 Heat Treatments

2.3.1 Principles of Heat Treatment in Metals & Alloys

Heat treatments are a type of dynamic process used to alter a material microstructure so that it will display desirable properties. During heat treatments, the microstructure is modified, causing changes in: composition, surface, chemical composition, phase, grain size, and grain orientation and, in turn, a change in material properties. A material may undergo multiple heat treatment processes, with different time and temperature parameters, to produce the required properties [27].

The heat treatment process has three main stages [27]:

1. Heating the material to a specific temperature below its melting point.
2. Holding the material at that temperature for a certain time period.
3. Cooling the material to room temperature or below, where the cooling rate is controlled by a variety of different methods.

Each stage in the heat treatment process contributes to the production of the desired properties, based on the parameters selected. The first stage in the heat treatment process allows the entirety of a material sample to heat to the same temperature to avoid abnormalities in the crystal structure during heating. Once the desired temperature is reached, a material is held at that temperature for the time needed to reach the required degree of microstructural homogenisation to produce the desired properties post-cooling. Cooling then subsequently forms the final microstructure, where the rate of cooling dictates the rate of nucleation and recrystallisation during the transformation to room temperature or below [27]. The cooling rate and heating temperatures are significantly dependent on the phases within the material; this is discussed specifically for steel in Section 2.3.2.

2.3.2 Heat Treatment of Steel

Heat treatments of steel often change the phase of the microstructure and can lead to the formation of equilibrium (as discussed in Section 2.2.3) and non-equilibrium phases. The achievement of equilibrium through the formation of metastable phases within steel, as characterised by the iron-carbon phase diagram, is dependent upon the operating temperature and carbon content. The production of non-equilibrium phases, which are not present on the main iron-carbon phase diagram, is caused by rapid changes in temperature during the cooling stage of the heat treatment process. In some cases, multiple phases or alternative phases may also be formed by steel undergoing several heat treatment processes to produce the desired properties [28].

The main heat treatments used on steel are annealing, normalising, quenching and tempering, details of which are given below. These methods generate favourable properties and lead to the formation of a combination of phases present in the iron-carbon phase diagram, as well as some alternative phases [19]. Annealing is the only heat treatment which uses the iron-carbon phase diagram directly in its formation of new phases, where cooling is at such a rate as to form phases in equilibrium. The other three heat treatments have non-equilibrium, isothermal, cooling rates where the speed of cooling causes diffusional transformation and thus produces alternative microstructures [27]. This isothermal transformation behaviour of steel is described by the time-temperature-transformation (TTT) diagram. An example for hypoeutectoid steels (<0.83% carbon content), which are used in this research, is shown in Figure 2.3

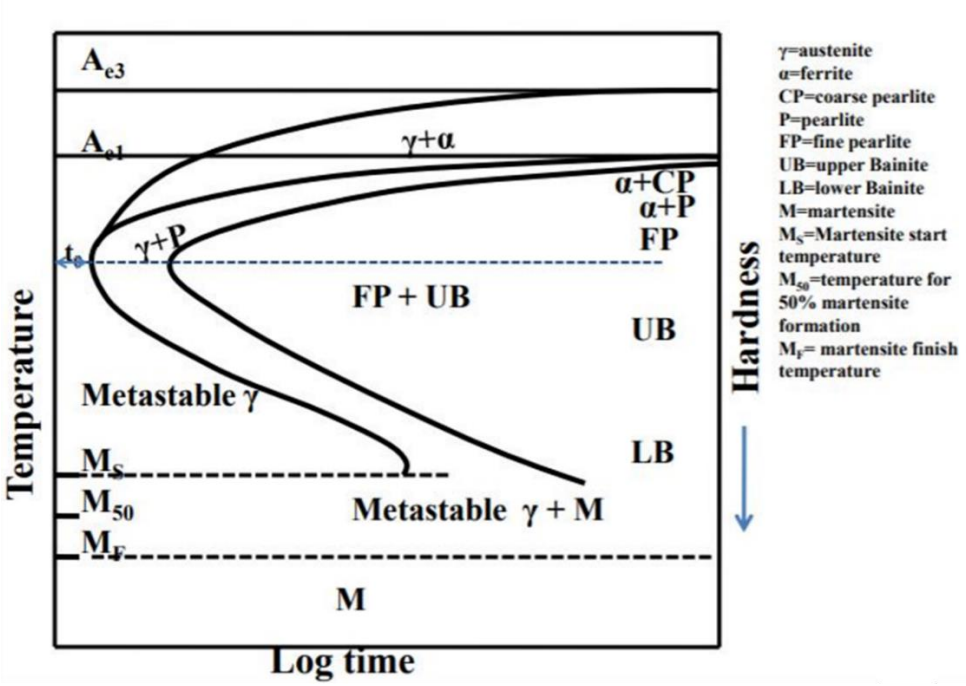

Figure 2.3: Time-temperature-transformation (TTT) graph showing the cooling path during the isothermal transformation of hypoeutectoid steel [29].

Annealing

Annealing of steel is a heat treatment process used to reduce hardness, increase ductility, and help eliminate internal stresses, making the alloy ideal for forming or machining. It begins with heating the sample within a furnace into the austenitic region to dissolve carbides into the iron. Once the alloy is fully austenitic, the heat source is turned off and the alloy allowed to cool within the furnace environment. This slow cooling process leads to a uniform microstructure of coarse pearlite and ferrite, the formation of which is shown in the iron-carbon phase diagram [30].

Normalising

Normalising is a similar process to annealing, in which the alloy is heat treated up to the austenitic temperature and held for a set period. However, cooling occurs at a slightly faster rate in air than in the furnace. This means that the decomposition of austenite to form a

mix of pearlite and ferrite creates grains of ferrite that are significantly smaller than in its annealed counterpart. Similarly, normalising also creates a finer pearlite grain size compared to annealing and thus improves the steel's machinability [31]. The normalising heat treatment process is also much faster than annealing, while still increasing the overall strength of the steel [27].

Quenching

The process of quenching is used to generate another phase, not previously mentioned, known as martensite. Martensite is formed by rapid cooling, or quenching, faster than the critical cooling rate of the steel after heating within the austenitic region. To achieve such cooling rates, the steel must be removed from the furnace and is generally placed in cold water or oil to dramatically reduce the temperature. The quenching process produces a super saturated single-phase of martensite with a body centred tetragonal structure, which thus contains a higher carbon content within the lattice. This process results in a very strong and hard, but brittle, steel [31]. The microstructure is dependent on carbon content but can be described as dendritic growth, where the greater the carbon content, the larger the plates of dendrites; an example of martensite's microstructure is shown in Figure 2.4. It is important to note that martensite does not feature on the phase diagram, Figure 2.2, as it is not in equilibrium. Instead, martensite is a meta-stable phase, which is formed by a diffusionless transformation, dependent on the TTT diagram, Figure 2.3, and can be easily dissolved via heating [1]. The formation of martensite is discussed further in Section 2.4.1.

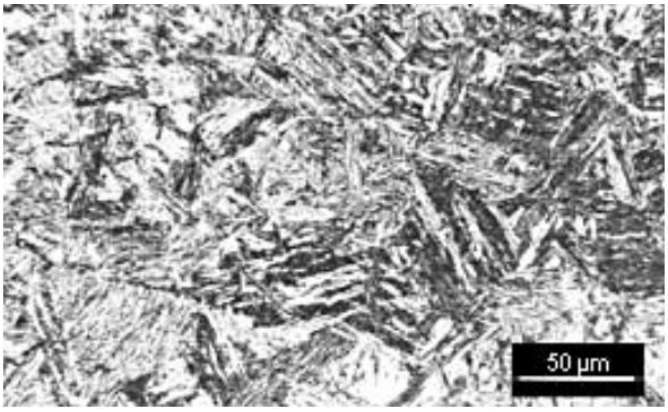

Figure 2.4: Example of meta-stable martensitic microstructure in a carbon steel [32].

Tempering

Tempering is a process conducted on martensitic steel to improve its ductility in exchange for a slight decrease in strength and hardness. During this process, the martensitic steel is heated at a temperature below the eutectoid point, which, owing to martensite's metastable state, leads to its decomposition. A range of tempering temperatures are used to generate different microstructures and thus different strengths and hardness. Microstructures produced include: a mixture of low carbon martensite and cementite, common at low-temperature tempering; a mixture of stable ferrite and cementite, common a high-temperature tempering; and very coarse cementite, common at just below the eutectoid point [1].

Other such heat treatments can also be conducted to produce less common phases, such as bainite, shown by the TTT diagram in Figure 2.3, as well as a combination of phases. This is an area that is continually being investigated and expanded on in industry, as other environmental factors aside from temperature can also have an impact on the final microstructure. However, these alternative heat treatments are not the focus of this thesis, which concentrates on the more common heat treatments described above.

2.4 Phase Transformations

2.4.1 Kinetics of Phase Transformations

The kinetics of phase transformations refers to the time dependence of the microstructural evolution during transition from one phase to another [7]. Most phase transformation kinetics are governed by a two-stage process of nucleation and growth, shown in Figure 2.5. In this process, nucleation refers to the formation of a stable particle (nuclei) in the form of the new phase. The location of nuclei formation can occur heterogeneously (Figure 2.5a), where the new phase nuclei appears along certain features such as grain boundaries or around impurity particles, or homogeneously (Figure 2.5b), where new phase nuclei spontaneously appear within the original phase. In either case, over time, multiple nuclei form and eventually these begin to agglomerate (Figure 2.5c). When nuclei reach a critical size, they start to grow (Figure 2.5d), and both growth and nucleation continue (Figure 2.5e) until complete transformation (Figure 2.5f). The rate of the overall phase change is dictated by a combination of the nucleation rate and growth rate. Generally, nucleation is quite a slow transformation process, but once growth begins, the initial speed of transformation rapidly increases before slowing in advance of the complete phase transformation [33][34].

In general, phase transformations are either diffusionless (e.g. martensite formation) or diffusion-driven (e.g. eutectic transformations), where diffusionless transformations occur by homogenous movement of many atoms at once, and diffusion-driven transformations refer to a phase change via long-range atomic movement [34]. However, both result in a significant change in crystal structure, and in the case of diffusionless and some cases of diffusion-driven, a change in composition can also occur [33].

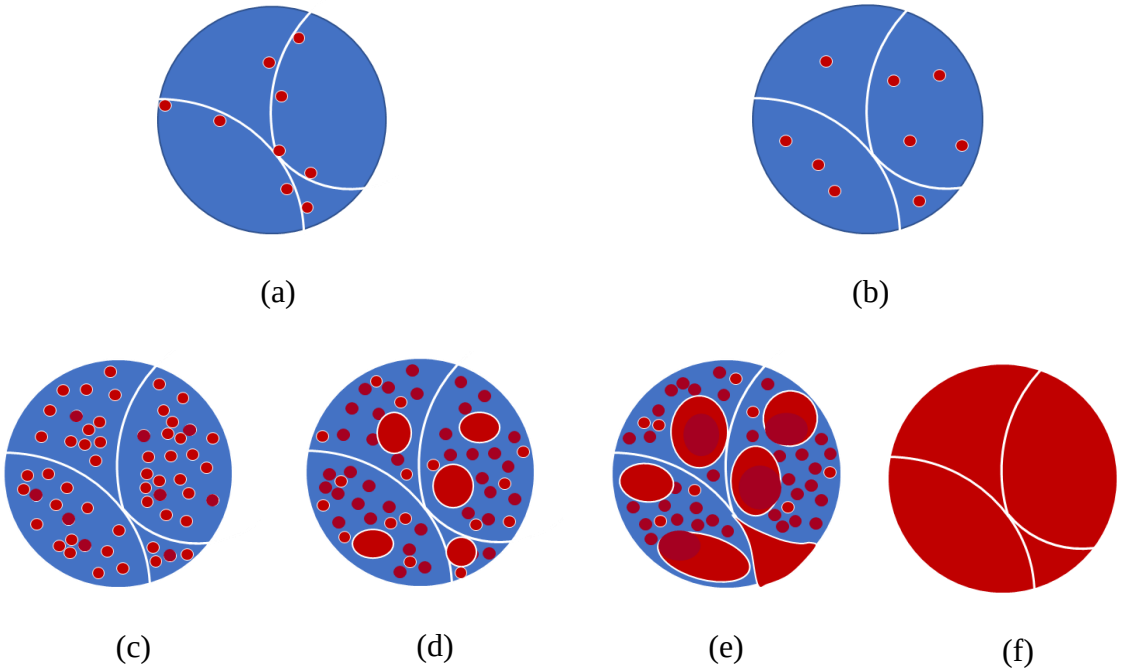

Figure 2.5: Nucleation and growth process where (a) is heterogenous nucleation, (b) is homogenous nucleation, (c-f) is initial homogenous nucleation followed by the growth process.

Diffusionless phase transformations are considered to be athermal as, although they often occur at high-temperatures they are thought to happen at such a velocity as to be independent of temperature [34]. Diffusionless kinetics are dependent on the nucleation and growth stages. However, as diffusionless transformations are considered to occur close to the speed of sound [34], they cannot be easily modelled analytically. Instead, the kinetics are dictated by the phenomenological theory of martensite transformation (PTMT), which is based on the formation of martensitic steel. PTMT is used to explain how rapid movement can occur within the crystal lattice to cause such significant microstructural changes in a short time period [35]. The model employs the original Bain deformation theory, describing lattice distortion, to identify the mechanism of deformation which governs diffusionless alloy phase transformations [36]. Recent studies using X-ray diffraction suggest that PTMT is closely representative of the martensite transformation in carbon steels [36]. However, further data is

needed to understand the kinetics of these diffusionless transformation. Due to the speed of the microstructural evolution, diffusionless transformations will not be the focus of this thesis.

Similarly, diffusion-driven solid-solid phase transformations can also be modelled via nucleation and growth. Additionally, the kinetics can be simply quantified analytically using the Johnson-Mehl-Avrami-Kolmogorov (JMAK) model,

$$f = 1 - e^{-kt^n} \qquad \textit{Equation 2.3}$$

where f is the volume fraction transformed, t is the transformation time, k is a temperature dependent constant that represents the influence of the heating rate on the nucleation and growth rates of austenite and n is the Avrami exponent of the equation [37], the derivation of which can be found in the appendix of Chapter 2. The solution for the JMAK model [38], Equation 2.3, predicts the volume fraction of the new phase during solid state isothermal phase transformations [7][39]. The JMAK equation assumes all transformations occur by nucleation and diffusion-controlled growth, where one phase disappears as a consequence of the new phase formation [37].

A simplified version of the JMAK, used for quantifying the phase change from ferrite to austenite specifically, is the Austin-Rickett (AR) equation [40],

$$\log\left(\frac{f}{1-f}\right) = k\log t + c \qquad \textit{Equation 2.4}$$

where f is once again the fraction of the transformation phase, t is time, k is a heating constant, and c is a temperature-dependent constant [40]. The AR equation is based on experimental results obtained from the decomposition of austenite at constant temperature via a case study of the existing data. The data indicate that the relationship between phase volume fraction and time could be plotted on a log-log graph as a straight line, which produces the expression for the AR equation, Equation 2.4 [40]. The JMAK and AR models for diffusion-

driven phase transformations have been used extensively to quantify *ex situ* phase transformation kinetics, as well as some *in situ*, using differential scanning calorimetry (DSC), dilatometry [7] and *in situ* transmission electron microscopy (TEM) data [37]. However, it has previously not been possible to collect larger, statistically significant, microstructural data sets during diffusion-driven phase transformations, which would further verify these models [41]. This will be investigated in this thesis.

2.4.2 Steel Phase Transformations

Phase transformations are a critical part of the heat treatment process of carbon steel. An understanding of the governing kinetics behind each transformation is key to enabling microstructural manipulation during heat treatment to produce favourable properties [7]. As discussed in Section 2.4.1, most phase transformations are governed by the nucleation and growth process and can be categorised as either diffusion-driven or diffusionless transformations [41]. However, the composition and original phase microstructure also have a distinct effect on the microstructural evolution during the transformation and are often unique to each phase formation [42]. This project focuses on the phase transformations of ferrite / pearlite to austenite and martensite to austenite; the specific kinetics and corresponding microstructural evolution relating to these transformations are discussed below.

Ferrite / Pearlite to Austenite Phase Change

The formation of carbon steel austenite from a ferrite or combined ferrite / pearlite phase is a diffusion-driven process via nucleation and growth [43]. During heat treatment, the transformation into the austenite phase has a significant impact on the final microstructure and equivalent material properties [33]. Hence, an understanding of the kinetics and microstructural evolution governing this phase formation is beneficial in generating favourable materials.

The austenite formation from a single phase of pure ferrite in hypoeutectoid steel has been extensively studied both *in situ* and *ex situ.* Studies concluded that nucleation occurs preferentially at austenite grain corners, followed by edges and then boundaries [44][7]. More recently, *in situ* heat treatment studies on the ferrite to austenite to ferrite phase changes indicate that the phase transformation of ferrite to austenite occurs preferentially at the triple junction, with the majority of new austenite grains forming around one ferrite mother grain [45][46]. During *in situ* experiments on carbon steel, it has also been observed that the growth kinetics of austenite to ferrite were faster than that of ferrite to austenite during cyclic heating [46]. However, this may not apply to all steels as observations of a hot rolled alloy steel indicated that the phase change from austenite to ferrite had the same average velocity as from ferrite to austenite and produced similar qualitative data to that found in dilatometry [47][45]. The differences in these two studies highlight the effect microstructural features have on the overall kinetics of the phase transformation and suggest that the presence of multiple phases during this transformation will impact the overall austenitic formation.

Understanding the microstructural evolution and corresponding kinetics of the pure ferrite to austenite phase transformation provides a good basis for investigating the ferrite / pearlite phase change. Dilatometric analysis coupled with the use of the JMAK model is commonly used to study phase changes. In the case of the ferrite / pearlite to austenite transformation, dilatometry data indicate a two-stage process of pearlite dissolution followed by the transition of pure ferrite grains into austenite [48]. These findings are further supported by microstructural data captured by interstitial rapid cooling after a short heat treatment, indicating the initial formation position of austenite with respect to pearlite and ferrite grain boundaries [49][50]. However, as has been conducted on the ferrite to austenite phase change, real-time microstructural observations are necessary to fully capture the specific grain evolution behaviour during this transformation [51].

Martensite to Austenite Phase Change

The reversion of martensite to austenite is of great interest to industry as it has been reported to cause substantial grain boundary strengthening [52], grain boundary refinement and a high dislocation density of reversed austenite [49][53], which all result in a high strength and more ductile material [52]. The effect applied is dependent on the mode of initial martensitic formation, and hence there is strong interest in studying the reversion process and its kinetics [54].

Current phase-field models indicate that the reversion martensite to austenite phase transformation is a function of the annealing temperature and time where at higher annealing temperatures (975-1010 K), reversion is much faster, and a greater volume fraction of martensite reverts to austenite. The phase-field model also indicates that reversion begins at the martensite lath boundaries and proceeds inwards over time [55]. The authors noted that the model also showed good agreement with localised *in situ* TEM hot stage experiments, dilatometry and X-ray diffraction [53][54]. These *in situ* methods also indicate a heating rate dependent transformation. Below a heating rate of 10 K/s, the reverse transformation is diffusion-driven, whereas above this rate, it is diffusionless and forms via a shear mechanism [54]. This indication of a diffusionless transformation suggests that the martensite to austenite phase change may not follow the JMAK or AR phase transformation equations. The use of *in situ* high-temperature SEM techniques to gather real-time microstructural evolution data would provide insight into the kinetics of this phase change, enabling further development of the current martensite reversion models.

2.4.3 Principles of Magnetic Phase Transformations

Phase transformations are not always accompanied by a rearrangement of microstructure as they simply refer to a change of thermodynamic equilibrium. Hence, during heat treatments, metals and alloys may also undergo a magnetic transformation. The most common magnetic phase change is the relationship between the paramagnetic and ferromagnetic phases, which undergo transformations via heating and cooling [56].

A ferromagnetic crystal is stable due its low total crystal free energy despite the destabilising effect of the magnetic interaction. Ferromagnetism occurs because the close ordered proximity of atoms within certain materials create an internal magnetic field, as first proposed by Weiss in 1907 [57], which is retained after the removal of the external magnetic field. This internal magnetic field is strong enough that all unpaired electrons in each atom not only align in parallel with each other within individual atoms (as in paramagnetism) but align with all other unpaired electrons in other atoms. The internal field occurs due to a parallel alignment of the elementary magnetic dipoles. The overall magnetic dipoles of each atom are a combination of individual electron spin about its axis, electrons circulating about the nucleus and the rotation of positively charged atoms in the nucleus [58]. Hence, while in paramagnetism materials can become magnetised in a magnetic field but lose this property once the field is removed, in ferromagnetism the material retains these magnetic properties after removal of the magnetic field [56].

The transformation of ferromagnetic to paramagnetic occurs during heating. Here, the magnetization changes according to the Curie-Weiss law [57]. The transition attributed to this magnetic transformation was first observed by examining the change in the specific heat capacity of nickel with temperature. This experiment produced a second order transition using the Ehrenfest criteria showing a lambda-shaped specific heat capacity versus temperature graph during the magnetization transformation [57][59]. The point at which the

transformation occurs is known as the Curie temperature; after this point, the thermal agitation begins to break down the electron alignment until it is destroyed, consequently decreasing the metal's magnetization with increasing temperature. At this point, electron spins are randomised by thermal energy and the dipoles are not aligned [60]. This transition is considered to have some effect on other electrical and magnetic fields, such as within an SEM [58].

Examining the Curie temperature transition point, experimental data has shown that nickel's magnetization stays constant up to 150 °C (~40% of Curie temperature) [57][56]. After this point nickel's magnetization decreases with increasing temperature until nickel reaches its Curie temperature, estimated experimentally to be between 350 °C and 360 °C [57][61]. The magnetic properties of iron, and hence plain carbon steels, are also dictated by the Curie-Weiss Law [57] and as a result, like nickel, are temperature-dependent. At room temperature, iron is ferromagnetic, but as it reaches the Curie temperature, T_c, of approximately 1043 K (~770 °C), it undergoes a magnetic ordering transition to paramagnetic [62]. A similar magnetic transition, from ferromagnetic to paramagnetic, is observed in steel, when in their ferrite phase, at 1041 K (~768 °C) [7].

2.5 Grain Growth

2.5.1 Grain Growth Kinetics

Grain growth occurs in order to reduce the overall internal energy of a system by decreasing the number of grain boundaries, via reduction in the number of grains [63]. Types of grain growth can be categorised into normal and abnormal. Normal grain growth refers to homogenous grain growth throughout the specimen while abnormal grain growth indicates a heterogenous distribution where some grains grow significantly faster than others [64]. In either case, grain growth is a diffusion controlled process [15], which is common during the phase transformation of metals and alloys owing to the temperatures at which phase transformations occur [1].

The kinetics of grain growth can be modelled by the power law,

$$d^n - {d_o}^n = kt \qquad \textit{Equation 2.5}$$

which was originally derived by Burke and Turnbull [65], where d is the average grain diameter at a given time t, d_o is the grain diameter at $t = 0$, and k and n are material parameters. $k = k_o e^{\frac{-Q}{RT}}$, where Q is the activation energy, R is the gas constant, T is the temperature at which grain growth occurs, and k_o is a material constant [65]. Burke and Turnbull's original derivation was for a parabolic law ($n = 2$), where it was assumed that: the material was homogeneous, all forces acting on the boundaries were due to surface curvature, and the average radius of curvature of a boundary was proportional to grain diameters while the rate of the change of the diameter was proportional to the driving force [66].

Since this, research has indicated that the parabolic law does apply to the increasing size of a soap bubble when it is frothed, suggesting that the analysis and assumptions were correct [65]. Furthermore, Monte Carlo simulations of grain growth have yielded similar growth kinetics predicted by the parabolic law [67]. However, further experimental studies

on metals and alloys produced a variety of *n* values ranging between 1 and 10 where, even for the purest of metals *n* rarely equals 2. Research indicates that this is likely due to the effect of other features and imperfections within the grain structure, such as precipitates or dislocations, which may limit boundary mobility or have a pinning effect [65][68][69].

Further studies on grain growth have attempted to characterise the microstructural phenomena that dictate the value of the material parameter *n*. It is widely accepted that the value of *n* changes with heating conditions [70]. Grain growth *n* values are also anticipated to be affected by the size and distribution of second-phase particles, which subsequently determine the ease at which grain growth can occur. The smaller exponent values indicate that there are significant stable compounds within the material with second-phase particles generating a pinning effect limiting growth [71][72][73]. There are also some unique *n* values associated with specific microstructural evolution. One such example is described as abnormal grain growth, where a number of large grains grow rapidly at the expense of smaller ones; this is commonly associated with a linear distribution power law ($n = 1$) [74]. However, as with the other exponent values, the exact microstructural evolution driving the kinetics and the subsequent relationship to the original power law is unclear.

2.5.2 Effect of Precipitates on Grain Growth Kinetics

As well as being affected by multiple phases, the rate of grain growth can also be affected by the presence of external particles such as precipitates [75], as mentioned in Section 2.5.1. In some cases, the presence of these features can lead to grain growth retardation. One cause of grain growth retardation due to the presence of precipitates is known as Zener pinning, shown diagrammatically in Figure 2.6. Zener pinning occurs where a moving grain boundary intersects with a particle, and movement is therefore stopped or

'pinned' at the particle. This phenomenon occurs because, when a moving (growing) grain boundary intersects with a particle, that grain boundary's area is reduced, and the grain becomes pinned at the point at which it intersected with the particle. For that grain boundary to continue to move at the point of intersection, a new grain boundary would have to form around the precipitate; this is not energetically favourable for the system as the aim of grain growth is to reduce the number of grain boundaries. Hence, this leads to the slowing, and in some cases prevention, of grain growth as the grains become pinned at specific places, preventing further movement of the grain boundaries [76].

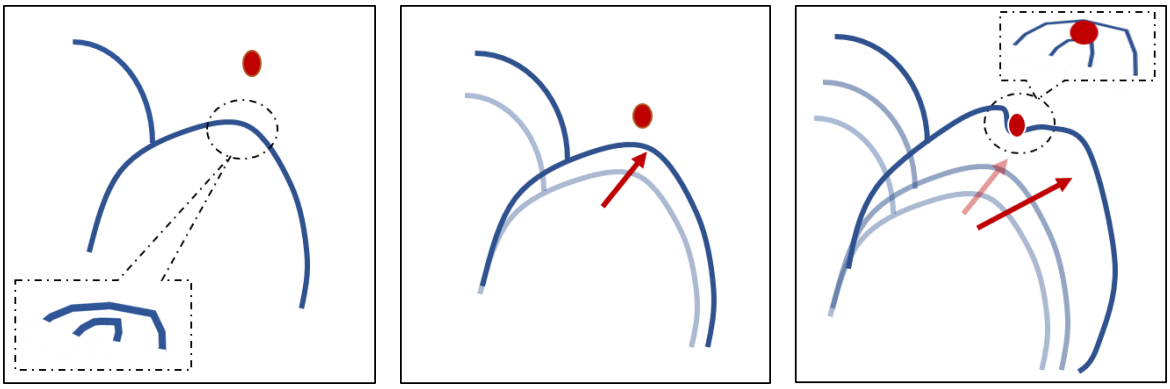

(a) *(b)* *(c)*

Figure 2.6 The classic process of Zener pinning of a grain boundary when a precipitate is present within the sample showing (a) initial grain boundary, (b) normal movement when precipitate is not present, and (c) resulting pinned grain boundary movement around the precipitate.

2.5.3 Grain Growth during Heat Treatment of Steel

Grain growth commonly occurs during the heat treatment of steel and it is well known that grain growth correlates to heat treatment parameters including time and temperature. Grain growth also controls the physical and mechanical properties produced [77]. Additionally, it is widely accepted that grain growth of steel, over time, can be modelled by the general power law equation (Equation 2.5).

Ex situ studies on carbon steel post-heat treatment report a variety of power law constant (n) values between 2 and 8 [78]. Subsequent attempts at modelling have had reasonable success in predicting the growth within the austenitic region of carbs based on a combination of thermal modelling and *ex situ* data [79]. Recent, *in situ* high-temperature studies of steel have examined the ferrite to austenite phase change using EBSD. Such studies have carried out cyclic austenite to ferrite to austenite phase transformations of a few localised grains, which demonstrates austenite grains shrinking upon cooling as ferrite grains grow during the transformation (Figure 2.7) [80]. However, there is little understanding about microstructural evolution of the grain size during the ferrite to austenite to ferrite phase change or the effects of a secondary phase, such as pearlite, being present, as well as once the final microstructure is austenite.

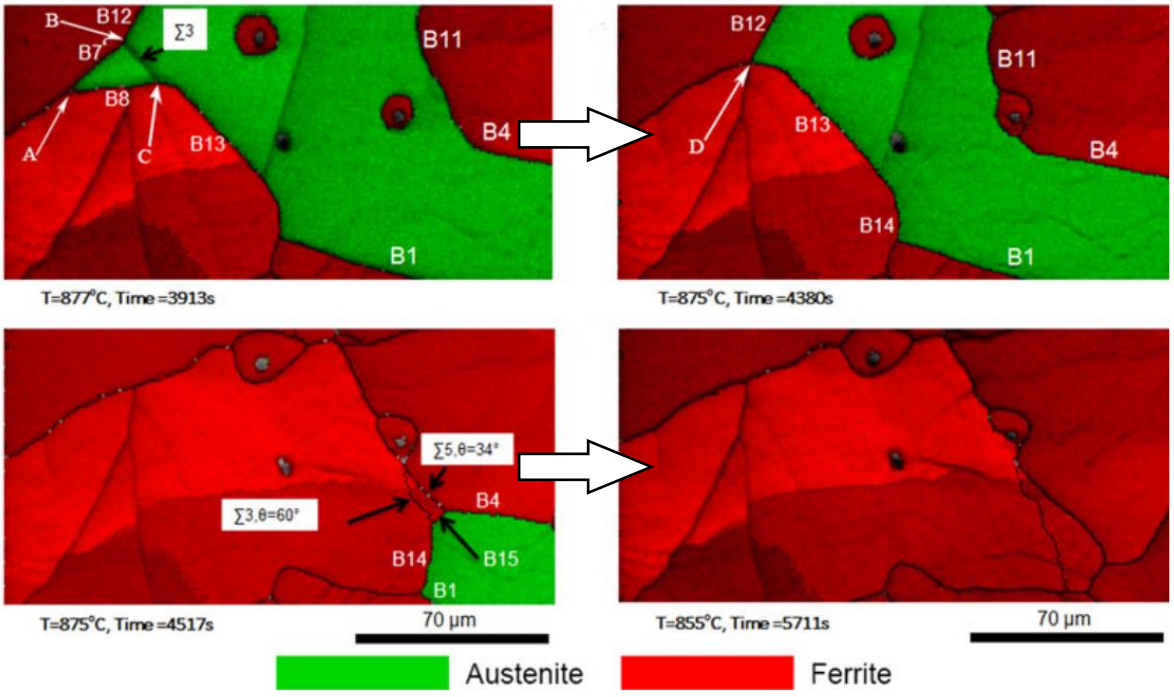

Figure 2.7: Two cyclic loading results of localised austenite to ferrite transformation during cooling, where austenite shrinks at the triple junction point as ferrite grows. (Top) a mix of ferrite and austenite at 877 °C after 65 minutes' heating. After a further 13 minutes of cooling, the small ferrite grain (arrowed) has been absorbed by the larger austenite grain at the triple junction point. (Bottom) a similar formation in the same position later in the cooling cycle after 15 minutes of cooling and after 35 minutes cooling to be fully transformed to ferrite [80].

2.6 Thermal Etching

2.6.1 Stationary Boundaries

Thermal etching often occurs on the surface of polished, heat treated carbon steel and has been previously used to quantify grain sizes *ex situ*. It is defined as the development of a groove on the surface of a hot polycrystal where a grain boundary emerges to intersect the surface through exposure to elevated temperatures. The grain boundaries impinge on the specimen surface because of equilibration of the triple junction between the grain boundary and the free surface. Here, the surrounding specimen surface rises away from the boundary when it reaches a critical angle, as shown in Figure 2.8 [81].

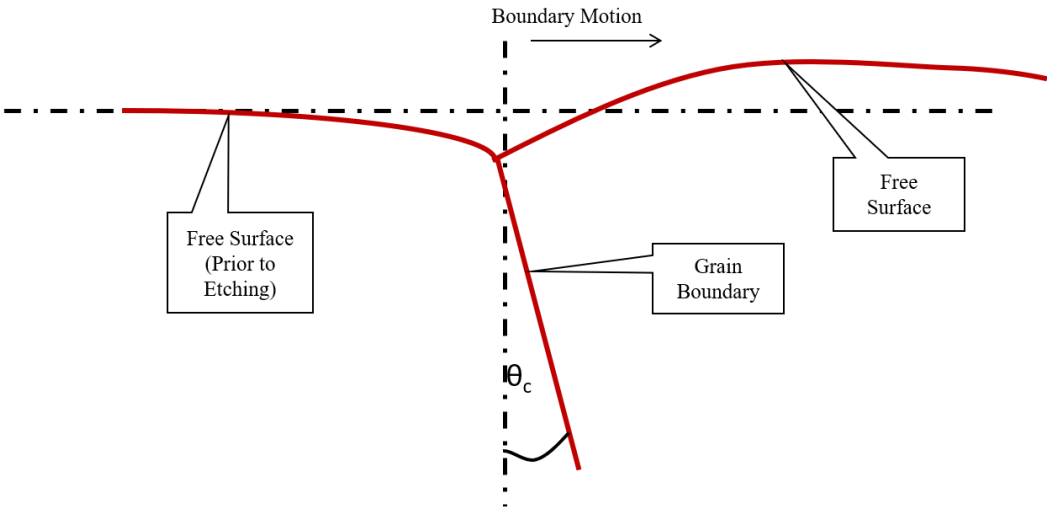

Figure 2.8: Diagram of the profile of a grain boundary as thermal grooving occurs. This is dictated by the critical angle Θ_c.

The theory behind the development of these surface grooves for stationary grain boundaries was first investigated by Mullins, by considering the relationship between surface diffusion potential and the driving force which facilitates a change of shape. By combining the principles of the Gibbs-Thomson formula of chemical potential with the Nernst-Einstein equation, Mullins derived a general PDE for the rate of change of the profile of a surface via surface diffusion for a stationary boundary that was dependent on temperature, curvature and

surface tension. The change in curvature is defined with respect to the change in depth. Mullins' PDE derivation makes the following physical assumptions:

- The system is closed and contains a metal polycrystal in quasi-equilibrium with its vapour.
- The properties of an interface are independent of its orientation with respect to the adjacent crystal.
- The only mechanisms associated with the transport of matter are evaporation-condensation and surface diffusion.
- Slope angles are assumed small.
- The process of grooving is adequately described by macroscopic concepts as surface curvature and surface free energy.
- Ignore crystalline imperfections.
- There is a negligible flow of matter out of the boundary; the boundary's role is to maintain the correct equilibrium angle.

Assuming these physical assumptions apply, a PDE, with $y(x,t)$ representing the groove profile where x and y are the cartesian coordinates and t is time can be subsequently solved using the boundary conditions $y(x,0)=0, y'(0,t)=\tan(\theta)=m, y''(0,t)=0$ and the small angle approximation to produce a relationship between the groove profile, time and temperature in the form of Mullins' groove profile equation,

$$y = m(Bt)^{0.25} z\left[\frac{x}{(Bt)^{0.25}}\right] \qquad \textit{Equation 2.6}$$

where m is an experimental constant, t is time, $B = \frac{D_S \gamma_S \Omega^2 \nu}{KT}$ where D_s is surface diffusion, K is Boltzman's constant, T is temperature, Ω is volume per atom, ν is the number of atoms per unit of surface energy, and γ is surface tension. $z = \sum_0^\infty a \frac{x}{(Bt)^{0.25n}}$ is the

summation of atoms in the *x*-direction as they vary with time and temperature [81]. The derivation of Equation 2.6 can be found in the appendix of Chapter 2.

2.6.2 Moving Boundaries

Mullins' theory of grain boundary grooving for stationary boundaries is widely accepted owing to the large amount of experimental evidence where the equation has been used to determine the surface diffusion coefficient and subsequent groove depth [82]. However, thermal etching also occurs if the grain boundaries are not stationary and Mullins stipulated that, for moving grain boundaries some of the assumptions for Equation 2.6 would not apply [83]. Thus, this theory was re-examined by Mullins and then later investigated by Allen, who derived an equation to describe the velocity of grain boundary movement [84],

$$v_o = B\left(\frac{M}{w_l}\right)^3 \qquad \textit{Equation 2.7}$$

where $v_{o,}$ is the velocity of grain boundary movement which is dictated by the maximum size of thermal etching of a moving grain boundary w_l, M is a constant and B is defined as in Equation 2.6 [84]; A full derivation of Allen's and Mullins' work on moving grain boundaries can be found in the appendix of Chapter 2.

For moving grains, Mullins also indicated that the size of the grain would likely impact its ability to move with the thermally etched boundary. This is based on the principles of the catenoid, which depend on the ratio of: the radius of curvature of circulator trace to the sheet thickness. The curvature is defined as the angle of the groove, and the sheet thickness is the depth of the groove, demonstrated diagrammatically in Figure 2.9. Theoretically this means that the ratio of the area of the grain, a, to the radius of the groove, r, must be greater than the critical angle for which the grain can pull away from the current grooved grain boundary, θ_c. Thus, if the curvature ratio is sufficiently small, the grain boundary is able to grow, producing

a second etching where the new grain boundary becomes stationary, known as 'ghost etching', or simply by dragging the first etching with it [83]. Both phenomena have been observed experimentally [85][86].

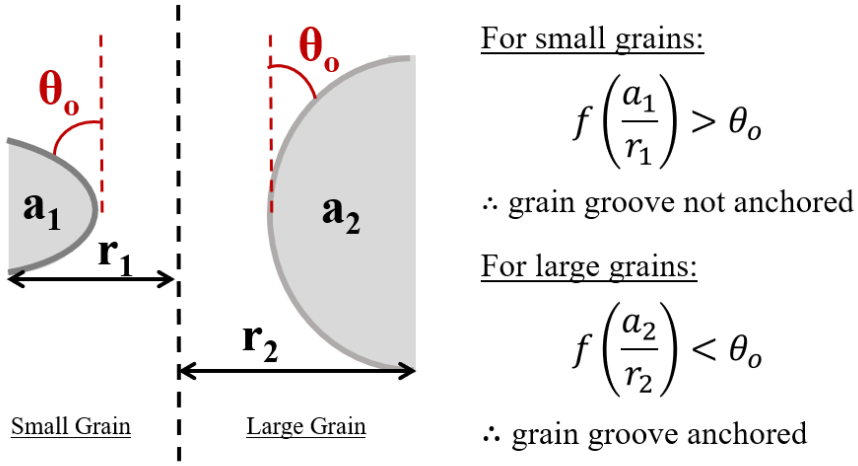

Figure 2.9: The principles of a catenoid used to demonstrate the point at which a thermally grooved grain boundary may hinder grain growth.

2.6.3 Experimental Evidence

The experimental evidence relating to stationary grain boundaries is widely accepted and indicates that Mullins' theory of stationary grain boundary grooving applies [82]. However, for moving grain boundaries, grooving becomes much more complex and has produced mixed experimental results, particularly with regards to how grooving may impact subsequent grain growth. Experimental data indicate that factors like the atmosphere or the appearance of precipitates may also have an influence. For example, Aristov *et al.* considered the motion of a grain boundary with and without etching, and indicated that the movement was quite sporadic when thermal etching occurred [87]. Another example is the effect of faceting on thermal grain boundary grooving, observed by examining thermally etched tungsten using atomic force microscopy (AFM). It was noted that grooves within the tungsten

that developed between faceted and unfaceted grains produced different growth kinetics to those predicted by Mullins and Allen [88].

Additionally, grain boundary grooving is a surface effect and has therefore also been investigated with respect to thin films. In one such case, by adding titanium oxide to a film of gold, data showed that the titanium oxide layer underneath the gold inhibited grain growth at 200 ºC, when compared to the grain growth in a thin film of pure gold. It was observed that some oxygen was present in the grain boundary grooves for the titanium oxide film compared to the pure gold film, indicating that oxidation of the grooves may inhibit grain growth [89]. Studies of the surface effects under heat treatment specifically suggest that, at certain temperatures, oxidation can also occur [89], even under vacuum. Hence, it is considered that this may further impact thermal grooving and subsequent grain growth. The examination of these surface effects *in situ* during the formation of the thermal grooving is required for a greater understanding of the impact on the surface microstructure.

2.7 Thermal Oxidation

2.7.1 Principles of Thermal Oxidation

In this thesis, thermal oxidation refers to the high-temperature oxidation of metals and alloys, which commonly occurs during heat treatment. The phenomenon is a diffusion-driven process, where oxidation of the orignal material forms on exposed surfaces at elevated temperatures [90]. The presence of thermal oxidation is quantified by the thickness or weight of oxide across a surface with respect to temperature and time. The Pilling-Bedworth law, first formulated from experimental results [91], is most commonly used to model thermal oxidation of metals and alloys [92]. The parabolic form of the equation is,

$$w^2 = k_x t + w_0^2 \qquad \textit{Equation 2.8}$$

where w is the additional weight of oxidation gained at a specific temperature, w_o is the initial weight of oxidation, t is the time and k_x is the parabolic constant defined by the Arrhenius equation where $k_x = k_o e^{\frac{-Q}{RT}}$, Q is the activation energy, R is the gas constant and T is the temperature at which the oxidation occurs [92].

The morphology and microstructure of thermal oxidation is specific to individual metals and alloys, and is therefore elaborated on in Sections 2.7.2 and 2.7.3 for nickel and steel respectively; the two materials which are the focus of this thesis.

2.7.2 Thermal Oxidation Studies: Nickel

The thermal oxidation of nickel is highly temperature dependent. Extensive experimental work in the temperature range of 500-1400 °C demonstrates that oxidation of nickel above 1100 °C is concluded to be parabolic and the rate of oxidation is determined by bulk diffusion. At temperatures below 1000 °C, the oxidation kinetics indicate sub-parabolic

behaviour, where the oxidation rate decreases significantly faster over time than for high-temperature oxidation [93].

Furthermore, at these temperatures, oxidation is also found to be dependent on surface treatment and environmental pressure. The different surface treatments produce a range of surface morphology and texture. In one study, there was a difference of up to four orders of magnitude between oxidation rates, depending on the cavity formation during the surface treatment pre-thermal oxidation, and the temperature at which thermal oxidation occurred [94]. Oxygen pressure dependence also changes with temperature; higher temperatures are less affected by lower oxygen pressures compared to results under atmosphere, Figure 2.10 [93].

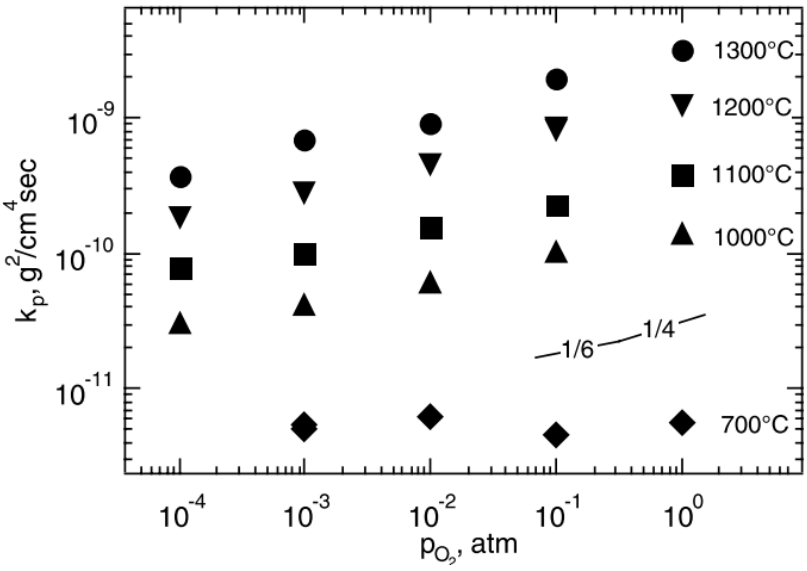

Figure 2.10: Variation of parabolic rate constant and thus level of oxidation as a function of ambient oxygen pressure at temperatures of 700, 1000, 1100, 1200 and 1300 °C for a study on thermal oxidation of nickel [93].

Overall, studies of thermal oxidation of nickel indicate a wide variety of time, temperature, pressure, and surface dependent results that, in some cases, have been documented to impact the surface microstructure [93]. However, when operating under vacuum at temperatures below 1000 °C, data conclude that there is negligible thermal oxidation present [93]. Owing to the *in situ* SEM heating studies in this thesis being conducted under vacuum conditions at temperatures below 1000 °C, thermal oxidation of nickel will not be the focus of this thesis and, based on the literature, is not anticipated to impact imaging.

2.7.3 Thermal Oxidation Studies: Steel

The formation of oxide layers during heat treatment in air and oxygen-rich environments, thermal oxidation, often impacts the resulting surface properties of carbon steel. Studies of oxidized carbon steel surfaces confirm that theories concerning the kinetics and mechanisms with regards to rate are valid and well understood [95]. Cross sections taken of oxidised carbon steel surfaces using SEM and AFM demonstrate that three main oxide layers form during the heat treatment of carbon steel: wüstite, haematite, and magnetite. The exact combination and composition of these layers is dependent on time, temperature, oxidation level, and pressure. For short periods of heating, the formation of layers is not dissimilar to that occurring in pure iron, generating an initial wüstite scale layer and, after a longer period, leading to layers of haematite and magnetite. During further prolonged heating periods, wüstite scales are less defined and eventually the scales interfere with each other; at temperatures of 850 °C and above this temperature, the oxide scales may result in blistering [92]. An example of the cross section of oxidised steel is shown in Figure 2.11.

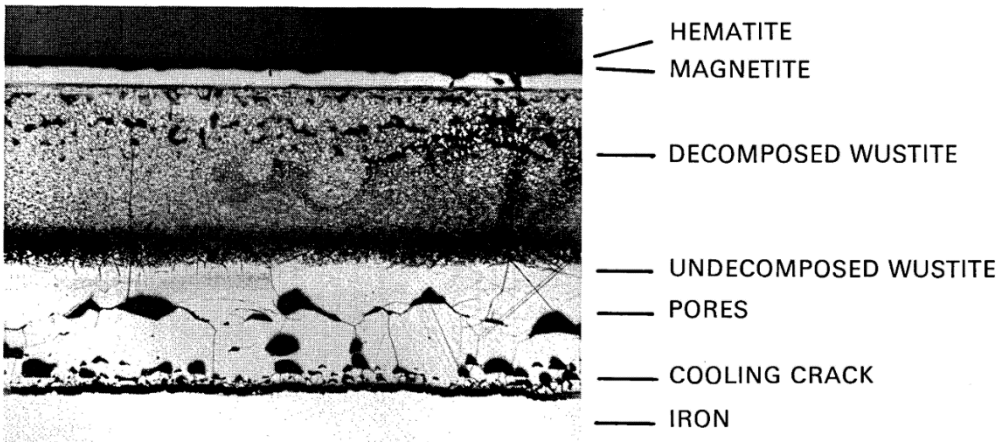

Figure 2.11: Thermally oxidised steel structure over a longer heating time period leading to pores [95].

Blistering is the appearance of pockmarks or irregular shapes on the surface of thermally oxidised carbon steel, formed of a cavity between the scale and a substrate composed of haematite and magnetite layers with some wüstite [92]. Examples of blistered steel are shown in Figure 2.12. Studies indicate that a gas phase, produced either from carbon oxidation or inert gas in the surrounding atmosphere [96], is necessary for blistering to occur [92]. Without the gas phase, it is thought that, after blister formation, the cavity may be healed by annihilation mechanisms (creep / plastic flow of the scale) [97]. This healing mechanism is believed to explain why there are conflicting data on blistering behaviour [98][96]: blisters may have formed during oxidation but have subsequently healed. Additionally, oxidation surfaces produced under low gas atmospheres also show an absence of blisters. Again, this is thought to be due to the lack of gas available to sustain blister formation during the cooling process, resulting in healing [98].

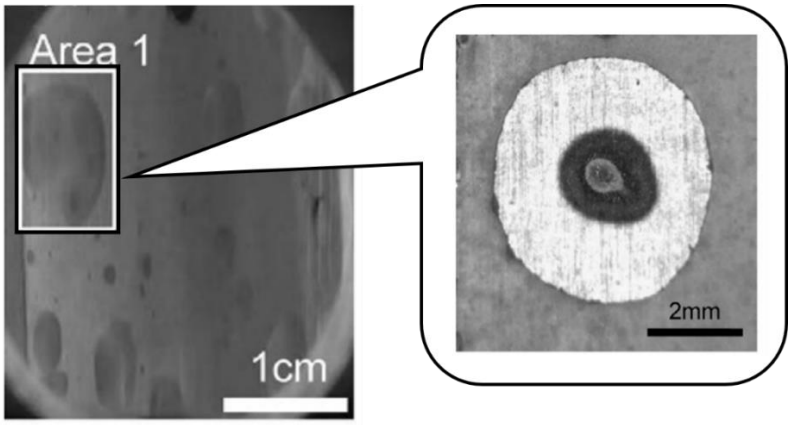

Figure 2.12: Blistering formed on the surface of steel heat treated at 950 °C in an air atmosphere environment for 120 s. Inset is a zoomed-in image of the blister in 'Area 1' [99].

To mitigate against the formation of these oxide layers, carbon steels are often heat treated under what is commonly described as 'fine' vacuum (~10^{-4} mbar) [100]. However, it has been documented that some oxidation of the surface can still occur even at these vacuum levels [101]. This is due to the 'fine' vacuum environment being formed in a chamber that has initially contained air; as such, sufficient levels of oxygen remain to cause oxidation during the heat treatment process. Under such conditions, oxidation has a significantly slower initial oxidation rate compared to the oxidation rate in pure oxygen or air [102]. Additionally, the oxidation scale composition is heavily dependent on pressure and oxygen levels, as identified using a combination of neutron diffraction *in situ* studies and electron spectroscopy. *In situ* neutron diffraction measurements have provided compositional data that indicate that under low oxygen / air pressures above temperatures of 570 °C, the dominant layer is wüstite [102]. To compliment the compositional *in situ* data available, attempts have been made to understand the morphology of steel formed *in situ* [103][104]. One such study focused on the oxidation of carbon steel within the first 30 seconds of hot-rolling using a CCD camera. This demonstrated that the grain boundaries appeared visible following exposure to high-temperature, indicating that diffusion through steel grain boundaries may influence oxide formation [103].

2.8 Conclusions

This literature review, focusing on material behaviour at high-temperature, indicates that there is further scope to investigate microstructural evolution under experimental conditions. The addition of real-time SEM data would provide insight into the current time-temperature dependent kinetic models such as the power law for grain growth, the JMAK law for phase change, and the Pilling-Bedworth equation for oxidation, to name a few, from a crystallographic, morphological and microstructural perspective. Research suggests that current studies, which make use of such *in situ* microscopy techniques as TEM and X-ray tomography, have provided a significant contribution to the understanding of microstructural evolution and how processes can be adapted to create favourable microstructures that display specific properties. Hence, this is an aspect of the microscopy field that is continuing to develop with an emphasis on metals and alloys; the focus of this thesis.

Evaluation of the literature surrounding steel and nickel, the materials chosen for this thesis, indicates that there is scope to both develop novel *in situ* high-temperature SEM techniques and advance scientific understanding of the microstructural changes during high-temperature processes (such as heat treatments). In the case of nickel, the literature documents that it has a highly stable microstructure when operating at temperatures less than 900 °C making it ideal for developing novel imaging techniques. Moreover, the common use of nickel in modern alloys provides a basis to study more complex nickel based microstructures at temperature using these *in situ* high-temperature imaging techniques. Examination of the current studies on steel shows that it is a favourable material for investigation using *in situ* high-temperature SEM owing to the drastic changes in microstructure at temperature. Moreover, there is a distinct lack of data and understanding of the effects of heat treatments on the microstructure with respect to grain growth, grain orientation, and phase change during the heating and cooling processes. Understanding the microstructural developments in these

three areas, and how they relate to each other, will provide an insight into the structure-property-composition relationship of steel and facilitate improved heat treatments to generate preferential properties. Investigations into steel heat treatment will also focus on the development of new *in situ* SEM techniques to enable imaging at high-temperature accompanied by *ex situ* microscopy methods. The current methodologies used to examine microstructural and compositional changes are discussed in Chapter 3.

Chapter 3

Literature Review of Experimental Techniques

3.1 Introduction to Microscopy

The use of microscopy in material science, and more specifically in this thesis, has enabled the observation and characterisation of materials' composition and physical properties, as well as dynamic behaviour [105]. In general, microscopy is the examination of objects by means of a microscope, an instrument that provides an enlarged image of an object to show detail not otherwise visible to the naked eye [106]. The ability to enlarge or 'magnify' an object has existed since Roman times, when glass with a thicker centre and thinner edges was used to make objects appear larger when viewed through the glass. These early forms of the lens were referred to as 'magnifiers' [107]. The invention of the microscope occurred significantly later towards the end of the 16th century when the Dutch lens makers Zacharias and Hans Janssen developed a compound microscope, made up of several lenses with a magnification of 9× (Figure 3.1) [108][109].

Figure 3.1: The original three-lens microscope produced by Zacharias and Hans Janssen, now on display in Middleburg, Netherlands[109].

The three-lens microscope design led to multiple improvements in microscopy throughout the 17th century; most notably by Robert Hooke and Antonie van Leeuwenhoek. Hooke, one of London's best early scientists, designed and modified a three-lens microscope produced by London instrument maker Christopher Cock (Figure 3.2a). By adding a glass globe filled with water to focus the light from a flame onto the specimen, and hence to counteract the darkened images, the microscope facilitated image magnification between 20× and 50×. Hooke's work on microscopes led to the publication of his book, *Micrographia*, in 1965. *Micrographia* contained detailed drawings of life under the microscope, including a fly's head (Figure 3.2b [110]), snowflakes and a full stop printed on a page. In contrast to Hooke's multi-lens microscope, van Leeuwenhoek used several simple single-lens microscopes, some of which facilitated magnification by more than 250×, enabling him to study a range of natural objects, including animal tissue, blood, vinegar, and water. The investigations into water also led to the observation of eel-like creatures swimming in water, which are now identifiable as bacteria [110][108].

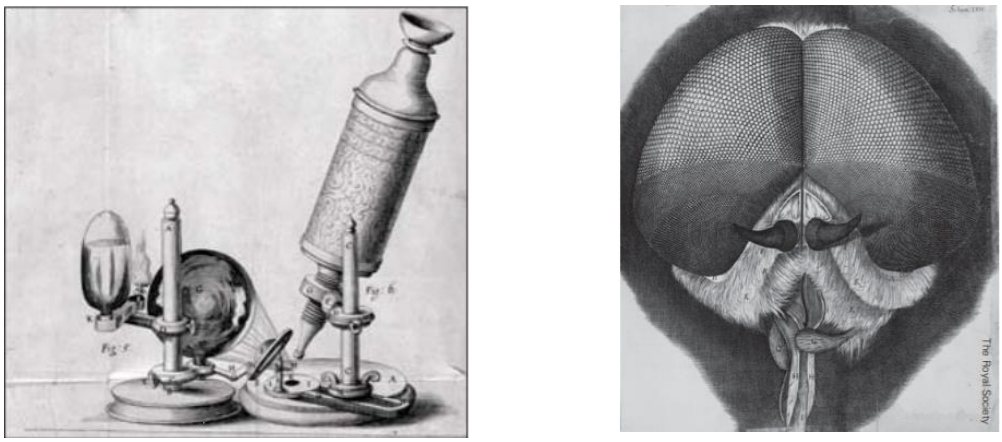

(a) *(b)*

Figure 3.2: Drawings from Hooke's book, Micrographia, *depicting (a) the microscope he used, and (b) a drawing of a fly's head as viewed under the microscope* [110].

The microscope continued to develop into the middle of the 19th century when the German company Zeiss began to manufacture the refined devices recognisable today [107]. However, these optical lenses were greatly limited in magnification owing to the use of visible light. Hence, in the 1930s, German scientists Max Knoll and Ernst Ruska's discovery that beams of electrons could be used instead of light rapidly increased resolution, and paved the way for the first electron microscope. By the mid-1940s resolutions as low as 2 nm had been achieved [111], which were attained using transmission electron microscopy (TEM). TEM technology utilised Knoll and Ruska's beam of electrons, but in this case the electrons passed through a very thin specimen, enabling the observation of features such as structure and morphology [112]. This development was shortly followed by the first scanning electron microscope (SEM) in 1965, which revolutionized the world of materials science [107]. A more detailed history of SEM can be found in Section 3.2.

Today, a variety of microscopic techniques are used to observe the microstructural evolution of materials, including optical microscopy, electron microscopy, atomic force microscopy (AFM) and focus ion beam (FIB) microscopy. A combination of these techniques facilitates the assessment of material properties and behaviours [105]. Furthermore, it is well documented that characterising the microstructure of materials, specifically metals and alloys, through the use of microscopy, advances the understanding of the subsequent physical and mechanical properties [77]. Thus, this chapter explores current microscopy and other supporting techniques documented within the literature for characterisation of materials, specifically metals and alloys at high-temperatures.

3.2 Scanning Electron Microscopy (SEM)

3.2.1 History of SEM

SEM is a form of high resolution microscopy that provides an understanding of a material's microstructure at resolutions as low as 5 nm [113]. The SEM principle was first proposed by Knoll in 1935 [114], before being prototyped by Manfred von Ardenne [115]. Von Ardenne's SEM evolved from Knoll and Ruska's TEM [116], with von Ardenne adding scan coils to the TEM source to facilitate scanning of a rastor pattern, recognisable as a scanning transmission electron microscope (STEM) [111]. The modern-day SEM was subsequently developed from the work of Vladimir Zworykin, James Hillier, and Richard Snyder in 1942, who recognised the ability to create an image from the reflected secondary electrons (SEs) if a thick sample were used (see Section 3.2.3 for details); their work predominantly focused on the examination of metals [117]. Zworikin, Hillier, and Snyder's SEM initially utilised a cold field emission sharp cathode as an electron source, but a lack of stability caused them to return to the thermionic electric gun (from a heated tungsten filament) [111], a set-up commonly used today. In 1967, Alec Broers' research at IBM led to the development of the LaB_6 gun (lanthanum hexaboride), as an alternative electron source to the tungsten filament, being both considerably brighter and longer lasting [118]. Advances throughout the 1970s and 1980s continued to make improvements to the SEM with a focus on contrast and processing through software development [117].

The main drawback of SEM is that it requires conducting materials for SEs to be reflected to produce an image. As such, biological and other non-conducting samples must go through a lengthy sample preparation process, such as gold coating, which may change the morphology of the sample. However, this all changed in 1988 when the first commercial environmental SEM (ESEM) was produced by ElectroScan Corp. The development of ESEM, also known as "wet", "leaky" [16], low vacuum (LV) or variable pressure SEM, has

revolutionised electron microscopy. It facilitates high resolution imaging of samples in their natural hydrated state, enabling the study of dynamic processes and mechanical responses [119]. SEM has since been further advanced through new detectors and software as a tool to examine the topology and topography of surfaces providing high quality images in a vacuum and, in the case of ESEM, a non-vacuum environment [113].

3.2.2 Operation of the SEM

The SEM operates by an electron gun producing a finely focused beam of electrons, which is accelerated by an anode and travels through two condenser lenses. The condenser lenses use electromagnetic fields to focus the beam onto the sample while under vacuum. The beam is then guided by a series of deflection scanning coils, an objective lens and apertures, concentrating it to a spot size of less than 10 nm [116]. These lenses facilitate the scanning of the beam across the sample's surface in a rectangular frame, referred to as the raster pattern [120]. The beam interacts with the specimen and produces a variety of signals, which are detected by X-ray, backscattered electron (BSE), SE and electron backscatter diffraction (EBSD) detectors; discussed further in Section 3.2.3. A diagrammatical representation of the basic SEM is shown in Figure 3.3.

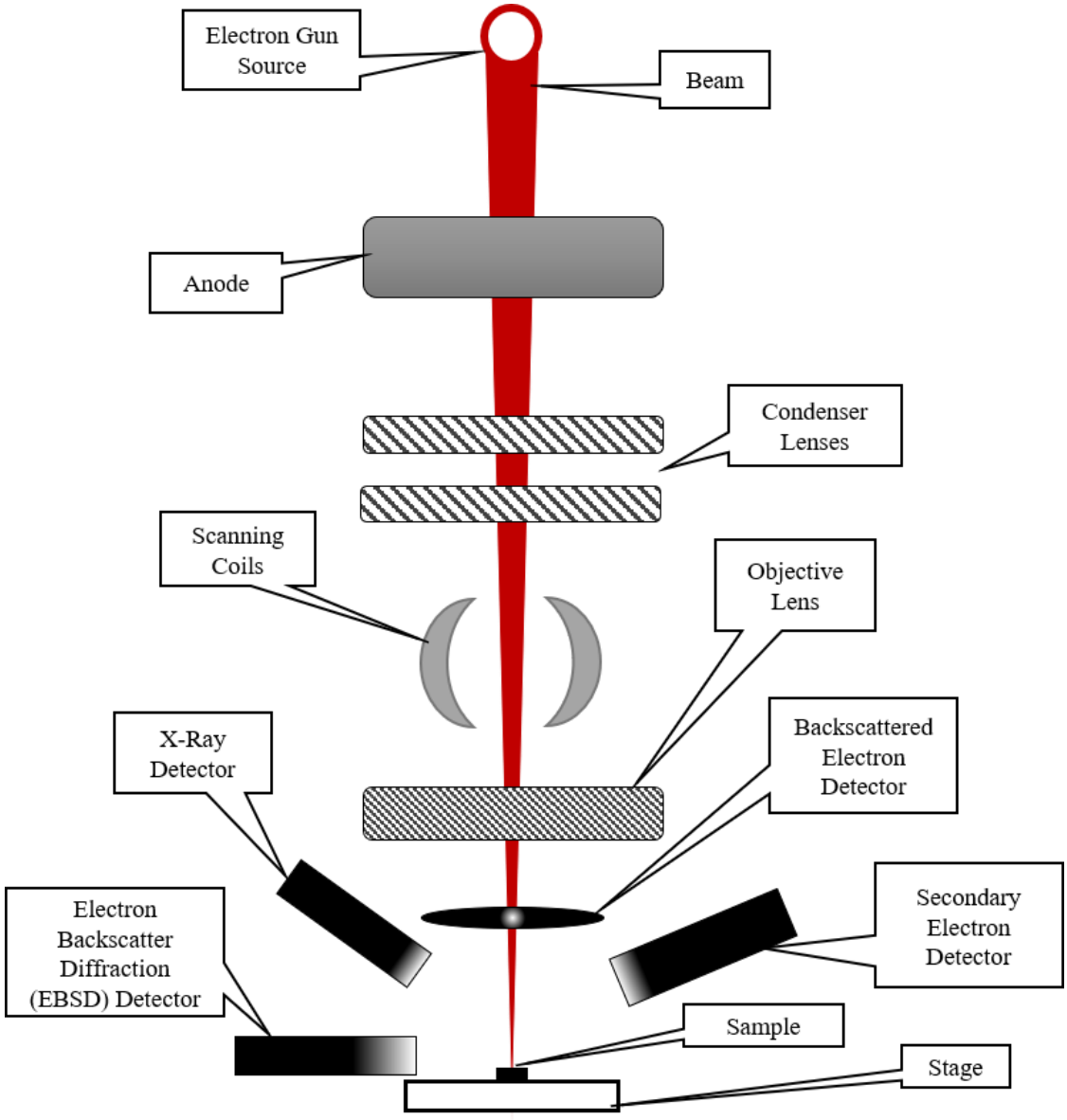

Figure 3.3: Key features of a scanning electron microscope (SEM)

Considering the operation of the SEM in more detail, it is important to document the effect that the type of electron gun source can have on imaging. There are two types of electron guns: thermionic and field emission, shown in Figure 3.4. Thermionic sources apply thermal energy to a source that is made up of either a tungsten filament or LaB_6 (lanthanum hexaboride) crystal. The application of thermal energy to the source enables the electrons to overcome the energy barrier between the metal and vacuum, and hence to produce a concentrated beam of electrons. These two sources are specifically chosen as they have a high

melting point and low work function[2]. Field emission sources create a strong electrical field, which pulls electrons away from atoms; there are two main types: cold field emission and Schottky. Cold field emssion guns generate a strong electric field concentrated on the tip of a single crystal of tungsten where electrons are forced out of the tip. A Schottky electron gun source uses a tip coated with ZrO_2, where a strong electric field is applied while heating, resulting in the emission of electrons [121].

(a) (b) (c)

Figure 3.4:SEM gun source types commonly used: (a) tungsten thermionic emission, (b) LaB_6 thermionic emission, and (c) field emission [122].

The main difference between thermionic and field emission sources is the image quality. The use of a field emission gun gives a more coherent beam with a concentrated emission of a few nanometres, compared to 50 µm for a tungsten filament, producing a higher brightness and an improved signal to noise ratio. Hence, field emission sources produce significantly higher resolution and higher quality images in comparison to its thermionic emission counterparts. However, field emission guns require a much higher gun column vacuum of 10^{-10} mbar compared with 10^{-5} mbar for a tungsten source. In addition, the lifetime of an field emission source is also longer when compared to a tungsten filament; 10,000 hours and 100-500 hours respectively [123].

[2] The work function is the minimum thermodynamic work (energy) required to remove an electron from its material to the surrounding vacuum.

As an alternative to the tungsten thermionic emission, LaB_6 sources still do not have the same resolution level compared to a field emission source but have an improved image quality when compared to the tungsten filament. The LaB_6 crystal has a lower work function than its tungsten counterpart (2.7 eV versus 4.5 eV) and thus at low temperatures produces a higher current density, resulting in images being 10× brighter leading to improvements in image quality. Furthermore, the LaB_6 source also has a significantly longer lifetime than the tungsten filament at around 1,000 hours. However, although LaB_6 crystals do not require as higher-quality gun chamber vacuum as a field emission source, they require a lower gas pressure in the vacuum than the tungsten (10^{-6} mbar) to prevent oxidation [124]. A comparison of the properties of these different sources is provided in Table 3-1.

Gun Type	***Tungsten***	***LaB_6***	***Field Emission***	***Schottky***
Source Material	*Tungsten (Filament)*	*Lanthanum Hexaboride (Single Crystal)*	*Tungsten (Single Crystal)*	*Zirconium (Single Crystal)*
Source Temperature (K)	*2600*	*1800*	*Room Temp*	*1700*
Source Work Function (eV)	*4.4*	*2.6*	*4.1*	*2.6*
Source Diameter	*30 µm*	*10 µm*	*5 nm*	*20nm*
Brightness (comparable)	*1*	*10*	*1000*	*100*
Lifetime (hrs)	*100*	*1,000*	*10,000*	*10,000*
Resolution (at 30 kV)	*3 nm*	*2 nm*	*1 nm*	*1 nm*

Table 3-1: Comparison of the different types of SEM electron gun source [124][123].

As well as the electron beam source impacting the image quality, the other main driving factor is the specimen-beam interaction. This is highly specimen dependent, but the basic principles and corresponding detectors are detailed in Section 3.2.3.

3.2.3 Specimen-Beam Interaction Principles

The specimen-beam interaction results in the generation of various emissions, the most common of which are:

Secondary Electrons (SEs): A product of inelastic interactions, which occur when the electron beam collides with an electron from an atom's inner shell, displacing the electron, which exits the specimen as an SE [125].

Backscattered Electrons (BSEs): A product of elastic collisions of electrons in the beam with atoms, causing a change in the electron's trajectory, which results in it exiting the specimen [120][125].

X-rays: When the incident beam generates “holes” from SEs leaving the inner shells of the atoms, the outer shell electrons move to the inner shell, emitting energy in the form of X-rays [120].

Both SEs and BSEs can be measured using the Everhart Thornley detector, also known as an SE detector, which produces an image of the surface topography of a specimen [120]. The SE detector is formed of a scintillator, a luminescent material (in this case phosphate based), which, when struck by electrons absorbs their energy and re-emits the absorbed energy as light; and a faraday cage. The faraday cage collects the electrons and the scintillator processes them into light where they are amplified by the photomultiplier to form an image [126]. To boost the efficiency of SE detection, the SE detector is placed at the side of the electron chamber at an acute angle to the gun, shown in Figure 3.5.

BSEs can also be detected by a dedicated BSE detector which is insensitive to SEs. A BSE detector is most commonly a p-n junction, which produces an electric current when interacting with BSEs [120]. The BSE detector not only generates similar surface topographical information to an SE detector, but also enables easier distinction of sample phases and compositions. The ability of the BSE detector to differentiate phases and composition is attributed to the fact that the number of electrons scattered by an atom in producing the BSEs is proportional to the atomic number [125] and, thus, the intensity of the signal. The intensity of the BSE detector can be controlled via four poles: when all four poles are enabled, the contrast of the image depicts the element's atomic number. However, by activating specific quadrants, topographical information from the sample can be imaged [127]. The BSE detectors are placed above the sample, directly below the beam, in order to maximise the collection of BSEs (Figure 3.5).

X-rays can also be used to provide more in-depth compositional data using an energy dispersive X-ray (EDX) detector. The EDX detector detects photons and assigns their energies to the specific elements present within the beam-excited interaction volume, resulting in a composition specific image and corresponding composition percentage [120]. For the EDX detector to work accurately, the sample must be placed very close to the detector [128], which is positioned at an angle to the gun, shown in Figure 3.5. The collection of X-rays using the EDX detector is also dependent on the gun voltage, where ideally a higher gun voltage (30 keV) should be used in order to maximise the interaction volume and hence the number of X-rays produced [120].

Although the three main signals provide data on the overall topology, topography and composition, they are not able to provide complete crystallographic structures. Hence, SEMs are often combined with other specially developed detectors to facilitate a greater

understanding of composition-structure-property relationships [129]. These include EBSD detectors, details of which can be found in Section 3.3.

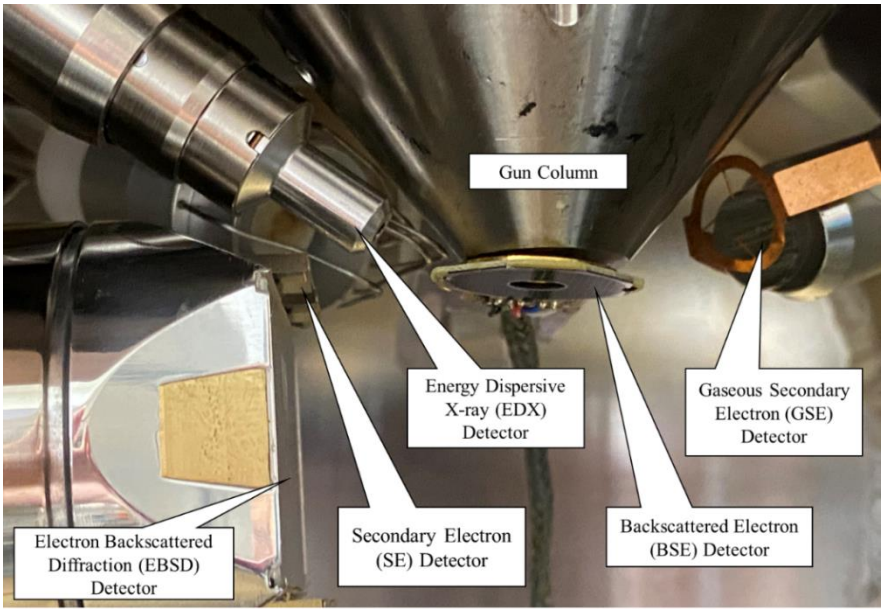

Figure 3.5: SEM chamber with key detectors labelled.

3.2.4 SEM Specimen-Beam Interaction Models

Mechanisms for Beam Interaction

The specimen-beam interaction within an SEM dictates the quality of the image produced. Thus, fundamental physical models have been constructed to understand the effect of electron interactions on different materials. The two main mechanisms for beam interaction are inelastic and elastic collisions, shown in Figure 3.6. Inelastic collisions, Figure 3.6a and Figure 3.6b, are the result of interactions with shell electrons that lead to the loss of energy of the incoming electron. During these interactions, SEs are produced by the ejection of weakly bound outer shell electrons (a) and the ejection of inner shell electrons, which subsequently also leads to the movement of outer shell electrons to the recently vacated inner shell space, leading to the production of X-rays (b). Elastic collisions (Figure 3.6c) occur when the beam electron is deflected by the positively-charged nucleus of an atom, resulting in the electron

deviating from its previous trajectory, some of which are eventually detected by the BSE detector. The number of elastic collisions is dependent on the nuclear charge of the atom (indicated by the atomic number) and the energy of the beam [120].

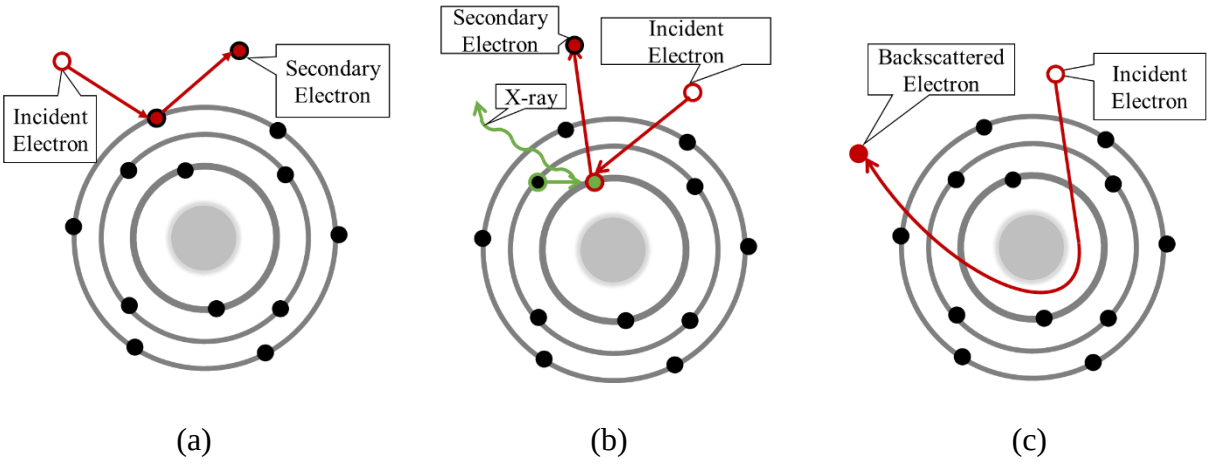

Figure 3.6: Specimen-beam interactions on an atomic level showing: (a) inelastic collisions producing SEs, (b) inelastic collisions producing X-rays, and (c) elastic collisions producing BSEs.

The result of these inelastic and elastic collisions leads to various electron trajectories, which dictate the interaction volume of the sample. Material interaction volume is defined as the elastic mean free path of electrons [130], which is a measure of the depth to which the electrons penetrate the material surface to produce SEs, BSEs and X-rays. The interaction volume for different signals produced, a schematic of which is shown in Figure 3.7, can be calculated for a range of materials via modelling. These models include both analytical and iterative solutions, often simulated using Monte Carlo simulations. The most common models used for specimen-beam interaction are the Bethe equation, Range equation, and CASINO and Joy Monte Carlo simulation, which are discussed below.

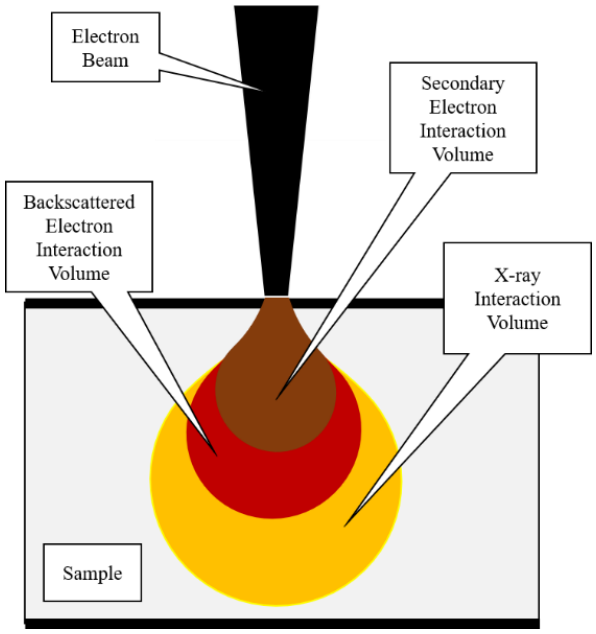

Figure 3.7: Specimen interaction volume for SEs, BSEs and X-rays with respect to specimen surface.

The Bethe Equation

The depth of electron beam penetration was first quantified using the Bethe equation,

$$\frac{dE}{ds} = -7.85\left(\frac{Z\rho}{AE}\right) ln\left(\frac{1.166E}{J}\right) \qquad \textit{Equation 3.1}$$

where E (keV) is the beam energy, s is the distance the energy has travelled, Z is the atomic number, ρ (g/cm^3) is the density, A (g/mol) is the atomic weight and J (keV) is the mean ionization potential defined as $J = (9.76Z + 58.5Z^{-0.19}) \times 10^{-3}$ [131].

The Bethe equation summarises the properties of inelastic scattering by approximating the effects as a continuous energy loss across the electron beam's total distance travelled [131]. The equation can be used to determine the total inelastic scattering distance (known as the Bethe range) by integrating across the beam energy. By calculating the Bethe range for elements of varying atomic number, the results demonstrate that the smaller the atomic

number the larger the range, and thus the greater the penetration depth at which inelastic scattering occurs [120]. However, this theory cannot so easily account for elastic scattering owing to the assumption that inelastic collisions only cause the electron beam to deviate slightly from the initial path, whereas elastic scattering occurs over a much broader angle.

The Range Equation

To account for both elastic and inelastic scattering, Kanaya and Okayama produced the Range equation,

$$R = 27.6\left(\frac{A}{Z^{0.89}\rho}\right)E_0^{1.67} \qquad \textit{Equation 3.2}$$

where E_0 (keV) is the incident beam energy and A, Z, and ρ are defined in Equation 3.1. The Range equation gives an analytical estimate of the interaction volume. This estimate is defined by the radius of a hemisphere centred on the beam impact points, which contain 95% of a trajectory [132]. However, the Range equation only provides a single interaction volume accounting for all SE, BSE and X-ray interactions, providing a 'maximum' interaction volume. Additionally, the Range equation also only applies to elements and, although its quick analytical calculation is helpful, it is not necessarily accurate for more complex compound or alloy systems. Thus, for quantifying the interaction volume of alloys or compounds, or for a breakdown of the different interaction volumes for different types of signals produced during specimen-beam interaction, Monte Carlo electron trajectory simulations are more commonly used.

Monte Carlo Electron Trajectory Simulations

A Monte Carlo electron trajectory simulation simulates the electron path, by a probabilistic model, to represent the physical interactions between the electron beam and sample and subsequently to calculate electron trajectories [120]. An electron trajectory is described by a combination of discrete elastic and inelastic scattering events approximated by the mean energy loss model between two elastic scattering events [133]. Joy produced one of the first commercially available SEM Monte Carlo electron simulations. The model is based on the Bethe equation and facilitates the modelling of SEs and BSEs in solids [134].

More recent models now also simulate X-rays alongside the SE and BSE emissions. One such model is CASINO, which uses a single-scattering Monte Carlo simulation of electrons operated for the acceleration voltages of 0.1–30 kV to simulate BSEs, SEs and X-ray emissions. The simulation shows good agreement with the Kanaya-Okayama Range equation and is able to simulate multiple alloys at a variety of angles [135]. CASINO is one of the more commonly used simulations and, hence, has been utilised in the current project.

In general, the electron beam interaction volume is dictated by the beam voltage. A low accelerating voltage (<5 keV) provides only details of the very surface of the specimen, while a high accelerating voltage (15-30 keV) can penetrate up to 1 µm below the surface [116]. Both the Range equation and Bethe equation show a dependent relationship between the electron energy (dictated by the voltage) and interaction volume [120]. Figure 3.8 depicts the interaction volume for a range of elements based on the Range equation, which shows a positive correlation between the interaction volume and the voltage. Thus, the higher the voltage the greater the depth to which the electrons penetrate the sample; but this is sample dependent (Figure 3.8) and can further be influenced by external environmental factors [136]. The overall interaction volume of the sample influences the quality of the image produced; this is investigated in Chapter 4.

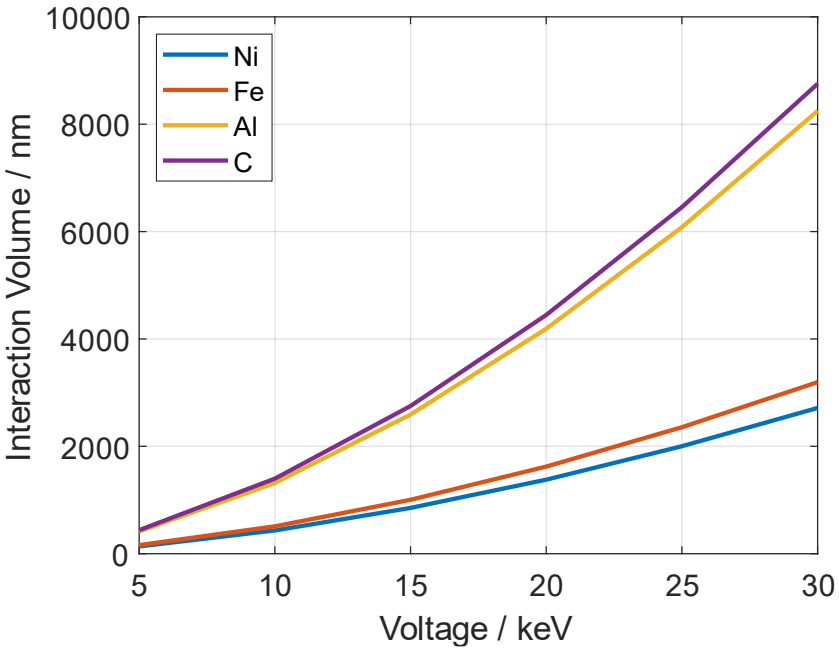

Figure 3.8: Range equation results of nickel, iron, aluminium and carbon for various voltages showing a positive correlation between voltage and interaction volume.

3.3 Electron Backscatter Diffraction (EBSD)

3.3.1 Scientific Principles of EBSD

EBSD, also known as orientation imaging microscopy (OIM), provides crystallographic orientation information and can highlight salient features that are otherwise unobserved using standard SEM imaging [129]. The discovery of the fundamentals of EBSD was in 1928 by Shoji Nishikawa and Seishi Kikuchi, who used a beam of electrons of 50 keV incident at an angle of 6º to the face of a calcite crystal to produce a diffraction pattern described as 'black and white lines in pairs, due to multiple scattering and selective reflection' [137]. The technique was further extended and combined with the introduction of the commercial SEM in 1965, leading to the development of electron backscatter patterns (EBSP) by J.A. Venables and C.J. Harland in 1973 [138].

The modern EBSD detector is based on work by D.J. Dingley in 1984 [139], who developed the technique using a phosphor screen combined with a TV camera. The phosphor screen is still used today but with a low-light charge coupled device (CCD) camera rather than a TV camera [113]. EBSD is performed on a flat (highly polished) specimen surface at an incident angle of 20º to the electron beam. The beam is diffracted by atomic layers in crystalline materials [140]. When electrons impinge on a surface, they undergo elastic collisions. The elastic scattering produces BSEs in all directions, a fraction of which will travel along angles, relative to the atomic plane, that satisfy Bragg's Law,

$$N\,\lambda = 2D\,sin\,\theta \qquad \textit{Equation 3.3}$$

where N is an integer, λ is the incident electron wavelength, D is the lattice spacing, and θ is the electrons' scattering angle; a diagram is shown in Figure 3.9. Bragg's law, a special case of Laue diffraction, the proof of which is in the appendix of Chapter 3, facilitates the calculation of the angle at which electrons are elastically scattered along the crystal lattice. This scattering, at the Bragg angle, forms diffraction cones of electrons (commonly known as Kossel cones), which provide the geometry of the material's crystallographic planes [141].

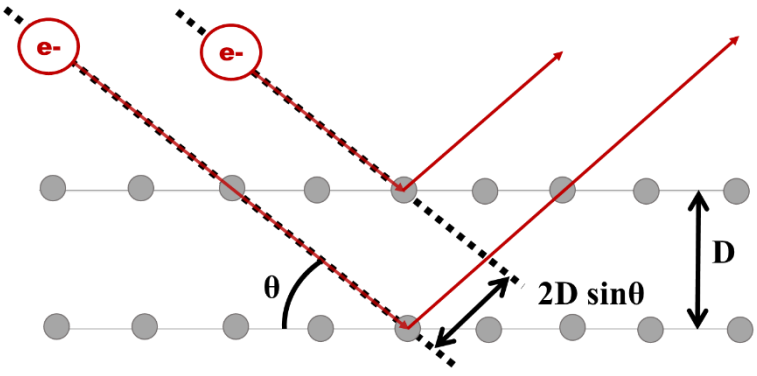

Figure 3.9: Bragg's law

In EBSD, these Kossel cones of electrons are detected by impingement on the detector phosphor screen, which fluoresces forming EBSP, or Kikuchi patterns, shown in Figure 3.10. From these patterns, the position of the centre line between these two lines is accepted to be the gnomonic projection of the diffraction plane onto the observed screen. The spacing between the pair of lines, also known as band width, corresponds to twice the Bragg angle [142]. From this geometry, crystallographic angles are obtained and subsequently the crystallographic orientation maps can be produced using an optimised Hough transform. The Hough transform detects and converts the Kikuchi patterns into the Hough space (an angle and position based coordinate system), where every pixel denotes a unique line in the EBSP. The location of these bands in Hough space provides a relationship to each individual pixel's crystal orientation as the angles between bands represent the angles between lattice planes [143]. Hence, by plotting the orientation at each point a complete crystallographic orientation map can be created. This phenomena enables the identification of grain size, crystal orientation, phases, grain boundaries, and slip systems, using a range of indexing algorithms [144].

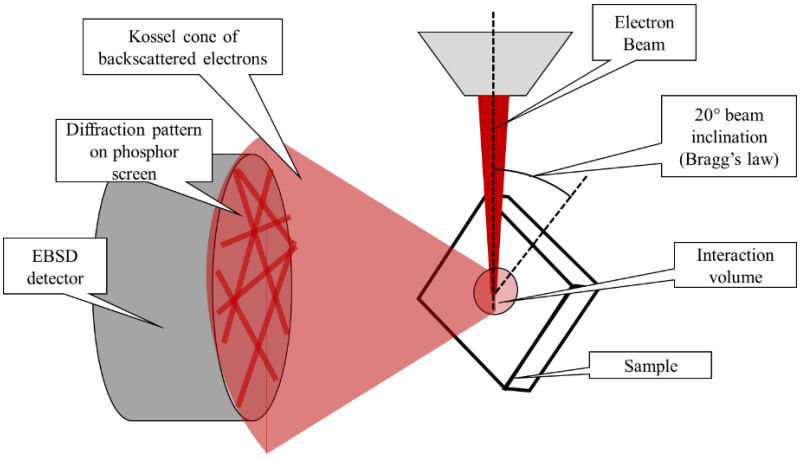

Figure 3.10: Schematic of the EBSD detector with respect to the SEM and sample showing the Kikuchi patterns projected on to the phosphor screen. These Kikuchi patterns form as a result of the Kossel cone of BSEs created by elastic collisions of the beam electrons with the sample which satisfy Bragg's law.

3.3.2 Sample Preparation

One of the main challenges of EBSD mapping is the sample preparation procedure; the surface must be sufficiently smooth and flat to produce good EBSD patterns [113]. EBSD is a surface sensitive technique as the depth below the specimen surface that the signal can penetrate is limited due to the mean free path of BSEs [145]. This mean free path of BSEs, also known as the interaction volume, is dictated by the accelerating voltage of the electron beam and atomic number of the specimen [130]. Although the effectiveness of other detectors, such as the BSE detector, is dependent on the interaction volume of BSEs, EBSD reduces this interaction volume due to the high tilt of the sample [146]. As described in Section 3.3.1, the tilt allows the coherent scattering of electrons along the crystal lattice plane to be detected at the appropriate angle so as to satisfy Bragg's law. This subsequently produces Kikuchi patterns, which provide a relationship to the crystallographic structure [147]. Thus, by reducing the roughness of the sample surface, the likelihood of electrons being dispersed along unfavourable scattering lines decreases, as there are fewer perturbations in the crystal lattice, leading to more electrons diffracted at the appropriate angle [130].

The guidelines for EBSD specimen preparation are documented for many materials in a range of industry technical notes [148]. The traditional process for EBSD specimen preparation follows four main stages; cutting, mounting, grinding, and polishing. Most sample preparation guides agree that cutting should minimise surface degradation and physical damage to the rest of the specimen. Post-cut, to facilitate automatic polishing, EBSD samples are mounted, either by hot mounting with resin or cold mounting using Basalt, before being fitted into an automatic polishing machine [149]. It is noted that for subsequent thermal or mechanical tests, the specimen must then be removed from the mould either by dissolving (cold mounting) or cutting the specimen out under pressure (hot mounting), both of which

can lead to damage of the polished specimen surface. Hence, alternatives of mechanical mounting or hand grinding and polishing (of unmounted specimens) are often used to prevent the likely damage to the surface of the specimen during mould extraction [150]. For the grinding stage, a range of silicon carbide grinding papers are viewed as the most practical and efficient way to prepare metallographic specimens, before final polishing, to remove most scratches. Samples are ground in increasing grades of grit (decreasing grades of roughness) on a polishing wheel before moving onto the polishing solution [149]. For polishing, a range of techniques and solutions are detailed below.

Mechanical Polishing

Mechanical polishing generally uses a diamond solution (grades including 9, 3, 1 µm), owing to its inertness and abrasive properties [144]. For purely mechanical polishing, as opposed to combined chemical-mechanical polishing, higher grades of diamond solution are then used (as low as 0.1 µm) and finally alumina. These are purely mechanical polishing abrasives as they are inert substances; as a result, the smoothness is limited by the grade of solution used and hence mechanical polishing can be a time-consuming process, particularly if it is not automated. Furthermore, these solutions will not remove impurities from the surface and, as such, if the polishing pad is not kept sufficiently clean, the surface may become scratched over time [148].

Mechanical & Chemical Ultrafine Polishing

To improve the grade of polish achieved by purely mechanical polishing, the stages of mechanical polishing are often followed by a combined mechanical polishing and chemical etching agent, such as colloidal silica. The use of colloidal silica not only provides a high-grade mechanical polish but also chemically reacts with metals to disperse precipitates and impurities on the surface. However, samples can become over-polished and grain boundaries

begin to etch, which lead to an increase in the surface roughness and subsequent decrease in EBSD map quality [151].

Broad Ion Beam Milling

Broad ion beam milling is often used after preliminary polishing with a low-grade diamond solution or after colloidal silica as an alternative to mechanical or chemical ultrafine polishing. The basic principle of broad ion milling is the bombardment of a specimen with energetic ions accelerated and formed into a tight ion beam. During the bombardment, material is removed from the sample resulting in a highly-polished area of interest. However, prolonged use of the high energy ion bombardment on a focused area can lead to artefacts from sample heating and radiation damage [152].

Electropolishing

An electropolishing method requires a liquid electrolyte with two electrodes: an anode (which is the sample to be polished) and cathode. A voltage is applied which forces the top layers of the anode sample to dissolve and deposit itself on the cathode as a coating, thereby leading to polishing of the surface of the sample [153]. The advantage of this is that grinding is only required down to P2000 grit silicon carbide, and the preliminary polishing stages are not required, speeding up the sample preparation process. Moreover, if the appropriate solutions and voltages are known, less than one minute of polishing is required for each sample, again making this a very efficient process [151]. However, each alloy composition requires slightly different parameters and if the incorrect parameters are used, electro-polishing can lead to etching or even pitting of specimens. Hence, this method is more beneficial when multiple specimens of the same composition are being prepared for EBSD [154].

A study [155] examined the effect of different polishing techniques on the quality of EBSD patterns produced. The study investigated Ti-6AL-4V, In718, CP600, and silicon[3] (Si), and showed that colloidal silica polishing (OP-S-polished) produced favourable results when compared to diamond solution polishing (polished) and ion milling (OP-S + ion milling), while the results from electropolishing (electropolished) were highly material dependent. A summary of the results from this paper (Figure 3.11) demonstrates the variance in relationship between EBSD pattern quality, quantified by the number of non-indexable points (zero-solutions), and the preparation method for different materials [155]. Although this study used focused ion milling, subsequent studies have shown broad ion beam milling can produce more favourable results when compared to purely mechanical or chemical polishing [156]. Furthermore, to improve the final quality for any of the above polishing processes, subsequent plasma cleaning is often used to remove hydrocarbon contaminants from specimens [157].

Although sample preparation is a necessity for EBSD imaging, for many other detectors within the SEM, sample preparation is optional. This makes the SEM an ideal environment to image samples in an environment that mimics their standard operating conditions. The opportunities that this provides are discussed in Section 3.4.

[3]Note silicon is commonly used to calibrate EBSD detectors

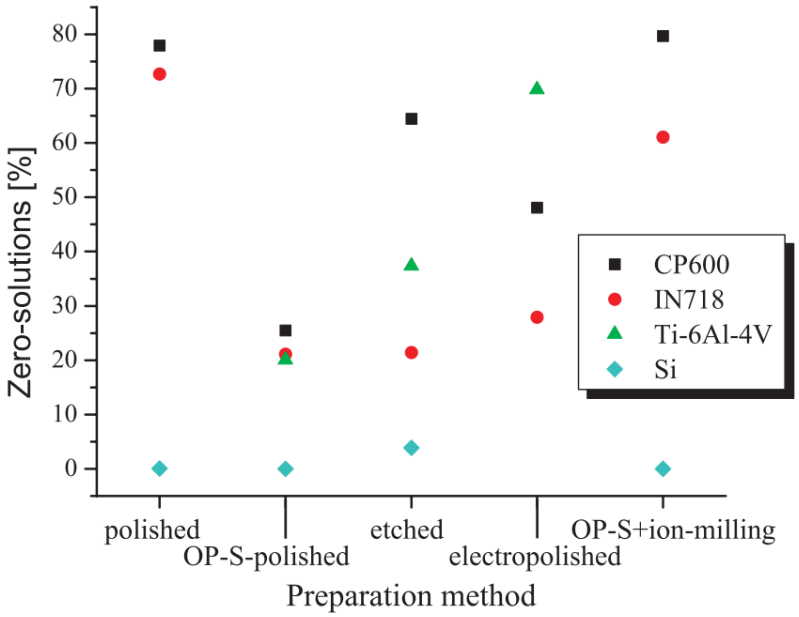

Figure 3.11: Summary of the number of indexable points (percentage of non-zero-solutions of individually scanned pixels during EBSD scan) compared to the preparation method for different materials. Note that the lower the percentage of zero-solutions, the better the polishing method [155] .

3.4 In Situ SEM

3.4.1 Background of *In Situ* SEM

Due to the non-invasive nature of SEM, combined with their large microscope chamber, thermal and mechanical experiments are often conducted within the chamber. This facilitates imaging during testing, which captures the real-time microstructural evolution, as opposed to before and after processing. This type of experiment is known as *in situ* SEM. The use of elevated temperatures or mechanical loading within an SEM facilitates the observation of changes in grain, phase and surface effect while load and / or controlled temperatures (including heating / cooling) are applied. These microstructural features in turn dictate the physical and mechanical properties of materials on a macro-scale and hence the use of this technique is beneficial for the understanding and future development of materials.

3.4.2 High-Temperature *In Situ* SEM

High-temperature *in situ* SEM incorporates a variety of detectors including SE, BSE, and EBSD used for studying changes in surface morphology, grain structure, precipitate movement, and in the case of BSE and EBSD changes in phase. Early reports of *in situ* SEM imaging at elevated temperature combined a Phillips Electroscan ESEM 2020 and purpose-built hot stage. The stage (Figure 3.12) used electrical resistance heating of a platinum sample holder to observe metals at temperature up to 1000 °C [158]. The development of this new technology facilitated *in situ* studies on the oxidation of iron, nickel and chromium by observing the formation of oxide layers within an SEM [159][158]. The technology also enabled examination of metal dusting corrosion of nickel using an SE detector [160].

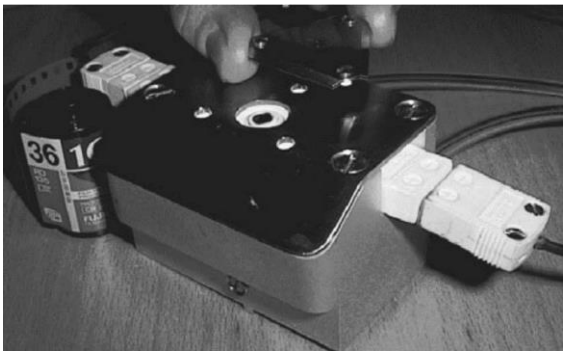

Figure 3.12: Philips Electroscan ESEM hot stage with shielding lifted to reveal resistive heating element [158].

More recent *in situ* observations have used electrical resistance heating combined with EBSD imaging. These purpose-built *in situ* heaters (Figure 3.13) have allowed the successful capture of grain boundary migration during the recrystallization of a thin tantalum ribbon at temperatures between 750 °C and 1030 °C [161]. Tantalum was used owing to its excellent thermal conductivity and its single-phase BCC grain structure (which is ideal for EBSD

imaging). The same apparatus was subsequently modified for grain growth studies of other materials by spot welding samples to the tantalum ribbon and heating the sample via heat conduction [161]. The electrical resistance heating combined with spot welding greatly reduces the temperature gradient across the sample; however, it also results in the heater being single use.

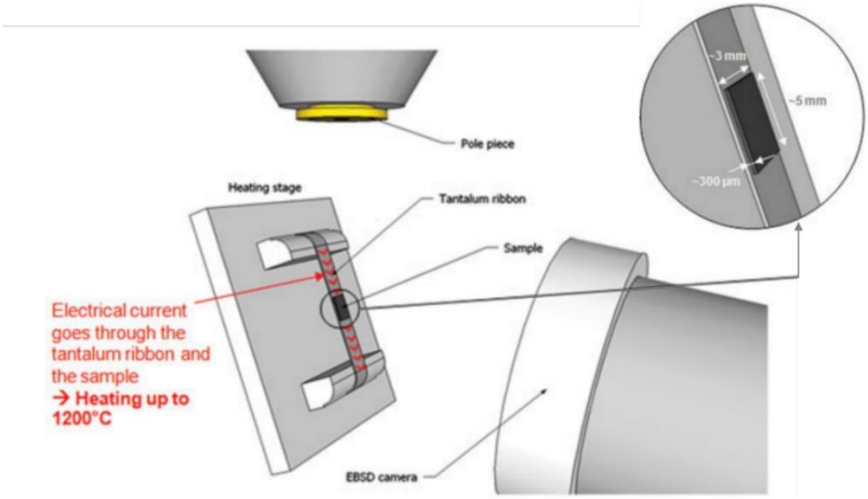

Figure 3.13: Schematic view of the electrically resistive tantalum ribbon heat stage [161].

To produce reusable heaters, alternative studies have made use of a laser powered heating stage; shown in Figure 3.14. The stage was designed for high vacuum applications in an SEM at temperatures up to 1000 °C [162], to study phase transformations in steel using EBSD and SE imaging [46]. Similarly, reusable ceramic plates have been used for the conductive heating of specimens [163][45]. Here, *in situ* SEM / EBSD observation of the alpha to gamma phase transformation in Fe-Ni alloys was performed using a purpose-built ceramic heating plate combined with shielding, that operated up to temperatures of 730 °C within a Hitachi Field Emission Gun-SEM (S4200) equipped with an EDAX TSL OIM analysis system [163].

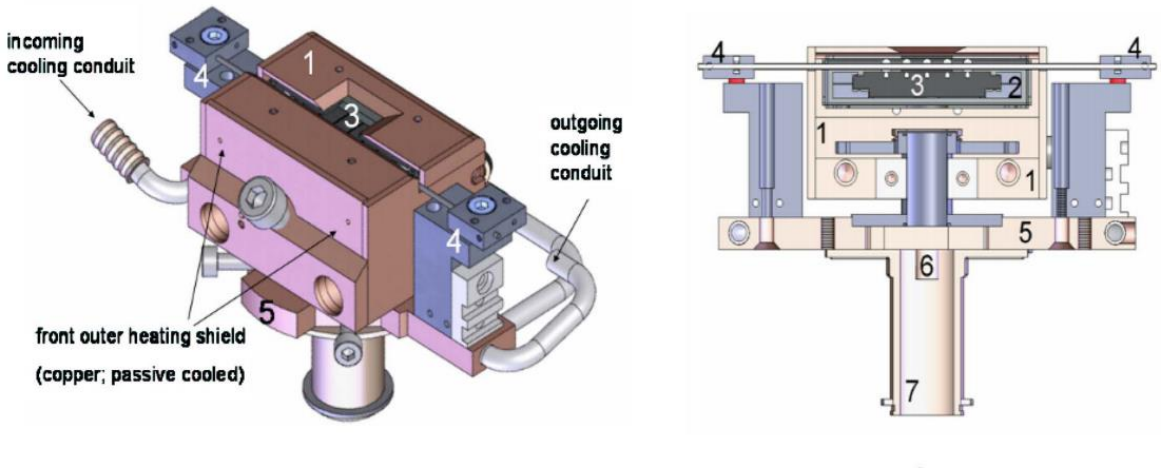

Figure 3.14: Laser powered heating stage showing the basic outer parts and a cross section of the interior showing: (1) rear outer copper heating shield, (2) internal tantalum heating shield, (3) silicon carbide sample holder, (4) tungsten clamp for specimen mounting, (5) heating stage copper base, (6) optical fibre guidance and (7) goniometer stage adapter [162].

The combination of high-temperature *in situ* testing has been used for a number of metal and ceramic applications, including documenting the evolution of refractory castables [164] and the thermal recovery of asbestos [130] up to temperatures of 1500 °C using SE imaging data. The success of these experiments at these temperatures is attributed to the use of gaseous SE (GSE) detector (and in some studies a specialist GSE detector). This detector operates in non-vacuum environments and is less sensitive to the high temperatures, which has enabled elevated temperature testing of both conducting and non-conducting materials [164].

Commercially available, standalone heating stages have also been developed to facilitate further studies of metals and alloys. Two examples of these stages are shown in Figure 3.15; the Gatan Murano heater and the Kammrath & Weiss ceramic heating module. These commercially available heaters have been used for a number of applications including to demonstrate the interphase boundary motion of the ferrite to austenite to ferrite phase

change using EBSD maps at temperatures up to 860 °C. In this study, low resolution EBSD scans were taken. The scan time needed to be less than 100 s at temperatures above 800 °C, because the temperature of the EBSD detector phosphor screen must not exceed 120 °C (the maximum EBSD detector operating temperature). To prevent this, the detector was retracted to cool between scans [165]. Commercially available stages have further been combined with BSE imaging of nickel superalloys to capture slip band movement under loading at temperatures up to 750 °C [166]. Other commercially available stages have made use of extensive shielding and water cooling to facilitate EBSD images during studies on the recrystallization in bronze alloy strips cast on steel substrates [167] and the surface crystallisation of glass [168] at temperatures up to 1000 °C.

(a) *(b)*

Figure 3.15: Commercially available in situ *SEM heating stages: (a) Gatan Murano heater* [169]*, and (b) Kammrath & Weiss ceramic heating module* [170].

Overall, the current literature indicates that high-temperature SEM is a powerful tool for observing the dynamic crystallographic and microstructural processes in materials. Recent literature has shown that the utility of this tool can be further extended when combining high-temperature and mechanical testing with SEM imaging, details of which are in Section 3.4.3.

3.4.3 Combined Thermo-Mechanical *In Situ* SEM

Combined heating and mechanical testing stages facilitate microstructural observations of specimens at controlled temperatures while under loading. *In situ* thermo-mechanical stages include the tension, compression, torsion and cyclic loading of materials during heating, while simultaneously imaging within an SEM. It is often difficult to understand the nature of high-temperature microstructural processes purely from the traditional post-mortem microstructural study of materials. Hence, *in situ* thermo-mechanical testing provides greater insight into the mechanisms of microstructural evolution by capturing a subset of the material microstructure during the experimental procedure.

The first example of a combined thermo-mechanical stage performed cyclic loading up to temperatures of 750 °C. Heating was facilitated by a resistive heater of coiled tantalum wires mounted in boron nitride blocks, which enveloped the specimen grips, and provided radiative and some conductive heating; the key features are shown in Figure 3.16. Extensive radiative shielding with two small ports where the electron probe could enter and SEs could exit, combined with liquid cooling were utilised around the stage, along with liquid cooling surrounding the SE detector to prevent overheating [171]. The stage enabled the investigation of high-temperature crack-tip micromechanics and fracture behaviour under cyclic loading in stainless steels, aluminium alloys, [171] and titanium-aluminide alloys [172][173]. To facilitate better observation of the grain structure surrounding propagating cracks, titanium aluminide alloys were electro-polished and subsequently ion milled to enhance the visibility of the beta phase [172].

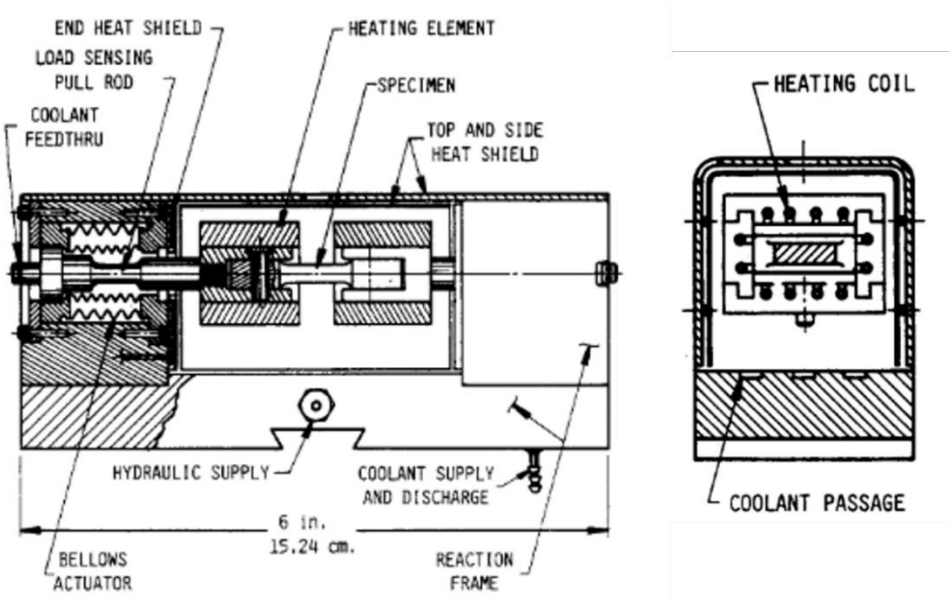

Figure 3.16: A schematic of the assembly drawing of the first example of the combined thermo-mechanical stage, accompanied by a cross-section through the centre line [171].

Thermo-mechanical stages for SE imaging used to capture topography and changes in texture later focused primarily on radiative heating in order to minimise contact with the specimen and hence prevent interference with stress-strain results [174]. However, owing to the requirement for extensive sample preparation, combined with EBSD detector sensitivity to radiative emissions from both heat and noise interference, it wasn't until much later that the first *in situ* thermo-mechanical EBSD data were captured [175]. The stage first used to capture EBSD data, Figure 3.17, mitigated against thermal interference by using a specimen block that was resistance-heated in the range 100-550 °C by a small cartridge heater. Furthermore, by powering the motor and heating block using a low voltage DC supply, the stage had minimal interference with the beam or detector [175]. To facilitate EBSD, specimens were both mechanically polished and electropolished to produce a very smooth initial surface. During experiments, the microscope was also operated at 10 keV, as *in situ* static annealing tests had shown this maximised orientation and topographic contrast at elevated temperatures [175][176].

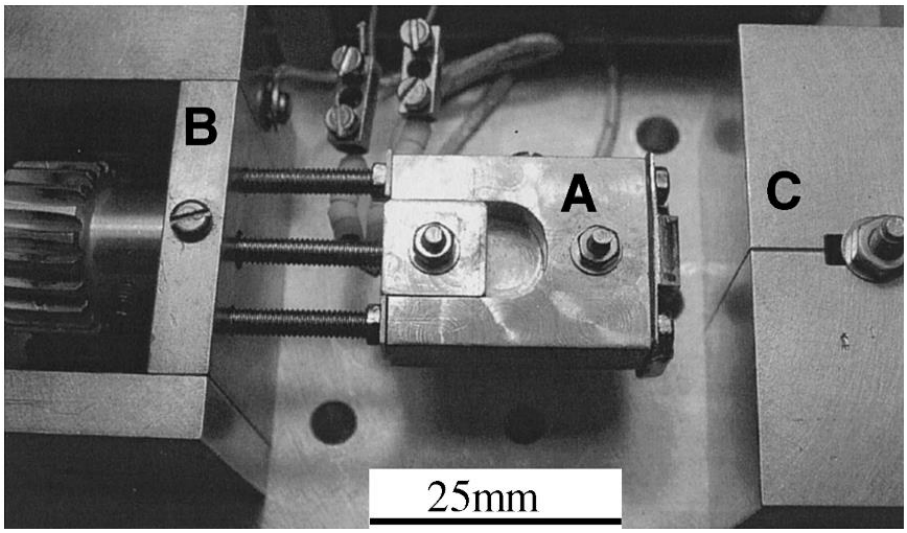

Figure 3.17: Thermo-mechanical heating stage used to take high-temperature EBSD images; three key stage elements labelled are: (A) stainless steel heating block for resistive heating of specimen. (B) worm gear used by a geared DC motor to drive a 3 mm threaded rod for the mechanical testing, and (C) copper block which can be pressed against the specimen block and increase the cooling rate up to (-50 ºC/min) [175].

The stage, shown in Figure 3.17, was used for preliminary investigations including into substructure formation, dynamic sub-grain and grain growth, superplastic deformation in aluminium alloys, and dynamic recrystallization in copper. However, this study also highlighted some of the challenges of EBSD imaging *in situ.* These included a maximum stage operating-temperature of 550 °C to avoid overheating or over-exposure of detectors, and a limited scan time owing to the time sensitive process of capturing a changing microstructure during deformation. Hence, in this study, EBSD scans were limited to a single line [175].

Other stages have utilised radiative heating over resistive heating; one such study used a 6 mm diameter tungsten-based heater located just below the gauge section of the sample. This was combined with a chiller circulating cooled water through copper tubes to prevent the tensile stage from overheating, and was used to study creep and fracture behaviour in titanium alloys [177][178].

Since the success of combined thermo-mechanical stage with imaging EBSD, several commercially available stages have been developed, providing a variety of loading and heating mechanisms. A summary of the current commercially available thermo-mechanical stages is shown in Figure 3.18, with their key properties in Table 3-2.

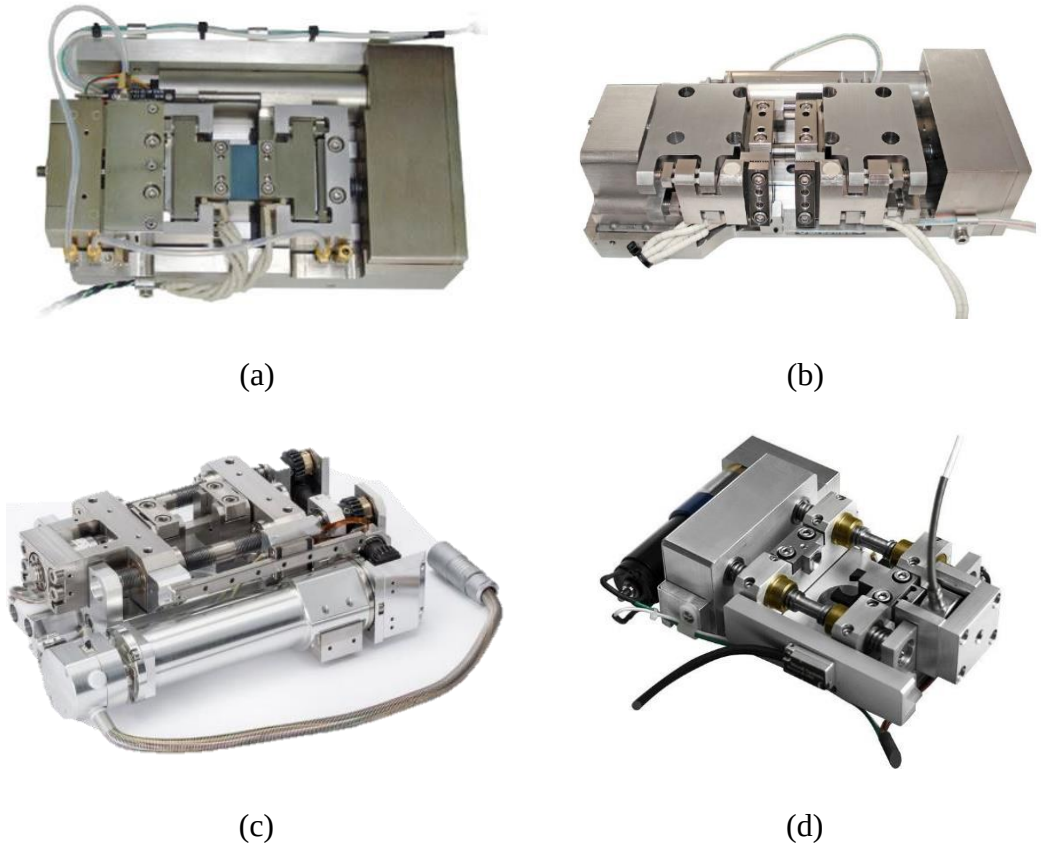

(a) (b)

(c) (d)

Figure 3.18: Summary of commercially available heating stages: (a) Gatan Microtest H5000 [169], *(b) Gatan Microtest EH 2000* [169], *(c) Kammrath & Weiss mechanical heat stage* [170] *and (d) MTI Instruments stage* [179].

These commercial stages, shown in Figure 3.18, have generally favoured resistive heating. Examples include tensile specimen heating via heated grips to study nickel superalloys under cyclic loading [180]. An alternative commercial stage has made use of a spring set up where a tungsten wire spring on the micro-tensile stage provides contact between furnace and the specimen. This stage has been operated at temperatures up to 900 °C to conduct *in situ* studies on super plasticity in titanium alloys [181], the tensile properties of

alloy 709 [182] and crack nucleation in high entropy alloys (HEAs) [183]. More recent developments have seen a return to purpose-built experimental stages. The use of tungsten as a conductive heating element combined with springs or sensors to minimise strain on the specimen, has also been used in further one-off stages to investigate the tensile deformation behaviour of HEAs [184] and titanium alloys [185].

Properties	***Gatan Microtest H5000***	***Gatan Microtest EH 2000***	***Kammrath & Weiss Mechanical Heat Stage***	***MTI Instruments Stage***
Maximum Operating Temperature (°C)	600 °C (via heated grips)	600 °C (via heated grips)	Sample imaging up to 800 °C (heater up to 1500 °C)	1000 ºC (optional heater)
Max Force (kN)	5	2	10	9
Stage size (mm)	200 x 118 x 51	196 x 96 x 53	150 x 55 x 220	207 x 130 x 72
Stage Mass (kg)	4	3.4	4	2.2 (excluding heater)
Specimen Geometry	Dog-bone 10 mm specimen thickness	Dog-bone 5 mm specimen thickness	Dog-bone 4 mm specimen thickness	2.5 mm thickness

Table 3-2: A comparison of the commercially available thermo-mechanical stages and their main attributes [169], [170], [179].

In general, most stages share common attributes of shielding and cooling, to minimise signal to noise ratio and prevent damage from overheating detectors. The optimisation of specimen and stage geometry, however, is often a challenge as it is necessary to minimise temperature gradients while still ensuring results are representative of the bulk material. These challenges, along with others, are further investigated in Section 3.4.4.

3.4.4 Challenges of *In Situ* SEM

Operating experiments at high-temperature while simultaneously imaging within an SEM comes with a range of challenges. Section 3.4.2 discusses the challenge of providing heat to the specimen, but there are also technical challenges of heating to high temperature. These include preventing the loss of vacuum pressure, stopping the overheating of the detectors, avoiding the degradation of the heating element, and minimising temperature gradients through the sample. The literature also describes further physical challenges associated with imaging at high-temperatures. An example of the challenges of thermal interference is the effect of the thermionic emission of electrons from heated samples on the signal to noise ratio from the detector [186].

It is noted that EBSD imaging is particularly challenging at high-temperatures owing to the proximity of the detector to the sample; a diagram of the location of the detectors with respect to the sample within the SEM is shown in Figure 3.19. Thus, the proximity of the detector to the sample leads to possible damage to the detector's phosphor screen, the temperature of which typically must not exceed 120 °C [165]. Other detectors are also heat sensitive where the EDX and BSE detectors have low maximum operating temperatures of 50 °C and 300 °C respectively [165], which can lead to similar problems of overheating. Currently, stage design predominantly focuses on the use of shielding and single use heaters to produce EBSD and SE data. Shielding is used to surround the sample in a furnace-like environment, minimising temperature gradients while protecting the detectors.

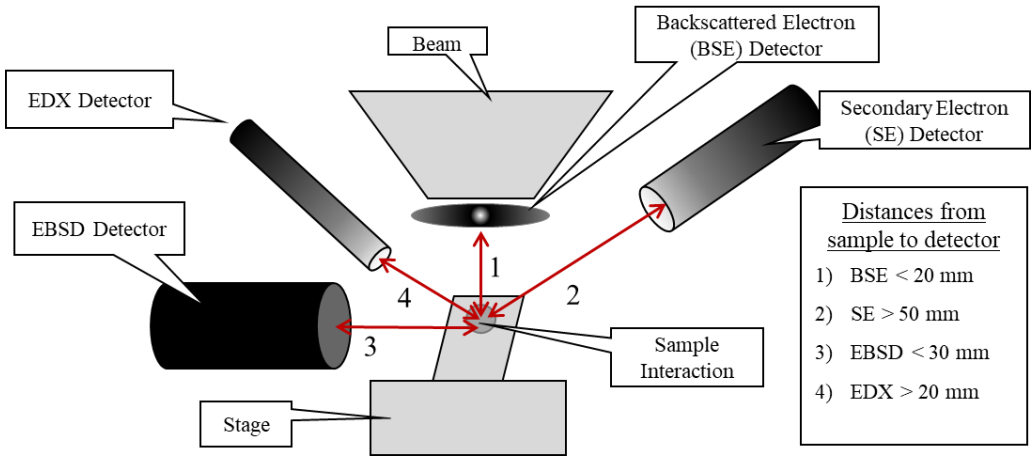

Figure 3.19: Proximity of detectors to sample.

One of the requirements unique to EBSD is the necessity for a smooth sample surface. This is particularly difficult to maintain during mechanical testing or at elevated temperature where stress relaxation, oxidisation or phase changes may occur over time. The increase in surface roughness during testing, as a result of changes in surface topography due to heating or mechanical loading, or thermal interference, may lead to a loss of scan quality. In addition, studies show that for each subsequent scan during an *in situ* heating and / or loading test, there will be a smaller fraction of scan points indexed successfully [143]. Thus, this issue requires further investigation.

Finally, when designing an *in situ* stage for EBSD imaging, there are often technical challenges. These include working distance, specimen mounting, and the equipment temperature of the stage itself. As such working distance should be less than 20 mm for EBSD imaging, and the stage geometry must be optimised to meet these requirements. Similarly, when mounting EBSD specimens, owing to the high-quality surface polish needed to image, any mounting onto the stage must not inadvertently damage the imaged surface. Also, although the stage itself is a heater, there are a number of parts, particularly when considering combined thermo-mechanical testing, that must not overheat [187]. All these constraints will need to be considered when designing a new *in situ* stage.

3.5 Alternative Microscopy Techniques

3.5.1 Introduction to Alternative Microscopy Techniques

The literature indicates that there is also scope for data captured within the SEM, particularly during *in situ* dynamic processes, to be supported by other microscopy techniques. Additionally, alternative microscopes may help to overcome some of the challenges that occur when using an SEM, including the limited field of view and the availability of surface imaging only. Hence, the use of optical microscopy helps provide a wider imaging field, which ensures the images captured within the SEM are representative of the bulk sample. Profilometry microscopy techniques, such as optical profilometry and AFM, enable the quantification of surface data through morphology and topography measurements, providing a greater understanding of the SEM surface observations. The following sections review of each of these microscopy techniques and their benefits.

3.5.2 Optical Microscopy

Optical microscopy is used to closely view a sample through a magnification lens with visible light [188]. The microscope is designed to create a magnified image of the sample, which enables different topographical details to be distinguished by the human eye. Optical microscopy for opaque materials, such as metals and alloys, operates by a light passing through the objective lens that then reflects from the sample surface back into the microscope's objective lens. The amount of light entering the lens is regulated by the condenser and diaphragm [189]. This technique is known as reflected light microscopy [190]; an example of an optical light microscope is presented in Figure 3.20. The benefits of optical microscopy over other microscopy techniques are the lack of sample preparation, the speed of imaging, and the fact that it is unaffected by electromagnetic fields. However, the speed and ease at which images can be taken often compromises the image resolution compared to other microscopy techniques [189].

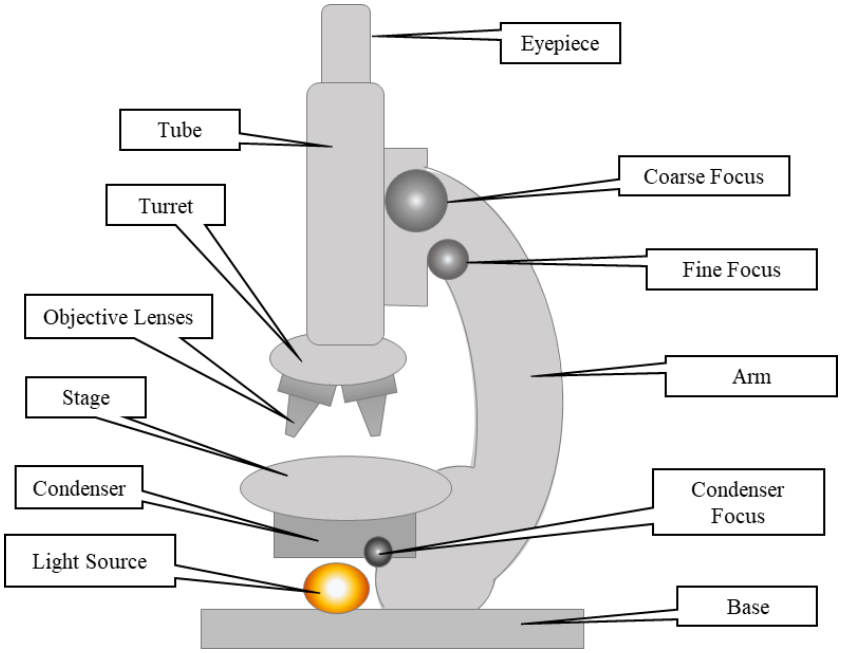

Figure 3.20: Diagram showing the key components of an optical light microscope.

3.5.3 Optical Profilometry

Optical profilometry further extends optical microscopy to facilitate 3D surface morphology measurements. This technique is used for surface analysis, profile analysis and area analysis, producing corresponding surface roughness, topology, and topography data via contactless scanning [191]. To gain surface and volume profiles using optical profilometry, light must be directed in such a way as to detect the surface in 3D. This can be executed in a number of ways: optical interference, the use of a confocal aperture, focus and phase detection, and the projection of a pattern onto the optical image [192].

The benefit of optical profilometry over other profilometry techniques is its ability to determine the variations in surface without contact with the sample; this means that the sample surface is unaffected by the measurement. It is also quicker than other profiling methods, such as stylus profiling, and can measure much larger areas of field. However, because it is an optical technique, its resolution is limited in magnification [191] .

3.5.4 Atomic Force Microscopy (AFM)

AFM is a form of profilometry that is executed with a stylus rather than an optical lens [193]. It is used to generate a 3D surface profile on a nanoscale with angstrom resolution, while also providing a variety of surface measurements, such as roughness. The main benefit of AFM over optical or electron microscopy is that it does not use lens or beam irradiation and hence is less limited in its spatial resolution. The principle of AFM operates by the use of the force between the cantilever tip and the sample, which detects the proximity of the tip to the sample (Figure 3.21) [194]. The size of the tip dictates the resolution measured on the sample surface. Owing to its high resolution, AFM has a limited lateral axis of less than 100μm [191].

In general, AFM has three modes: non-contact, contact, and tapping. In non-contact modes, as the tip of the cantilever approaches the surface, the close range, attractive forces between the surface and the tip cause the cantilever to deflect downwards, as the tip moves towards the cantilever surface, the oscillation amplitude changes indicating the topography. A laser beam is then used to detect this deflection by reflecting an incident beam off the tip of the cantilever. To prevent contact, a specially designed feedback loop moves the cantilever tip in line with the amplitude deviations.

For contact AFM, the cantilever tip is in contact with the sample surface throughout the duration of the measurements. Hence, the resulting attractive forces used for non-contact measurements no longer apply as the repulsive forces between the tip and the surface dominates and cause the cantilever to deflect away from the surface. Again, the laser beam is deflected accordingly, and an image produced.

Finally, tapping mode operates on a similar principle to the non-contact mode, but at a much higher amplitude of oscillation, resulting in some tip-surface contact during feedback.

As a result of this, the tip encounters the surface, frequently resulting in the blunting of the tip, but it does lead to feedback that is easier to control, and produces faster imaging [195][196]. It is important to note that during tapping and contact modes, both the tip and the sample surface may be significantly degraded or contaminated, and thus this can be considered an invasive technique [191].

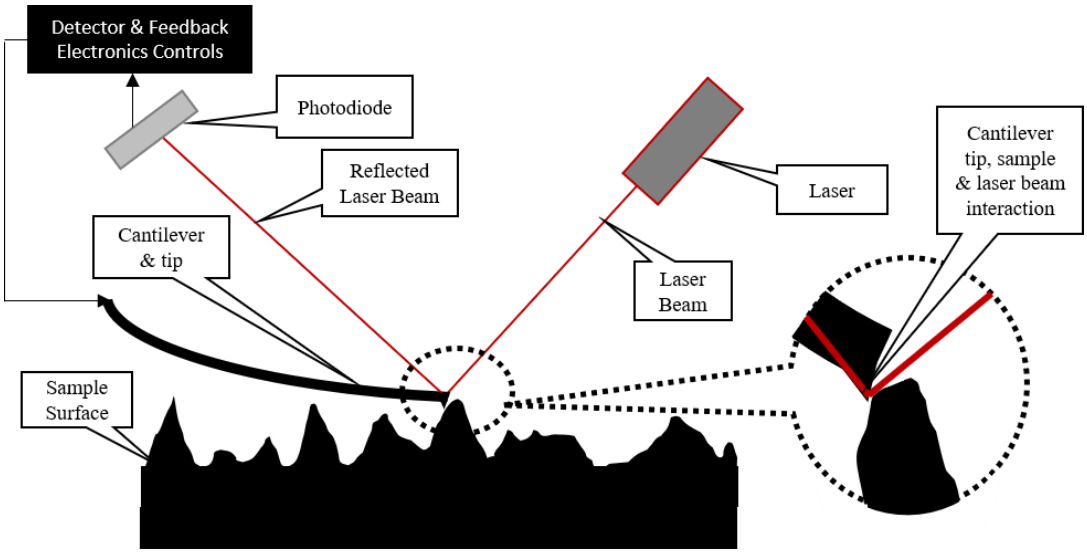

Figure 3.21 AFM principle of operation showing the feedback to the cantilever tip from the laser.

3.6 Measuring Grain Size

3.6.1 Measuring Grain Size: ASTM Standards

Microscopy techniques are often used to capture the grain size of materials to understand how the microstructure affects the material properties. ASTM standards dictate that there are three main recognised geometric methods for determining the average grain size in metallic materials; these are detailed below [197].

Comparison Procedure

The comparison procedure (Figure 3.22a) compares the grain structure to a series of graded images (G numbers) via four standardised charts, using plastic overlays or an eyepiece reticule. In general, grain sizes appear to be coarser by 1/2 to 1 G number lower when compared to other grain sizing methods. However, the repeatability of results suggests that grain size can be predicted to an accuracy of +/-1 chart rating, assuming that measurements are taken of at least three representative areas. It should be noted that this method is only valid for specific single-phase metallic materials with a grain structure that matches the pre-published charts.

Planimetric Procedure

For the planimetric procedure, more commonly known as the Jeffries procedure, the number of visible grains within a known area is counted (Figure 3.22b). The number of grains per unit area (*Na*) can further be compared to the ASTM grain size number or used to find the average area of the grains. The precision of this method is assumed to be +/- 0.25 with a result repeatability of +/- 0.5. However, the area measured must contain at least 50 grains to be representative of the whole sample distribution.

Intercept Procedure

The intercept procedure (Figure 3.22c) counts the number of grains intercepted by a test line or the number of grain boundaries' interactions with a test line per unit length of the test line. These are used to calculate the mean linear intercept length, which provides the average grain size. Both linear and circular intercept procedures have been used. This method has a positive correlation between accuracy and grain numbers but, unlike the other two methods, it can also be applied to whole samples with a few large grains.

In all test procedures it is assumed that the grains have a unimodal distribution of grain areas and that the nature of grain distributions within a sample cannot be found. Characterisation also focuses on grains in a 2D plane and so assumes that this is representative of the grain size in the bulk of the specimen [198].

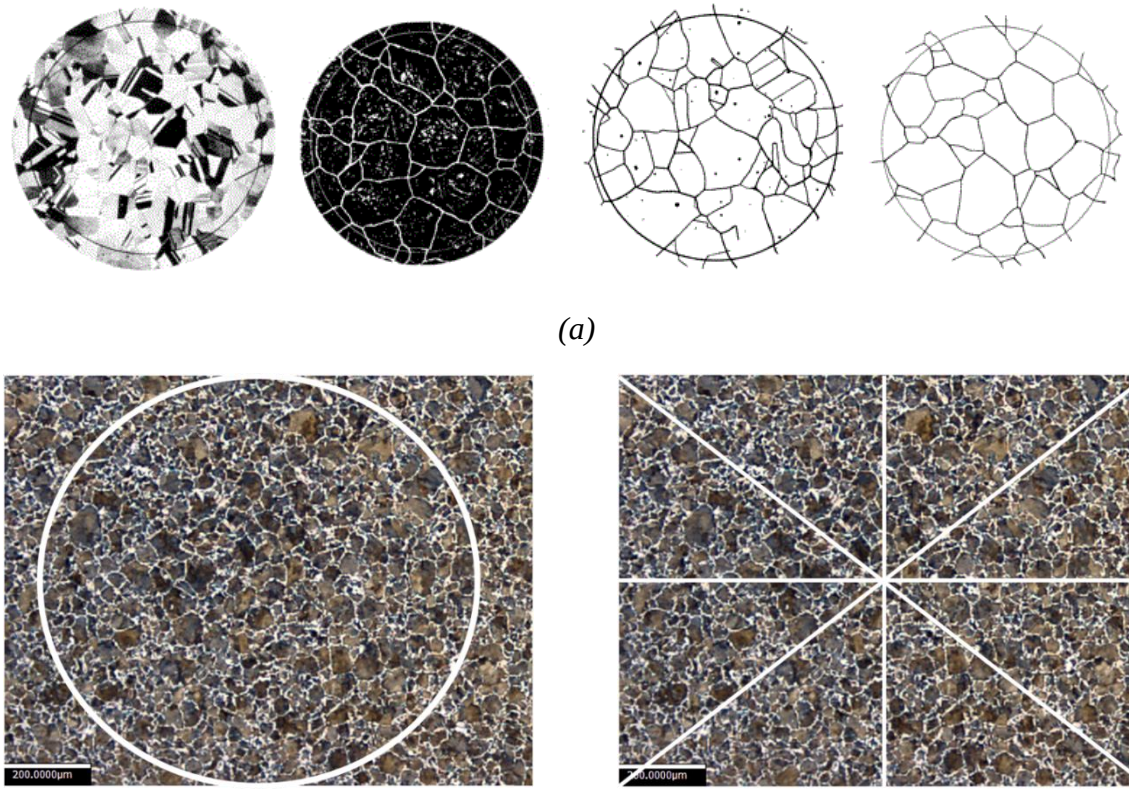

(a) *(b)* *(c)*

Figure 3.22: Three ASTM standard methods for measuring average grain size: (a) Comparison [197]*, (b) Planimetric, and (c) Intercept.*

3.6.2 Measuring Grain Size: Alternative Methods

The ASTM standard methods provide an estimation of the average grain size with a corresponding standard deviation. However, the ASTM methods do not provide information on the distribution of grain sizes. To achieve this, the size of each grain must be measured individually (often using edge detection algorithms and other tools, see section 3.6.3) to determine the area [199]. Each grain's area can further be converted to a corresponding diameter using the equivalent circular area method [200],

$$d = \sqrt{\frac{4a}{\pi}} \qquad \textit{Equation 3.4}$$

where d = equivalent grain diameter and a = the measured grain area. The equivalent circular area method assumes that the average area can be approximated to a circle, as shown in Figure 3.23. This equivalent diameter can either be calculated for individual grain diameters or as the average circular diameter across all grain areas. Hence, the data can provide a distribution of grain geometry with respect to the location and numbers of grains of a specific size [200].

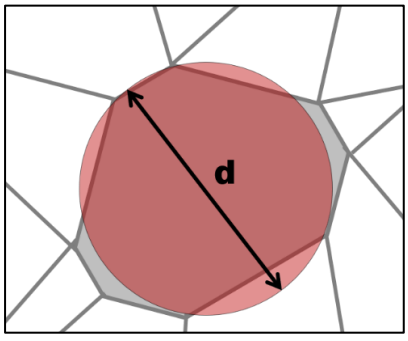

Figure 3.23: Average circulate grain diameter (d) representing a single grain's overall area (a).

An alternative method, which minimises the number of grain measurements required for metals and alloys, is the Hall-Petch effect. The Hall-Petch effect is an experimental relationship between the strength of materials and their corresponding grain size, which indicates that strength increases as the grain size decreases [201]. The work by Hall [202] and Petch [203] on the strength of metals led to,

$$\sigma_y = \sigma_0 + kd^{-x} \qquad \textit{Equation 3.5}$$

where d is the grain size, σ_y is the stress at yield or a flow stress at higher plastic strains corresponding to the material with grain size d, σ_0 is the corresponding stress for large single crystals or very large grained material (referred to it here as the bulk stress), and k and x are constants, which are theoretically predicted or experimentally measured [201].

The Hall-Petch relationship can subsequently be used to estimate the grain size of metals and alloys based on their yield strength, if there are multiple samples of the same material with different grain sizes due to undergoing different heating / cooling treatments. Studies have shown that the Hall-Petch equation accurately predicts the grain size of metallic materials; examples include steel [204][205], copper [206][207], brass [208] and titanium [209][210]. The benefits of this are that it decreases the number of grain size calculations required by simply finding the strengths and grain sizes of a few samples to determine a relationship, which can be applied to multiple grain size samples. The Hall-Petch relationship can subsequently be verified experimentally by testing the yield strength of a single / large crystal structure of the material. However, it does not completely negate the need for some grain measurements.

3.6.3 Grain Measurement & Edge Detection Algorithms

In order to remove human error from grain size calculations, as well as to increase the speed of the process for multiple specimens, grain measurement software, accompanied by image enhancement and edge detection algorithms, is often used. Two commonly used image processing software are ImageJ and MATLAB, but image processing can be conducted in many programming languages. The aim of image processing is to enhance the grain boundaries to make it easier to calculate the grain size and number of grains. The use of thresholding, which segments greyscale images into features and backgrounds along with filtering (via Fourier transforms or Gaussian distributions), can be used to increase the clarity of the grain boundaries [211].

Once images have been satisfactorily processed, edge detection algorithms are subsequently used to identify grain boundaries so that they can then be measured, automatically or manually, using one of the methods described in Sections 3.6.1 and 3.6.2. The two most common types of algorithms used are Sobel and Canny algorithms.

Sobel Algorithm

Sobel is an edge detection algorithm used for object detection against a background. The Sobel algorithm operates by the derivative approximation using a pair of 3×3 matrices, known as the Sobel operators, of each pixel to find the edges of objects. Using this method, only edges where the gradient of the considered image is at its maximum are returned. However, there must be enough contrast between the edge and the image in order to produce an accurate outline and hence successful edge detection [212]. This method is the inbuilt edge detection algorithm used in ImageJ [213]. There are also alternative edge detection methods based on the Sobel method that use different operators; examples include Prewitt and Roberts [214].

Canny Algorithm

The Canny operator is a multi-step algorithm that works by detecting edges while simultaneously suppressing noise. It assumes linear filtering and additive Gaussian noise. The algorithm works by first smoothing the image with a Gaussian filter before applying one of the Sobel, Prewitt or Roberts operators to find the gradient between pixels. A threshold is then applied where any noise is removed that occurs in specific grayscale boundaries and is not 'stronger' than the threshold value, before all non-maximum pixels (those that do not define the edges) are suppressed. A further threshold is applied to the image, again to remove any noise on the edges, before presenting an image of only edges [215]. This algorithm can be a very powerful tool for grain boundary exposure, as it combines the edge detection algorithms described above with image processing. However, it can lead to over- or under-detection of grain boundaries, depending on the level of thresholding applied [216].

Owing to their unique edge detection algorithms, Canny and Sobel often produce substantially different edge outlines. Sobel is more commonly used to differentiate foreground and background images while Canny is used for outlines of smaller objects on a background. An example of the difference is shown in Figure 3.24, where the focus in the Sobel image is an overall outline and smoothness of the edge. In contrast, the Canny shows a greater amount of detail but at the expense of possibly showing excess features which are not relevant to the image.

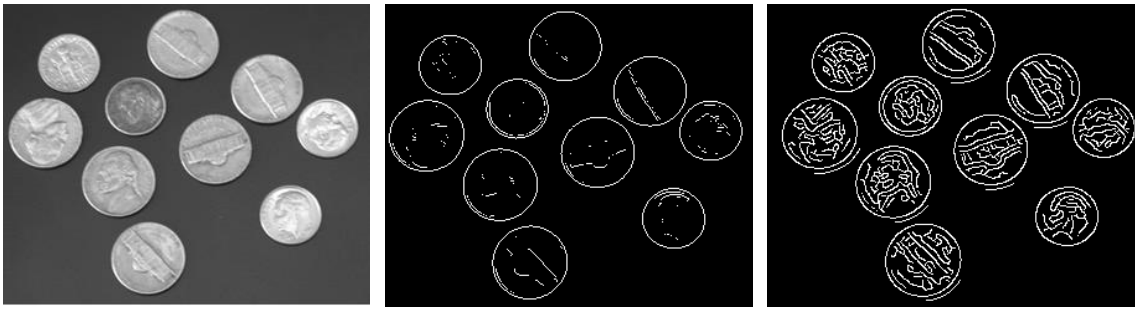

(a) (b) (c)

Figure 3.24: An image has undergone edge detection using both a Sobel and a Canny algorithm where: (a)is the original image, (b) is the Sobel edge detection result, and (c) is the Canny edge detection result [217].

Once a binary image of the outlined grain boundaries is produced, various automated tools can be applied to the standard grain size measurement procedures in Sections 3.6.1 and 3.6.2, and thus to calculate the size of the grains. This can include the use of standard software, such as in ImageJ, which automates the calculation of the number of grains in an image and the average grain area [211], or by line detection functions in MATLAB or other programming languages. However, care must be taken during processing and should be validated by a manual calculation to ensure that accurate grain size measurements have occurred.

3.7 Conclusions

This chapter details the current literature available on the wide range of microscopy techniques, several of which will be used and extended in this thesis. In particular, the literature demonstrates the new developments of *in situ* SEM imaging at high-temperature alongside some of the challenges. It is noted that the current high-temperature *in situ* studies are often limited by working distance, detector temperature and loss of surface quality, which impact the size of SE and EBSD datasets both spatially and with respect to time. Furthermore, owing to the limited *in situ* SEM data, there is a lack of investigation into the equivalence of *in situ* studies compared to their *ex situ* counterparts. Consequently, although current heating stages for *in situ* studies on alloys have produced good data, a more in-depth investigation is required to capture extended heat treatments of alloys and form a more complete comparison to the results from *ex situ* studies produced under the same conditions. This thesis aims to identify and solve some of the challenges of *in situ* SEM imaging at high-temperature highlighted in the literature, as well as to showcase the benefits of this technique for metallographic dynamic processes.

Alongside the *in situ* SEM literature, this review establishes the benefits of different experimental microscopy techniques, which can be used to gain a fundamental understanding of the microstructural evolution of materials. Hence, the advantage of cross-referencing microscopy methods will be further demonstrated in this thesis alongside new combinations of these methods to simultaneously capture microstructural changes at temperature. When studying the microstructural evolution of materials, the appropriate analysis tools must be used. A range of grain detection and measurement methods have been widely explored for microstructural images captured at room temperature. However, there is little documentation on how images captured at high-temperature may be quantified using these measurement techniques; this will be considered in this thesis.

Chapter 4

Investigative *In Situ* High-Temperature SEM Imaging

4.1 Introduction

The development of new experimental methods for micro-scale examination at elevated temperatures facilitates an increased understanding of the structural evolution of materials in aggressive environments. These include the aerospace and nuclear power industries, or during high-temperature processing. In particular, the use of scanning electron microscopy (SEM) at high-temperatures has enabled the observation of changes in grain size and phase during heating [46]. These microstructural features in turn play a role in controlling the physical and mechanical properties of materials on a macro-scale.

The current literature indicates that high-temperature SEM is a powerful tool for observing the dynamic crystallographic and microstructural processes in metals and alloys, with studies detailing these processes in steel and nickel. In addition to providing heat to the specimen, as discussed in Chapter 3, the technical challenges of heating to high temperatures within an SEM include preventing the loss of vacuum quality, the overheating of detectors and the degradation of the stage's heating element, and minimising the temperature gradient through the sample. The literature also describes further physical challenges associated with imaging at high-temperatures. An example of this is the effect on the signal to noise ratio from the detector of the thermionic emission of electrons from heated samples [186]. It is noted that electron backscatter diffraction (EBSD) imaging is particularly challenging at high-

temperatures owing to the close proximity of the detector to the sample, which threatens to damage the detector phosphor screen, the temperature of which typically must not exceed 120 °C [165]. Currently, stage design predominantly focuses on the use of shielding and single-use heaters to produce EBSD and secondary electron (SE) data. Shielding is used to surround the sample in a furnace-like environment, minimising temperature gradients while protecting the detectors from radiative heat. The limitations of shielding are that it decreases the visible imaging area and may also cause damage to the specimen surface, which can prevent collection of EBSD data. Furthermore, it may also limit the working distance. Single use heaters, where specimens are spot welded to the heater, are very effective at minimising the temperature gradient by providing direct contact between the heater and the specimen, facilitating good conduction. However, as well as being consumable and thus potentially expensive to the user, spot welding the specimen to the sample to facilitate heat transfer prohibits the testing of any electrically non-conductive samples. These solutions have been implemented to some extent in the literature, but there is a lack of studies documenting the impact of the heaters on their surroundings within the SEM, as well as the effect of specific material properties on the ability to image using EBSD at high-temperature.

This chapter will first describe the development of a novel heat stage that can be used *in situ* to enable imaging in both SE and EBSD configurations, without the need for shielding or consumable heaters. Subsequently, it will demonstrate the heat stage's stability within the SEM environment, including the impact on other detectors. Furthermore, material studies on nickel, for which, despite nickel studies at 800-900 °C [218], EBSD data of nickel at temperatures between 200 °C and 600 °C are not available, and steel, will show some of the material properties, which can impact the ability to image using EBSD over specific temperature ranges and time periods. This study will also highlight the advantages of high-temperature SEM imaging.

4.2 Methodology

4.2.1 Heat Stage Design

A series of experiments were conducted using a purpose-built heat stage, shown in Figure 4.1, designed in collaboration between the Laboratory for *In Situ* Microscopy and Analysis (LIMA) at The University of Oxford and Deben UK Limited. The heat stage is based on a HeatWave® Labs UHV Button Heater, Model 101136, combined with a purpose-built mounting, cooling, and temperature control system. The heater, an 8 mm diameter molybdenum cylinder, was chosen owing to its capability to reach temperatures of up to 1200 °C, its precision and stability, and the ease of sample mounting. The heater was mounted on a specially designed holder that consisted of brass heat shielding, as well as appropriate mounting fixtures to attach to a Zeiss EVO SEM stage at a 70° tilt for EBSD imaging. The PID temperature controller was designed around the use of a K-type thermocouple, which was inserted into the heater holder to contact the base of the heater.

One of the main challenges of *in situ* heat stage design was the prevention of heat loss from the specimen and overheating of detectors and the surrounding environment. Preliminary investigations of the stage design experimented with heat shielding. The aim was to ensure that shielding minimised heat transfer and overall interference to detectors, whilst not limiting the available imageable area of the specimen. To facilitate this, the geometry of the stage allowed the specimen to completely cover the exposed heater area. Specimens were then hold onto the stage, ensuring good contact with Macor clips. This design meant the Macor clips acted as an insulator creating a furnace like environment around the edge of the specimen which both minimised the temperature gradient around the specimen whilst also preventing loss of heat into the surrounding atmosphere.

The stage was purpose-built for EBSD imaging by optimising the working distance between the sample and both the gun and the EBSD detector. Optimisation of the working

distance focussed on image quality and detector temperature control. Vent holes were added to the casing to minimise vacuum pump down time, as well as maintain the vacuum quality by allowing the continuous degassing of the stage during imaging. By maintaining a good quality vacuum, the image quality improved and the heat transfer to the surrounding environment was minimised. An adapter was developed to fix the heat stage in a horizontal position for SE and backscattered electron (BSE) imaging. The heat stage development was part of a wider project with Deben UK Ltd which included the design of a combined thermo-mechanical stage, details of which can be found in the appendix of Chapter 4.

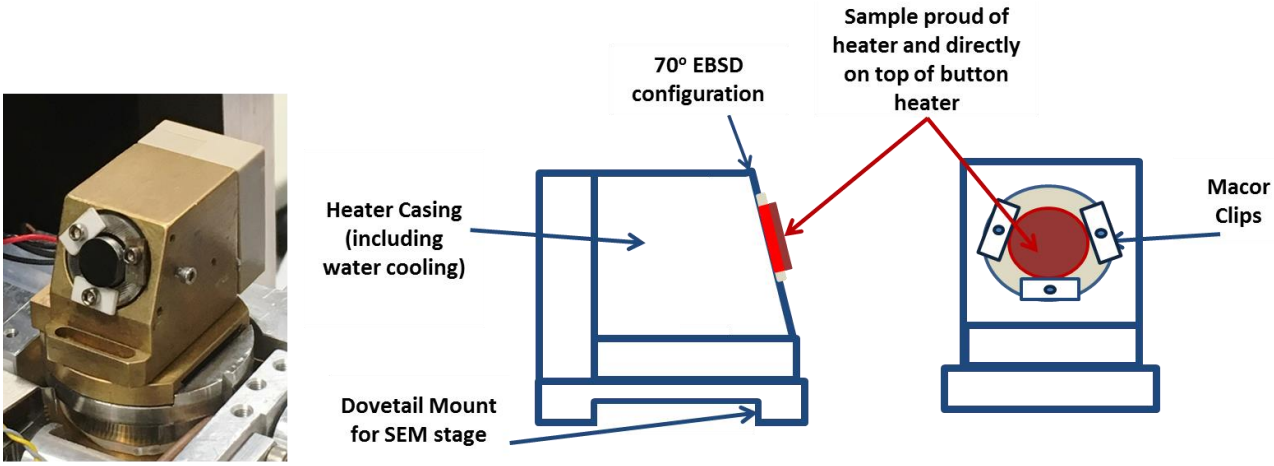

Figure 4.1: Heat Stage accompanied by a schematic showing key features.

4.2.2 Materials & Sample Preparation

During the initial testing of the heat stage, two main materials were used: industrially pure nickel, and 0.4 wt.% carbon steel. Details of the properties of these two materials can be found in Chapter 2. The different sample preparation techniques required for SEM imaging, particularly EBSD, of nickel and steel are discussed below.

Industrially Pure Nickel

Nickel was used for the initial investigation of imaging on samples heated using the heat stage *in situ* due to its high crystallographic orientation and high topographic contrast

from polishing, which make it ideal for EBSD imaging [129]. Hence, nickel is often used in the calibration of EBSD detectors [6]. Disk samples of nickel with a diameter of 8 mm were cut for both SE and EBSD imaging. All samples were initially ground, using progressively finer silicon carbide papers (grades: P240, P400, P600, P800, P1200). Samples were then polished, firstly using three grades of diamond suspension (9, 3, 1 μm) and finally colloidal silica (0.07 μm) combined with a water-based lubricant, down to a thickness of approximately 1 mm. This is a standard procedure for preparing nickel for EBSD imaging and also greatly improved the quality of SE images gained, compared to a non-polished sample where surface imperfections in the material may not be representative of the bulk of the specimen. By polishing the specimen pre-imaging, these impurities and imperfections are removed, including excess oxidation, dust and surface impurities that are not bonded to the specimen.

Carbon Steel

Unlike nickel, there is not a standard procedure for polishing carbon steel, which led to a range of techniques being tested in this project. The initial cutting and grinding procedures were identical to the nickel specimens and consistent for all polishing procedures tested. The polishing procedures also utilised a water-based lubricant. The final procedure chosen used diamond solutions of 9, 3 and 1 μm for 20 minutes each, followed by colloidal silica for 2 hours. The sample was cleaned with acetone between each preparation stage and dried with an air gun to minimise contamination between the polishing equipment and to prevent scratching. Colloidal silica is a chemical and mechanical polishing agent that disperses precipitates on the surface. However, it can lead to etching of steels if they are over polished and, as such, 2 hours was found to be the optimum line between over-etching the sample and generating a polished surface suitable for EBSD.

4.2.3 Heat Stage Thermal Investigations

In addition to the design and development testing conducted at Deben UK Ltd, final temperature stability tests were carried out to establish the temperature increase of the neighbouring detectors within the SEM during heating at the required experimental temperatures. This was particularly important as the energy dispersive X-ray (EDX), EBSD, and BSE detectors have low maximum operating temperatures of 50, 120 and 300 °C respectively [165]. K-type thermocouples were attached to the electron gun column and EBSD detector using small carbon tabs (Figure 4.2), and to the outer surface of the heat stage using Macor® clips. The heat stage was heated up to 850 °C and held for 2 hours in the position used for EBSD imaging. The temperatures of the heat stage and detectors were monitored and recorded over this time period using a Pico Technology TC-08 thermocouple data logger sampling at a rate of 1 Hz. Note that, during elevated temperature tests, the EDX detector was fully retracted out of the chamber owing to its very low maximum operating temperature of 50 °C. All EDX data detailed in this thesis were obtained at room temperature.

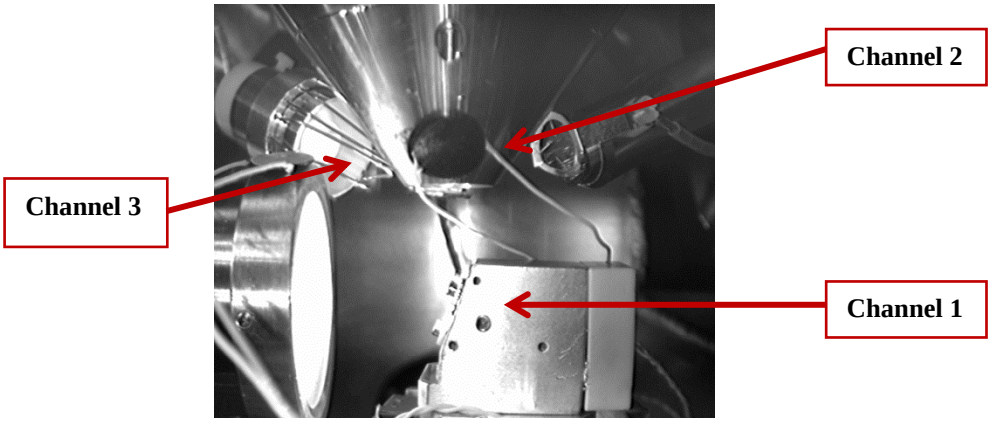

Figure 4.2 Experimental set-up for SEM detector and environment thermocouple measurements. Readings were taken at the heat stage surface (channel 1), on the gun (channel 2), and on the EBSD detector (channel 3).

Further temperature validation experiments were conducted with an industrially pure nickel specimen, approximately 1 mm thickness and 8 mm diameter, to quantify the surface

temperature of the specimen compared to that of the heater. Data were recorded every second from a K-type thermocouple mounted on the nickel sample surface during heating and after equilibrium was achieved. Data were compared to the heat stage set temperature and to analytical calculations performed using Fourier's law of heat conduction,

$$\dot{Q} = -\kappa A_s \frac{T - T_1}{\Delta x} \qquad \textit{Equation 4.1}$$

and the Stefan Boltzmann law,

$$\dot{Q} = \varepsilon A_s \sigma T^4 \qquad \textit{Equation 4.2}$$

where A is the specimen face surface area (m^2), Δx is the thickness of the specimen (m), $\dot{Q}$ is the heat flux from the specimen free surface (W), κ is the thermal conductivity of the specimen (50 W m^{-1} K^{-1}), ϵ is the emissivity of the specimen, σ is the Stefan Boltzmann constant (5.67x 10^{-8} W m K^{-4}), T is the specimen top surface temperature (K), and T_1 is the heat stage temperature (K). Making the heat flux due to conduction equal to the radiated heat provided the steady state surface temperature. The use of these laws assumes that the only heat loss from the specimen is radiation from the surface. Hence, this calculation neglected heat loss via conduction and convection; a reasonable assumption given the high vacuum environment within the SEM.

4.2.4 Investigative High-temperature Imaging

To investigate EBSD imaging ability at high-temperatures using the heat stage, industrially pure nickel (99.5% Ni) specimens were selected (details of the sample preparation of nickel can be found in Section 4.2.2). The nickel was mounted on the stage using Macor® clips, which were designed to align the sample in the centre of the stage without touching the sample surface. This mounting procedure avoided shadowing or damage to the polished specimen.

The nickel specimen was heated up to 800 °C (just below the maximum heat stage temperature of 920 °C) with scans recorded at 100 °C intervals. EBSD scans over 40 μm × 115 μm regions were taken after 5 minutes of heating at each temperature, using a raster step size of 0.5 μm. Each scan was completed in 3-4 minutes and taken in approximately the same location. Once the series of EBSD scans at 100 °C temperature intervals were complete, a large scan of 250 μm × 700 μm at a step size of 1 μm was carried out at 850 °C, which took 1.5 hours to complete. To further investigate the heat stage's stability, SE images were also captured during heating to observe any changes in the nickel surface with temperature and time. The SE images were taken at a magnification of 650× at 100 °C intervals up to 800 °C, at 850 °C, and upon cooling to room temperature. The magnification selected was a compromise between the need to capture a sufficient number of grains for analysis and the need to perform the scan in less than 5 minutes to minimise the adverse effects of beam drift. In the case of nickel, owing to the size of the grain structure, 5 grains were deemed sufficient to provide insight into any changes in microstructure (for which none were expected as nickel's microstructure is stable at these temperatures) or loss of EBSD image quality that occurred during heating.

Similar experiments were carried out on 0.4 wt.% carbon steel as an example application study, with EBSD imaging up to 850 °C. The steel sample had the same dimensions as the nickel sample and underwent a grinding and polishing process, outlined in Section 4.2.2. Phase change and grain development at these temperatures were monitored using EBSD imaging. Scans at 850 °C were of sizes 2 μm × 40 μm and 20 μm × 50 μm, both with step size 0.2 μm. Scans at temperatures between 100 °C and 800 °C were 30 μm × 60 μm in size. The EBSD scans took between 2 and 5 minutes each to complete, and scan times and magnifications were selected for similar reasons as for the nickel data. However, in this case,

the number of steel grains required was larger (>10 grains) owing to the need to conduct grain boundary and phase change analysis.

4.2.5 Temperature Impact on EBSD Surface Quality

To image using EBSD, a very smooth, polished surface is required. The level of surface roughness at which EBSD data can be captured is dictated by the material interaction volume. Material interaction volume is defined as the elastic mean free path of electrons [130], which is a measure of the depth to which the electrons penetrate the material surface, as defined in Chapter 3. This can be calculated for elements using the Kanaya-Okayama Range equation [120] or can be simulated for elements, alloys and compounds using a Monte Carlo simulation such as CASINO [135]. CASINO is a single-scattering Monte Carlo simulation of electron trajectory in a solid, which can be used to generate all recorded signals (X-rays, SEs and BSEs) in an SEM, for the acceleration voltages 0.1–30 keV [135]; see Chapter 3 for further details.

In this study, CASINO was used to estimate the interaction volume for carbon steel and nickel using the trajectories of the BSEs and SEs from the surface through the bulk of the specimen. The CASINO simulation parameters used were: 10,000 electrons at a range of voltages between 5 keV and 30 keV (beam voltage range used for SEM imaging) for a bulk sample tilted at 70° (standard angle for EBSD).

The corresponding interaction volume determined from CASINO simulations was compared to the roughness and depth profiles of steel and nickel samples before and after heating to supplement the EBSD and SE data and understand the effect that temperature may have on sample preparation. The roughness data were documented using atomic force microscopy (AFM), non-contact mode, and measurements were recorded over an area of 50 μm × 50 μm. Measurements were taken both after samples were prepared for EBSD

imaging, and again after a thermal cycle: heating up to 850 °C in 10 minutes holding for 1 hour and cooling to room temperature over 30 minutes, with three measurements taken each time. EDX scans of 5 minutes and maps of 200 frames, were also taken over an area of 500 μm × 400 μm of the steel sample, post-cooling, but while it remained in vacuum. The EDX data were used to identify where any oxidation may have occurred, and its resulting effect on image quality.

To determine the effect of heating on the sample surface, the roughness parameters *Ra, Rq* and *Rmax* were compared before and after heating. *Ra* is the arithmetic average of the absolute values of the profile height deviations (peaks and valleys) from the mean line, while *Rq* is the root mean square average of the profile heights from the mean. *Rmax* is the maximum roughness, which is defined as the maximum peak to valley dimension across the roughness area profiled. The depth distribution of roughness, defined as the percentage of the surface area that is at a given depth (from the topology data taken relative to the maximum height), was also compared, before and after heating, to the depth of the interaction volume.

The CASINO simulation was further supported by the Fraunhofer diffraction approximation to quantify the effect that roughness may have on beam intensity. The Fraunhofer diffraction shows the diffraction of waves when the diffraction pattern is viewed at a long distance from the diffracting object [219]. The standard solution for the multi-slit approximation was considered with respect to a step function representing roughness, to quantify the impact that roughness would have on electron diffraction intensity.

4.3 Results

4.3.1 Heat Stage Thermal Investigation Results

During pump down and testing, the vacuum in the chamber was monitored. The pump down time was approximately 1 hour, compared to a 3-5 minute pump down time for the chamber without the heat stage. The pump down time was attributed to the need to degas the stage to the equivalent vacuum level of the chamber with only a specimen inside. After pump down, the chamber pressure remained less than 9×10^{-5} mbar throughout the testing of the heat stage, which was comparable to that without the stage. Figure 4.3a depicts the results of the environmental and detector tests within the SEM. Figure 4.3b shows the surface temperature of the heat stage for 2 hours; the temperature is shown to be constant after the first 30 minutes. The corresponding temperature of the EBSD detector and bottom of the gun column during the heating are shown in Figure 4.3a. The detector temperature readings indicate that the detectors do not exceed 45 °C, even after heating the stage at 850 °C for 2 hours. The temperature of the EBSD detector reaches a plateau at approximately 100 minutes, suggesting that thermal equilibrium has been reached and heating over many hours would not cause a significant rise in detector temperature. It is therefore anticipated that *in situ* high-temperature imaging could be safely executed over a number of hours without damaging the EBSD or SE detector (based on the location of the thermocouple on the gun column), given that the detector temperatures reach thermal equilibrium during the time period monitored.

The temperature gradient results from the nickel specimen, Figure 4.4, showed the temperature at the surface of the sample and the set-point temperature of the stage. The data showed a 2 °C temperature difference between the heat stage and the sample surface, once thermal equilibrium is reached. Calculations indicated an expected difference of less than 1 °C across metal samples of 1 mm thickness, the exact value being dependent on the metal.

Given potential errors in the temperature measurements (e.g. K-type thermocouples are accurate to within ~2% of the indicated temperature) this is consistent with the data obtained.

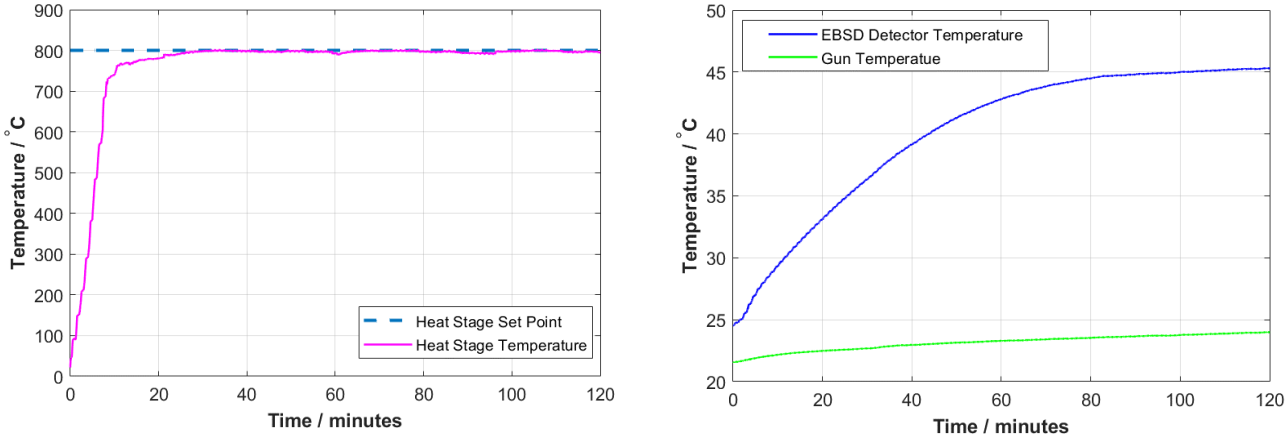

(a) *(b)*

Figure 4.3: Results of the detector temperature testing: (a) heat stage heating profile, and (b) accompanying detector temperatures during heating of the heat stage to 850 °C.

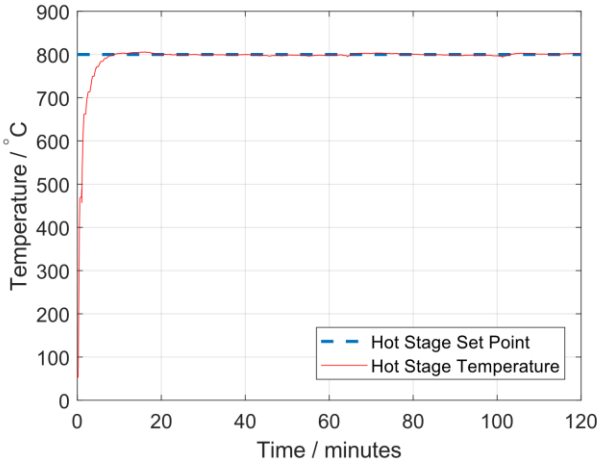

Figure 4.4: Achieved surface temperature for a 1 mm thick nickel specimen heated to a nominal temperature of 800 °C.

4.3.2 High-Temperature EBSD Imaging of Nickel

A set of 40 µm × 115 µm EBSD scans of nickel were taken at 100 °C intervals; a schematic of the heating profile is shown in Figure 4.5. Once each temperature was reached, the sample was held for 5 minutes and SE and EBSD images were taken, before increasing the temperature to the next interval. Figure 4.6 shows the nickel inverse pole figure that EBSD maps produced. It is noted that the scans are all taken in approximately the same location, excluding some slight beam drift; however, the clarity of the EBSD scans at 300 °C and 400 °C show significant deterioration compared to the others. It is known that the index-ability of the Kikuchi patterns is dictated by the uniformity of brightness and orientation of the bands [220]; an ideal example is shown in Figure 4.7a. Although a Kikuchi pattern may be easily visible to the human eye, it may not be recognisable by the software once the Kikuchi pattern is transformed into Hough Space. In particular, indexable Kikuchi patterns may not be produced if the bands are non-uniform in intensity, i.e. a mix of light and dark, as shown in the 300 °C Kikuchi patterns, indicated in Figure 4.7b. Similarly, if the bands are significantly blurred, as they are at 400 °C (Figure 4.7c), this may impair the Hough transform's accuracy, accounting for a loss of EBSD image quality at this temperature.

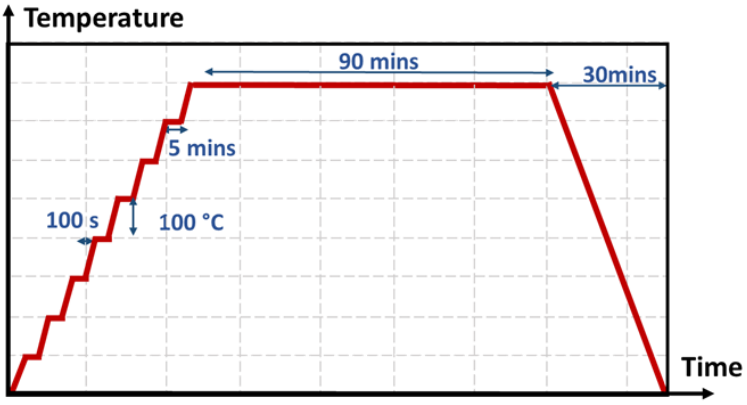

Figure 4.5: Schematic of the heating profile of nickel for all EBSD and SE images taken.

The EBSD pattern quality can be quantified by two main parameters, the Fit and the Confidence Index (C.I.). The Fit is defined as the average angular deviation between the recalculated bands[4] and the detected bands [2]. An ideal Fit is as small as possible but is generally accepted as between 0.5° and 2° [221]. The C.I. measures the probability of correctness of an orientation solution relative to other interpretations of the data. A common approach is to calculate the average C.I. across the whole image and only use images with an average C.I. value greater than 0.3 [221]. Figure 4.8 shows the C.I. and Fit versus temperature for nickel and indicates a drop in C.I. below the acceptable level at 300 °C and 400 °C, followed by a return to acceptable levels at higher temperatures. Similarly, scans of all temperatures except 300 °C and 400 °C show an average Fit of between 1.2° and 1.4°. However, at temperatures of 300 °C and 400 °C, the Fit worsens, with a significant increase from 1.2° to about 1.8°; hence the reliability of the statistical analysis is reduced, and the pattern is not indexable.

[4] Recalculated bands define where the bands should appear based on the orientation obtained from the material crystallography [2].

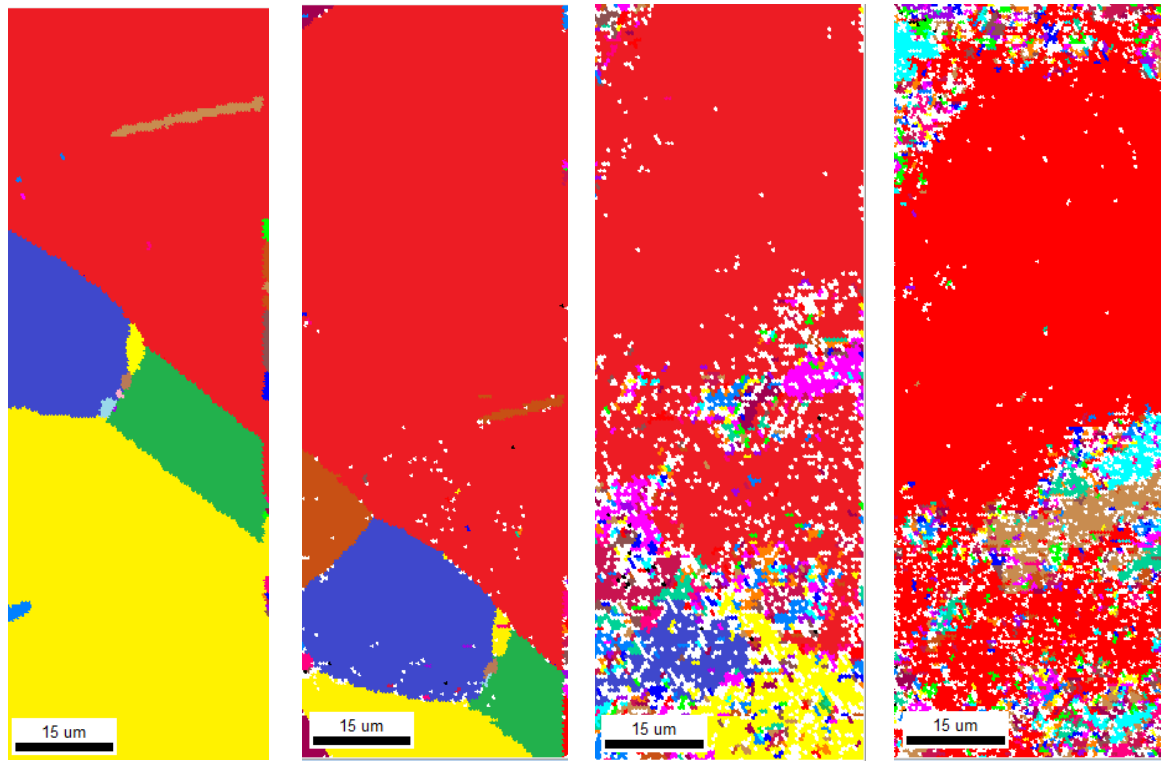

(a) 100 °C *(b) 200 °C* *(c) 300 °C* *(d) 400 °C*

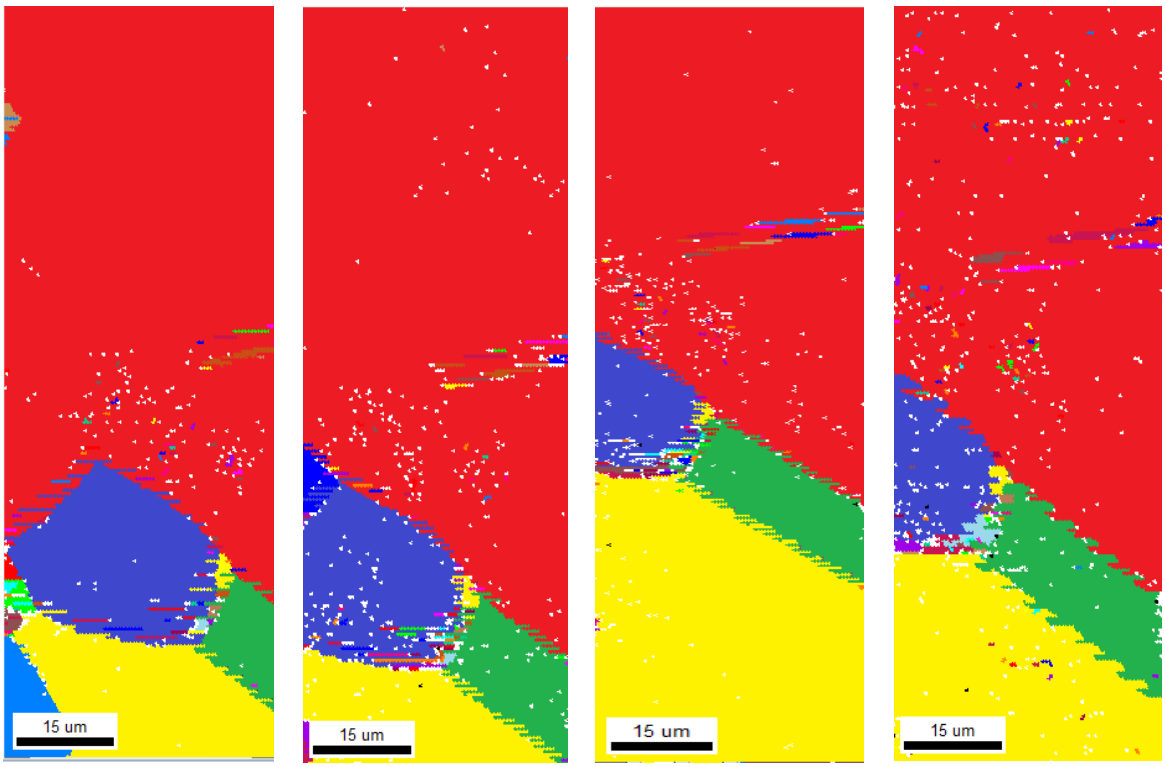

(e) 500 °C *(f) 600 °C* *(g) 700 °C* *(h) 800 °C*

Figure 4.6: Raw (uncleaned) grain maps of nickel at various temperatures, demonstrating a significant loss of image quality at 300 °C and 400 °C.

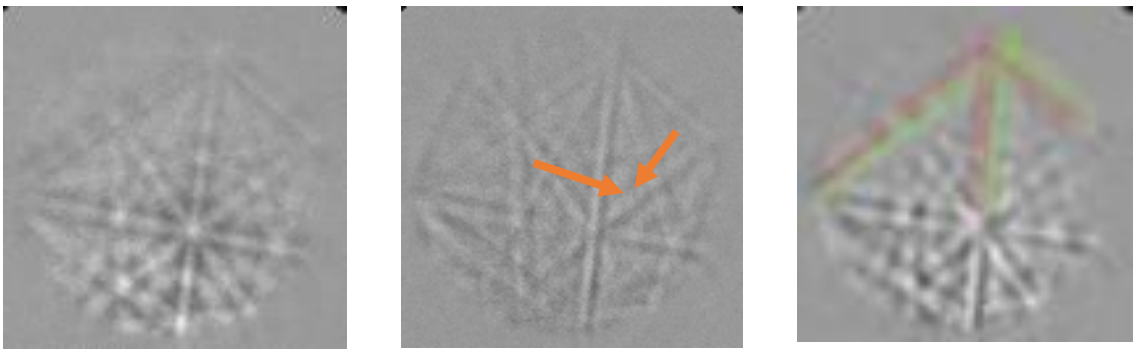

(a) 200 °C *(b) 300 °C* *(c) 400 °C*

Figure 4.7: An example of nickel Kikuchi patterns demonstrating the types of degradation of Kikuchi patterns that can occur. For example: (a) at 200 °C, showing uniform bands, (b) at 300 °C, showing, a loss of uniformity in band intensity indicated by the arrows where one side of a band is significantly darker than the other, and (c) at 400 °C, depicting blurring and duplication of bands at a slightly off angle as highlighted.

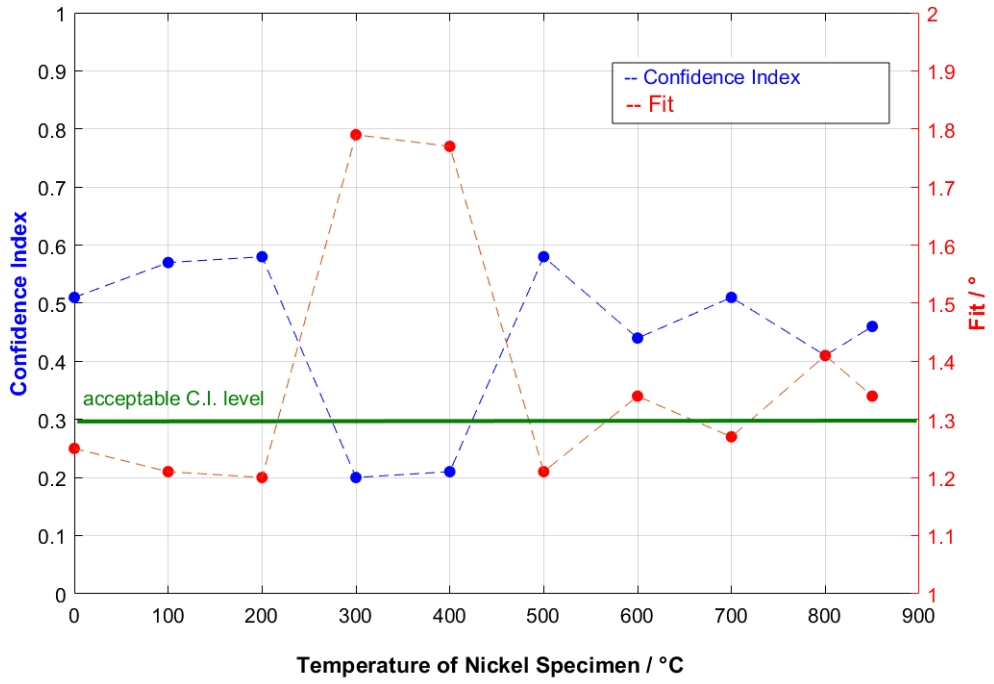

Figure 4.8: Confidence Index (C.I.) and Fit of the whole scanned area at each temperature showing a significant drop in C.I. in scans at 300 °C and 400 °C to below the acceptable C.I. level of 0.3 (represented by the green line). The plot also shows an increase in the Fit value around these temperatures, suggesting that the Kikuchi patterns are a poor match to those held in the statistical database.

4.3.3 High-Temperature SE Imaging of Nickel

SE images, which are slightly foreshortened due to the 70° tilt for EBSD, were also taken at 100 °C intervals during heating between 100 °C and 800 °C; see Figure 4.5 for the heating profile. Figure 4.9 shows the development of grain boundary outlines during heating through the temperature intervals and over time from room temperature (Figure 4.9a), 500 °C (Figure 4.9b), 700 °C (Figure 4.9c) and then at room temperature after cooling for 30 minutes from 800 °C (Figure 4.9d). The grain boundaries appeared after a total heating time of 40 minutes (5 minutes for each previous interval, with 100 s of heating between temperatures) at 700 °C, but were not seen at lower temperatures. Once revealed, nickel grain boundaries shown by the red arrows in Figure 4.9c and Figure 4.9d, remained visible after cooling. The small, rectangular darkened regions in the SE images shown by the yellow arrows Figure 4.9b and Figure 4.9c are due to EBSD beam damage [222].

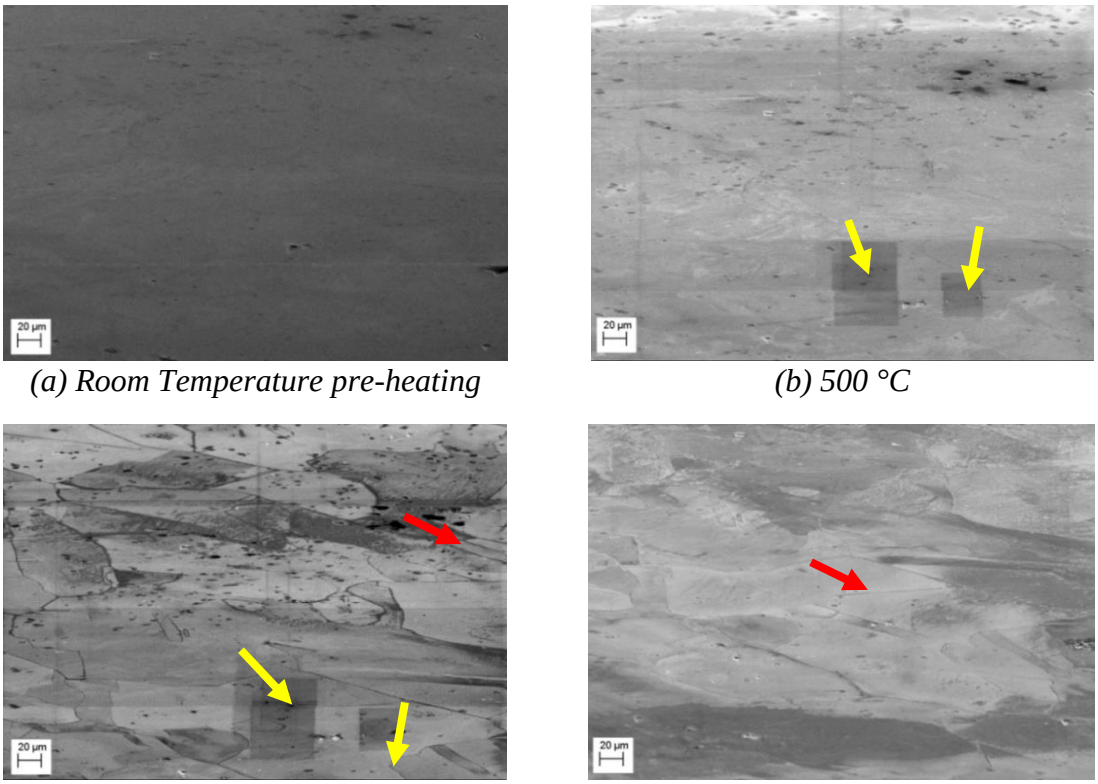

(a) Room Temperature pre-heating

(b) 500 °C

(c) 700 °C

(d) Room Temperature post-heating

Figure 4.9: SE Images of (a) pre-heating room temperature, (b) 500 °C, (c) 700 °C, and (d) post-heating room temperature. Dark rectangles (see yellow arrows) are from EBSD surface damage. The dark lines are grain boundaries (see red arrows).

4.3.4 High-temperature Steel Imaging Results

EBSD images of 0.4 wt.% carbon steel were also captured at temperatures up to 850 °C, demonstrating an ability to image steel at these high-temperatures. For data presented in Figure 4.11 and Figure 4.12 steel was heated up to 850 °C in 10 minutes and held for 60 minutes; Figure 4.10a shows a schematic of the temperature versus time profile. Data recorded in Figure 4.13 were obtained from a sample heated to 800 °C over a period of 83 minutes, pausing at 100 °C intervals to take SE and EBSD images (Figure 4.10b).

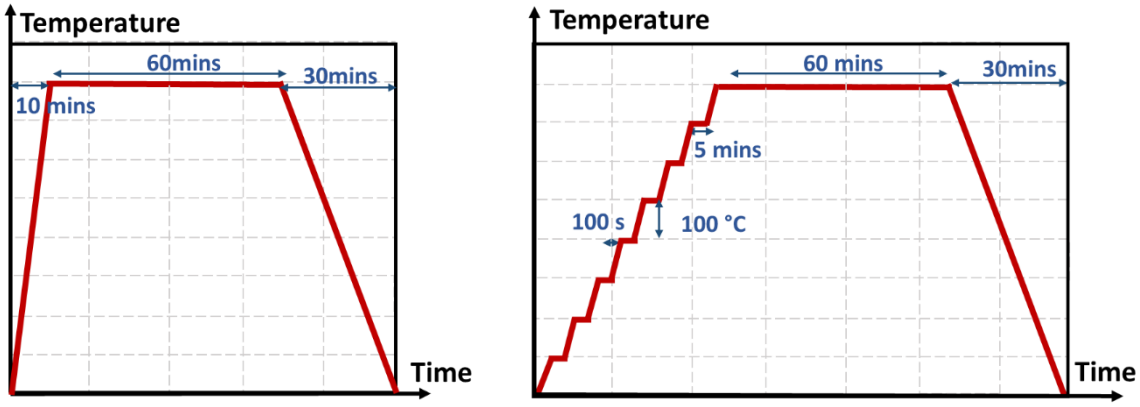

(a) *(b)*

Figure 4.10: Schematics of temperature profiles for the two sets of steel data: (a) shows the temperature profile corresponding to results in Figure 4.11 and Figure 4.12, (b) shows the stepped temperature profile corresponding to the results in Figure 4.13.

Figure 4.11 depicts the EBSD inverse pole figure and phase maps at room temperature and after 10 minutes of heating at 850 °C, and shows visible microstructural changes. In particular, Figure 4.11c and Figure 4.11d show the phase transformation from ferrite (red) and pearlite (green), at room temperature, to austenite (yellow) at 850 °C. However, the speed at which scans must be undertaken as a compromise between beam drift and scan size (the scans were captured in less than 3 minutes) can impact the scan clarity. Further heating of steel to observe the phase change using EBSD at 850 °C is shown in Figure 4.12. The scan quality shows degradation over time, with a significant loss of image quality after 21 minutes of heating when imaging the same area (Figure 4.12c).

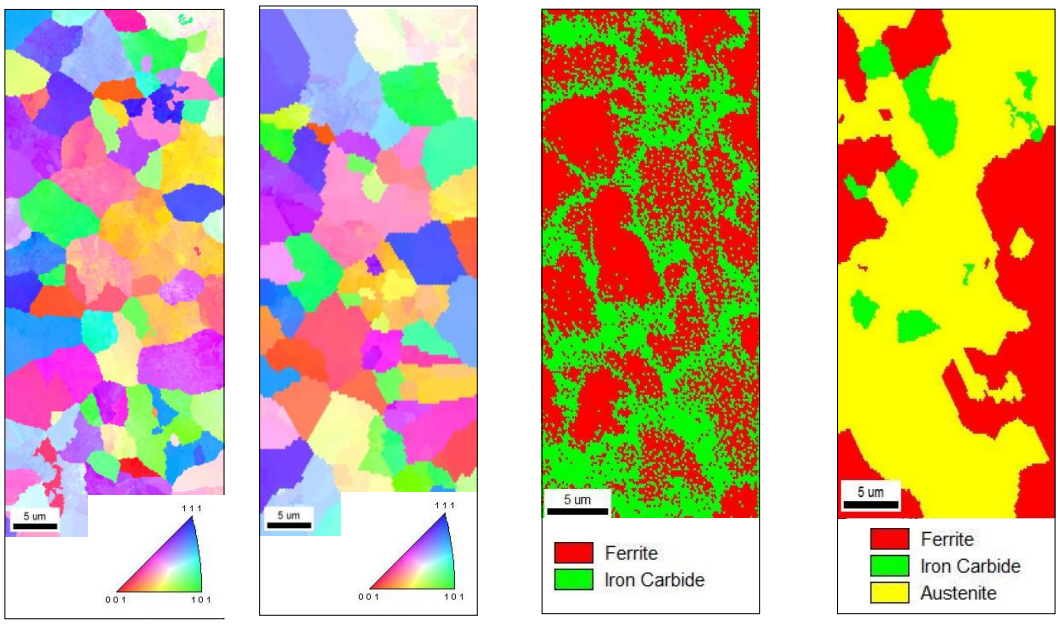

(a) Room Temperature *(b) 850 °C* *(c) Room Temperature* *(d) 850 °C*

Figure 4.11: : EBSD maps of 0.4 wt.% carbon steel where (a)&(b) show inverse pole figure maps and (c)&(d) show phase maps.

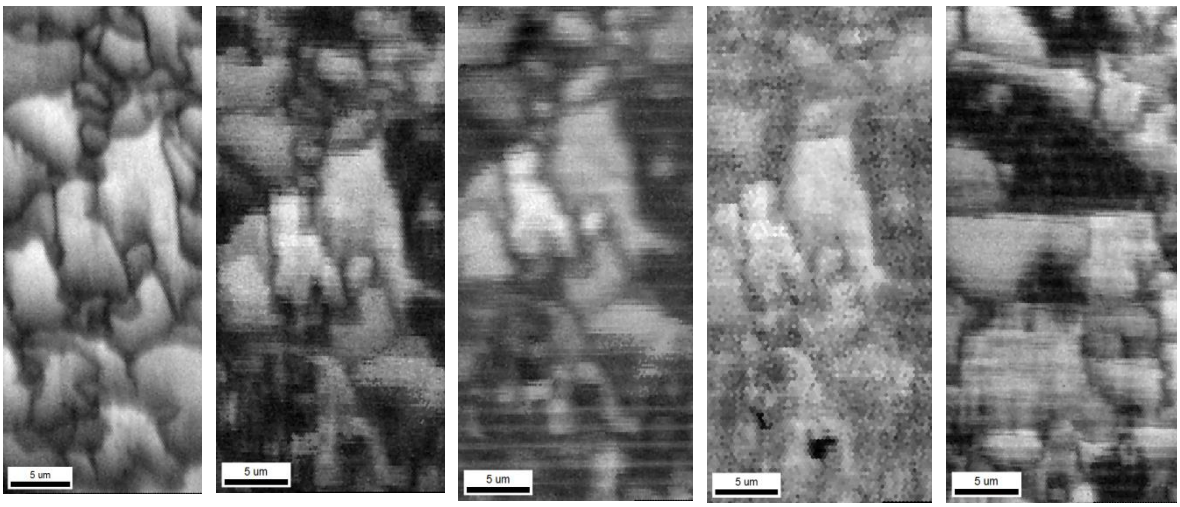

(a) 2minutes *(b) 10 minutes* *(c) 21 minutes* *(d) 31 minutes* *(e) 40 minutes*

Figure 4.12: EBSD image quality maps of the same area after holding at 850 °C, showing a significant loss of image quality after 20 minutes and limited usability of images after this time. The grey-scale operates from light to dark with the lighter, brighter grains indicating a better quality image than the darker grains. The black outlines show the grain boundaries.

Steel samples were also observed during stepped heating using SE and EBSD imaging (see Figure 4.10b for the heating profile). The EBSD image quality progressively worsened with increasing time and temperature (Figure 4.13). However, Figure 4.11 has already demonstrated images obtained at 850 °C after rapid heating, when the temperature was taken straight to 850 °C within 10 minutes rather than over a prolonged period of time as occurred with the interval images depicted in Figure 4.13.

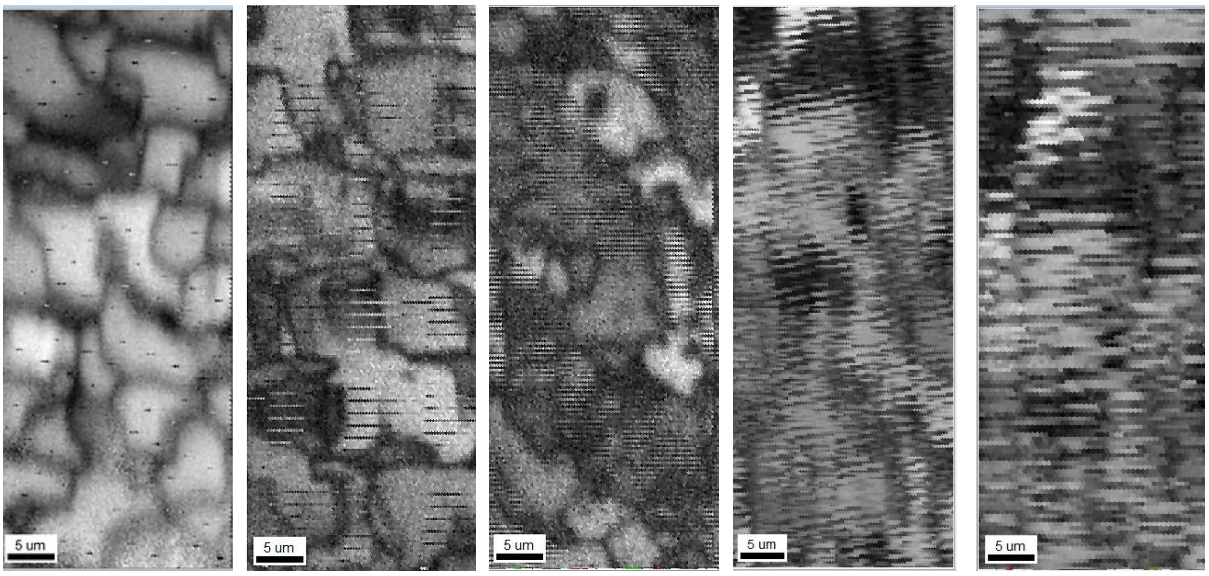

100 °C *300 °C* *500 °C* *(d) 700 °C* *(e) 800 °C*

Figure 4.13: Image quality EBSD maps of 0.4 wt.% carbon steel of the same surface area showing progressively worsening image quality with increasing temperature, and significant loss at 700 and 800 °C. The grey-scale operates from light to dark with the lighter, brighter grains indicating a better quality image than the darker grains. The black outlines show the grain boundaries

4.3.5 Effect of Heating on Specimen Surface Quality

EDX scans were taken of the steel samples post-cooling from 850 °C after 1 hour of heating (heating profile Figure 4.10a) to determine the level of oxidation post-heating and its possible impact on surface quality, and are shown in Figure 4.14. Figure 4.14 indicates that there are a few small areas of oxidisation, attributed to remaining colloidal silica from surface preparation but that the majority of the sample surface is free from oxygen. This is also shown in the EDX spectra in Figure 4.15.

To further investigate the difficulty of imaging steel after heating for 1 hour at 850 °C, surface topography measurements were carried out using AFM on steel samples pre- and post-heating (Figure 4.16). The scans showed a significant increase in the roughness parameters; before heating *Ra* = 44.1 nm and *Rq* = 37.4 nm, while after the heating and cooling cycle, *Ra* = 83.2 nm and *Rq* = 63.4 nm. The maximum roughness also increased, with the highest values of maximum roughness being 447 nm before heating and 1059 nm afterwards. AFM surface topography measurements were also carried out on nickel samples before and after heating, shown in Figure 4.17.

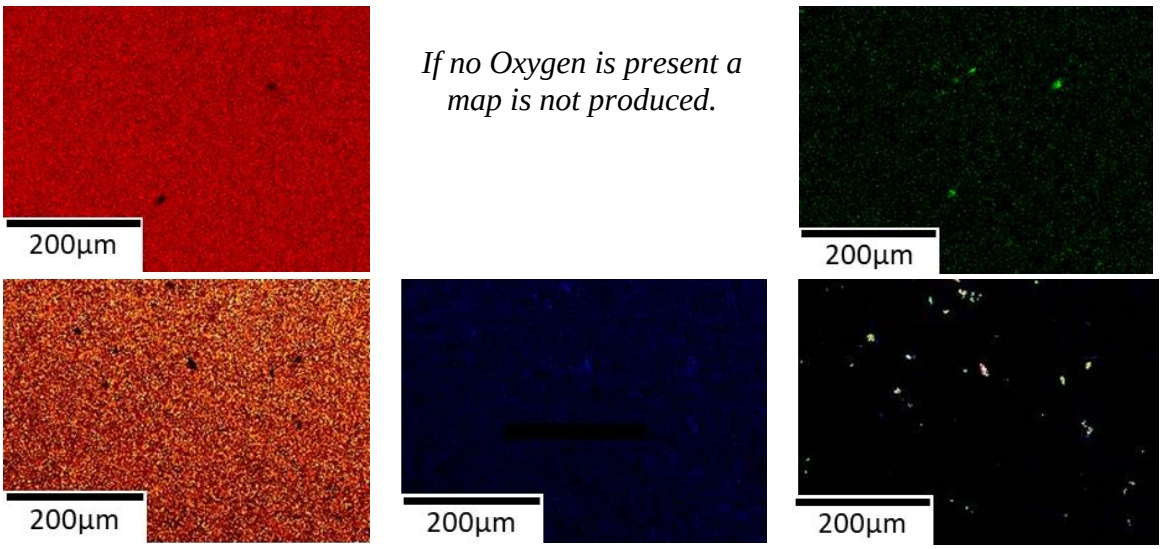

(a) Iron *(b) Oxygen* *(c) Silicon*

Figure 4.14: EDX steel maps, (top) pre-heating and (bottom) post-heating.

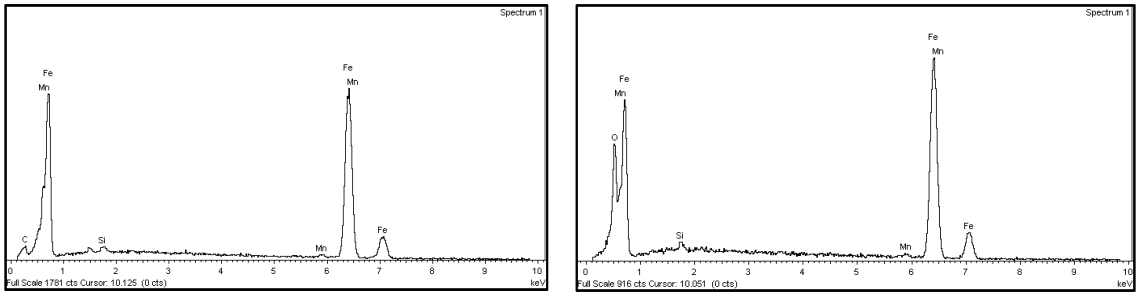

(a) *(b)*

Figure 4.15: EDX spectra showing: (a) no detectable oxygen before heating of carbon steel sample post-polishing, and (b) oxygen present after heating.

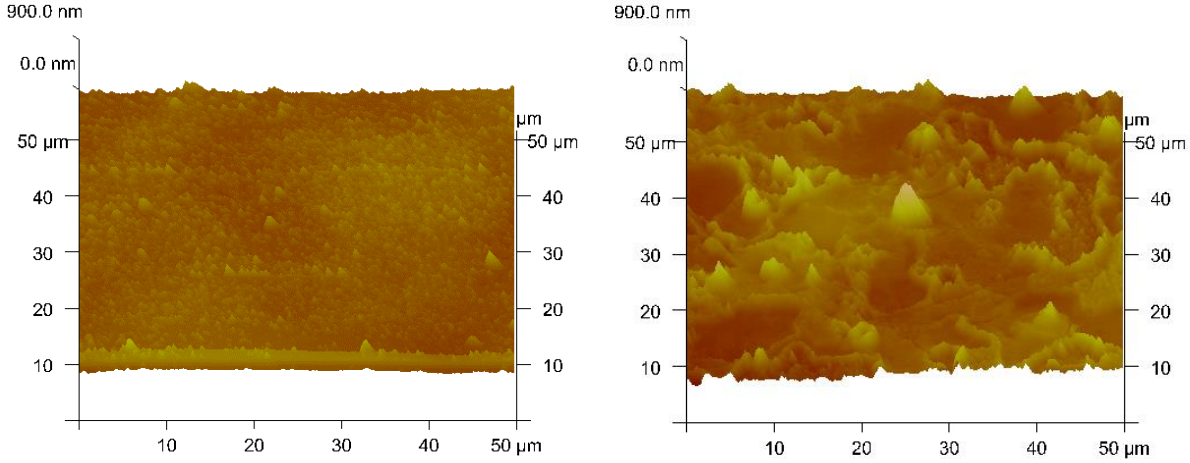

(a) Pre-Heat Treatment *(b) Post-Heat Treatment*

Figure 4.16: AFM roughness profiles of steel (a) pre-heating and (b) post-heating.

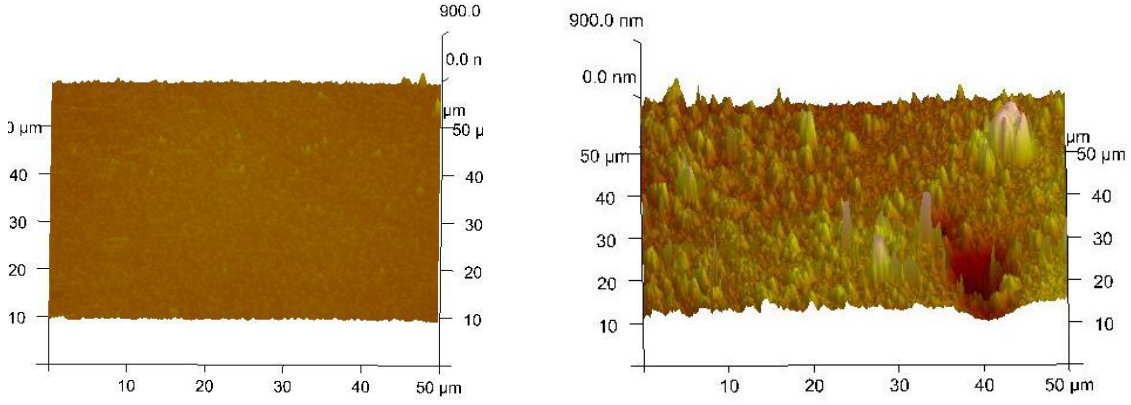

(a) Pre-Heat Treatment *(b) Post-Heat Treatment*

Figure 4.17: AFM roughness profiles of nickel (a) pre-heating and (b) post-heating.

4.3.6 Surface Quality Simulations

Surface quality models using the CASINO simulation were used to determine the impact of roughness on the quality of the image. The CASINO simulation examined the overall beam interaction volume and how this may subsequently be impacted by increased roughness. This was further supported by the Fraunhofer standard solution for multi-slit, stepped approximation.

The level of acceptable surface roughness is dictated by the interaction volume [145]. To quantify this, CASINO simulations were run for nickel and steel in an EBSD 70^{o} configuration with 10,000 electrons simulated at a voltage of up to 30 keV. An example of the CASINO simulation produced, giving the distribution of electrons for the 30 keV voltage is shown in Figure 4.18. The rest of the raw data for these simulations can be found in the appendix of Chapter 4.

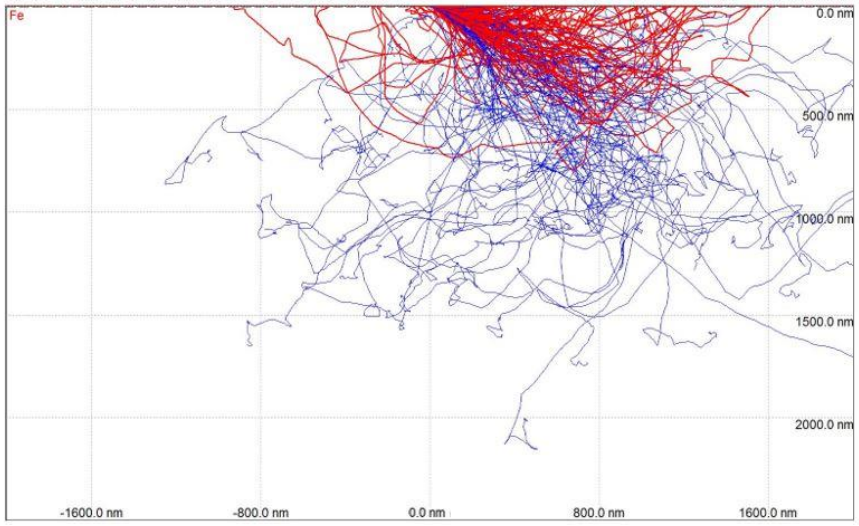

Figure 4.18: CASINO Simulation for steel at 30 keV showing the interaction volume of depth of primary electrons that will produce BSEs (red path) and SEs (blue path).

The CASINO simulation shows clearly that SEs have a much greater interaction volume than BSEs. A summary of the interaction volume distribution of electrons at 5, 10, 15, 20, 25 and 30 keV for nickel and steel is shown in Figure 4.19. As expected, there is a positive correlation between the electron voltage and the interaction volume for both BSEs and SEs. The interaction volume for steel and nickel are similar, with steel having a slightly greater interaction depth. The size of the maximum interaction volume for steel BSEs is found to be about 940 nm at 30 keV, compared to 920 nm for nickel.

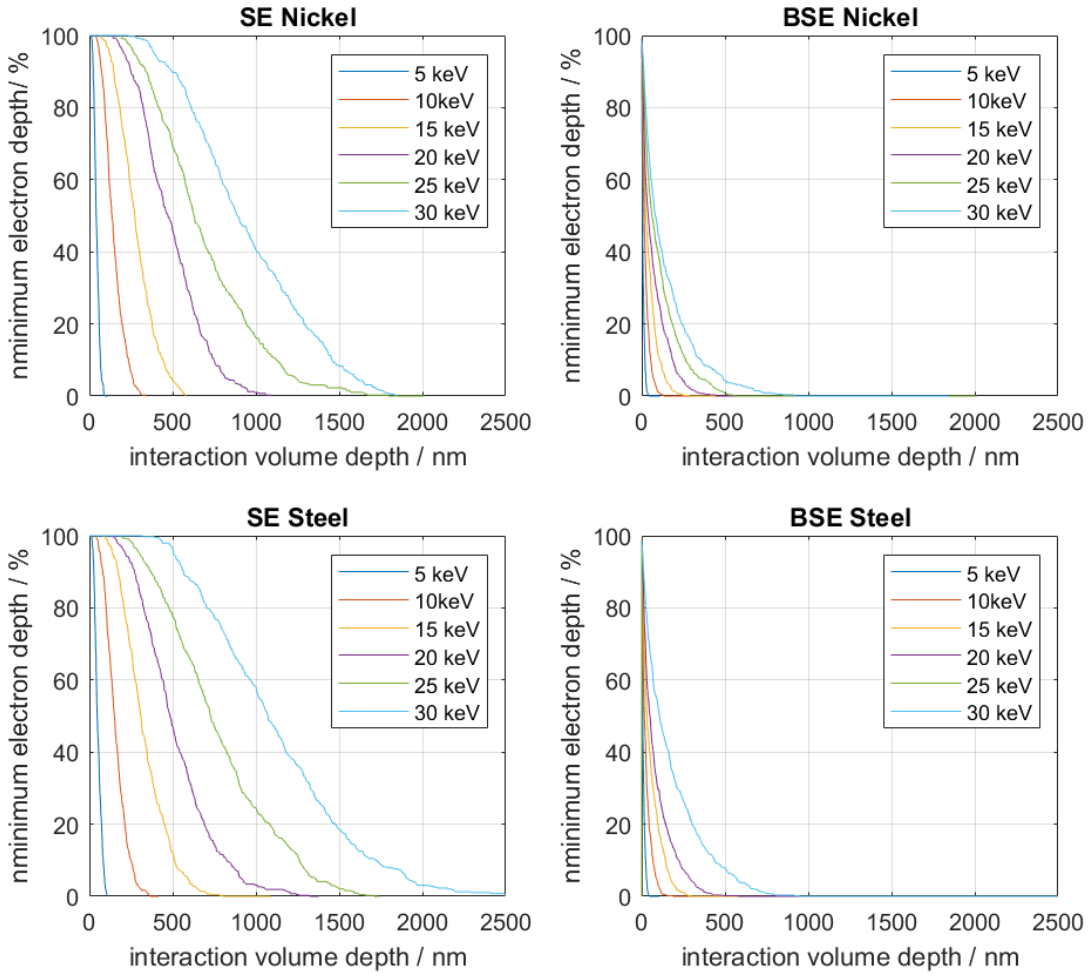

Figure 4.19: SE and BSE electron voltage interaction distribution of all results in CASINO shown as the minimum electron penetration depth against the number of electrons that reach that depth.

4.4 Discussion

The data obtained demonstrate that imaging at high-temperature enables the microstructure of metals and alloys to be monitored in real time. Additionally, the SE and EBSD images can be used to highlight a number of interesting observations, which indicate both the benefits and challenges of imaging at such high temperatures. Further analysis and discussion of the possible uses of these data and causes of the features and phenomena are given below.

4.4.1 Heat Stage Thermal Investigation Discussions

The data demonstrating the effects of holding specimens at elevated temperature on the detectors and SEM environment suggest that detectors will not need to be retracted or removed during testing, with the exception of the EDX detector. Moreover, as the sample surface temperature for a 1 mm thick specimen is almost identical to the heat stage surface temperature, surface-mounted thermocouples are not essential for measuring the temperature of the specimen, as this can be assumed to be the heat stage set point temperature. This is advantageous in preventing shadowing or loss of surface quality from thermocouple mounting.

4.4.2 EBSD Image Quality Degradation: Temperature Dependence

A significant degradation in the EBSD scan quality for nickel at 300 °C and 400 °C, compared to higher and lower temperatures, was observed, as quantified by a drop in C.I. and an increase in the Fit angle at these temperatures. A potential explanation that infrared radiation from the sample interferes with the detector was discounted as neither the phosphor screen nor the CCD camera are sensitive to the wavelengths emitted at a temperature of 300 °C to 400 °C, owing to the presence of protective coatings and filters. Furthermore, steel showed no significant change in C.I. or Fit at these temperatures, despite having a similar

emissivity. Hence, this loss of imaging is considered to be dependent on intrinsic material properties.

Nickel is ferromagnetic at room temperatures. However, its magnetization is temperature-dependent and its susceptibility follows the Curie-Weiss law [57], with a Curie temperature, T_c, of approximately 355 °C, above which nickel is paramagnetic [60]. Nickel's magnetization stays relatively constant up to 150 °C (~2/3 T_c). After this point, magnetization decreases with increasing temperature, until it becomes negligible at the Curie temperature.

Studies into the effect of a magnetic field on SEM imaging indicate that it can affect the ability to image and cause a loss of image intensity. Brodusch *et al*. [220] illustrated the influence of local magnetization on electron trajectories resulting in a change in the contrast intensity of BSEs and small shifts in the location and sharpness of Kikuchi bands. Close to the Curie temperature, the nickel sample may be expected to have mixed phases (i.e. mixed paramagnetic and ferromagnetic) with the spatial arrangement of these being easily disturbed by external influences. This may cause a significant loss of Kikuchi pattern intensity, as in the case of the 300 °C nickel pattern, owing to the spreading out of the interaction volume because of the coexistence of the two magnetic phases close to the Curie point. The slight shifts in Kikuchi patterns attributed to the presence of a magnetic field may also cause blurring or duplication of the Kikuchi bands, as seen in the nickel Kikuchi patterns at 400 °C, resulting in a low quality EBSD map.

Steel is also ferromagnetic at room temperature, having a Curie temperature of approximately 770 °C, the exact value being dependent on alloying elements and composition [58]. On this basis, degradation of EBSD quality may be expected between 700 °C and 800 °C, with indexable patterns to return above this temperature. In the present study, a severe degradation of EBSD quality was seen from 700 °C to 800 °C. However,

there is also reduced EBSD quality at elevated temperatures that are nevertheless less than 700 °C. This suggests that other factors, such as phase changes or loss of surface quality as a result of prolonged heating may be significant.

Overall, the data for nickel strongly suggest that the quality of the Kikuchi patterns is affected close to the Curie temperature. This limits the ability to index EBSD data. However, for steel, other factors appear to be significant requiring further explanation. This is discussed below.

4.4.3 EBSD Image Quality Degradation: Time Dependence

In general, the *in situ* imaging of steel indicates that the speed at which images are taken during phase changes and grain growth may also have an impact on the clarity of the scans. Hence, a very high polish will be required initially, as this has been found to help facilitate good image quality when rapid scans with a 0.3 µm to 1 µm step size, over areas as large as 40 µm × 90 µm, are taken in 2-3 minutes. Often, high quality scans can take several hours with step sizes of 0.1 µm, while microstructural changes may occur on the timescale of seconds to minutes. Repeated imaging of an area can also lead to visible surface damage of the sample as can be seen in Figure 4.9, and this can also impact the quality of the scan, leading to the necessity for quick scans that are evenly spaced over a period of time.

The EBSD scans of steel also showed significant degradation over time during heating at 850 °C. The reasons for this are thought to be either oxidation or an increase in roughness. Oxidation would likely have a negative impact on image quality if an oxide layer constitutes a significant fraction of the sampled volume, as the EBSD detector may then be unable to differentiate the oxide and the steel patterns. However, the EDX scans in Figure 4.14 indicate that, in the present study, oxidation is localised, so this does not appear to account for the loss of image quality. EBSD is also dependent on having a smooth diffracting surface to avoid

spatial blurring of the Kikuchi patterns. The AFM measurements show a significant increase in roughness during the heat cycle. Thus, the change in surface finish during the heating process may be linked to the loss of image quality of EBSD scans when imaged over a long period of time, as has been observed in these experiments (Figure 4.12 and Figure 4.13).

The Fraunhofer multi-slit approximation when applied to a step function shows a loss of intensity compared to that of a flat surface [219]. This indicates that there will be fewer electrons scattered (lower intensity) when roughness (represented in the form of a step function) is present. However, as mentioned previously, the level of acceptable surface roughness is also dictated by the interaction volume [145]. The CASINO simulations showed that for both steel and nickel the interaction volume of SEs was greater than for BSEs.

A comparison was performed between the surface roughness depth profiles before and after heating and the interaction volume depth profile (Figure 4.20). The graph shows the percentage of the surface area at a given depth (from the topology data taken relative to the maximum height), and the percentage of electrons that penetrate a given interaction volume[5] (from the CASINO data), for both nickel and steel specimens. The data for steel show that there are a significant number of electrons penetrating the sample at a greater depth than the surface topology before heating. However, post-heating, the surface roughness is deeper than the penetration depth of nearly all electrons.

On the other hand, the nickel topology data show that although the roughness increases, it does not increase to a greater depth than the electrons are able to penetrate. This is likely to be the cause of the loss of indexable patterns in steel after 20 minutes of heating at elevated temperature; the increase in surface roughness is sufficient to impede the electron-sample interaction required for EBSD.

[5] Interaction volume refers to the depth to which an electron penetrates.

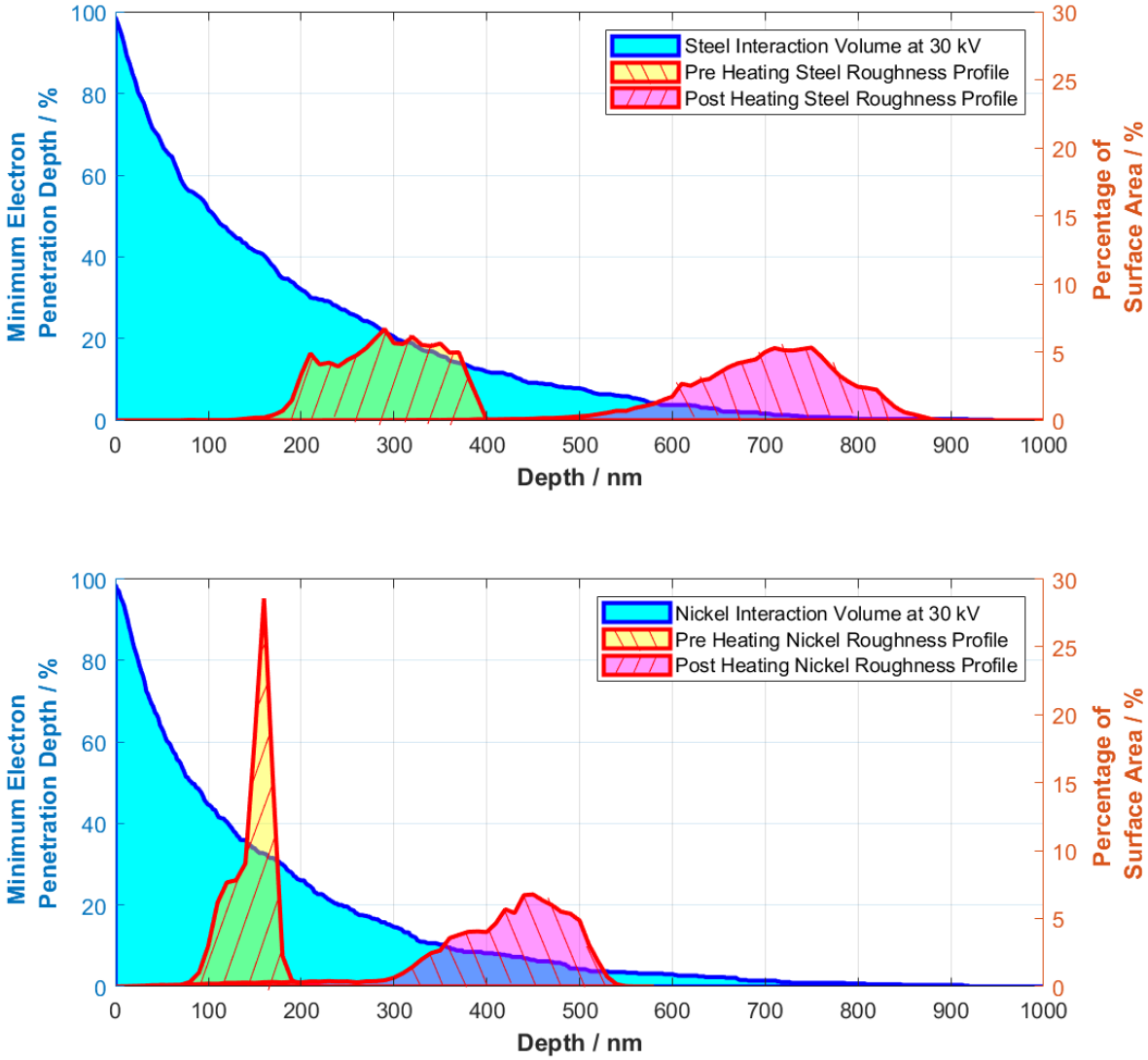

Figure 4.20: Surface depth profiles across the 50 µm × 50 µm scanned area before heating (yellow and forward-slash hatched) and after heating (magenta and back-slash hatched) compared to the interaction volume (electron depth penetration) for: (Top) nickel, and (Bottom) steel. The interaction volume is represented by the blue line showing the normalised distribution of the CASINO simulated interaction depths of 10,000 scattered electrons, simulated at 30 keV within the corresponding surface.

4.4.4 SE Image Grain Boundary Visibility

The nickel SE images show that the outlines of grain boundaries become visible over time at temperatures above 700 °C, a phenomenon known as thermal etching. Thermal etching is the development of surface grooves at the grain boundaries through exposure of a polished surface to elevated temperatures. The grain boundaries impinge on the specimen surface and, as a result of thermodynamic equilibration of the triple junction between the grain boundary and the free surface, the specimen surface rises away from the boundary [81]. The phenomenon of thermal etching is further discussed in Chapter 3. In this case, *in situ* heating of the nickel demonstrates the formation of thermal etching at around 700 °C and during heating to 800 °C, which led to the etch being retained upon cooling (Figure 4.9). The phenomenon of thermal etching of grain boundaries was confirmed by comparing the EBSD and SE images of the same area of nickel at 850 °C, which were found to match with good agreement.

The etch, as observed in images taken at 850 °C, was also compared to the SE image taken after cooling, along with their respective EBSD image quality maps; these are shown in Figure 4.21. The SE images indicate that some change in grain structure occurred during the cooling of the grains (outlined in white and indicated with red arrows) where the grain boundaries of smaller grains are lost. However, in the EBSD images, the sub-grains are still visible. Thus, it appears that the sub-grain boundaries disappeared from the SE image during cooling, but the sub-grains remained, as shown by the highlighted boundaries in the room-temperature EBSD image in Figure 4.21d. Previously, thermal etching observed post-cooling has been assumed to represent the grain boundaries that form at elevated temperatures. However, the data here, highlighted in Figure 4.21, suggest that thermal etching is best used for *in situ* studies. Data obtained after cooling may not accurately reflect the grain structure at temperature, due to the loss of visibility of etched grain boundaries in smaller grains. The

effects of thermal etching on the overall surface microstructure are further investigated, alongside other surface features that have been observed, in Chapter 5.

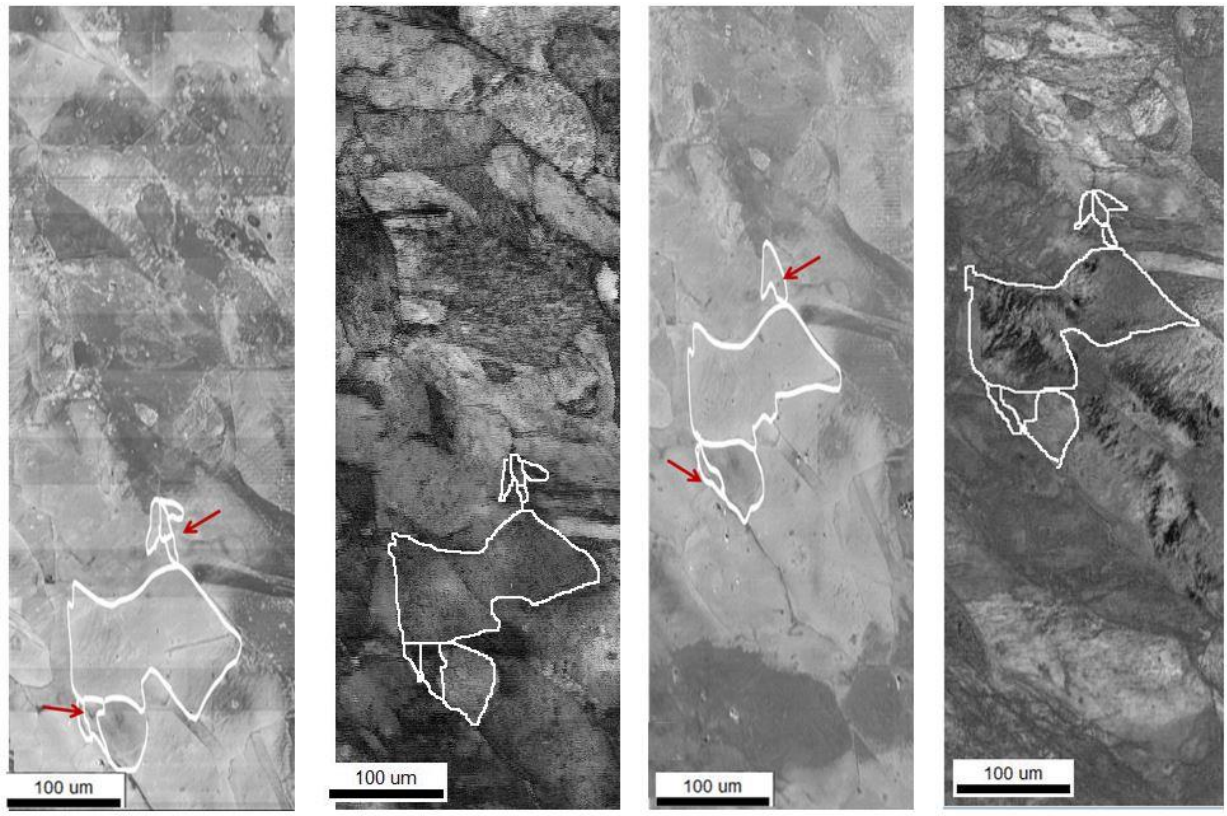

(a) *(b)* *(c)* *(d)*

Figure 4.21: (a) Thermal etching of nickel at 850 °C, SE image. (b) Corresponding EBSD image quality map. (c) SE image after cooling to room temperature; some etching remains. (d) The corresponding room temperature EBSD image quality map. Select grain boundaries have been outlined in white.

4.5 Conclusions

The EBSD and SE images in this study demonstrate the ability to consistently image within an SEM at temperatures up to 850 °C using a novel heat stage without the need for shielding or detector modification.

Furthermore, the results presented in this chapter illustrate some of the advantages and new experimental data that can be gained from *in situ* high-temperature imaging. In particular, the SE images of nickel enabled the observation of thermal etching formation at temperature. A comparison between images at 850 °C and at room temperature, post-cooling indicates that when room-temperature imaging is used to re-examine materials after thermal etching, there can be loss of visibility of grain boundaries around smaller grains, leading to a less accurate representation of the microstructure at temperature. Another advantage of the method was the ability to capture and document phase change, with the preliminary data of the steel ferrite / pearlite to austenite phase change used as an example.

Examination of both steel and nickel demonstrate the effect of material properties on imaging at high-temperature. In nickel, the observed loss of EBSD image clarity between 300 °C and 400 °C is attributed to the transition of nickel from ferromagnetic to paramagnetic. It should be noted that this may lead to difficulties observing similar ferromagnetic materials around their Curie temperature. In steel, the effect was less clear owing to the phase change also occurring between 700 °C and 800 °C. In addition, steel showed a significant increase in surface roughness after exposure to elevated temperatures for a prolonged period of time (>1 hour). The roughness became greater than the typical depth of steel interaction volume, which impacted image quality, limiting the amount of imaging that can be performed when the material is heated for an extended time period.

In conclusion, this chapter documents not only the stability of the beam and vacuum in the image quality and detectors in the temperature when using the newly designed heat stage but the effects of material properties at temperature on the ability to image using SE and EBSD. The effects and use of SE imaging for *in situ* microstructure observations are further investigated in Chapter 5, and EBSD imaging in Chapter 6.

Chapter 5

Surface Changes During *In Situ* SEM Heat Treatment of Carbon Steel

5.1 Introduction

The ability to study microstructures in the SEM at elevated temperatures, as demonstrated in Chapter 4, has a number of important applications. One example is the heat treatment of carbon steels. Such treatments are applied in order to form controlled microstructures, which in turn produce desirable mechanical properties [223], as discussed in Chapter 2.

However, while working *in situ*, an understanding of whether surface observations produce data representative of the evolution of the bulk material microstructure is required, as this can have implications for the interpretation of *in situ* data and their comparison to corresponding *ex situ* measurements. This chapter investigates the main *in situ* surface observations and the impact they have on carbon steel heat treatments. In particular, there are two surface effects that are observed at elevated temperatures: thermal etching and thermal oxidation, both of which can affect microstructural evolution on the surface of the material. Therefore, the effects of these phenomenon must be understood if bulk properties are to be inferred from surface measurements. These effects will now be described.

5.1.1 Thermal Etching

Thermal etching, also known as thermal grooving, is the development of a groove where a grain boundary emerges to intersect the surface of a hot polycrystal [83]. The current literature, as discussed in Chapter 2, suggest that thermal etching of moving grain boundaries is not well understood [82]; some results indicate that thermal etching impacts grain growth [87], while other literature suggests the effect is negligible [224]. Further studies have also acknowledged that thermal etching and its impact on grain growth, may be affected by the atmosphere or the presence of precipitates [89].

Thermal etching was observed during *in situ* observations of nickel (Chapter 4). However, as nickel's microstructure does not change at the temperatures imaged in Chapter 4, the presence of thermal etching had little impact on the evolution of the grain structure. Moreover, the thermal etching allows accurate images of the nickel microstructure, when compared to electron backscatter diffraction (EBSD) data, to be obtained at elevated temperature using secondary electron (SE) imaging. The benefit of SE imaging over EBSD is that sample preparation is simpler, as well as the speed at which microstructural data can be captured. Thus, SE imaging facilitates the capture of a larger number of grains, giving a quantitative representation of grain growth.

In the case of carbon steels, *in situ* studies have shown that thermal etching occurs in carbon steel during heat treatment in the austenitic region [225]. While undergoing heat treatment, microstructural and magnetic changes also occur; see Chapter 2 for details. As such, it is important to understand the impact of the thermal etching on microstructural changes observed *in situ* at elevated temperatures.

5.1.2 Thermal Oxidation

The heat treatment of carbon steel in air- and oxygen-rich environments often leads to the formation of oxide layers, a process known as thermal oxidation, which affects the resulting surface properties. To mitigate against thermal oxidation, carbon steel is often heat treated under what is commonly described as a 'fine' vacuum (~10^{-4} mbar) [7]. However, it has been documented that some oxidation of the surface can still occur even at these vacuum levels [8]. The literature detailed in Chapter 2 shows that there is an absence of data documenting the processes by which oxide scales form on carbon steels under a vacuum environment and during heat treatment cycles. As such, there is a lack of understanding of how this effect may impact three key factors; the first being the surface microstructural evolution during the heat treatment process; the second being the interaction of oxidation with other surface effects such as thermal etching; and the third is the ability to observe heat treatments *in situ*. The use of microscopy, and *in situ* high-temperature SEM imaging, has the potential to provide additional understanding of the formation of the carbon steel oxide layer and its effects on the heat-treated microstructure.

5.1.3 Chapter Overview

The research presented in this chapter aims to improve understanding of the mechanisms that impact surface grain growth relative to that in the bulk of the material; looking in particular at thermal etching and oxidation. Current studies indicate that some phenomena could impact grain growth both in the surface and bulk of the material during heat treatment of carbon steel [76]. By studying the surface changes during heat treatment *in situ*, supported by *ex situ* data, this study aims to identify the impact of oxidation and thermal etching on the high-temperature microstructural evolution. From this, *in situ* surface data, which has been confirmed to be representative of the bulk of the specimen, will be analysed, to provide insight into the grain evolution during the carbon steel heat treatments.

5.2 Methodology

To determine the effect of thermal etching and environmental conditions on surface grain growth during heat treatment, the microstructural evolution of carbon steel was studied using high-temperature *in situ* SEM imaging. The *in situ* heat treatments were also repeated in a standard furnace (referred to as furnace heat treatments) to enable microstructural comparisons to the SEM data. To support the *in situ* data, the microstructure was further examined optically *ex situ* for both the *in situ* and furnace heat treatments.

5.2.1 Materials

A 0.4 wt.% carbon steel was selected as it commonly undergoes heat treatment at temperatures above 780 °C, this being the temperature at which 0.4 wt.% carbon steel becomes fully austenitic [27]. These heat treatments lead to changes in its microstructural properties. Two types of starting structure were used:

- **Drawn Form Carbon Steel**: Directionally drawn carbon steel with no heat treatment applied and a coarse grain starting structure.
- **Fine Form Carbon Steel**: A finer, more uniform starting grain structure than the drawn form carbon steel.

More detail about the properties and application of 0.4 wt.% carbon steel can be found in Chapter 2, and optical images of the pre-heat treatment microstructure are in the results section of this chapter.

5.2.2 Heat Treatments

All heat treatments were conducted in the austenitic region (temperatures > 780 °C [226]) on disk samples with a diameter of 8 mm; a mixture of polished and unpolished specimens were used. Polished specimens were prepared by initial grinding using progressively finer silicon carbide papers (grades: P240, P400, P600, P800,

P1200), and then polishing, first using three grades of diamond suspension (9, 3, 1 μm) and finally colloidal silica (0.07 μm) combined with a water based lubricant. The final thickness of the specimen was approximately 1 mm.

In situ heat treatments of the specimens were facilitated by a purpose-built heat stage [15]. Several different heat treatments were applied *in situ* on two sample types: drawn, and fine grained. The samples were heated from room temperature to 800, 850 and 920 ºC at heating rates of 3.5 °C/minute and 60 °C/minute. Samples were held at the elevated temperature for between 18 minutes and 4 hours before cooling at either 3.5 °C/minute or 20 °C/minute to 50 °C[6]. The hold temperatures were chosen to be within the austenitic region of 0.4 wt.% carbon steel, which is the phase required for normalising and annealing heat treatments. Figure 5.1 shows the heating and cooling profiles for a hold temperature of 850 °C. This study predominantly focuses on heating profiles in Figure 5.1d, g, and h, with supplementary compositional data obtained from the other heating profiles. *In situ* testing was conducted under vacuum between 1×10^{-4} mbar and 9×10^{-5} mbar. SE images of the surface microstructure were captured at regular intervals during heat treatment.

Heat treatments were also conducted on drawn samples within a furnace at pressures between 1×10^{-4} mbar and 1×10^{-5} mbar. The furnace vacuum operated via conduction heating of the sample where the entirety of the furnace volume was heated to the required temperature, as opposed to the SEM chamber where only the sample was heated. Polished cylinder samples of 8 mm diameter and 5 mm thickness were heated using the same profiles for those used *in situ*. The polished surface was heat treated, both face down on a ceramic plate in the furnace, referred to as covered, and face up, referred to as uncovered. The former was done to minimise environmental effects and the latter to mimic the *in situ* data.

[6] 50 °C was chosen as it was assumed that no further microstructural changes occur between this and room temperature. It was also a safe temperature at which to vent the SEM chamber.

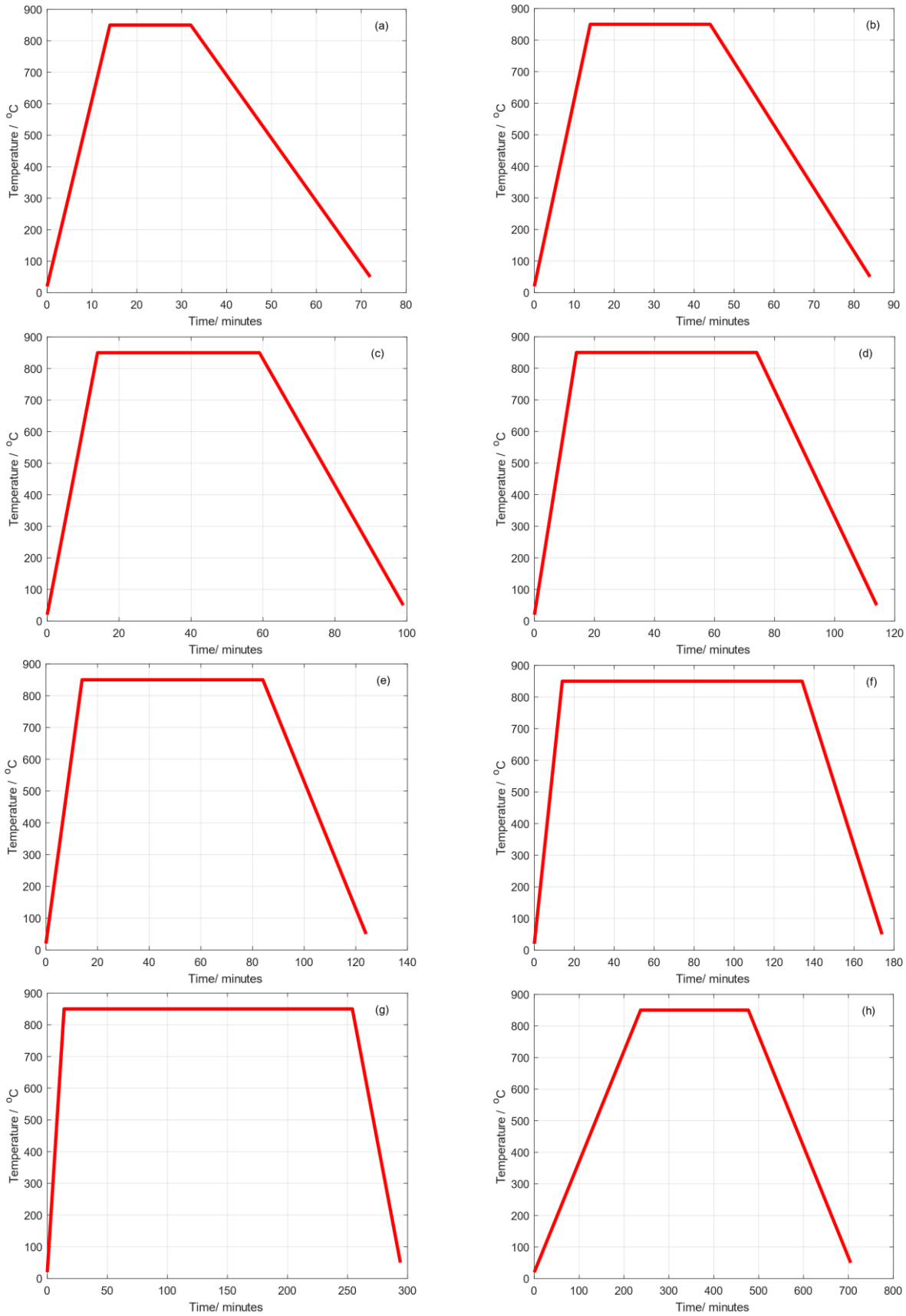

Figure 5.1: Heating profiles for all heat treatments of carbon steel.

5.2.3 Optical Characterisation

Optical images of the specimen surfaces at room temperature were taken using an Alicona profilometer at 5×, 10×, 20×, 50× and 100× magnification. This was done pre- and post-heating to provide *ex situ* data on the microstructural changes. Pre-heating, samples were polished (as described above) and chemically etched using 2% nital before optical imaging. After the heat treatment, optical images were taken of the thermal etch before re-polishing the surface by less than 1 µm and chemically etching, after which further images were taken. Following this, samples were ground to half their thickness before repeating the polishing and etching process in order to observe the microstructure in the bulk of the specimen.

5.2.4 Compositional Characterisation

To evaluate the elemental changes to the sample surface, energy dispersive X-ray (EDX) scans were taken before and after the heat treatment. EDX maps were captured for an area of 100 µm × 100 µm of 200 frames, with a 5 minute scan time. In particular, the level of oxidation was quantified using the EDX software.

To compare specimen oxidation to current thermal oxidation models, the EDX measurements of weight percent oxygen (O_{wt}) were converted to relative oxidation mass (w),

$$w = \int_0^z A_s \rho O_{wt}\, dz \qquad \textit{Equation 5.1}$$

where z is the penetration depth of the EDX measurements (based on Chapter 4 CASINO simulations for carbon steel), A_s is the scan area, and ρ is the material density (carbon steel). The oxidation mass results were compared to the standard Pilling-Bedworth model, used to quantify the level of oxidation,

$$w^2 = k_x t + {w_0}^2 \qquad \textit{Equation 5.2}$$

where w is the weight of oxygen gained at a specific temperature, w_o is the initial weight of oxygen, t is time and k_x is a constant defined by an Arrhenius type equation, $k_x = k_o e^{\frac{-Q}{RT}}$,

where Q is the activation energy, R is the gas constant, T is the temperature at which the oxidation occurs, and k_o is a material-dependent constant [92].

5.2.5 Measuring Grain Growth

Post-experimental analysis consisted of image processing of *ex situ* optical images at 20× magnification covering a large proportion of the specimen surface. Grain sizes were analysed using the intercept method, following ASTM Standard E112 [197], due to the large number of grains, and the planimetric method to enable comparison to *in situ* data. The results for the average grain size were fitted to the widely accepted general power law equation, originally derived by Burke and Turnbull [65],

$$d^n - {d_o}^n = Kt \qquad \textit{Equation 5.3}$$

where d is the average grain diameter at a given time t, d_o is the grain diameter at $t = 0$, n is a material parameter and K is defined by the Arrhenius type equation, $K = Be^{\frac{-Q}{RT}}$. In this equation, Q is the activation energy, R is the gas constant, T is the temperature at which the grain growth occurs at and B is a material constant [65].

The *in situ* microstructural data were also used to quantify the change in grain size during heat treatment, again using the power law equation (Equation 5.3). However, owing to the smaller number of grains, a combination of the mean grain area, and the planimetric method were used. The planimetric method involved counting the total number of grains in a given area, following ASTM Standard E112 [197] for each SEM image, as detailed in Chapter 3. The mean grain diameter at each time interval was then calculated from the mean area using the equivalent circular area diameter equation [200],

$$d = \sqrt{\frac{4a}{\pi}} \qquad \textit{Equation 5.4}$$

where d is the equivalent circular area diameter and a is the mean grain area.

5.3 Results

5.3.1 *Ex situ* Grain Size Characterisation

Before examination and analysis of the *in situ* data were conducted, optical microscopy profiles were captured and analysed pre- and post-heating, both at the surface and in the bulk of the specimen, for the heating profiles in Figure 5.1d and Figure 5.1g. The comparison of surface and bulk microstructures post-heating identified some differences in grain growth.

A summary of the optical *ex situ* grain size data for heat treatments conducted on the drawn sample, which had a starting average grain size of ~20 μm, are shown in Figure 5.2. The corresponding optical images for these data can be found in the appendix of Chapter 5. Samples shown were heated to the required temperatures (800, 850 and 920 °C) at a rate of 1 °C/s and held for 1 and 4 hours before cooling over a 1-hour period within the SEM chamber. After both 1 hour and 4 hours, the grain growth in the bulk increased with time and temperature in accordance with the power law (Equation 5.3) [16][17]; a comparison to the law is shown in Figure 5.3.

Examination of the data in Figure 5.2 at 800 °C indicates that the surface grain growth after 1 hour was comparable to that of the bulk. However, after 4 hours, the surface experienced little additional grain growth, despite significant grain growth in the bulk of the specimen. Similar discrepancies between the bulk and surface grain growth were identified at both 850 °C and 920 °C after the 4-hour heat treatments. Moreover, this discrepancy between the bulk and surface appears to increase with temperature; at both 850 °C and 920 °C the surface exhibits negligible grain growth, while the bulk grain growth is significant.

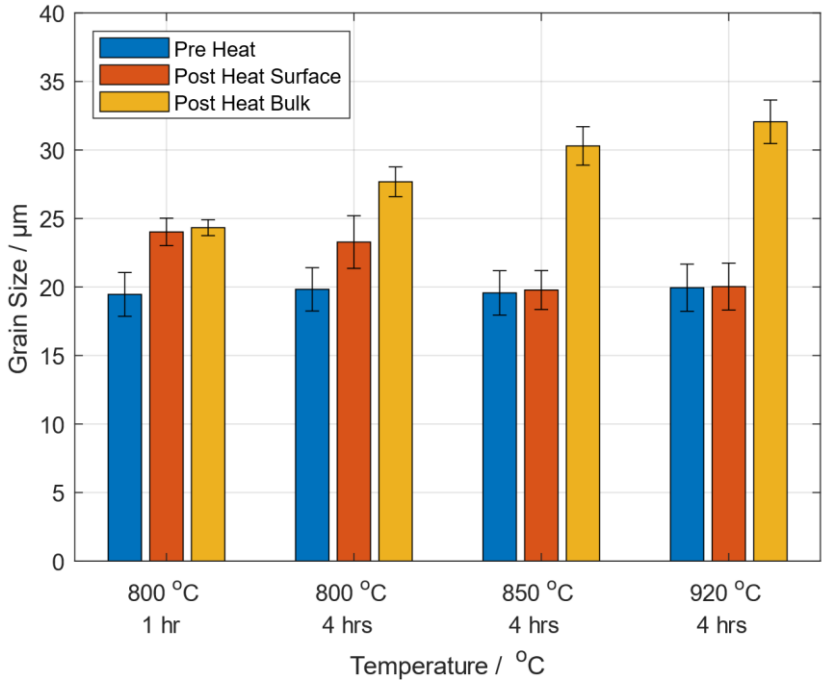

Figure 5.2: Bar Graph depicting a summary of all ex situ *grain growth data for samples of drawn material comparing pre-heat treatment with the surface and bulk post-heat treatment for polished and unpolished samples. The standard error for each of the grain growth measurements is shown and is calculated based on the average grain size.*

Two heat treatments of 45 and 60 minutes' hold time at 800 °C (heating profiles in Figure 5.1c and Figure 5.1d respectively) were also conducted on a fine grain sample with a significantly smaller starting grain size of ~10.5 µm. The *ex situ* grain growth measurements after the 45 minute heat treatment indicate a substantial increase in surface grain size from 10.5 µm to 13 µm (~25% increase in grain size), shown in Figure 5.4. A similar increase was also found in the bulk of the specimen post-grain growth; unlike the drawn sample, the surface shows the same grain size increase as the bulk.

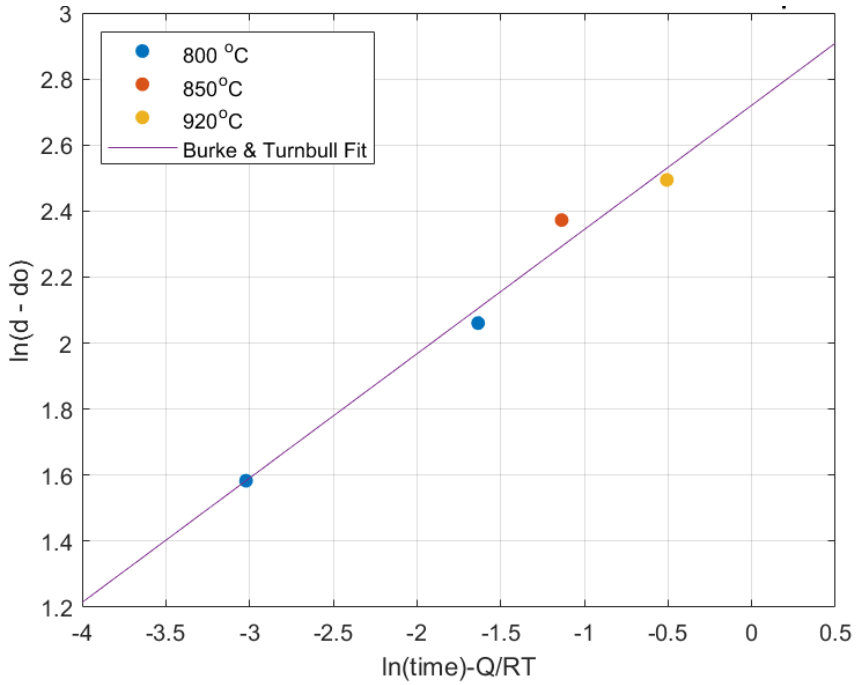

Figure 5.3:Bulk grain growth data plotted with respect to the Burke & Turnbull grain growth power law indicating n~2. Q was fitted using an iterative function, see the MATLAB script in the appendix of Chapter 5.

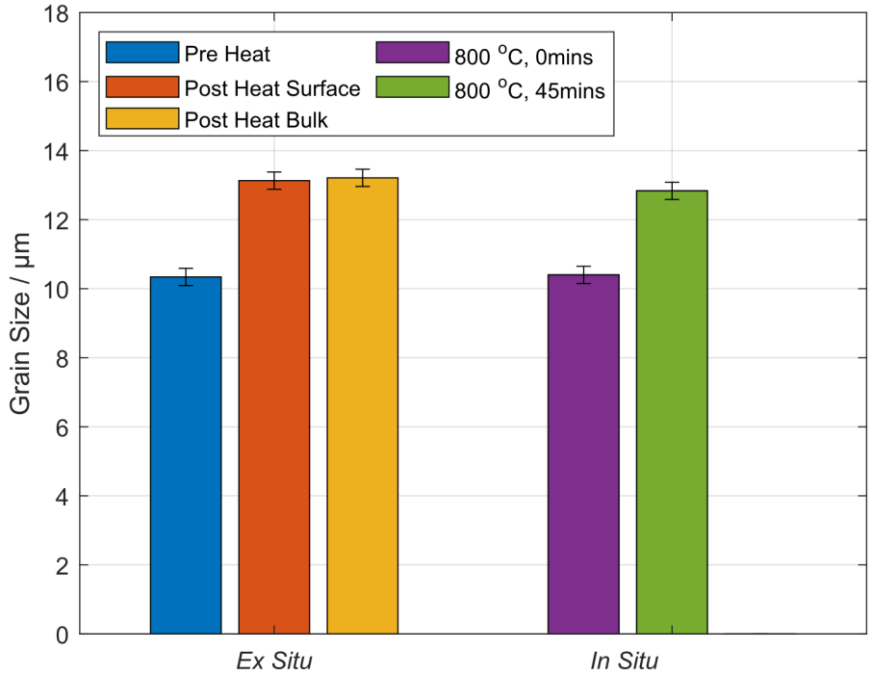

Figure 5.4: Bar graph depicting the grain size change of the fine grain steel measured both ex situ *pre- and post-heating, and* in situ *after heating at 800 °C for 0 minutes and 45 minutes.*

The difference between the bulk and the surface *ex situ* grain sizes of the drawn specimens, after the 4-hour heat treatment at 800, 850, and 920 °C, was attributed to either a temperature gradient through the sample or to surface effects. The temperature gradient through the sample was minimal as shown in the extensive studies on temperature gradients of this heat stage and sample type (discussed in Chapter 4). Thus, the possibility of surface effects, including environment and thermal etching, were investigated. To identify the effect that thermal etching may have on grain growth, both a polished and an unpolished sample were heat treated at 850 °C for 4 hours *in situ*. The results, Figure 5.5, indicate that the grain growth on the surface of the unpolished specimen was comparable both to its own bulk grain growth and to the bulk of the corresponding polished sample. These results suggest that a polished surface, which facilitates thermal etching, unfortunately also leads to retardation of the surface grain growth. However, further *ex situ* compositional characterisation, combined with examination of the *in situ* results, is necessary to understand the mechanisms that may result in the difference in surface and bulk grain growth.

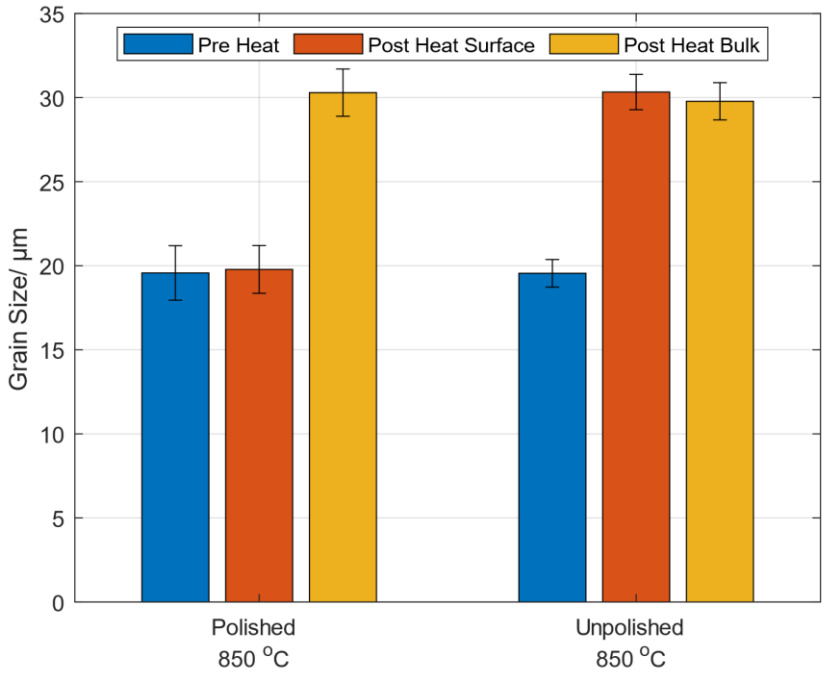

Figure 5.5: Polished versus unpolished ex situ *grain sizes after 850 °C 4-hour heat treatment.*

5.3.2 *Ex situ* Surface Composition Characterisation

Before further examination and analysis of the *in situ* data were conducted, EDX compositional data were taken pre- and post-heating. The EDX data highlighted changes in composition and allowed for identification of the morphological features, observed using *in situ* SE images, which corresponded to those changes in composition. Figure 5.6a shows the typical spectrum (in black) obtained for a carbon steel specimen before heat treatment, where it is clearly observed that there is no oxygen detected on the surface and the expected carbon steel composition (detailed in Chapter 2) is present. In contrast, EDX data post-heating, for heat treatments of 1 hour and 4 hours at 800, 850, and 920 °C, indicated, despite the vacuum, that oxidation had occurred to some degree. An example of this is shown in Figure 5.6b, corresponding to a sample of carbon steel heat treated for 4 hours at 850 °C, indicating oxygen is clearly present. The post-heating oxidation level for all samples is shown in Figure 5.7. The data showed a wide range of oxidation levels, with oxidation being as low as 3% after a 1-hour heat treatment at 800 °C, compared to 25 % after a 4-hour heat treatment at 920 °C. The EDX spectra post-heating are listed in the appendix of Chapter 5, along with the quantified elemental compositions of the carbon steel post-heat treatments.

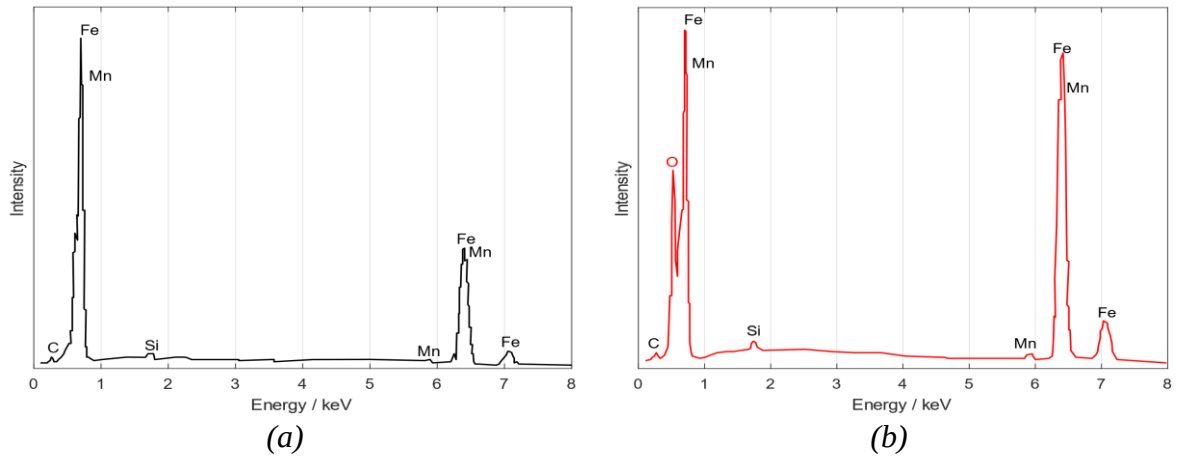

Figure 5.6: EDX spectra showing (a) no detectable oxygen before heating of the polished carbon steel sample, and (b) detectable oxygen after 4 hours of heating at 850 °C.

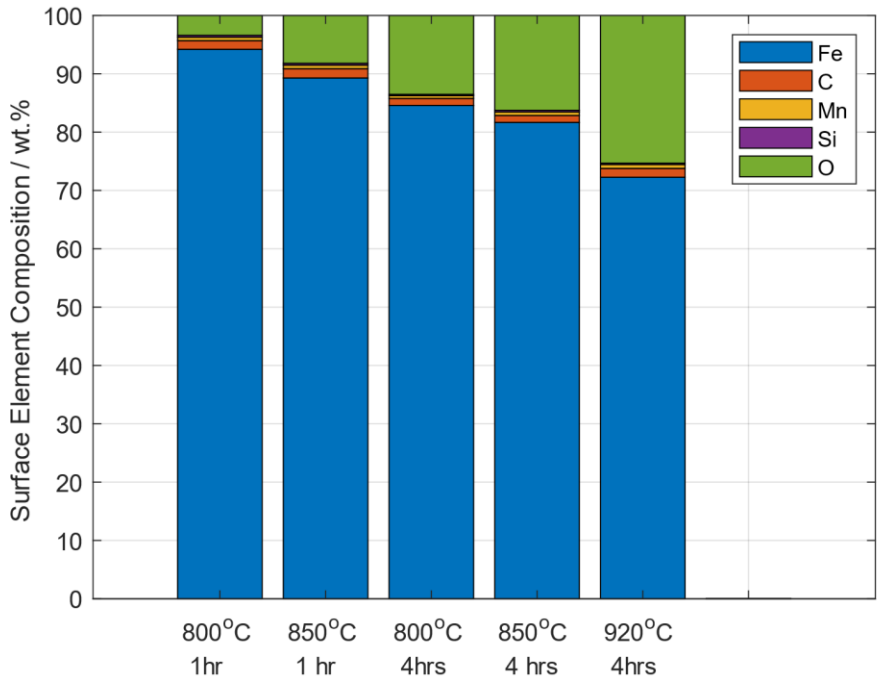

Figure 5.7: Summary of the post-heating oxidation levels.

To understand the dependence of the levels of oxidation formation on the time and temperature of the heat treatment, the EDX compositional results were converted to surface masses of oxygen and compared to the Pilling-Bedworth theory (details of which can be found in the appendix of Chapter 5). The results, presented in Figure 5.8, indicate that the oxidation quantified from the EDX data provides a good fit to this model and shows a parabolic relationship between oxidation and time. In this case, oxidation levels were taken for specimens held for 1 and 4 hours at 800 and 850 °C, and 4 hours at 920 °C, with heating profiles as shown in Figure 5.1. Supplementary compositional data were also collected from specimens held at 25, 42, and 100 minutes at 885 °C to confirm the model fit, as these temperatures were expected to be equivalent to oxidation levels for 1 hour at 800 °C, 1 hour at 850 °C, and 4 hours at 800 °C respectively. The consistency of oxidation between these temperatures and timescales further confirms that the surface oxidation of the specimen that occurred during the *in situ* heat treatment of carbon steel, followed the Pilling-Bedworth model.

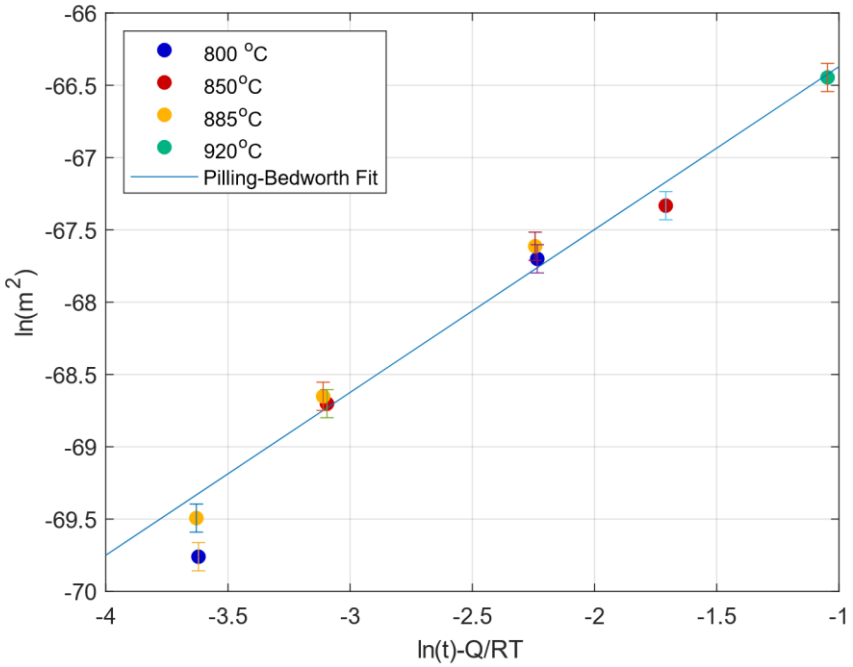

Figure 5.8: Pilling-Bedworth Equation compared to EDX data taken post-heating of carbon steel samples in situ, where m is the oxidation mass (kg), t is time (s), Q is the activation energy, R is the gas constant, and T is the temperature at which the heat treatment was performed.

To identify the areas of the surface that were oxidising, and hence correlate the morphologies observed in the SE images with composition, EDX maps pre- and post-heating were examined. An example of the significant morphologies observed before and after heating are shown in Figure 5.9 and Figure 5.10 respectively; these figures show the EDX maps pre- and post-a 4 hour heat treatment at 850 °C. Figure 5.9 identifies a large nodule shown in the SE image as a concentrated area of carbon precipitate (circled in black) and the smaller areas as other alloying elements (circled in red). The maps obtained pre-heating indicated that no oxygen was present. Examination of the composition after heating at 850 °C for 4 hours (Figure 5.10a) shows two distinct types of morphology. One morphology observed in the SEM is characterised by raised white areas, and the other depicts darker, smoother areas. Figure 5.10b identifies the white raised area as predominantly composed of oxygen (yellow) whereas the smooth non-white areas are iron (green). With this compositional

information, the high-temperature SE images can be analysed with the ease of distinguishing oxygen formation from the original steel surface as EDX data collection is not possible during the high-temperature carbon steel heat treatment.

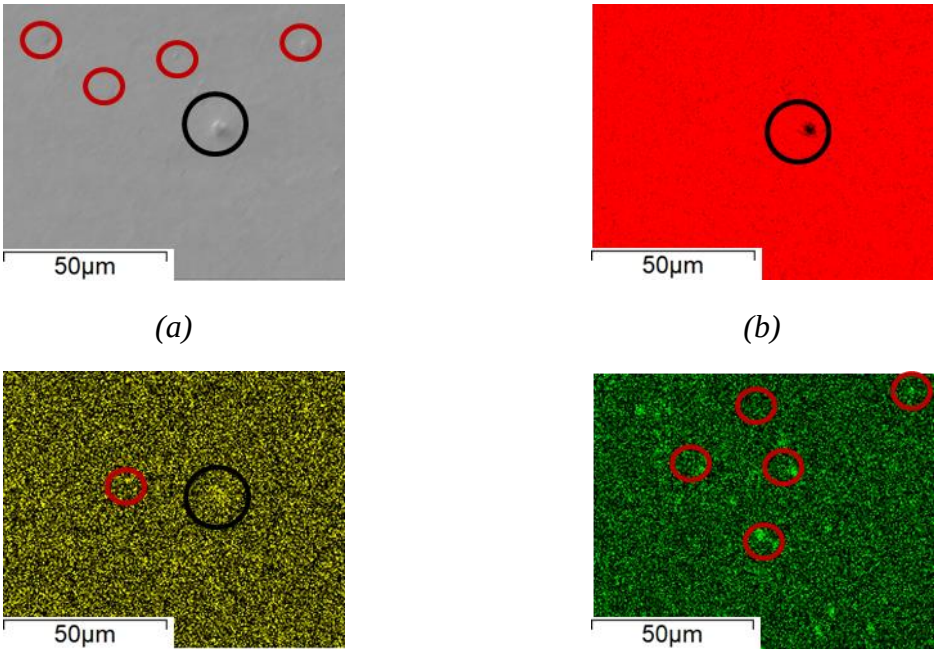

(a) *(b)*

(c) *(d)*

Figure 5.9: EDX composition maps of steel pre-heat treatment. (a) SE imaged area used to capture EDX maps corresponding to (b) iron, (c) carbon, and (d) manganese. They demonstrate, as in the EDX spectrum, a complete absence of oxygen.

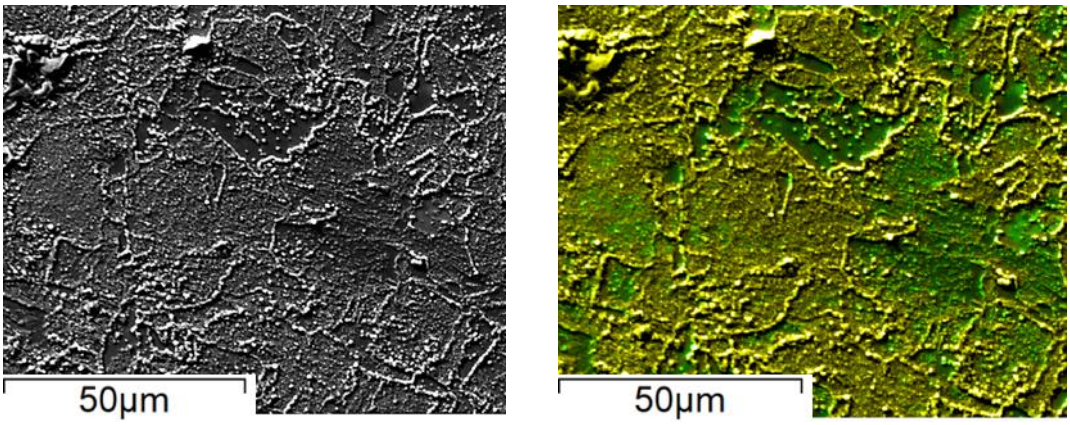

(a) *(b)*

Figure 5.10: EDX composition maps of steel post-heat treatment showing the dominant surface compositions of oxygen and iron. (a) SE imaged area used to capture the EDX data showing two distinctive morphologies. (b) Combined composition EDX map showing iron (green) and oxygen (yellow) corresponding to dark and lighter areas of the SE image respectively.

Compositional characterisation was also conducted on specimens' that had been heat treated in the furnace, for both samples, where the polished surface was covered and uncovered, and compared to *in situ* SEM data gathered under the same heating profile. Figure 5.11 shows the EDX compositional results obtained, which indicate similar levels of oxidation for the uncovered furnace and *in situ* heat treatments (14 wt.% O), but negligible oxidation (<1 wt.% O) for the covered furnace heat treatment.

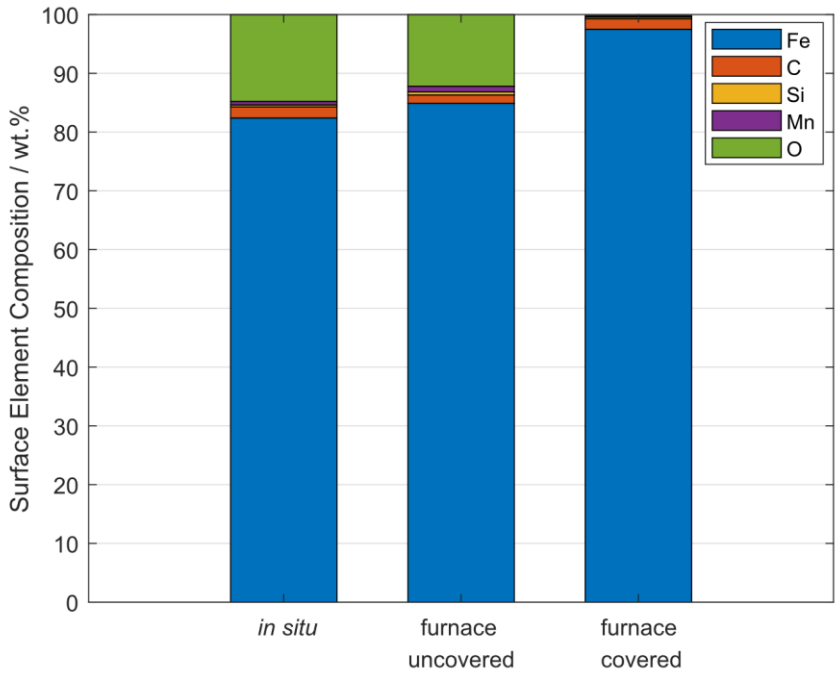

Figure 5.11: Comparison of the EDX surface composition for slow heat treatment in situ and both uncovered and covered heat treatments within the furnace.

To further understand the reason for the difference between oxidation levels in the covered and uncovered furnace samples when compared to the *in situ* samples with the same heating profile, optical images were obtained to identify any observable surface difference between samples. Figure 5.12 shows optical micrographs of the three specimen types at 20× magnification. Figure 5.12a and Figure 5.12b show no ghost etching (the principle of which is discussed in Chapter 2) on the *in situ* SEM and *ex situ* uncovered sample, both of which

also show discolouration of the surface. The presence of ghost etching is as a result of surface grain growth occurring where the grain boundary has been able to move and re-etch, meaning that the original grain boundary etch becomes a ghost etch.

Figure 5.12a shows significant changes in surface morphology and the identification of grains is very difficult. Figure 5.12b presents some grain structure, but it is still difficult to clearly identify the grain structure *ex situ*. The difference in surface morphology of the samples, despite the same heating process and similar environmental conditions, may be attributed to the difference in heating mechanisms where Figure 5.12a is heated via a button heater and Figure 5.12b by a furnace. In the latter case, the surrounding atmosphere within the furnace (although minimal owing to the 10^{-4} mbar pressure) is also heated, whereas the atmosphere within the SEM is relatively cool in comparison to the specimen temperature. Hence, as both environments are at the same pressure, but the furnace atmosphere is at a significantly higher temperature, the furnace sample is less likely to oxidise as there will be less oxygen present in the same volume. Therefore, this has had some effect on the oxidation levels, as shown in Figure 5.11. Additionally, inspection of Figure 5.12c, the covered furnace heat treated specimen, shows ghost etching lines, which suggest grain boundary movement. Furthermore, the furnace covered EDX data showed no observable oxidation (Figure 5.11).

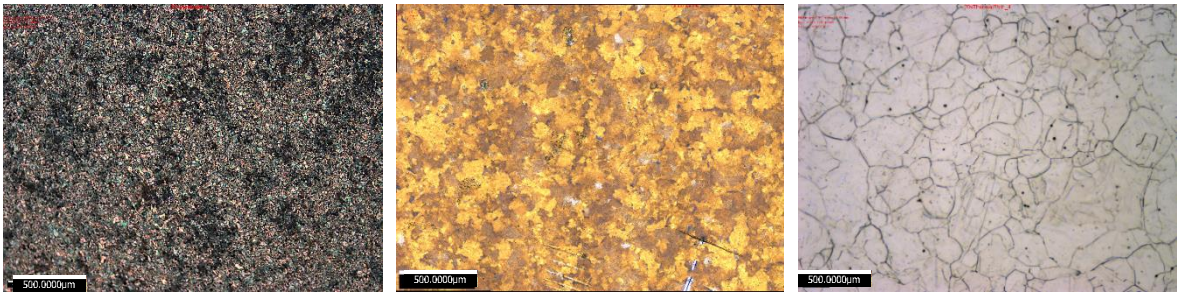

(a) *(b)* *(c)*

Figure 5.12: SEM images after heat treatment showing (a) in situ SEM (b) furnace uncovered surface (c) furnace covered surface.

The *ex situ* composition and optical data provide some indication of the microstructural surface difference as a result of oxidation, which may indicate why there is such a substantial difference between the bulk and surface grain growth. However, it is necessary to understand the *in situ* microstructural evolution during this heat treatment process to appreciate the specific surface effects occurring during the heat treatment that may cause grain growth retardation.

5.3.3 *In situ* Surface Observations

To observe the formation of the oxide layers identified from the compositional data, and the grain growth apparent from the *ex situ* optical grain size analysis, SE images captured *in situ* were examined. Most heat treatments used a 20 µm starting grain size (drawn sample); samples with this starting size were tested at all temperatures, which had the benefit of requiring a lower magnification to image a large dataset. Owing to the observed *ex situ* surface grain growth at 800 °C, a second grain size of 10.5 µm (fine sample) was also heat treated at this temperature to observe any effect that grain size might have on grain growth and to observe more clearly the change in grain size *in situ*. As there was no surface grain growth observed *in situ* or *ex situ* at 850 °C and 920 °C, only the drawn sample was examined at these temperatures.

Both the SE *in situ* and *ex situ* data indicate that the microstructural evolution is time and temperature dependent (as expected). The *in situ* data indicate that the surface observations also vary with the temperature and duration of the heat treatment; these are discussed in detail below.

In Situ Evolution at Temperature: 800 °C

Heat treatments at 800 °C for both the drawn (20 µm) and fine (10.5 µm) samples showed similar initial surface microstructural evolution within the first hour. Figure 5.13 presents a selection of *in situ* images obtained during a 4-hour heat treatment of the drawn steel at 800 °C. Once the required temperature is reached, Figure 5.13a shows the presence of the outline of grain boundaries (red arrow). The grain boundaries are visible due to thermal etching, as discussed in Chapter 4.

The difference in contrast and brightness of some of the grains is also captured in Figure 5.13a. The different grayscale levels of an SE image can indicate that more than one phase is present [120]. The image colouring increases in uniformity through Figure 5.13b and by Figure 5.13c the image is a uniform grayscale tone; this indicates that the phase change is complete and the imaged area is fully austenitic. EBSD studies on carbon steel during heat treatment have shown that the phase change from ferrite / austenite to pure austenite doesn't always happen immediately despite the surface reaching the fully austenitic temperature [227][228]. This is discussed in Chapters 4 and 6. Hence, the observation of this two-tone SE image at 800 °C was not unexpected.

Focusing on the surface evolution at 800 °C, Figure 5.13b shows some movement in the thermally etched grain boundaries after 20 minutes' heating, in the form of ghost etchings. The ghost etchings, highlighted in the zoomed in image by the red arrow, show that grain growth is occurring, as the grain boundary has been able to move and re-etch. However, after 45 minutes of heating at 800 °C, no further movement of the thermally etched grain boundaries is observed. Instead, Figure 5.13c depicts a formation of white nodules within the grain boundary grooves, previously identified as oxidation using *ex situ* EDX data. After 90 minutes of heating the presence of oxidation formation has increased and the white lines of oxidised grain boundaries are very prominent (Figure 5.13d). Finally, after 4 hours of

heating, oxidation has become visible on parts of the steel surface, circled in red, as well as within the thermally etched boundaries (Figure 5.13e).

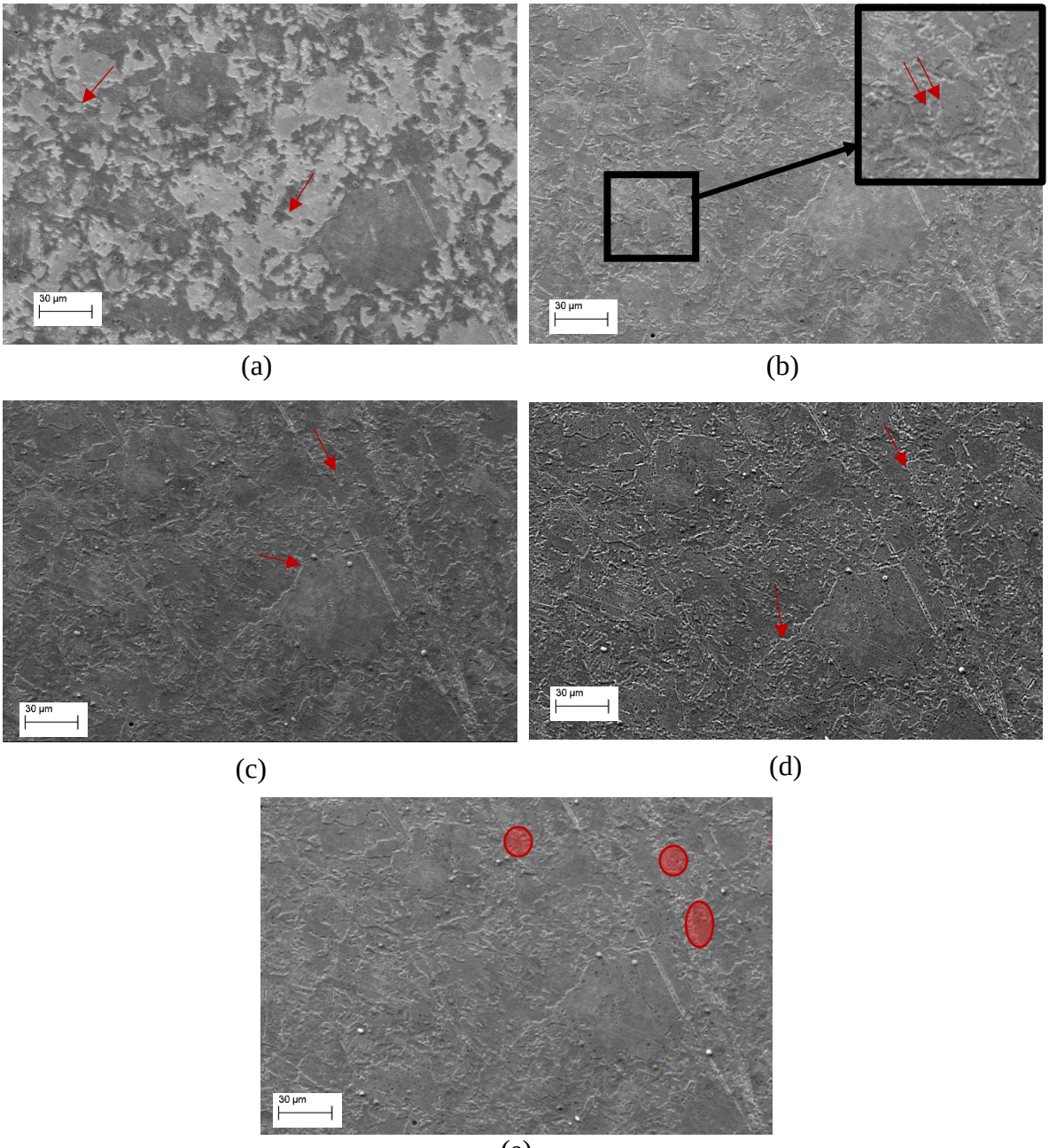

Figure 5.13: In situ SE image showing some ghost etching at 800 °C at time increments of (a) 5 minutes, (b) 20 minutes, (c) 45 minutes, (d) 2 hours, and (e) 4 hours.

Based on the above SE data, the timeframe of interest for the grain growth of carbon steel at 800 °C occurs within the first hour of heat treatment, before the thermally etched grain boundaries appear to stop moving and oxides form. As such, coupled with the *ex situ* grain growth data, the fine grain samples with a smaller starting grain structure (10.5 µm) were examined at this temperature. The SE images (Figure 5.14) of the smaller grain steel obtained at 800 °C, over a time period of 45 minutes, enabled the evaluation of grain size evolution in the austenitic region; this is a previously undocumented measurement. Here, the grains can be clearly identified in the SE images of the thermally etched specimen and movement can be seen occurring, thus these were used for grain growth quantification. The results also show some residual silica from sample preparation (white spots) and carbon deposits, which are the first to oxidise and become increasingly apparent with time. Unfortunately, Figure 5.14c shows some noise in the form of horizontal lines across the image. This is attributed to electrical interference from the heating stage, but only occurs when the stage voltage changes in order to hold the set temperature. The interference is minimal and does not affect the ability to collect quantifiable data; however, it is unavoidable if it is desired to capture SE data at regular time intervals. As with the first hour of heat treatment at 800 °C of the larger grain, there is no visible movement of the grain boundary grooves after 45 minutes.

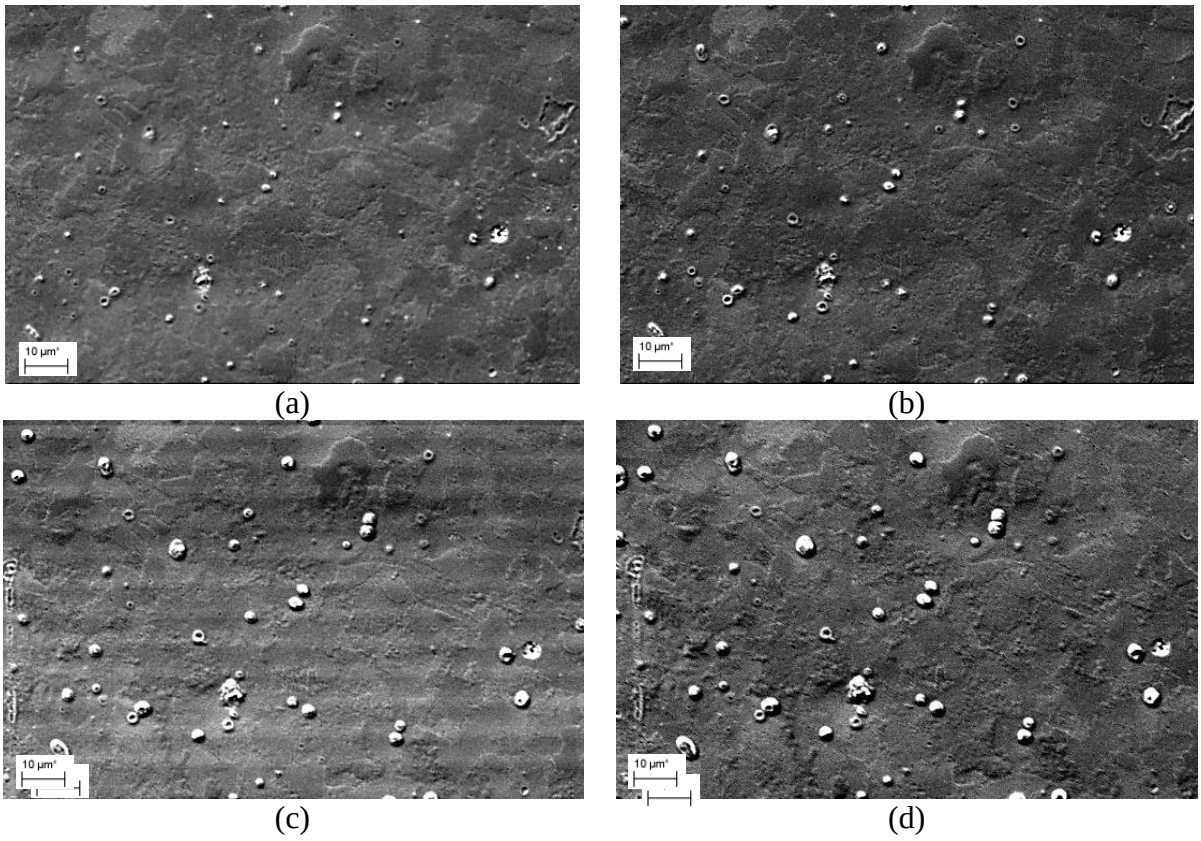

Figure 5.14: In situ SE images of thermally etched carbon steel at 800 °C showing grain growth at (a) time = 0 minutes, (b) 10 minutes, (c) 30 minutes, (d) 45 minutes.

In Situ *Evolution at Temperature: 850 °C*

Heat treatments at 850 °C were conducted on drawn specimens of starting grain size 20 µm. In contrast to the SE images at 800 °C, the *in situ* data for the drawn steel captured at 850 °C shows a constantly changing surface evolution. Figure 5.15 displays no movement in the thermally etched grains at timescales up to 4 hours heating at 850 °C. Figure 5.15a shows the SE image of the carbon steel surface once the required heat treatment temperature of 850 °C was reached. Here, the initial formation of the outline of grain boundaries is observed; arrows show clear points where the grain boundary grooves begin to emerge. This is not dissimilar to what happened at 800 °C. However, at this initial heating stage the SE image already indicates the start of possible oxidation in the 2 to 3 highlighted white dots, which were not present at 800 °C for at least the first 30 minutes. The initial areas of oxidation at this temperature, as at 800 °C, occur where the topography is raised, identified as concentrated

areas of carbon or other alloying elements in the EDX maps in Figure 5.9. After 10 minutes of heating there appears to be minimal further oxidation (Figure 5.15b). However, as in the 800 °C there is a significant change in the ratio between the darker and lighter areas of the image, indicating a phase change. After 20 minutes of heating at 850 °C (Figure 5.15c) there are almost no dark areas remaining, signifying that the phase change is complete. The first signs of oxidation of the steel surface, rather than just specific points, can also be seen by the presence of the lighter grain boundaries where thermal etching has occurred; Figure 5.15d shows this more clearly in the higher magnification SE image.

Whereas the oxidation of grain boundaries takes a significant amount of time at 800 °C and minimal further surface oxidation is observed (even over a 4 hour heating period), this is not the case at 850 °C. Once the oxidation of the new grain boundary surface is complete, oxidation begins to occur on the original surface. Figure 5.15e, at nearly 1 hour of heating, shows this: the oxidation can be seen more clearly in the zoomed in area, with specific areas of clustered white nodules circled in red. The formation of the small white nodules represents the initial growth of the oxide scale, which appears to encroach on the grain from the edges of the grain boundaries towards the centre. This pattern continues to be the case after 95 minutes (Figure 5.15f). Figure 5.15g displays the surface after heating for over 2 hours at 850 °C, which shows some grains to be completely oxidised (highlighted in yellow). A similar rate of increasing oxidation, by observation, occurs through the third (Figure 5.15h) and fourth (Figure 5.15i) hours of heating. After 4 hours, most of the surface is covered in oxide scales, appearing to run along the grain boundaries, with some areas of oxide agglomeration. This surface appearance remains the same, post-cooling (Figure 5.15j). Although, the scales are slightly clearer owing to the lack of light pollution, which can affect image quality at high-temperature [227]. The surface shown in Figure 5.15j is the morphology commonly imaged post-heating *ex situ* [229].

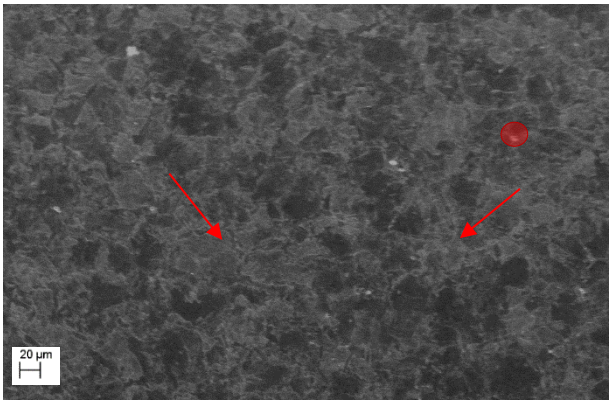

(a)

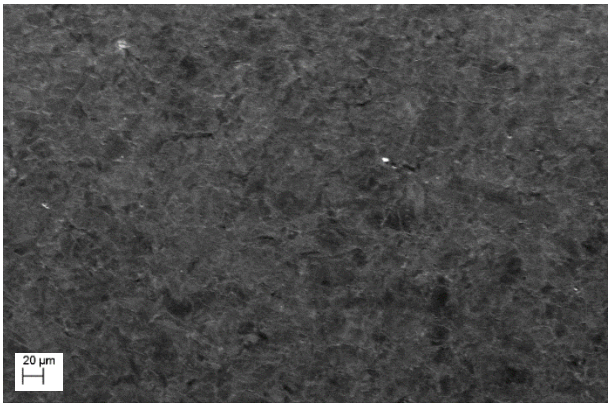

(b)

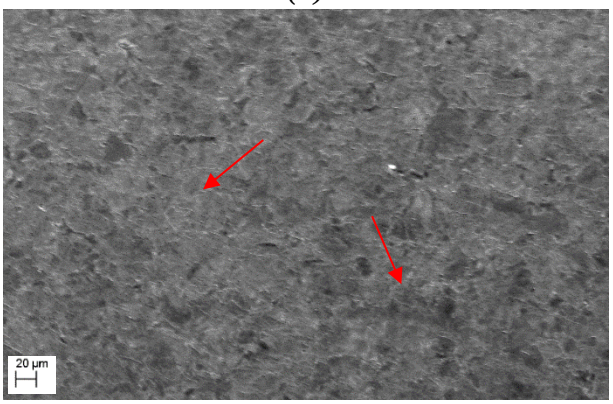

(c)

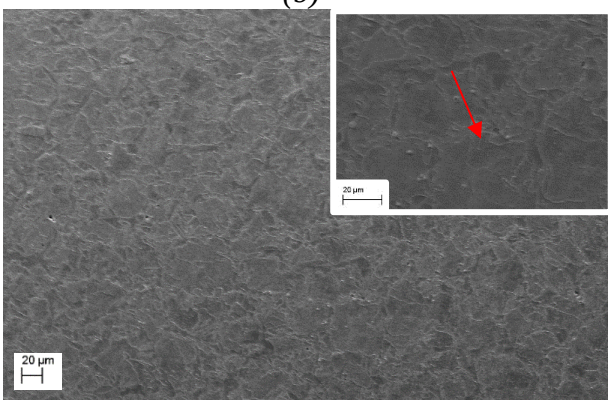

(d)

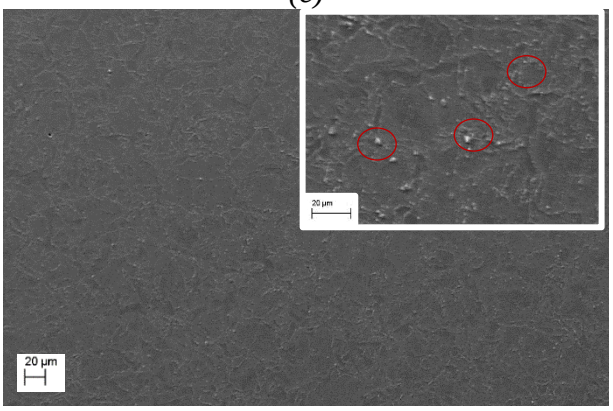

(e)

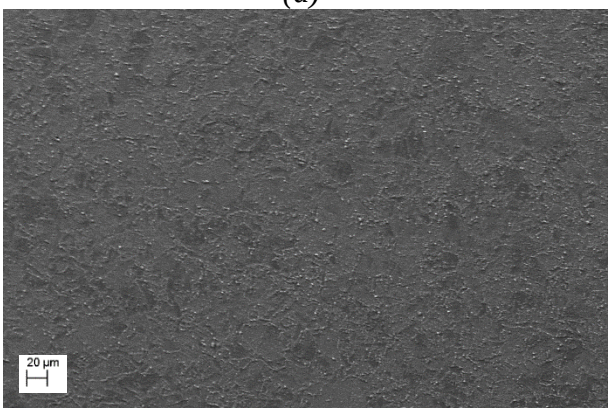

(f)

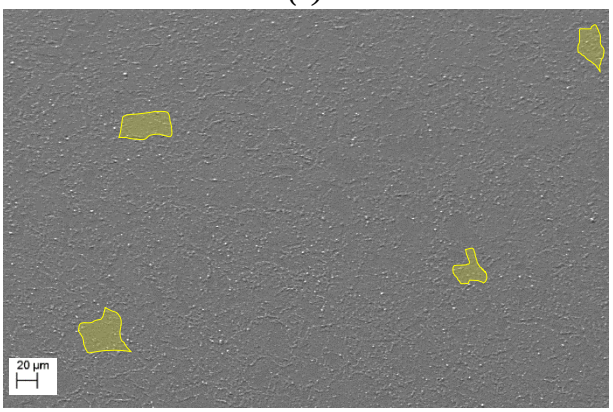

(g)

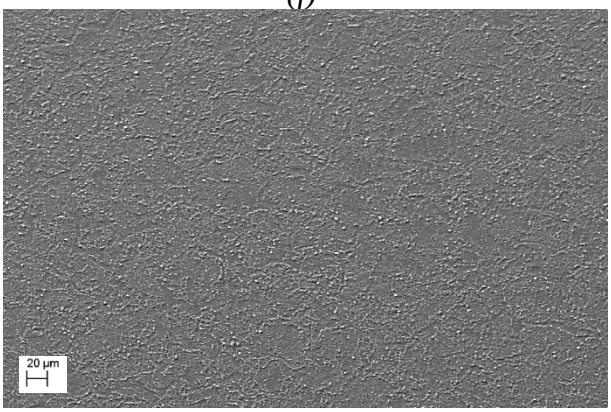

(h)

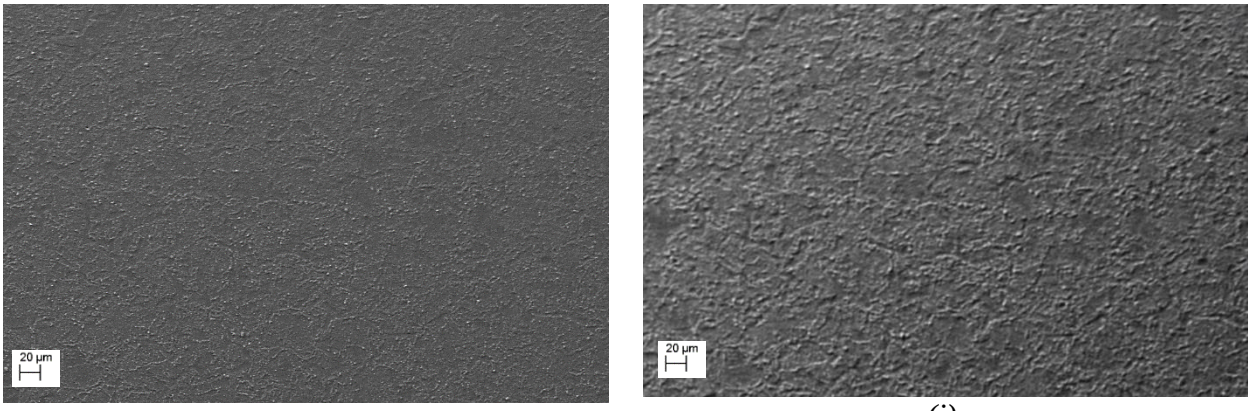

(i) *(j)*

Figure 5.15: In situ *SE images showing the oxidation progression of the 4-hour heat treatment at 850 °C at (a) 0 minutes, (b) 10 minutes, (c) 20 minutes, (d) 25 minutes, (e) 55 minutes, (f) 95 minutes, (g) 130 minutes, (h) 195 minutes, (i) 4 hours. (j) Post-cooling room temperature image after heating for 4 hours.*

In Situ Evolution at Temperature: 920 °C

Heat treatments conducted at 920 °C provide further evidence of surface oxidation. The SE data at 920 °C again showed no movement of the grain boundaries, as reflected in the lack of surface grain growth measured *ex situ* after both 1- and 4-hour heat treatments at this temperature. The use of a higher temperature facilitated the exploration of the oxide formation observed at 850 °C and how this affects microstructural changes during the heat treatment. Figure 5.16 presents a selection of SE images taken at 920 °C at a magnification of 2 k×. Figure 5.16a shows once again the initial formation of the thermal etching after 5 minutes of heating at 920 °C, while still being subjected to some phase change, as described for temperatures of 800 and 850 °C. However, oxidation happens at an increased rate at 920 °C as compared to at 800 °C or 850 °C, and after 10 minutes of heating (Figure 5.16b) oxidation can be clearly seen in the thermal grooves. By 20 minutes, the white nodules have begun to form on the edges of the surrounding grains, as highlighted in Figure 5.16c, and these have grown substantially by 40 minutes (Figure 5.16d). At just under 1 hour the white nodules are at a similar level to that of 2 hours at 850 °C (Figure 5.16e), and continue to encroach on the grains; some grains are completely covered. After 80 minutes (Figure 5.16f) the surface

oxidation is at a similar level to that reached at the 4 hours at 850 °C, and has followed the same growth pattern. However, at 2 hours the nodules have agglomerated across the grain boundaries in several places (see arrows in Figure 5.16g); now, the entire surface is oxidised. Although the scale likely continues to grow in depth through the formation of new nodules, this is not easily captured using surface imaging. As such, Figure 5.16h (after 4 hours' heating) looks not dissimilar to Figure 5.16g (after 2 hours' heating).

Overall, these *in situ* images provide insight into the changing surface morphology with respect to both oxidation and grain growth at a range of times and temperatures. By comparing the surface evolution during heating, the impact of different temperatures on the final microstructural changes that occur becomes clear. By further analysing the *in situ* data, alongside the compositional and optical data, greater insight will be found on the surface effects during the *in situ* heat treatment of carbon steel within the austenitic region.

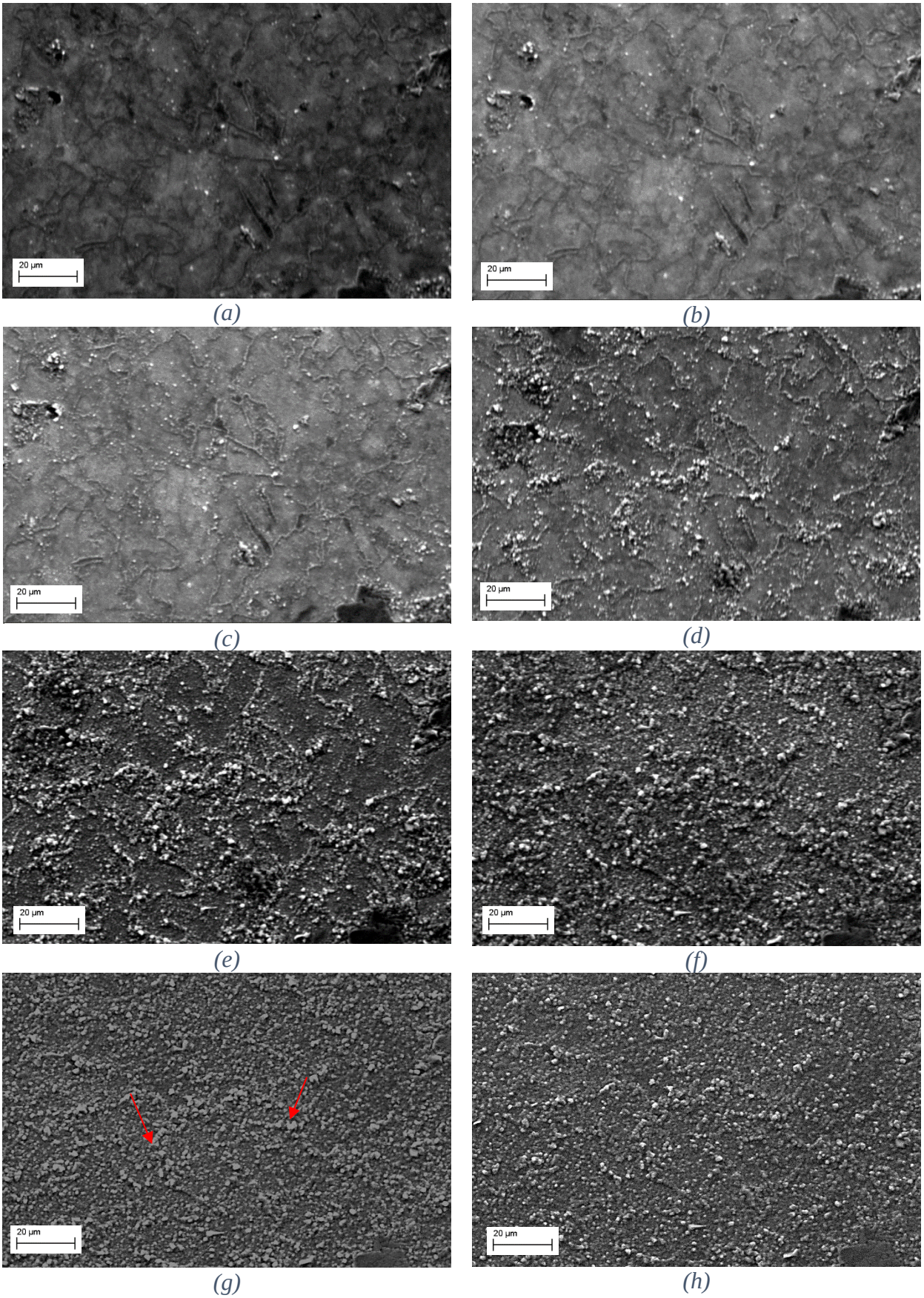

Figure 5.16: In situ *SE images showing the progression of the 4-hour heat treatment at 920 °C after heating for (a) 5 minutes, (b) 10 minutes, (c) 20 minutes, (d) 40 minutes, (e)55 minutes, (f) 80 minutes, (g) 2 hours and (h) 4 hours.*

5.3.4 Tracking Grain Growth *In Situ*

According to the *ex situ* grain growth data, the surface grain growth is only representative of the bulk of the specimen at heat treatments of 800 °C[7]. Although *ex situ* data indicate some surface grain growth in both the drawn and fine grain specimens, at 800 °C, the grain growth in the drawn specimen is not significant enough, owing to the larger grain starting structure, to quantify grain growth *in situ*. Thus, the only measurable grain growth from the *in situ* SE images occurred during the 1-hour heat treatment of the fine grain carbon steel, as discussed in Section 5.3.3. Hence, analysis of grain growth tracking within the austenitic region during heat treatment of carbon steel focused on the fine grain data.

The grain boundaries were outlined manually using ImageJ [211] and the average grain area calculated using the Planimetric method; outlined grain boundaries at 800 °C at times of 0 minutes and 45 minutes are shown in Figure 5.17. These were analysed using the equivalent circular diameter method to produce diameters (Figure 5.18). These data were, in turn, used to fit the general power law equation (Equation 5.3). The data give a linear relationship between time and grain size; the general power law constants are $n = 1$ and $K = 0.054\ \mu m^n$/minute. This phenomenon of linear grain growth is associated with the growth of large grains at the expense of smaller ones, commonly known as abnormal grain growth [29], and the predominant type of grain growth in this study. The significance of this is discussed further in Section 5.4.3.

[7]Note that surface grain growth may also represent the bulk of the specimen at temperatures below 800 °C. However, as this study specifically examined the heat treatments in the austenitic region of carbon steel (normalising), where the required minimum temperature is 800 °C for 0.4 wt. % carbon steel to become fully austenitic, no heat treatments below 800 °C were conducted.

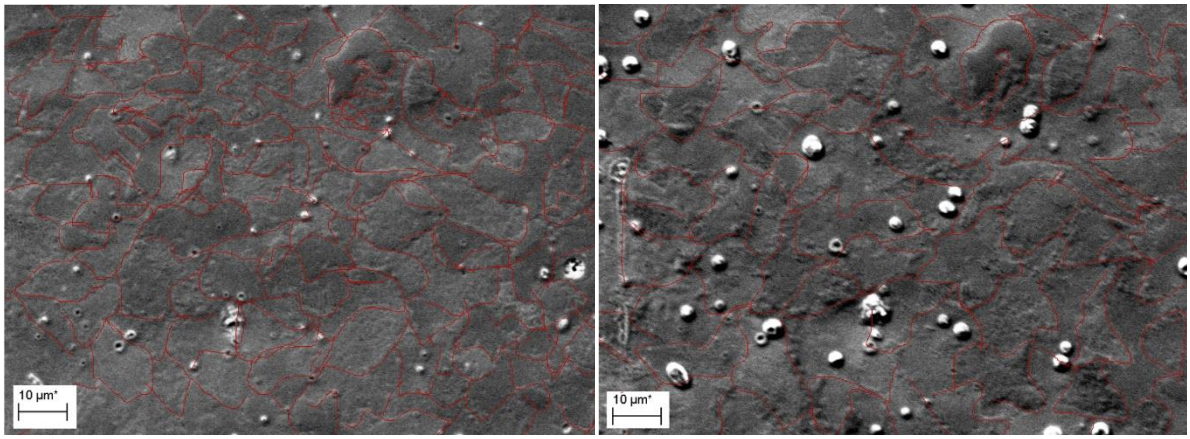

(a) *(b)*

Figure 5.17: In situ *SE images at 800 °C after (a) 0 minutes and (b) 45 minute. The red lines identify the grain boundary locations, identified by the thermal etch and outlined in ImageJ [15].*

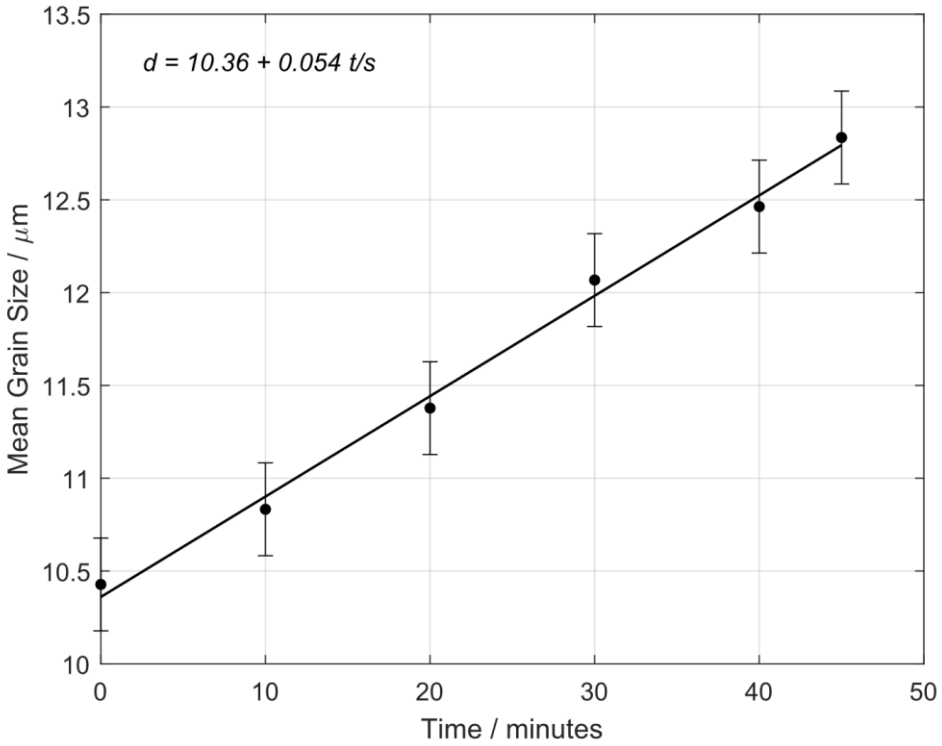

Figure 5.18: Mean grain size of carbon steel at 800 °C as a function of time; an error bar of +/-0.25 µm is shown for each data point as standard for the ASTM Standard E112 planimetric method [197]*. At least 90 grains were identified for each image.*

5.4 Discussion

The new *in situ* SEM surface data supported by *ex situ* microstructural and compositional measurements have facilitated further understanding of the microstructural evolution of carbon steel during heat treatment and added to the fundamental understanding of processes during this treatment such as oxidation and grain growth. Hence, the use of SE imaging at high-temperature coupled with thermal etching has enabled observation and analysis of a grain growth using a large dataset in the austenitic region. The SE data have also allowed an understanding of how surface effects, such as thermal oxidation and thermal etching may impact grain growth under specific heat treatment parameters.

5.4.1 Surface Oxidation Formation

The observation of scale morphology over time documented during this *in situ* study demonstrates the formation of oxide layers on the surface of carbon steel during heat treatment. For all temperatures, it is evident that oxidation begins at the grain boundaries, which are visible owing to thermal etching, rather than the rest of the surface. Thermal oxidation forms on newly exposed surfaces, which have a higher surface energy than the original sample surface [90], due to the recent bond disruption which occurs when forming the new surface. As a result of the higher surface energy, the diffusion-driven oxidation process is more likely to occur along the newly exposed grain boundaries rather than on the original surface. The presence of oxidation within the grain boundary groove has previously been documented in thin films [85]. Once the oxidation of the grain boundaries is complete, small white oxide nodules form, which agglomerate to form a complete oxide scale and produce a morphology commonly imaged post-heat *ex situ* [229].

The observation of scale morphology over time, documented during this *in situ* study, may also provide an insight into the type of surface oxide that forms during heat treatment

under a 'fine' vacuum environment. Although this SEM / EDX approach does not determine the exact composition of the surface oxide layer, there are several factors suggesting that the dominant type of oxide is wüstite. First, cross-sections of the oxide layer formed under these conditions present a wüstite oxidation layer with sharp boundaries between the wüstite scale columns [95][229]. Based on this new data set, the scale boundaries observed during cross-sectioning are likely to be a result of the thermal etching that occurs during heating, which subsequently leads to formation of individual oxide scales. Additionally, when imaging the cross section of the oxidised surface of steel, SE images have shown the appearance of wüstite to be significantly lighter when compared to that of magnetite and haemetite [92]. The SE images documented in this study (Figure 5.7) also show a large shade contrast between the steel and oxide layers. In further support of these morphological observations, studies documenting *in situ* neutron diffraction data taken during the heat treatment of steel under low pressure show that the dominant oxide layer is 95% wüstite compared to 4% and 1% of magnetite and haemetite respectively [102]. By considering the thermodynamics of oxide formation through examiation of the Ellingham diagram, a plot of the standard Gibbs free energy of reaction versus temperature relationship, used to compare the relative stabilities of each metal oxide based on the partial pressures of oxygen, also suggests that wüstite is likely to be the dominant phase present [230]. Moreover, the diffusion coefficient of iron in wüstite is much greater than in magnetite or haemetite making it more likely to form in a lower oxygen environments [92], such as in this study.

The *in situ* images also highlight a lack of blister formation, a common phenomenon during heat treatments of steel (as discussed in Section 5.1.2) at all temperatures and timescales. The lack of blister formation may be due to either a lack of the magnetite and haemetite oxide layers, or to a lack of gas within the chamber. It is thought that the presence of a gaseous environment is also important for blisters to be observed on the oxidised surface

post-heating. However, the requirement for sufficient gas to be present is considered to be necessary only to maintain a blister throughout the whole heat treatment cycle, not for formation. Without sufficient gas, it is expected that the blister will heal or collapse [92]. Despite the heat treatment occuring at a temperature and over a time period where blistering would be expected to occur, neither the formation nor the healing or collapse of blisters is observed during the *in situ* heating process, suggesting that a sufficient level of gas (i.e. a non-vacuum environment) is also required for blisters to form.

5.4.2 Discrepancies Between Bulk & Surface Grain Growth

In general, grain growth is known to be dependent on grain boundary movement, where a grain boundary is a defect in a crystal with an associated energy. Grain growth occurs to decrease the overall energy of the system by reducing the total grain boundary area. AFM studies indicate that the thermal etching does not modify or reduce the total grain boundary areas but simply creates a deeper etch on the surface where the grain boundary resides [231]. Furthermore, the current data, supported by the literature [224], indicate that it is possible for grain growth to occur under these heat treatment conditions via thermal etching owing to the presence of ghost etchings when thermal oxidation does not occur. However, compositional, *in situ* and optical data indicate that both thermal oxidation and thermal etching are present during some of the heat treatments in this study.

From the *in situ* observations at 800, 850 and 920 °C it is evident that oxidation initially occurs along the grain boundary grooves prior to oxidation of the sample surface. Considering oxidation with respect to grain growth, it is well documented that the presence of a foreign body that intersects with a moving grain boundary results in that grain boundary no longer existing, leading to pinning. For that grain boundary to continue to move, a new

grain boundary has to form around the precipitate; this is not energetically favourable for the system. This process is known as Zener pinning and is discussed in Chapter 2 of this thesis.

It is thought that the presence of oxidation within the thermal grooves, where the grain boundaries lie, has a similar impact to the presence of a precipitate in a non-thermally etched grain boundary. As the oxidation effectively fills the grain boundary groove, thereby removing the grain boundary, it is no longer energetically favourable for grain growth to occur on the surface. Figure 5.19 shows this effect diagrammatically: (a) shows the initial grain boundary movement, (b) shows oxidation formation beginning to occur and hence some pinning, and (c) shows the point at which no grain growth occurs as there is sufficient oxidation to pin the groove completely. Moreover, the data indicate that the greater the oxidation level, dictated by time and temperature through the Pilling-Bedworth equation, the slower the grain growth becomes until it is negligible. This correlates well with the principle that oxidation is the mechanism by which the grooved grain boundaries are pinned.

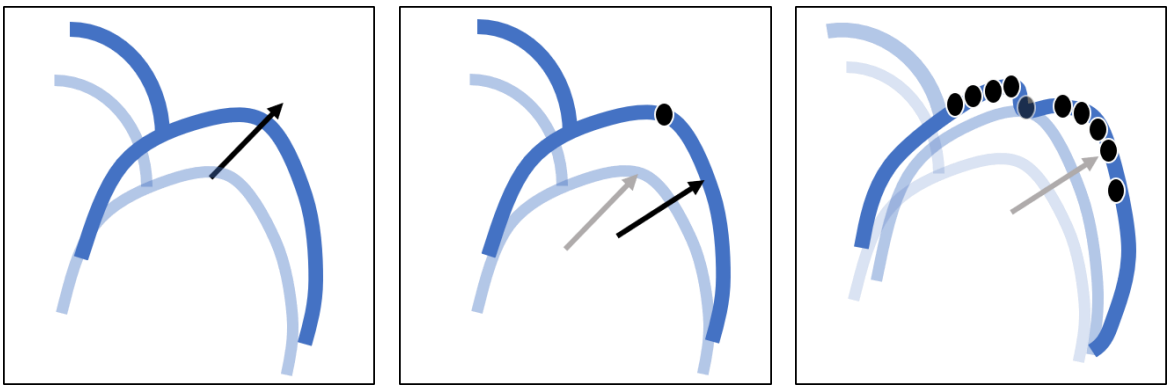

(a) *(b)* *(c)*

Figure 5.19: Diagram of oxidation within the grain boundary groove resulting in the retardation of grain boundary movement and hence prevention of grain. (a) shows the classic grain boundary movement of grooved grain boundary, (b) shows oxidation beginning to form changing the direction of movement around the pinned point, and (c) shows the point of complete oxidation and no grain boundary movement.

5.4.3 Fine Carbon Steel Grain Growth in the Austenitic Region

Despite some surface changes impacting surface grain growth, as detailed above, datasets where oxidation levels were minimal and grain growth was significant provide insight into how grain growth can be tracked *in situ.* Furthermore, the *in situ* fine grain data obtained at 800 °C demonstrate the effectiveness of using SE imaging combined with *in situ* thermal etching to capture microstructural changes that arise at elevated temperatures in the absence of oxidation. These SE images present a unique dataset that show the grain growth during the ferrite to austenite phase transition, as well as within the austenitic region. By tracking the grain growth *in situ* at elevated temperature, it is possible to observe and quantify changes over time without having to account for the effects of heating and cooling. Thus, *in situ* data provide a clearer understanding of the high-temperature evolution than examination post-heat treatment, which may only provide partial insight.

EBSD has also previously been used to track grain growth *in situ*. However, due to the time limiting factor associated with EBSD scanning of an evolving surface, only localised grain growth (<10 grains) has been captured, as shown in Chapter 4. By combining SE imaging and thermal etching, the current study has been able to image multiple grains in a very short space of time, providing data that are more representative of the overall grain structure. Furthermore, EBSD often requires extensive sample preparation, and during heating the surface quality has been shown to degrade over time, impeding image quality [227]. Conversely, a much shorter preparation time is required to facilitate *in situ* thermal etching and the image quality does not degrade as rapidly during heating.

As well as highlighting the benefits of the *in situ* thermal etching technique, observation of microstructural changes during the heat treatment show that grain size increases linearly with time. This phenomenon is associated with the growth of large grains at the expense of smaller ones, commonly known as abnormal grain growth [74], and is

considered to be the predominant type of grain growth within the carbon steel austenite region at 800 °C. Given that previously documented *ex situ* post-heat treatment data from carbon steel indicate normal non-linear grain growth, [78] this study highlights the importance of *in situ* analysis, demonstrating the value of this technique and data.

To confirm these observations, further measurements were performed. Two examples are shown in Figure 5.20 and Figure 5.21: Figure 5.20 is taken from the images shown above and Figure 5.21 is from further images taken over a period of 1 hour at 800 ºC at a higher magnification. The Figures show both the grains highlighted and the raw image to demonstrate the accuracy of thermal etching as a technique.

Figure 5.20a shows three small grains and one larger grain nearby. After 20 minutes, rapid growth of the larger grain leads to the absorption of two of the smaller grains and the slight growth of the third smaller grain (Figure 5.20b). After 45 minutes (Figure 5.20cc) the larger grain has continued to grow and has also absorbed the third smallest grain, signifying abnormal grain growth. Figure 5.21 shows a similar microstructural evolution.

The observation of abnormal grain growth, in this case, is likely attributed to some ferrite grains remaining at 800 ºC, despite the phase diagram indicating a fully austenitic microstructure. As such, the ferrite grains shrink over time alongside their austenite counterpart's growth, giving the illusion of abnormal grain growth. The retainment of ferrite within this carbon steel at 800 ºC has been confirmed using EBSD [227] (also observed in Chapter 4 of this thesis) and a similar localised phenomenon of ferrite shrinking as austenite grows has been documented during the cyclic phase change of steel [80]. These data indicate that abnormal grain growth may be characteristic of grain evolution during the ferrite to austenite phase change as well as in the fully austenitic region of carbon steel.

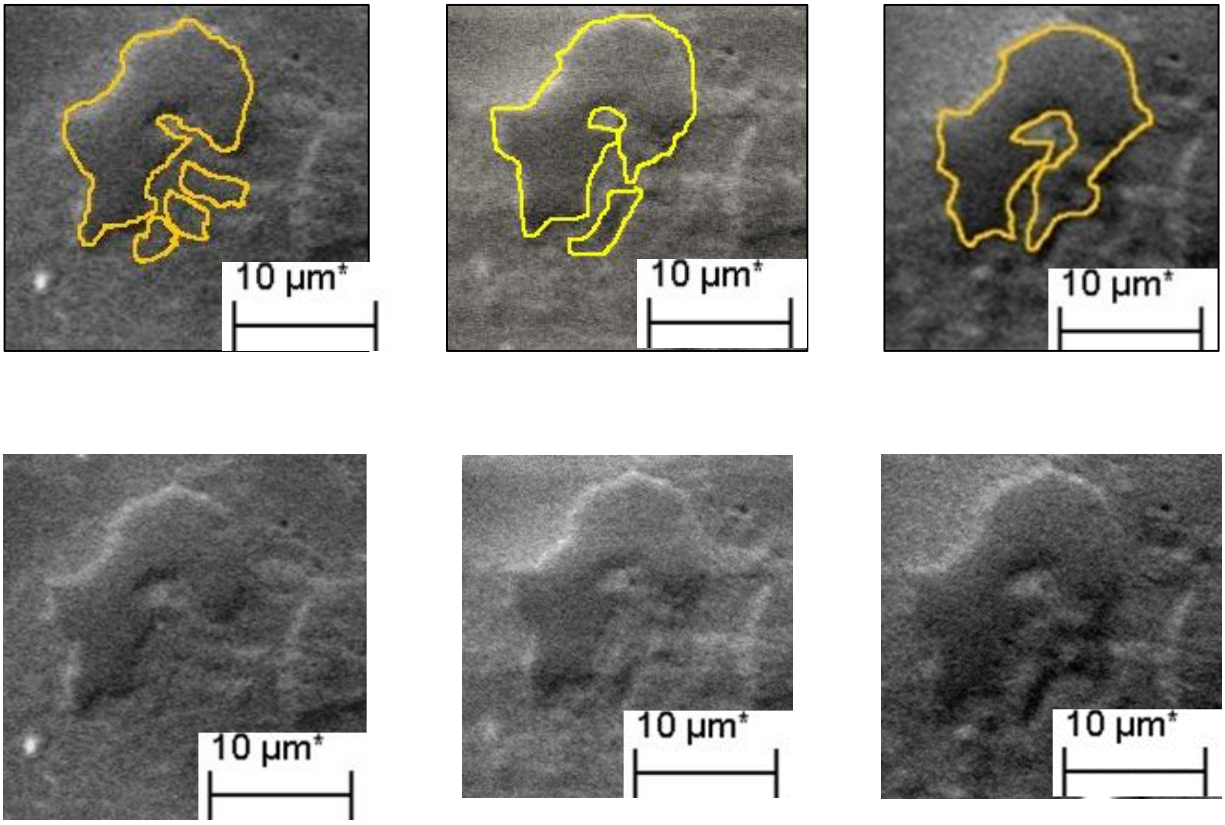

(a) *(b)* *(c)*

Figure 5.20: SE images at 800 °C depicting abnormal grain growth at (a) 0 minutes, (b) 20 minutes and (c) 45 minutes.

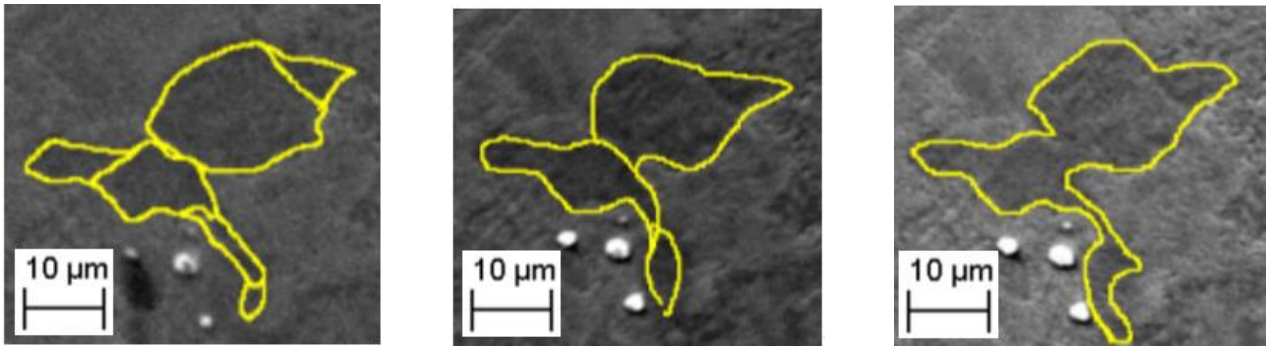

(a) *(b)* *(c)*

Figure 5.21: SE images at 800 °C depicting a second example of abnormal grain growth from another heating cycle that was focused on this small area at (a) 0 minutes, (b) 35 minutes, and (c) 45 minutes.

Due to the novelty of using the thermal etching technique *in situ* it is important to establish any effect that the sample preparation or the thermal etch itself may have on grain growth. Formation of the thermal etch occurs as a result of an equilibration of the triple junction between grain boundaries and free surfaces [81]. Subsequent movement of the grain boundary and hence the etch may, in theory, be dictated by the size of the grain. Smaller grains may escape the thermal etch more easily, while the grain boundary etch surrounding larger grains would continue to develop due to the grain boundaries being pinned here [83]. As a result, larger grains could appear to absorb smaller ones due to the less pronounced original grain boundary around smaller grains combined with the pinning of larger grains, rather than due to the grain growth itself. However, a comparison of the *ex situ* data post-cooling in the bulk and surface of the specimen, discussed in Section 5.4.2, and the *in situ* thermal etch data taken just before cooling, indicate that the thermal etch is representative of grain boundary movement. This confirms that grain growth under these conditions is not affected by thermal etching.

5.5 Conclusions

The research documented in this chapter demonstrates an alternative *in situ* SEM approach to studying surface morphology and microstructural evolution during the heat treatment of carbon steel. The use of the newly developed *in situ* SEM methodology, combining thermal etching and SE high-temperature imaging, has provided insight into the impact that surface effects have on the surface microstructure during the heat treatment of carbon steel. The *in situ* SE data are further supported by *ex situ* microscopy including optical, AFM and EDX data.

The *in situ* SE data, reinforced by the *ex situ* optical data, indicate that the difference in surface and bulk grain growth observed in steel when heat treated is due to the oxidation within the thermally etched grain boundaries. This preferential formation of oxidation within the grain boundaries led to a phenomenon not dissimilar to the Zener pinning effect. However, in this case the precipitates preventing movement of the grain boundaries formed during the heating process rather than already being present within the microstructure. The consistency between the surface and the bulk grain growth after heat treatment of 1 hour at 800 °C is attributed to insufficient oxidation occurring at this temperature to pin grain boundaries and thus prevent grain growth. These observations were supported by compositional EDX and *in situ* SEM data. At all other temperatures measured, the inconsistency between bulk and surface grain structure can be accounted for by the increasing presence of oxidation with temperature, as confirmed by the Pilling-Bedworth law.

Owing to the observed oxidation during heat treatment, this chapter also demonstrates an alternative *in situ* SEM approach to studying surface morphology resulting from thermal oxidation. The data presented provide further insight into the formation process of oxide layers in carbon steel, which is affected by the presence of thermal etching and the subsequent

agglomeration of oxide nodules, initially forming discrete oxide scales before eventually creating a more uniform oxide layer. Based on the morphology imaged in this study, combined with current data in the literature, it is thought that the composition of the oxide layer formed under these conditions is predominantly wüstite. The lack of blistering present, which would be expected at these temperatures and time scales, indicates that either multiple oxide layers are necessary for blistering to occur (indicating a lack of layers in this heat treatment), or a gaseous layer is required not only to support the blister and prevent collapse or healing, but also to facilitate its formation in the first place. Hence, these findings further the understanding of the mechanism by which iron-oxide layers form.

In addition to observation of the surface effects, examination of the *in situ* SE data at 800 °C facilitated the tracking of grain growth during the ferrite to austenite phase change within the austenitic region of carbon steel at this temperature. Tracking grain growth was only possible at this temperature due to the absence of significant oxidation, and the uniformity between the bulk and surface *ex situ* grain growth data. Furthermore, the *in situ* data at 800 °C demonstrate the benefit of using SE thermal etching over EBSD or other such methods to capture grain growth. The data suggest that microstructural evolution during the ferrite to austenite phase change transitioning into the austenitic region of carbon steel during heat treatment at 800 °C can be described by abnormal grain growth. This is based on the linearity of the results detailed in this paper as well as the observed shrinkage of ferrite grains as the austenite phase develops. Since the microstructural development had not been previously observed, owing to the lack of *in situ* high-temperature data, this demonstrates the benefit of high-temperature *in situ* SEM studies on heat treatment processes.

In conclusion, these findings show the advantages and challenges of using the SE *in situ* thermal etching technique to track microstructural evolution during the heat treatment of carbon steel.

Chapter 6

In Situ Microstructural Evolution of Phase Changes in Carbon Steel

6.1 Introduction

This chapter presents further investigations of the heat treatment of carbon steel, with a focus on the phase change into the austenitic region. Phase changes during processing affect the overall microstructure of the final, cooled material, and thus the mechanical properties. Investigations extending the novel *in situ* techniques developed in Chapters 4 and 5 provide a unique insight into the phase evolution of carbon steel from the starting microstructure into the austenitic region. The final microstructure obtained after heat treatment, is strongly dependent on the reverse transformation kinetics during austenite formation, which are dictated by the initial microstructure [48]. Hence, this chapter investigates two initial starting structures, ferrite / pearlite and martensite, which generate microstructures with desirable properties, when transformed into austenite during commercial heat treatment processes.

6.1.1 Ferrite / Pearlite to Austenite Phase Transformation

The initial starting structure of a ferrite / pearlite composition is a body centred cubic (BCC) structure (ferrite) interspersed with a two phased lamella structure (pearlite) composed of alternating layers of cementite (Fe_3C) and ferrite. The transformation of this complex phase structure into austenite is considered to be a diffusion-driven process of nucleation and growth [50]. Dilatometric analysis indicates a two-stage transformation process of pearlite dissolution followed by the transformation of the pure ferrite grains into austenite [48]. These

findings are further supported by microstructural data captured by interstitial rapid cooling after a short heat treatment, indicating the initial formation position of austenite with respect to pearlite and ferrite grain boundaries [5][2]. Despite this interesting and complex phase change being a key driver in the final microstructure formed during heat treatment, there is an absence of real-time microstructural data captured during this evolution to provide further insight into the overall grain migration.

Localised *in situ* microscopy studies of pure ferrite to austenite transformations using optical and laser scanning confocal microscopy, and electron backscatter diffraction (EBSD) imaging have shown the benefit of real-time microstructural observations in supporting dilatometric analysis. These microscopy studies have also provided insight into specific individual grain interface behaviour during the phase change. Nonetheless, these advances are subject to typical instrumental constraints including spatial resolution, imaging speed, and field of view [51]. Due to the complexity of the ferrite / pearlite to austenite phase change, the development of a technique that captures a greater number of grains would improve the understanding and quantification of the average microstructural movement that occurs during this process.

6.1.2 Martensite to Austenite Phase Transformation

Martensite is a single-phase, needle-like microstructure with a body centred tetragonal structure, which has a high carbon content. Owing to martensite's very strong but brittle properties, the reversion process of martensite to austenite is often used to retain the strength associated with a pure martensite phase while increasing the material's overall ductility [53]. As discussed in Chapter 2, current phase-field models indicate that the transformation begins at the boundaries of the martensite laths [55]. This observation has subsequently been supported by *in situ* transmission electron microscopy (TEM), dilatometry, and X-ray diffraction [53][54]. However, thus far, these observations have been highly localised to

individual grains. Therefore, extending this theory would require capturing multiple grain boundary movements simultaneously to gain an average of the microstructural evolution throughout the material.

It is clear from the literature that, at present, there is a lack of data on specific real-time microstructural evolution during these phase changes and, in particular, large data sets of multiple grains. The current chapter aims to remedy this with *in situ* real-time EBSD and secondary electron (SE) image data captured during these phase changes.

6.2 Methodology

The high-temperature *in situ* SEM imaging techniques developed during this project were extended to analyse the phase transformation of carbon steel during the heating stage of austenitic heat treatments. *In situ* SE and EBSD images were collected throughout the heat treatment process, which facilitated subsequent microstructural phase transformation characterisation from the *in situ* SEM data. The *in situ* evolution data, were further supplemented by *ex situ* optical and EBSD data both pre- and post-heat treatment.

6.2.1 Materials

As with previous heat treatment studies detailed in Chapter 5, a 0.4 wt.% carbon steel was selected for this study, which undergoes an austenitic phase change at 780 °C during heat treatment [19]. The study focused on this phase transformation during the heating period as it significantly affects the final microstructure that results from the heat treatment. Furthermore, the observation of microstructural changes during this evolution would facilitate improved control of the phase change, including the ability to generate desirable properties from the heat treatment. The austenitic phase transformation from two complex initial microstructures was examined; the starting microstructures were:

- **Drawn Form Carbon Steel**: The same form of carbon steel as used in Chapter 5; directionally drawn ferrite / pearlite phase microstructure with no heat treatment applied and a coarse grain starting structure.
- **Martensite Form Carbon Steel**: The carbon steel was first heated at 850 °C for 1 hour, before being quenched in water. This heat treatment forms a needle like grain structure known as martensite, which was the starting structure for the *in situ* phase transformation.

The detailed properties and use of the 0.4 wt.% carbon steel chosen can be found in Chapter 2.

6.2.2 Heat Treatment: SE Imaging

The phase transformations were observed during the *in situ* heat treatment of 0.4 wt.% carbon steel within the SEM. Both starting microstructures of 0.4 wt.% carbon steel were cut into disk shape samples with diameter of 8 mm. To facilitate thermal etching, and hence improve phase change observation with respect to grain movement, all samples were prepared by silicon carbide paper grinding followed by diamond suspension polishing, and finished with a colloidal silica polish with final thickness of 1 mm; as detailed in Chapter 5.

All *in situ* heat treatments of the specimens were facilitated by a purpose-built heat stage. During the *in situ* heat treatment, the initial microstructures were heated at a rate of 60 °C/minute up to 800 °C, which is the austenitic region of 0.4 wt.% carbon steel [226]. The samples were subsequently held at this temperature for 1 hour before cooling at a rate of 20 °C/minute to 50 °C[8]. The temperature of 800 °C was selected for two reasons. First, 800 °C is just above the austenitic transition point of 0.4 wt.% carbon steel. Hence, this temperature provides a suitably slow phase transformation into austenite while still becoming fully austenitic. The speed of the transformation dictates the ease at which the phase evolution could be observed via SE image capturing; a slower speed facilitated a greater number of distinct images and thus a more detailed exploration of the microstructural phase transformation. Second, as detailed in Chapter 5, extensive research has been conducted in this project to isolate the conditions under which surface observations during *in situ* SEM imaging are representative of the bulk of the specimen. It was shown that surface observations of microstructural evolution at 800 °C during the 1-hour heat treatment of 0.4 wt.% carbon steel under SEM vacuum conditions were representative of the bulk microstructural transformation. Hence, this set of parameters were used for this investigation.

[8] 50 °C was chosen as it was assumed that no further microstructural changes would occur between this and room temperature. It was also a safe temperature at which to vent the SEM chamber.

SE images were captured, using a 15 keV electron beam, at regular intervals during the 1-hour heat treatment, with a focus on the first 30-40 minutes, during which the main phase transformations from ferrite / pearlite (drawn form) and martensite (martensite form), to austenite occurred. As detailed in Chapter 5, the different greyscale levels of an SE image can allow differentiation between different phases [120]. This phase information, coupled with thermal etching, was used to track the changes in the microstructural evolution with respect to phase and grain size, and was further supported by EBSD imaging results.

6.2.3 Heat Treatment: EBSD Imaging

Alongside the SE imaging, EBSD *in situ* data were also collected during the heat treatment of 0.4 wt.% carbon steel in its drawn form. Heat treatments were conducted using the same heating and cooling profile as for SE imaging. EBSD images were taken with an Oxford Instruments' Nano-analysis EBSD detector, which is a change from the detector used to capture the images in Chapter 4. This facilitated faster data capture (a necessity when imaging a dynamic process *in situ*). The EBSD data were collected as the temperature reached 800 °C and then at approximately 15 minute intervals for 1 hour. As with SE, images were captured using a 15 keV electron beam with a LaB_6 source. The large time interval between scans is due to a combination of the speed of map acquisition and the need to prevent the detector from overheating. To minimise overheating, the EBSD detector was retracted between scans to allow it to cool. Although the temperature of the detector did not exceed 55 °C during the 1-hour heat treatment and the screen can be operated at temperatures up to 120 °C, it was observed that the processing of the data became significantly slower at elevated temperatures, as the camera processing chip is located at the front of the EBSD detector and thus is also subject to overheating. Scans were between 10 µm and 20 µm squared, with a step size of 0.35 µm, and took between 2 and 4 minutes to collect. The EBSD parameters were

chosen as a compromise between the need to image enough grains for analysis and the necessity to perform the scan in a short time period to capture the dynamic process. Post experimental analysis was conducted on the EBSD data using EDAX software to produce grain, phase, and inverse pole figure maps.

6.2.4 *Ex situ* Characterisation

To further supplement the *in situ* microstructural data captured at the phase transition temperature, optical images and EBSD scans were collected pre- and post-heating. This confirmed the significant change in microstructure attributed to the heat treatment process. Samples were imaged optically using an Alicona profilometer at 5×, 10×, 20×, 50×, and 100× magnification at room temperature pre- and post-heat treatment. To enable this, samples were polished and chemically etched using 2% nital to allow for optical imaging of the surface microstructure. To capture EBSD data, samples underwent grinding and polishing procedures (see Chapter 4) and were imaged immediately before heating began. Following the heat treatment, samples were re-polished before being reimaged using EBSD. Room-temperature EBSD scans before and after heating were 100 µm × 100 µm with a step size of 0.25 µm and a scan time of 8 hours using a 15 keV electron beam. To evaluate the compositional changes to the martensite sample surface, energy dispersive X-ray (EDX) data were gathered as, although the changes in composition during heat treatment have been examined extensively for drawn samples (see Chapters 4 and 5), this has not yet been considered for a martensitic starting structure. EDX data were captured, both before and after a 1-hour heat treatment of martensite steel at 800 °C, for a 100 µm × 100 µm area over 200 frames.

6.2.5 Data Analysis of Phase Change Kinetics

SE and EBSD images were analysed in order to further understand the phase change kinetics in the austenitic region of carbon steel at the 800 °C heat treatment temperature. SE data during the phase transformations were used to calculate the phase change rate and its relationship to the microstructural changes observed *in situ*. EBSD images were used to further support these measurements.

To quantify the phase change rate, SE data at 500-1000x magnification with a distribution of over 100 grains, which were visible owing to the presence of thermal etching, were processed using ImageJ analysis software. Histogram segmentation within ImageJ facilitated the separation of the phases visible in the SE image, distinguishable by the different greyscale levels. Hence, the phase percentage present at each time interval, every 5-10 minutes over the course of 1 hour, was calculated. The results were subsequently plotted as the phase percentage versus time to provide a rate of change of the phase transition from the moment that the temperature reached 800 °C. Understanding the effects of phase atomic density, combined with SE and EBSD images captured simultaneously, enabled the identification of which greyscale levels in the SE image were representative of each phase.

The results of the phase change rate calculation were fitted to the phase transformation equation, the Johnson-Mehl-Avrami-Kohnogorov (JMAK) model [232],

$$f = 1 - exp\,(-kt^n) \qquad \textit{Equation 6.1}$$

and were presented in its commonly rearranged form,

$$ln\left(ln\left(\frac{1}{1-f}\right)\right) = nlnt + lnk \qquad \textit{Equation 6.2}$$

where f is the volume fraction of the transformed phase (in this case austenite), t is the transformation time in seconds, k is a temperature dependent constant defined by the

Arrhenius type equation $k = Be^{\frac{-Q}{RT}}$, Q is the activation energy, R is the gas constant, T is the temperature at which the phase transformation occurs, B is a material constant and n is the Avrami exponent of the equation [37]. The JMAK model is used to predict and describe the kinetics of isothermal phase transformations, assuming that transitions occur by nucleation and diffusion-controlled growth [37]. Thus, it is widely accepted as a good fit for the pure ferrite to austenite phase transition [232].

6.3 Results

6.3.1 *Ex Situ* Microstructures

Optical and EBSD images, presented in Figure 6.1, show the overall microstructure of the drawn steel before and after a 1 hour heat treatment at 800 °C. Focusing on the optical micrographs of etched material surfaces, Figure 6.1a and Figure 6.1b, the presence of ferrite (red arrow) and pearlite (blue arrow) phases are clearly visible. The phase change, as expected, has caused an increase in the size of the larger grains and a decrease in the number of smaller ones; this can be slightly seen from the optical image. However, the use of EBSD to capture a localised area (Figure 6.1c and Figure 6.1d), shows a significant change in grain size, indicating that there has been grain growth during the phase change. The raw (uncleaned[9]) EBSD scans confirm that the heat treatment of ferrite / pearlite starting structure into the austenitic region led to grain growth *ex situ*, which is similarly observed during this heat treatment in Chapter 5. The significant microstructural change observed *ex situ* further demonstrate the need for *in situ* studies to identify the point at which this rearrangement is happening during the heat treatment, and how the phase transformation may affect this. Figure 6.2 produces the expected recrystallisation as a consequence of the martensite to austenite reversion process. Figure 6.2a depicts the standard martensitic lath like structure. Following heat treatment into the austenitic region. In Figure 6.2b, the microstructure has refined further due to the recrystallisation of austenite grains within the martensite laths. Capturing the moment within the heat treatment at which this refinement occurs is key to optimising the reversion martensitic heat treatment in order to produce favourable mechanical properties [54]. The recrystallisation of austenite within the martensite laths can be seen more clearly in the EBSD scans, Figure 6.2c and Figure 6.2d.

[9]Uncleaned or raw EBSD images refer to those that have not undergone post processing after data capture.

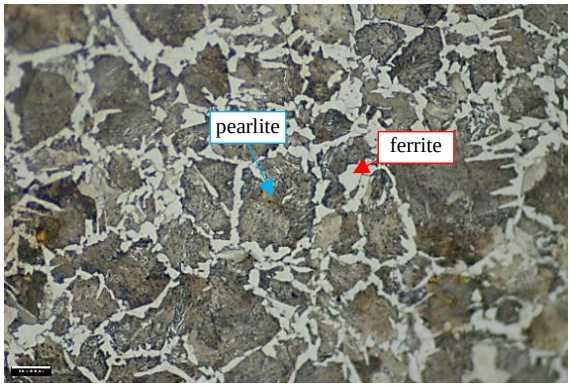

(a)

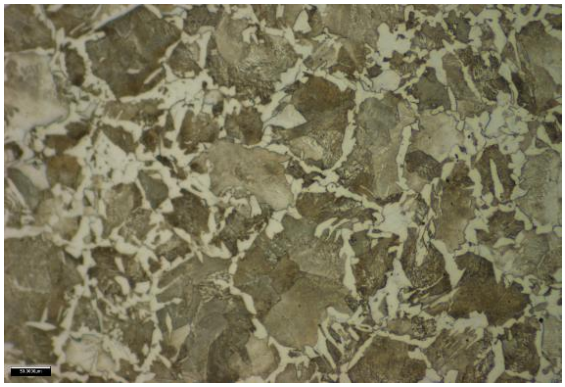

(b)

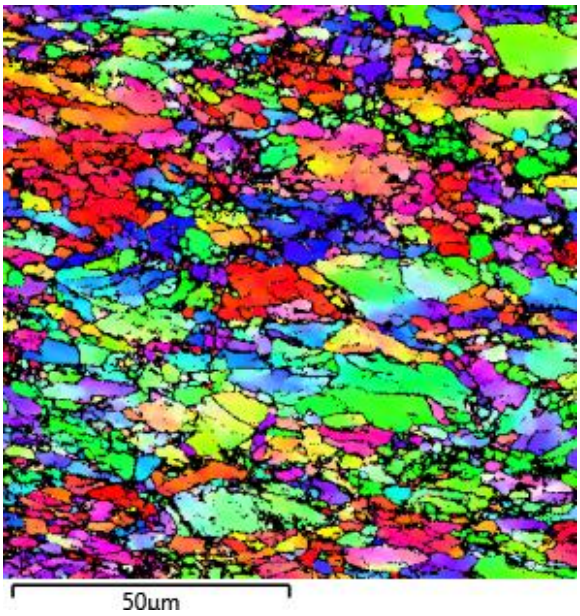

(c)

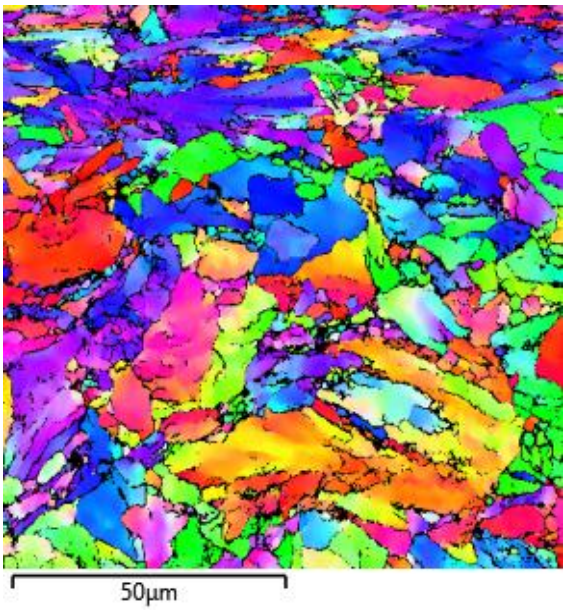

(d)

Figure 6.1: Optical (a)&(b) and EBSD (c)&(d) images at room temperature before (a)&(c) and after (b)&(d) heat treatment of ferrite / pearlite starting structure specimens.

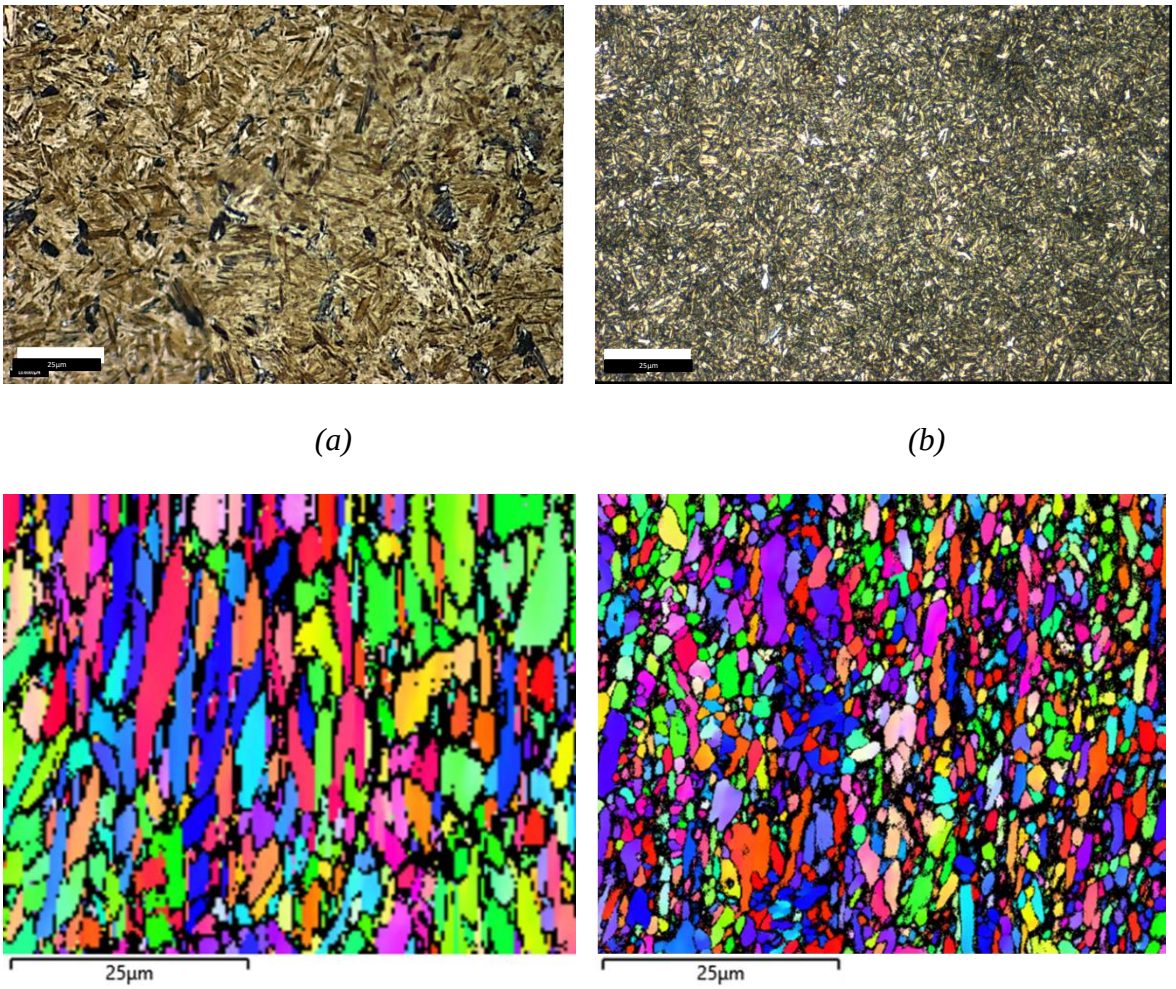

(a) *(b)*

(c) *(d)*

Figure 6.2: Optical (a)&(b) and EBSD (c)&(d) images at room temperature before (a)&(c) and after (b)&(d) heat treatment of martensite starting structure specimens.

6.3.2 *In Situ* Ferrite / Pearlite to Austenite: SE

In situ SEM imaging during the heat treatment enabled the documentation of the ferrite / pearlite to austenite phase change using both SE and EBSD imaging. Figure 6.3 shows a selection of SE images captured during the first 30 minutes of the heat treatment process; other SE images taken at this temperature and timescale can be found in the appendix of Chapter 6.

The SE images in Figure 6.3 show a significant variation in greyscale; no adjustment to the brightness or contrast was made between images. It is widely accepted that the different greyscale levels of the image (here called light, mid, and dark) can indicate the existence of different phases simultaneously in an SE image [17]. Therefore, the SE images presented in Figure 6.3 show the stages of the phase transition from a microstructural perspective. Figure 6.3a shows the SE image of the carbon steel surface once the required heat treatment temperature of 800 °C was reached. Here, an outline of the grain boundaries can be seen owing to the phenomenon of thermal etching, discussed in previous chapters. The outline also facilitates the identification of individual grains' phase presence, although this localised phenomenon is further investigated using EBSD high-temperature imaging. The SE images can be used to examine the changing ratio of the three different greyscale levels corresponding to the phases, as the transformation of ferrite / pearlite to austenite occurs in real time.

Focusing on the evolution of the darker areas, these evolve dramatically in the first 10-15 minutes, with limited grain growth but the dark areas appearing to turn to the mid grey shade, as identified in Figure 6.3b and Figure 6.3c and highlighted by the red arrows. During this transition, some of the darker patches appear to fill gradually with the mid grey spots, rather than the whole area transforming at once. Also, the smaller dark grains appear to change first ahead of the larger ones, this can be seen quite clearly in the difference between Figure 6.3b and Figure 6.3d. In the latter, almost all the smaller darker areas have transformed, shown

by the red arrow in Figure 6.3d. It is important to note the impact of thermal etching on the image. In Figure 6.3d, some of the darker areas appear to surround the grain boundaries; this can be accounted for by thermal etching presence showing the grain boundary outline. By 20 minutes (Figure 6.3f) all the darker areas have transformed to the mid greyscale phase and only the mid and light phases are present.

Also observed in this sequence of SE images is the change of the lighter phase into the mid greyscale. However, this change is not observed until after 12 minutes (Figure 6.3d). The growth of the mid greyscale phase then appears to accelerate, showing significantly more growth after 16 minutes (Figure 6.3e). Unlike the darker phase transformation, which occurs homogenously, the transformation to the mid grey phase from the lighter phase appears to occur from the edges moving into the centre (heterogeneously) – as can be seen quite clearly in the larger, light grain shown by the green arrow in Figure 6.3d, e and f. The smaller, lighter areas also begin to shrink quite rapidly and after 24 minutes (Figure 6.3g), these have almost all transformed. It is worth noting that Figure 6.3g also experiences some uncorrected beam drift; the green arrow highlights where the original large light grain is in the new position. This continues to shrink and by 32 minutes there has been a complete transformation (Figure 6.3h).

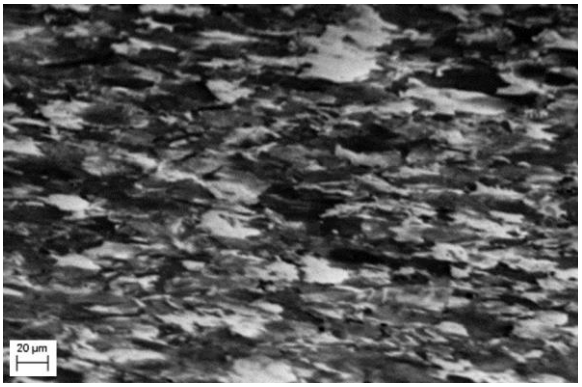

(a) 1 minute

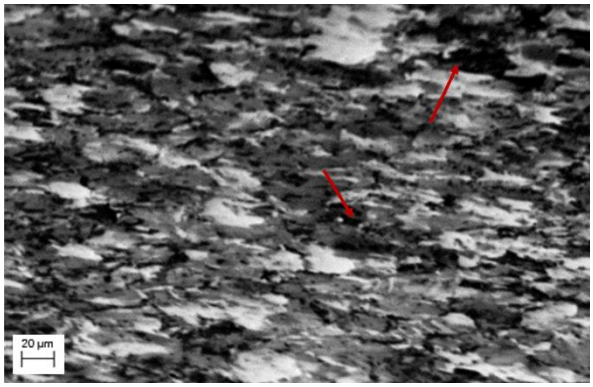

(b) 3 minutes

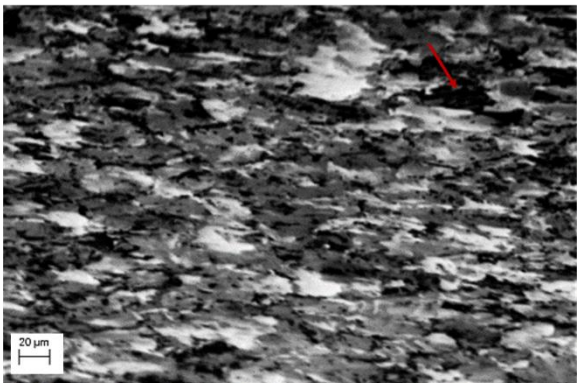

(c) 6 minutes

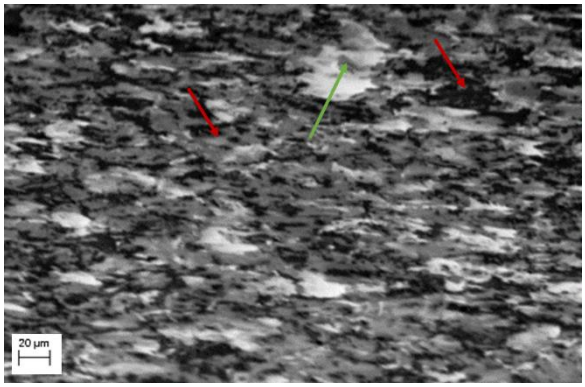

(d) 12 minutes

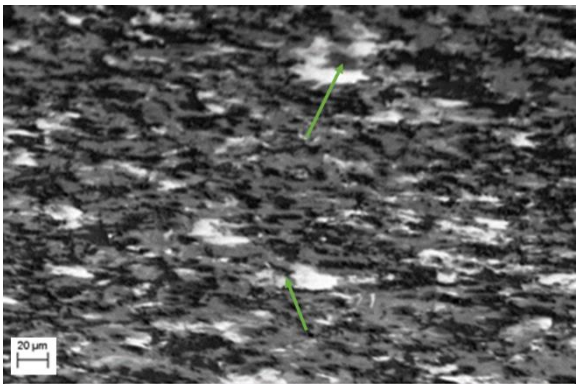

(e) 16 minutes

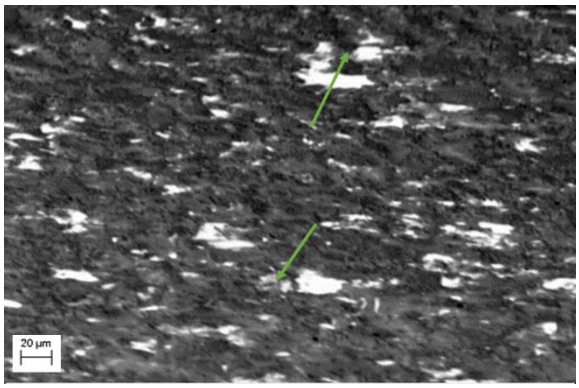

(f) 20 minutes

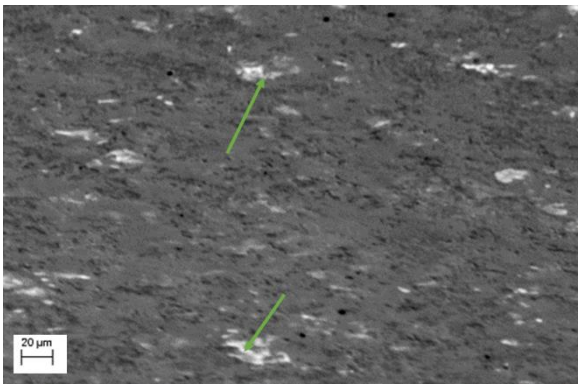

(g) 24 minutes

(h) 32 minutes

Figure 6.3: In situ *SE images during ferrite / pearlite to austenite phase change after heating at a temperature of 800 °C indicate a transformation of nucleation and growth of the individual phases with some overlap between each phase transformation.*

Noting the differences in the two phase transformations, Figure 6.4 shows a focused transformation over the first 30 minutes of the specific dark phase cluster, and Figure 6.5 presents a specific light phase cluster. Examining the darker phases in Figure 6.4a, b and c shows initial homogenous nucleation (red arrows), followed by rapid growth of the nucleation in Figure 6.4d and Figure 6.4e, until complete transformation at 20 minutes (Figure 6.4f). The lighter grains identified from the SE data show little to no transformation until 12 minutes (Figure 6.5a and Figure 6.5b). However, after 12 minutes of heating, Figure 6.5c shows the light grains begin to shrink from the outside inwards and continue to do so allowing the mid-grey phase to grow (Figure 6.5d, e and f), until around 30 minutes, (Figure 6.5g and Figure 6.5h), when there is little to no lighter phase present; a phenomenon that is also observed in the lower magnification SE images (Figure 6.3).

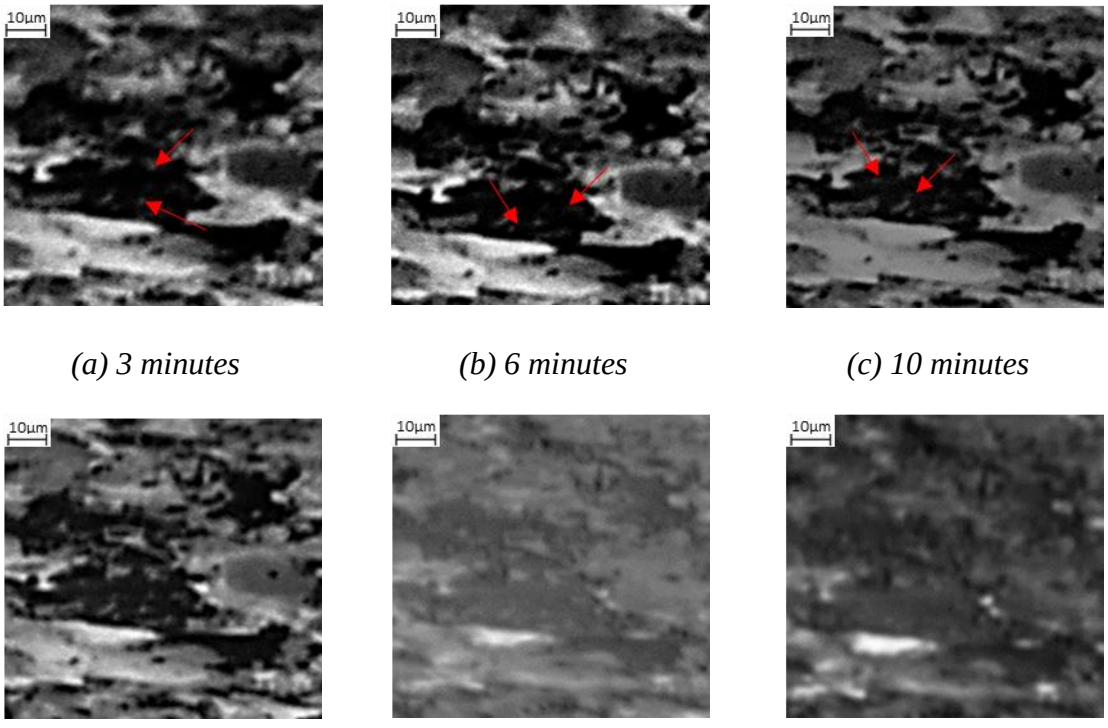

(a) 3 minutes *(b) 6 minutes* *(c) 10 minutes*

(d) 12 minutes *(e) 17 minutes* *(f) 20 minutes*

Figure 6.4: Phase transformation of a darker grain into the mid greyscale form via nucleation in (a), (b) & (c) followed by growth (d) & (e) and complete transformation (f).

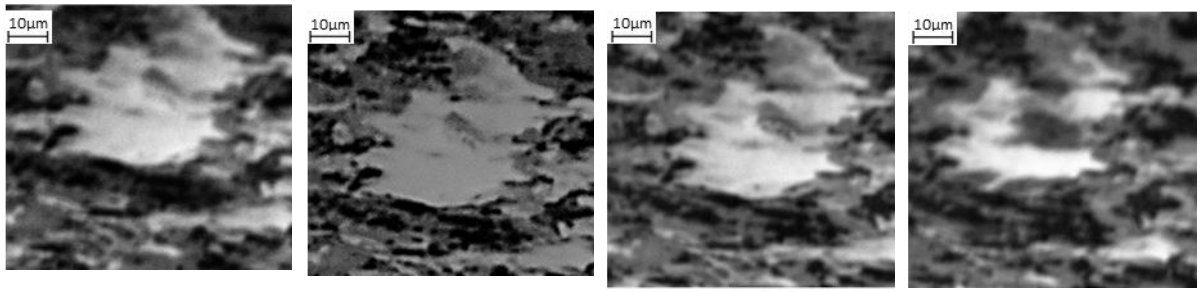

(a) 3 minutes *(b) 10 minutes* *(c) 12 minutes* *(d) 16 minutes*

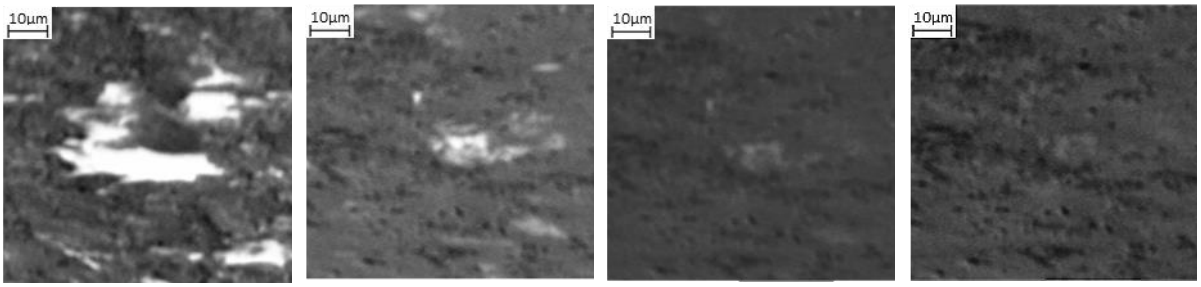

(e) 22 minutes *(f) 24 minutes* *(g) 29 minutes* *(h) 32 minutes*

Figure 6.5: Phase transformation of a lighter grain into complete mid greyscale form where transformation begins by homogeneous nucleation at 12 minute (c) and the mid greyscale phase continues to grow until complete agglomeration at 32 minutes (h).

6.3.3 *In Situ* Ferrite / Pearlite to Austenite: EBSD

EBSD imaging was used to confirm the representation of the different phases within the SE greyscale images. Examination of the Kikuchi patterns of the different phases present at 800 °C, shown in Figure 6.6, identified that the mid greyscale areas were austenite and the lighter area was BCC ferrite. Hence, it may be assumed that the darker areas within the SE images represent the pearlite phase; the only other phase present during this transformation. This conclusion is in line with the level of carbon present in each of the phases and the representation of the structure during SE imaging.

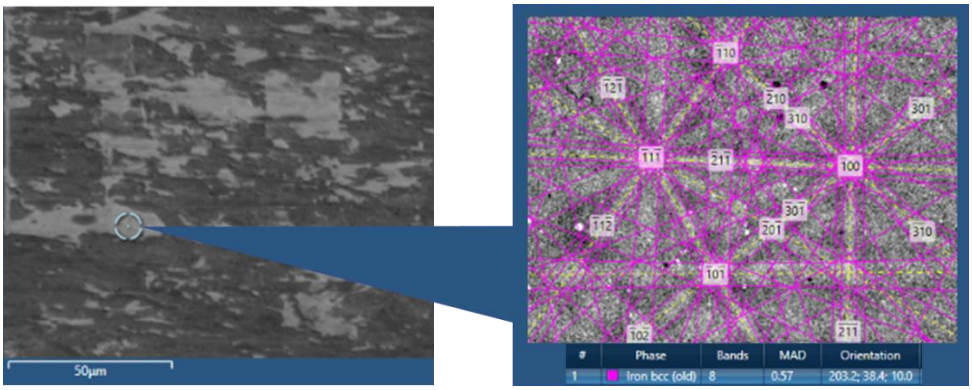

(a)

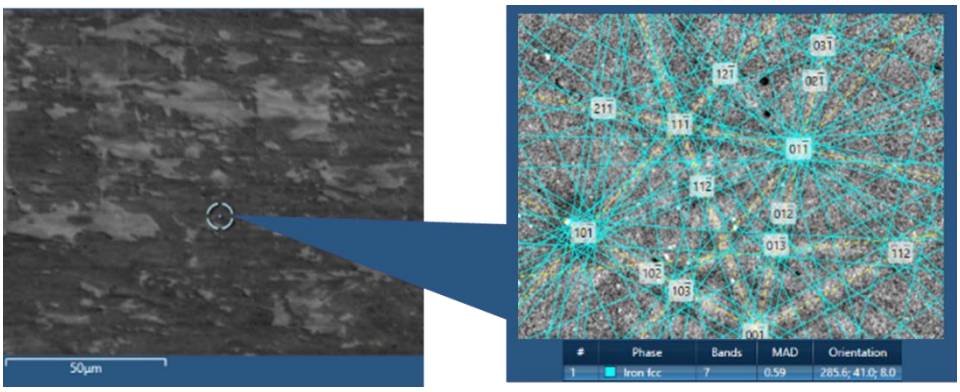

(b)

Figure 6.6: EBSD Kikuchi patterns, taken at 800 °C, identifying the phases present from the SE image. There is (a) a lighter area identified as BCC ferrite and (b)a darker area identified as FCC austenite.

Grain evolution was also captured using EBSD scans (Figure 6.7) facilitating a localised understanding of the microstructural evolution during the phase transformation from ferrite / pearlite to austenite; all EBSD scans are taken in the same position unless stated otherwise. Figure 6.7a and Figure 6.7b show there is a significant transformation in the orientation and size of the grains during the initial stages of heating from room temperature to 800 °C. There is also a change in phase, during which the small grains appear to transform prior to the larger ones. Examining the structure after 25 minutes, Figure 6.7c shows a further change in orientation and complete phase change, indicating that the transformation process is complete; this is a similar timeline to the observations in the SE images presented in Figure 6.3. EBSD images of the same area at 40 minutes (Figure 6.7d) show no change in phase and

minimal growth of grains. The EBSD image taken after 57 minutes of heating, Figure 6.7e, shows some beam drift (see the black arrow for direction) but provides enough of the localised microstructure to suggest there is little further evolution. This is expected based on the surface growth presented in Chapter 5 where, between 45 minutes to 1 hour, there is little surface microstructural evolution due to a combination of oxidation and thermal etching. Furthermore, once oxidation begins to encroach on the surface of the sample, EBSD data can no longer be captured.

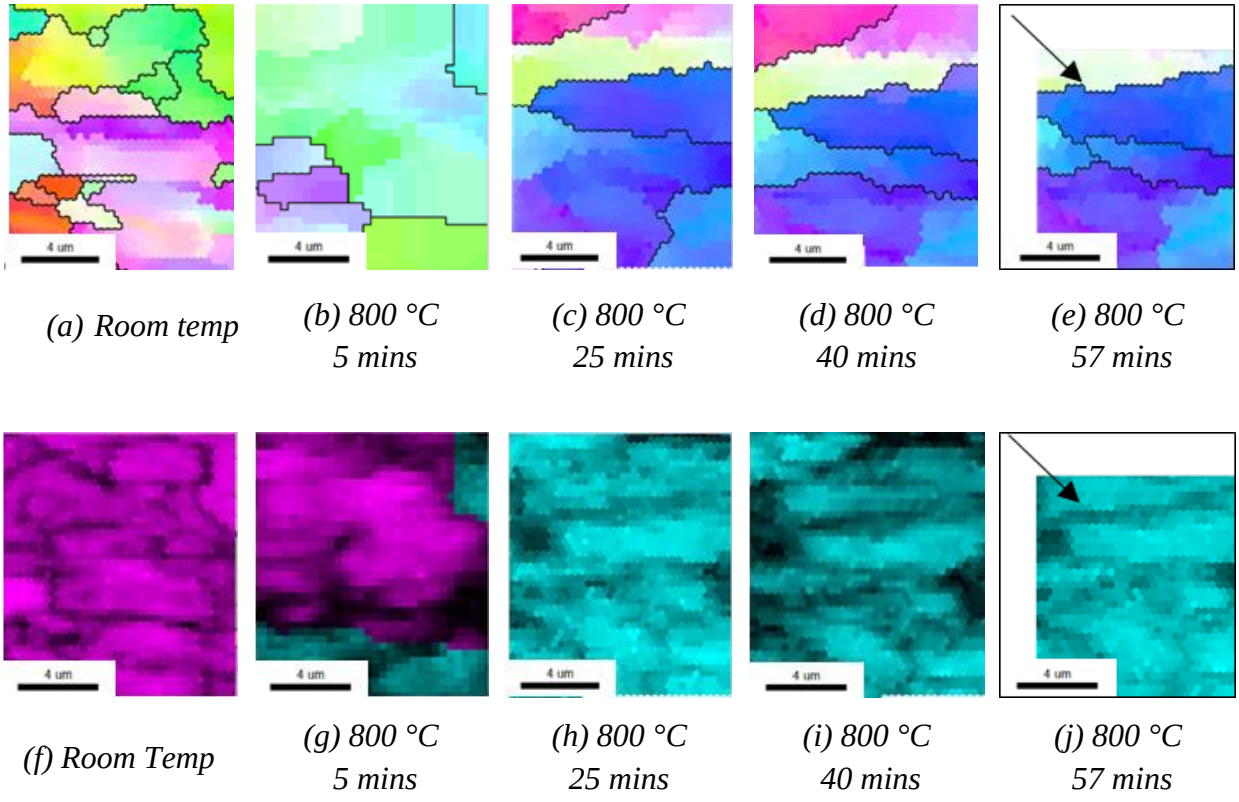

(a) Room temp *(b) 800 °C 5 mins* *(c) 800 °C 25 mins* *(d) 800 °C 40 mins* *(e) 800 °C 57 mins*

(f) Room Temp *(g) 800 °C 5 mins* *(h) 800 °C 25 mins* *(i) 800 °C 40 mins* *(j) 800 °C 57 mins*

Figure 6.7: Evolution of ferrite / pearlite to austenite phase transformation captured via EBSD inverse pole figure (a), (b), (c), (d) & (e) and phase (f), (g), (h), (i) & (j) maps.

Owing to the speed of the phase transformation, as seen in the EBSD images, the observation of the phase transformation is limited to the first three EBSD scans in Figure 6.7. However, additional EBSD scans at this temperature, shown in Figure 6.8, further support the SE data. The scans indicate that, as well as smaller grains transforming first, some initial

nucleation of austenite grains occurs within the ferrite / pearlite formation, and this is where transformation first occurs. Figure 6.8 depicts an initial room temperature scan ((a) & (b)) and a second scan in the same position after just 2 minutes of heating at 800 °C ((c) & (d)). Where smaller grains have formed, the phase scan in Figure 6.8d indicates that these areas are austenitic (indicated by the blue). The findings in Figure 6.8a show an initial austenite nucleation between the pearlite grains; represented as a small agglomeration of ferrite grains on the right hand side of the image. Previous, rapid heat treatment followed by quenched cooling EBSD studies have indicated that, at temperatures of 700 - 800 °C, austenite nucleates preferentially as a block at triple junction at high angled grain boundaries [13]. The inverse pole figure data, presented in Figure 6.6, also indicates this, where austenite forms preferentially at these grains. However, due to the similarities between pearlite and ferrite, it is often difficult to distinguish the two phases using EBSD, hence the benefit of SE imaging to support these findings [12].

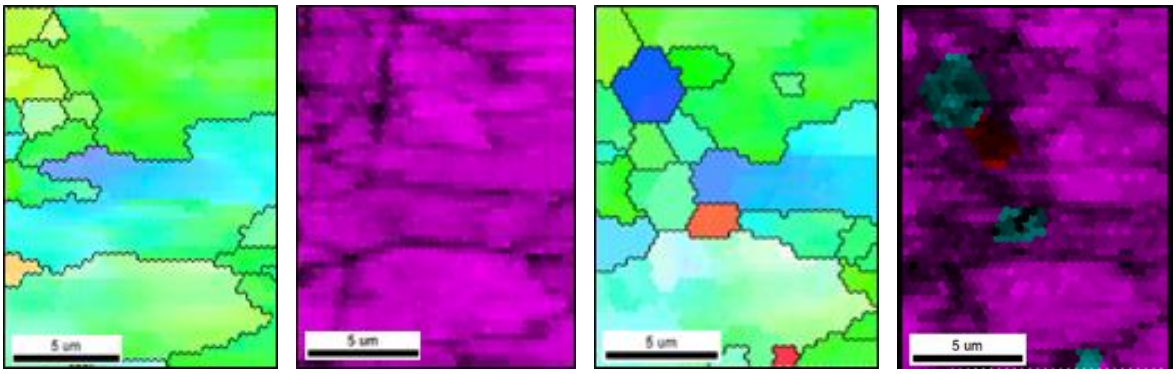

(a) Room-Temperature | *(b) Room-Temperature* | *(c) 800 °C, 2 mins* | *(d) 800 °C 2 mins*

Figure 6.8: EBSD scans represented by the inverse pole figure (a) & (c) and corresponding phase maps (b) & (d) capture the preliminary formation of austenite within a ferrite / pearlite microstructure when heated to 800 °C within an SEM. (a) & (b) show the initial area, and (c) & (d) show the same area where the phase transformation occurs and austenite (in blue) has begun to agglomerate and form in the smaller grains

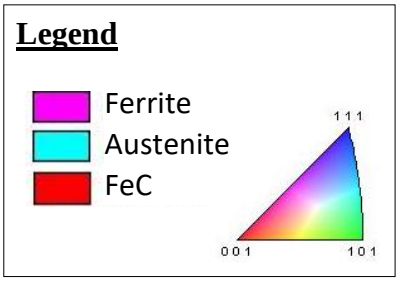

6.3.4 Tracking Ferrite / Pearlite Phase Changes

The SE images were taken at sufficient frequency to facilitate the quantifiable tracking of the ferrite / pearlite to austenite phase change *in situ*. Percentages of the three phases quantified using ImageJ's histogram segmentation tools were plotted against time; a full set of the quantified histograms relating to the SE images can be found the appendix of Chapter 6. The combined results of three separate data sets are presented in Figure 6.9, on a log-linear graph, as is standard practice for phase transformations [51]. The graph demonstrates that the extreme greyscale ends (light and dark) representing ferrite and pearlite respectively, decrease as the austenite phase increases and the graphs form a sigmoidal shape.

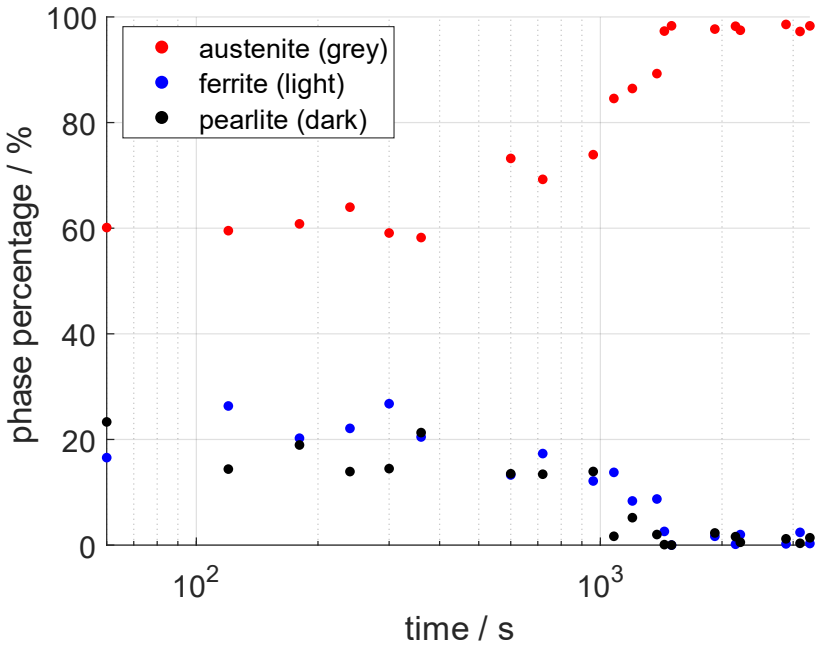

Figure 6.9: Offset sigmoidal plot, the data for which were quantified from the SE images of three data sets showing the phases: austenite, ferrite and pearlite as red, blue and black respectively on log-linear plot.

To further compare these findings to other datasets, the well-documented JMAK model was used. Here the data is plotted as $ln\left(ln\left(\frac{1}{1-X}\right)\right)$ versus lnt in the form of the rearranged JMAK model (Figure 6.10). The results, plotted in Figure 6.10, show only the first

30 minutes of the data; once the phase change is complete, the model no longer applies. The graph presents two distinct linear regressions, highlighted by the black and red lines respectively, with a turning point of between 10 and 12 minutes, circled. The two linear regressions, in the JMAK model, suggest two separate stages in the transformation process that are governed by two distinct systems of nucleation and growth. The initial slow rate, and hence the lower gradient correlation (black line in Figure 6.10), is attributed to the formation of nuclei of the new phase [234]. Once nuclei numbers reach a critical mass they begin to agglomerate leading to rapid growth of the new phase cluster [235]; this is demonstrated by the higher gradient graph (red line in Figure 6.10). This distinct difference in rate of the two step process means that, when any nuclei begin to agglomerate the growth phase takes priority even if some nuclei may still be forming [235].

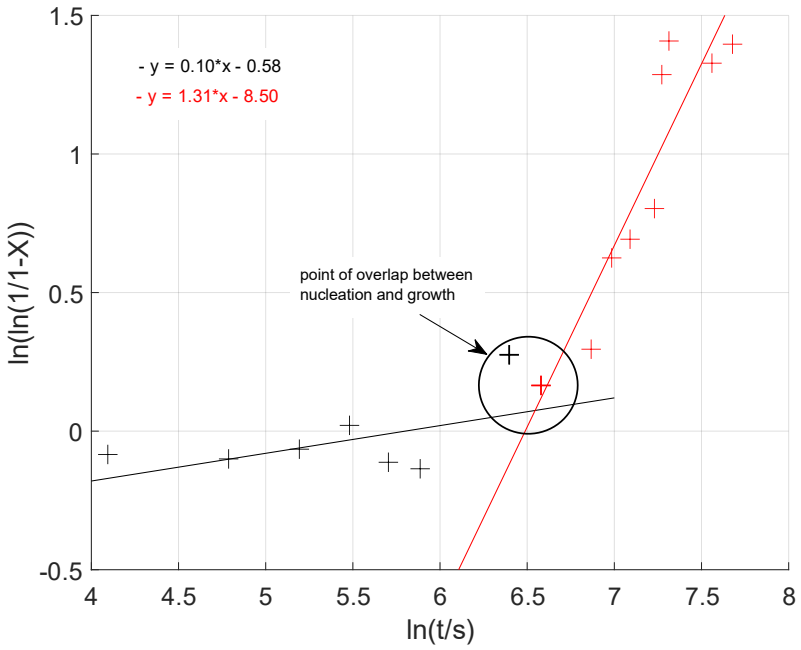

Figure 6.10: JMAK model applied to the SE data collection during the ferrite / pearlite to austenite phase transformation at 800 °C. The model indicates two distinct kinetics of nucleation and growth governing the phase transition.

6.3.5 Martensite to Austenite Phase Change Data

Due to the success of the thermal etching technique in capturing and quantifying the ferrite / pearlite to austenite phase change, this methodology was also applied to samples with an initial martensite microstructure. Figure 6.6.11depicts the rapid evolution of martensite into the austenitic phase. The initial SE image, Figure 6.6.11a, presents the martensite sample after it has been chemically etched prior to being re-polished and subsequently heated. The image provides a scale and comparison of the initial martensite laths. Figure 6.6.11b shows the sample at room temperature preheating, where you can see the presence of precipitates (circled in white). Once the sample reaches temperature (Figure 6.6.11c), some preliminary thermal etches are beginning to form (shown by the white arrow). After an additional 10 minutes of heating (Figure 6.6.11d), the presence of significantly smaller outlined grain boundaries, is observed (as indicated by the green arrow), alongside some small artefacts (a selection of which are circled in red).

After 17 minutes at 800 °C (Figure 6.6.11e), the number of small grains has increased significantly. New grains are shown by the blue arrows, and the small artefacts appear to have grown. Figure 6.6.11f, at 30 minutes, shows little change in the number of small grains present within the original martensite laths, but the thermal etching has made the grains slightly more easily identifiable. At the end of the heating time (60 minutes), Figure 6.6.11g indicates that there is still no further change in the small grains, although the small artefacts have begun to glow bright white, likely due to a combination of oxidation and charging within the microscope. Thus, the SE data indicates a very rapid initial phase transformation where the small grains form followed by a second, possibly surface transformation, characterised by the evolution of the small artefacts.

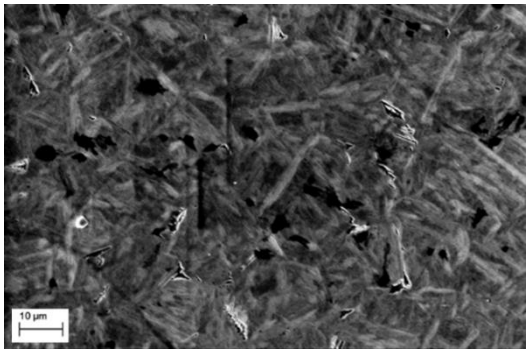

(a) Room Temperature, Chemical Etch

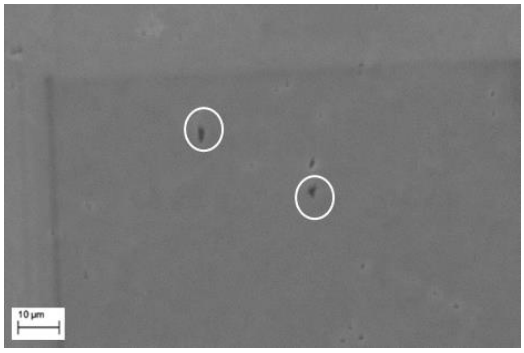

(b) Room Temperature, Polished

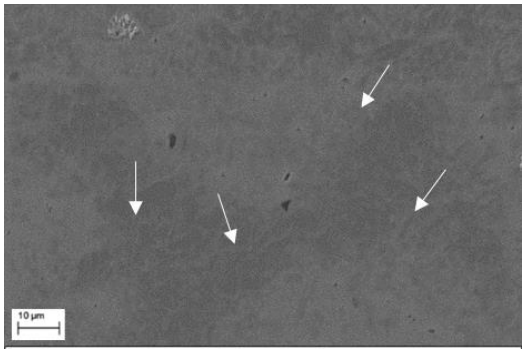

(c) 800 °C, 5 minutes

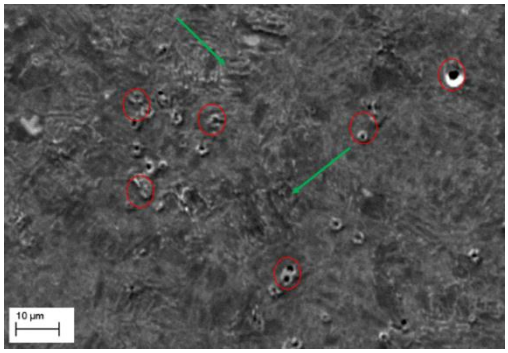

(d) 800 °C, 14 minutes

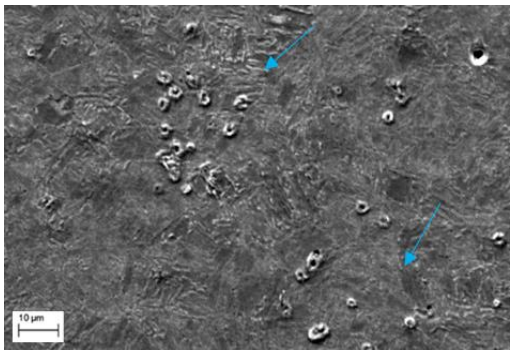

(e) 800 °C, 17 minutes

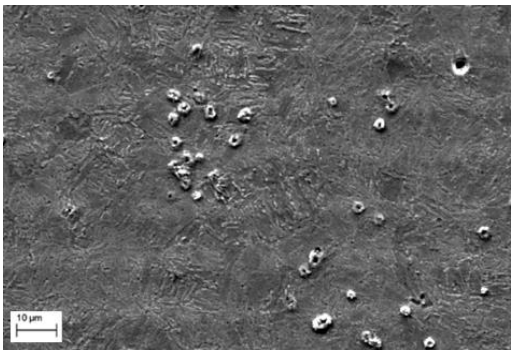

(f) 800 °C, 30 minutes

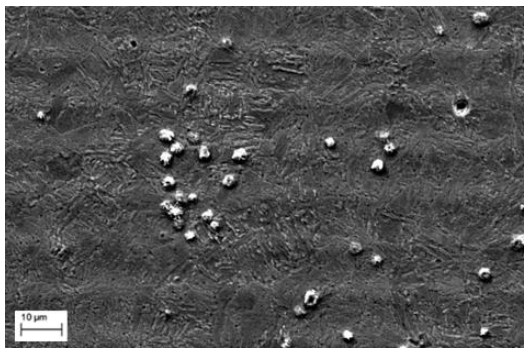

(g) 800 °C, 60 minutes

Figure 6.6.11: In situ *SE images of martensite to austenite reverse phase transformation.*

To understand the possible compositional evolution taking place on the surface of the sample, EDX results were collected before and after the *in situ* heat treatment. Figure 6.12 presents the EDX maps corresponding to the *in situ* heat treatment in Figure 6.6.11. The mapping confirms that some oxidation has occurred during the heat treatment of martensite as there was no oxygen present in the pre-heat treatment mapping (Figure 6.12b and Figure 6.12f). The data obtained before heat treatment, Figure 6.12a, b, c and d suggest that the small artefacts initially visible on the surface are precipitates of concentrated manganese, owing to their presence in Figure 6.12c and their absence in the iron map (Figure 6.12d). This is further supported by the post heat treatment images, which also show these precipitates to be heavy in manganese (Figure 6.12e and Figure 6.12g); a common precipitate in carbon steel that forms during the casting process [27]. However, the content of manganese is considered to be negligible and so has a minimal impact on the phase transformation. Nonetheless, the EDX data does indicate that these precipitates undergo oxidation (Figure 6.12f) and this would account for why these artefacts appear to evolve and glow bright white in the SE image sequence presented in Figure 6.6.11. However, there is negligible change in the EDX chemical composition, as would be expected from this phase change.

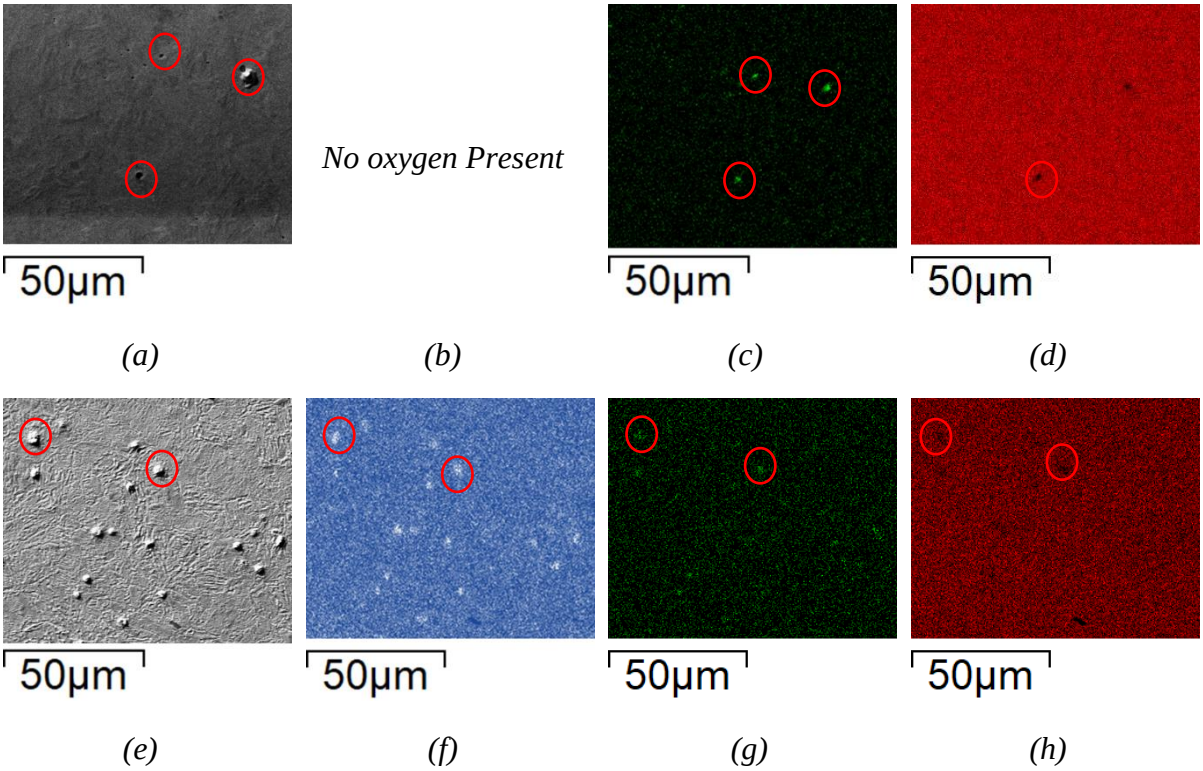

Figure 6.12: EDX data composition shown pre (a-d) and post (e-g) heat treatment of martensitic steel. (a&e) SE image, (b&f) oxygen, (c&g) manganese and (d&h) iron.

6.4 Discussion

6.4.1 Microstructural Evolution of Ferrite / Pearlite to Austenite

Previous *ex situ* microstructural and dilatometry data indicate that the formation of austenite from a ferrite / pearlite microstructure is driven by nucleation and growth, where heterogeneous nucleation begins at the ferrite / pearlite grain boundaries before these nucleating sites begin to grow [236][48]. The most common dynamic model for this two stage process is the JMAK model [237] (Equation 6.1), and by presenting the data in this familiar format; the data in Figure 6.10 supports this theory.

Observations of the SE microstructural images indicate that the individual transformations of nucleation and growth are not solely associated with the two phases, but both phases experience the nucleation and growth process when transforming into austenite as shown by Figure 6.3, Figure 6.4 and Figure 6.5. The SE images suggest that initial formation of austenite is predominantly focused in the pearlite region, as a combination of heterogenous and homogenous nucleation, followed by the rapid growth of austenite nucleation within the pearlite grains, until complete transformation. Additionally, the ferrite to austenite transformation, which appears to begin between 10 and 12 minutes after the pearlite, could either be attributed to the growth of the surrounding austenite grains into the ferrite or due to the heterogeneous nucleation of austenite grains around the ferrite grain boundaries. These observations suggest that the transformation of the ferrite and pearlite phases into austenite does not occur concurrently but has some overlap where both phases are transforming simultaneously.

The complex nature of the starting structure resulting in the apparent overlap of the pearlite / ferrite transition to austenite, like many dynamic processes, is dictated by the most energetically favourable transformation. In general, phase transformations into austenite are

governed by the diffusion of carbon into the newly formed austenite FCC phase, known as soft-impingement [237]. The rate of carbon diffusion is dependent on the ease with which carbon can be extracted from its current phase and hence rearranged into the FCC austenitic phase. The pearlite phase is made up of a lamella of cementite (a carbon rich iron phase of Fe_3C) and ferrite [50], while the pure ferrite phase is a simple BCC structure with interstitial carbon [7]. Thus, the initial nucleation within the pearlite grains, may be due to the higher, less tightly bonded, carbon content within the pearlite phase, which results in a significantly higher carbon diffusion rate. Hence nucleation formation of austenite within pearlite would occur prior to its formation within ferrite grains.

In further support of this observation, studies indicate that the rate of the reverse austenisation correlates positively to the number of boundaries serving as heterogeneous nucleation sites [238][239]. As such, the presence of lamella within the pearlite grains, which act as natural boundaries, would provide a more favourable, and subsequently faster, nucleation site than the uniform ferrite grains. This again indicates the possible reason for initial austenite formation within pearlite followed by ferrite. However, the phase transformations are not distinct, as observed in the current data, as the point at which the austenite nucleation clusters within the pearlite reach such a peak as to lead to growth, may also be the point at which the system has sufficient energy so as to begin transformation of the ferrite grains. The nucleation of austenite at ferrite grain boundaries, followed by the growth of austenite into ferrite, has been modelled and observed in previous studies of pure ferrite to austenite transformation [240][239]. As such, it is considered the likely process by which ferrite-austenite transformation occurs in the ferrite / pearlite starting microstructure.

It is noted that this two-stage process is not clearly characterised by the sigmoidal graph in Figure 6.9, which indicates that pearlite and ferrite are transforming at a similar rate in alignment with the rate of loss of the lighter and darker areas, as the mid grey area

(austenite) grows. However, observation of the SE image indicates that the pearlite grains appear to disappear before ferrite, as shown in Figure 6.3, but thermal etching then proceeds to occur, which initially shows up as darker areas before transforming to lighter oxidised areas. This makes it difficult to interpret the nucleation-growth transformation of ferrite and pearlite from the sigmoidal graph, as the phase data may be skewed by the thermal etching-oxidation transformation occurring simultaneously. Nonetheless, the qualitative examination of SE images, combined with the use of the JMAK model which focuses purely on the austenitic transformation irrespective of starting phase, demonstrates a clear two-stage transformation, that is somewhat dependent on phase. In addition, there is a distinct correlation between the SE images depicting the transition of pearlite to the growth phase, and the point at which the JMAK model becomes growth-driven. Despite the possibility that ferrite experiences some nucleation surrounding its grain boundaries after 12 minutes (the point at which the JMAK model indicates growth is the preferential process), the rate of growth within the pearlite grains at this time will supersede this and so growth becomes the observed dominant process.

6.4.2 Microstructural Evolution of Martensite to Austenite

Examining the martensite to austenite reversion process *in situ* has facilitated the capture of the microstructural formation of small austenitic grains within multiple martensitic laths during heating. This formation has previously been predicted by phase-field models, which suggest that reversion begins at the martensite lath boundaries and then grows inwards [55]. Additionally, more recent TEM *in situ* experiments studying individual grains have also captured the nucleation of austenite within individual grains [54][241], but not across such a large data set as this.

Considering the SE images overall transformation, the data indicate that it occurs over a 3- to 12-minute interval between 5 and 17 minutes, where there is a difference in the number of small grains present (Figure 6.6.11b, c and d). Prior to this, no nucleation appears to be present, and after this time, the only changes captured in the SE images are the growth of specific artefacts (circled in red in Figure 6.6.11). Subsequently, the EDX data in Figure 6.12 confirms that the growth of these artefacts is the oxidation of raised precipitates, but the rest of the surface shows no signs of oxidation during this period. The speed of the phase change coupled with the time taken to capture SE images at temperature, has meant that it is not possible to quantify the phase change with respect to time from these data. Nonetheless, the current dataset provides support to models and studies, which suggest a transformation via the nucleation of austenite within the pre-existing martensite formation.

6.5 Conclusions

This chapter demonstrates the utilisation of conditions that facilitate surface observations representative of the bulk sample, as discussed in Chapter 5. By using appropriate parameters, SE and EBSD *in situ* high-temperature data have been able to capture multi-grain carbon steel phase changes during the transformation. Consequently, the data provide both qualitative and quantitative insight into the mechanisms behind phase formation from ferrite / pearlite and martensite starting structures into austenite.

The process observed within the SE and EBSD images confirms the pearlite / ferrite to austenite phase transformation models, which suggest a nucleation- and growth-driven process. Real-time microstructural evolution SE images indicate that the transformation of the two-phases has a significant overlap in time where the nucleation of the pearlite phase begins initially in a homogeneous formation, followed by heterogeneous nucleation around the ferrite / pearlite grain boundaries. The nucleation processes of both phases lead to rapid growth of the nucleated austenite grains; first, in the pearlite and then second a growth from the edges to the centre in the ferrite grains until complete transformation. Quantification of the SE data in comparison to the JMAK model, combined with the qualitative examination of both SE and EBSD images, supports this multi-phase nucleation and growth theory.

Examination of the martensite to austenite reversion process using *in situ* SE data captured on a large scale (for the first time to the best of the author's knowledge) demonstrates the formation of austenite within the martensitic laths. It is observed that small grains of austenite nucleate within the preformed martensite laths very rapidly and little growth of these grains occurs due to the rapidity of nucleation formation. Post-heating EBSD data and an investigation into the literature further imply the homogeneous nucleation of these small austenite grains within the martensite lath, formed during the heating process. Additionally,

SE imaging *in situ*, supported by *ex situ* EDX data, indicates that during the transformation, small precipitates appear along the surface and these are subject to oxidation despite the vacuum environment. This further demonstrates the need for a combination of microscopy techniques to evaluate the complete microstructural evolution.

Overall, the findings presented in this chapter provide an alternative technique for capturing areas undergoing microstructural evolution during a phase change, which are representative of the bulk of the specimen. The data captured using these techniques clarify the timing and position of austenite formation within a ferrite / pearlite and a martensite starting structure. Hence, this research will improve the understanding of how to adjust these heat treatments to produce more favourable microstructural properties.

Chapter 7

Conclusions & Future Work

7.1 Conclusions

The focus of this research has been on technique, technology and methodology development for high-temperature *in situ* scanning electron microscopy (SEM) imaging. These advances have facilitated studies of microstructural evolution during the heat treatment of carbon steel. The specific microstructural phenomena investigated during carbon steel heat treatment include: the grain growth in the austenitic region, thermal oxidation, and the phase transformation from the starting structures of ferrite / pearlite and martensite to austenite. The fundamental scientific contributions of each of these applications are highlighted below.

7.1.1 *In Situ* SEM High-Temperature Stage Development

A novel stand-alone heat stage, for use within an SEM, has been developed and tested. The stage enables imaging at elevated temperatures, up to 850 °C for an electron backscatter diffraction (EBSD) detector and 920 °C for a secondary electron (SE) detector, without the need for shielding or detector modifications. Extensive testing concluded both the heat stage button heater and SEM vacuum were stable up to these temperatures for heat treatment cycles of at least 8 hours long.

To optimise for imaging conditions, the stage included a purpose-built mounting and cooling system to facilitate a good working distance for both SE and EBSD imaging, while avoiding overheating of the detectors. Owing to the proximity of the EBSD detector to the specimen, the EBSD detector was also retracted between scans to allow it to cool. In addition,

the size and position of the specimen was also designed to sit directly over the heater at the highest point on the stage, which had a dual purpose of minimising excess heating emissions from the heater, while also ensuring the specimen did not experience shadowing from the rest of the stage.

Overall, these unique design features coupled with a PID controller meant that this new heat stage was able to overcome some of the challenges of high-temperature *in situ* SEM imaging including, thermal interference, detector overheating, vacuum instability, poor working distance, and shadowing. Due to the positive result of the heat stage, further collaboration with Deben UK Ltd also led to the development of an *in situ* thermo-mechanical stage. These unique contributions show key progress in technology advancement for *in situ* SEM high-temperature imaging.

7.1.2 *In Situ* High-Temperature SEM Imaging Observations

Investigations into high-temperature imaging of both nickel and steel demonstrated important impacts of material behaviour on the ability to image at high-temperature using both EBSD and SE detectors. For EBSD imaging, results showed a loss of image clarity at temperatures around the Curie temperature transition (a magnetic transformation from ferromagnetic to paramagnetic). In addition, EBSD image quality was also affected when heating steel for an extensive period of time (>1 hour), during which time an increase in surface roughness occurred that was greater than the typical depth of the steel interaction volume for EBSD. This increase was attributed to a combination of thermal etching, microstructural evolution and oxidation. Furthermore, the quantification of the sample roughness, led to an understanding of the sample preparation stages required to image EBSD at high-temperature.

The presence of *in situ* thermal etching facilitated tracking of surface microstructural evolution using SE imaging. Investigations were conducted to identify the parameters required to ensure that microstructural changes observed on the surface, via thermal etching, were representative of the bulk of the specimen; these focused on the heat treatment of carbon steel. The data demonstrated that the difference in surface and bulk grain growth of steel, could be attributed to the formation of oxidation within the thermally etched grain boundaries, which caused a phenomenon not dissimilar to the Zener pinning effect. However, results showed that heat treatments conducted for less than 1 hour at 800 °C were representative of the bulk of the specimen. Hence, these were the parameters used for the fundamental application studies of microstructural evolution in this thesis.

7.1.3 Microstructural Evolution During Heat Treatment of Carbon Steel

The applications of these novel high-temperature *in situ* SEM techniques have focused on the heat treatment of carbon steel. During the heat treatment, the following microstructural changes were investigated.

In situ Grain Growth in the Austenitic Region

Examination of the *in situ* SE data at 800 °C facilitated tracking of grain growth during the ferrite to austenite phase change and within the austenitic region of carbon steel. The data suggested that microstructural evolution during this transformation could be described by abnormal grain growth. This was based on the linearity of the results detailed in this thesis, as well as the visible shrinkage in the SE images of the ferrite grains at the expense of the austenite phase formation; a microstructural development not previously observed.

Thermal Oxidation Formation

Formation of thermal oxidation during heat treatment of carbon steel was observed using *in situ* SE imaging. Data indicated that formation occurred by oxidation at the thermally

etched grain boundaries followed by subsequent agglomeration of oxide nodules. These nodules initially formed discrete oxide scales before eventually amalgamating to form a uniform oxide layer. The lack of blistering, which would be expected at these temperatures and time scales, indicated that either: multiple oxide layers are necessary for blistering to occur (indicating the lack of layers in this heat treatment), or a gaseous layer is required not only to support the blister and prevent collapse / healing but also to facilitate its formation in the first place. Based on these results, it was considered that under these heat treatment conditions the oxide composition was predominantly wüstite.

Ferrite / Pearlite to Austenite Phase Transformation

A combination of SE and EBSD *in situ* high-temperature data provided both qualitative and quantitative insight into the mechanisms behind phase formation from ferrite / pearlite to austenite. The process confirms the ferrite / pearlite to austenite phase transformation is driven by nucleation and growth. Furthermore, real-time microstructural evolution SE images provided a timeline for the transformation of phases, which suggested nucleation of the austenite phase within the pearlite phase began initially in a homogeneous formation followed by heterogeneous nucleation around the ferrite / pearlite grain boundaries. Both phase nucleation processes led to rapid growth of the nucleated austenite grains; first, throughout the pearlite grains, and then second, from the edges to the centre of the ferrite grains until complete transformation. This multi-phase nucleation and growth theory was subsequently supported by quantification of the SE data when compared to the JMAK model.

Martensite to Austenite Phase Transformation

Examination of the martensite to austenite reversion process using *in situ* SE data, captured on a large scale, demonstrated the formation of austenite within the martensite lathes. SE images showed that small grains of austenite appeared to nucleate very rapidly within the pre-formed martensite lathes. Subsequently, little growth of these grains occurred due to the

rapidity of the nucleation. The post-heating EBSD data combined with literature showing short post-heat treatment microstructures, further supported the observation of homogeneous nucleation of these small austenite grains within the martensite lathe formed during the heating process.

7.1.4 Summary

Overall, the findings presented in this thesis demonstrate development and application of alternative techniques and methodologies for capturing multi-grain and phase microstructural evolution during heat treatment. This specifically involved the design and testing of a novel heat stage, which led to the observation of thermal etching. Investigation into the impact of thermal etching on the surface microstructure during carbon steel heat treatment enabled the development of a unique high-temperature SE imaging thermal etching technique. Hence, this technique was used to observe surface microstructural evolution of both grain and phase, which was representative of the bulk of the specimen, during the holding stage of the carbon steel heat treatment. The data provided understanding of the timing and position of microstructural formation and transformation during the heat treatment of carbon steel. Hence, these techniques could be used to optimise heat treatments to produce more favourable microstructural properties. Ultimately, the research conducted in this project has laid the foundations for future, fundamental and industrially-relevant, research into the complex material behaviours that occur during the high-temperature microstructural evolution of alloys.

7.2 Future Work

7.2.1 Industry Focussed

The work presented in this thesis demonstrate the development, testing and applications of a standalone heat stage for use within the SEM up to temperatures of 920 °C. Due to the success of this heat stage, research was subsequently conducted on the preliminary design and testing of a combined thermo-mechanical stage. From this, future industrial development will focus on the *in situ* high-temperature imaging capabilities of the combined thermo-mechanical stage (not dissimilar to that conducted on the heat stage in Chapter 4) to ensure the vacuum is stable, the stage is sufficiently cooled and that good quality images can be produced. The combined thermo-mechanical stage will subsequently be used to track dynamic processes at high-temperature within the SEM; specific areas for fundamental research using this stage are discussed in Section 7.2.2.

7.2.2 Fundamental Research Focussed

The development of the novel heat stage, detailed in this thesis, led to an in depth study on the heat treatment of carbon steel, which focused on phase, grain and surface changes at temperatures from 800 to 920 °C. The success of this study indicates the wealth of applications that the novel heat stage could be used for to examine dynamic processes in metals and alloys. Based on the conclusions of this project, three areas for further investigation are suggested.

1. The project focused on phase transformation into the austenitic region of carbon steel from two starting structures: martensite and ferrite / pearlite, at temperatures of 800 °C. The investigation used a combination of high-temperature SE and EBSD imaging techniques that could be used to examine other steel phase transformations. One specific example is the heat treatment of 0.8 wt.% carbon steel at the eutectoid

point, which occurs at 723 °C for 0.8 wt.% C. At the eutectoid point the maximum number of allowable solid phases are in equilibrium, until enough time has passed that all but one phase is no longer present; in this case the three phases are austenite, ferrite and Fe_3C. Collection of real-time data at this point using the thermal etching high-temperature SEM imaging methodology would enable capture of a statistically significant number of grains. This would provide an understanding of the time and temperature dependence of this point and hence how the microstructure could be controlled to produce an ideal percentage of each phase. This is just one example of the many phase transformations and heat treatments that could be observed in steel. Capturing of these transformations would provide a fundamental understanding of how best to control microstructural evolution during heat treatment, which would ultimately produce more favourable material properties.

2. The elevated temperature imaging techniques used for phase changes in steels would also facilitate investigation into the stability of high entropy alloys (HEAs), a novel class of materials currently extensively studied by several research groups worldwide. Due to their high strength offered by a single phase, HEAs have the potential to replace super-alloys in elevated temperature applications. Of particular interest to this project is the Cantor alloy (CoCrFeMnNi), owing to the success of imaging nickel in this research, combined with recent studies of which indicate that the alloy forms an irreversible sigma secondary phase and an $M_{23}C_6$ phase in the form of Cr-rich precipitates after prolonged exposure to elevated temperatures of 700 °C. Furthermore, the secondary phase generation occurs more quickly if the alloy has undergone severe plastic deformation, in which case it becomes visible within 1 hour of heating. Hence, in situ EBSD and SE imaging of this alloy at elevated temperatures

(both in an as cast form and after high pressure torsion) would improve the understanding and provide new data of when and how the secondary phase develop as well as whether it is reversible. This would further strengthen HEA investigations into the reasons for their phase stability despite the number of elements present.

3. A key area of the project has focused on combining the use of SEM imaging at elevated temperatures with mechanical testing, which would allow in-depth studies of the effects of strain rate and temperature on microstructure evolution and mechanical response, respectively. This combination of imaging is highly applicable to the aerospace industry with respect to microstructure development, such as grain boundary sliding and rotation. It has been noted that further understanding of the microstructural effects of super plasticity is required to develop and optimise the material properties. Studies of Ti-64 grain recrystallization at medium strain rates at elevated temperatures, would provide further insight into the mechanisms of grain boundary sliding and grain rotation in super plasticity. The data could then be compared to existing models (e.g. Rachinger grain boundary sliding) and hopefully extended and / or modified to include the novel *in situ* crystallography element.

Bibliography

[1] D. R. Askeland, *The Science and Engineering of Materials*. Stanley Thornes Ltd, 1998.

[2] EDAX, "Welcome to OIM Data Collection," 2013.

[3] S. I. Wright, M. M. Nowell, R. De Kloe, P. Camus, and T. Rampton, "Electron imaging with an EBSD detector," *Ultramicroscopy*, vol. 148, pp. 132–145, 2015.

[4] G. Spanos and W. T. Reynolds, *Microstructure of Metals and Alloys*, Fifth Edit., vol. 1. Elsevier, 2014.

[5] A. Lavakumar, "Crystal Structures," in *Concepts in Physical Metallurgy Concise lecture notes*, IOP Publishing, 2017.

[6] H. Clemens, S. Mayer, and C. Scheu, "Microstructure and Properties of Engineering Materials," in *Neutrons and Synchrotron Radiation in Engineering Materials Science*, Weinheim, Germany: Wiley-VCH Verlag GmbH & Co. KGaA, 2017, pp. 1–20.

[7] E. Pereloman and D. V. Edmonds, *Phase transformations in steels. Volume 1: Fundamentals and diffusion-controlled transformations*. Woodhead Publishing, 2012.

[8] M. McLean, *Encyclopedia of materials science and technology*, vol. 31, no. 1. Elsevier, 1986.

[9] D. Mogk, "Gibbs' Phase Rule: Where it all Begins," 2021. [Online]. Available: http://serc.carleton.edu/research_education/equilibria/phaserule.html.

[10] B. Cantor, "High-Entropy Alloys," in *Encyclopedia of Materials: Science and Technology*, Elsevier, 2011, pp. 1–3.

[11] T. Sourmail, P. Opdenacker, G. Hopkin, and H. K. D. H. Bhadeshia, "Metals and Alloys Annealing Twins," *Univ. Cambridge-shows twin boundarys*, pp. 1–7, 2014.

[12] E. O. J.S. Koehler, F. Seitz, W.T. read, W. Shockley, *Dislocations in Metals*. The American Institue of Minig and Metallurgy Engineers, 1954.

[13] ThermoFisher Scientific, "Product specification: Nickel Foil," 2020.

[14] A. M. Howatson, P. G. Lund, and J. D. Todd, "Engineering Tables and Data," *Eng. Tables Data*, no. April, 1972, doi: 10.1007/978-94-010-9314-9.

[15] V. Rothová, M. Svoboda, and J. Buršík, "The effect of annealing conditions on grain growth and microstructure in nickel," *Met. 2009 - 18th Int. Conf. Metall. Mater. Conf. Proc.*, no. January, pp. 473–480, 2009.

[16] "Nickel - Properties, Fabrication and Applications." [Online]. Available: https://www.azom.com/article.aspx?ArticleID=2193. [Accessed: 23-Jun-2020].

[17] "Commercially pure nickel alloys." [Online]. Available: http://www.substech.com/dokuwiki/doku.php?id=commercially_pure_nickel_alloys. [Accessed: 22-Mar-2021].

[18] M. Bruckard, "Adding carbon to steel makes it harder and stronger. Is this true for all metals?," *PhysLink.com*. [Online]. Available: https://www.physlink.com/education/askexperts/ae341.cfm. [Accessed: 16-Jun-2020].

[19] A. H. W. N. R.E. Smallman, *Modern Physical Metallurgy*, no. 2013. 2019.

[20] M. Mamlouk and J. Zniewski, *Materials For Civil And Construction Engineers*, 4th editio.

Pearson, 2017.

[21] A. Velling, “Iron-Carbon Phase Diagram Explained,” *Fractory*. 2020.

[22] John D. Verhoeven, *Steel Metallurgy for the Non-Metallurgist*. ASTM International, 2007.

[23] M. Knyazeva and M. Pohl, “Duplex Steels: Part I: Genesis, Formation, Structure,” *Metallogr. Microstruct. Anal.*, vol. 2, no. 2, pp. 113–121, Apr. 2013, doi: 10.1007/s13632-013-0066-8.

[24] M. G. Pujar, U. K. Mudali, R. K. Dayal, and T. P. S. Gill, “Susceptibility of as-welded and thermally aged type 316LN weldments toward pitting and intergranular corrosion,” *Corrosion*, vol. 48, no. 7, pp. 579–586, 1992, doi: 10.5006/1.3315975.

[25] A. Kapito, R. J. Mostert, W. E. Stumpf, and C. W. Siyasiya, “Carbide-free bainitic steels for rail wheel applications,” in *IOP Conference Series: Materials Science and Engineering*, 2019, vol. 655, no. 1, doi: 10.1088/1757-899X/655/1/012012.

[26] S. Hamada, D. Sasaki, M. Ueda, and H. Noguchi, “Fatigue limit evaluation considering crack initiation for lamellar pearlitic steel,” in *Procedia Engineering*, 2011, vol. 10, pp. 1467–1472, doi: 10.1016/j.proeng.2011.04.245.

[27] M. K. Banerjee, *Fundamentals of Heat Treating Metals and Alloys*, vol. 2–3. Elsevier Ltd., 2017.

[28] Z. Liu *et al.*, “The effect of heat treatment on the hardness and impact properties of medium carbon steel,” *IOP Conf. Ser. Mater. Sci. Eng.*, vol. 114, 2016, doi: 10.1088/1757-899X/114/1/012108.

[29] R. Manna, “Time Temperature Transformation (TTT) Diagrams,” 2011.

[30] J. L. Dossett and H. E. Boyer, *Practical Heat Treating*, 2nd editio. ASM International, 2006.

[31] S. S. Sharma, P. R. Prabhu, and R. Chadaga, “Thermal treatments & characteristics study on unalloyed structural (AISI 1140) steel,” *Int. J. Mech. Mechatronics Eng.*, vol. 4, no. 10, pp. 1072–1077, 2010.

[32] TWI, “Martensite Formation.” [Online]. Available: https://www.twi-global.com/technical-knowledge/faqs/faq-what-are-the-microstructural-constituents-austenite-martensite-bainite-pearlite-and-ferrite. [Accessed: 14-Jul-2020].

[33] M. Azene, *Introduction to Materials Science*. 1989.

[34] E. Belin-Ferré, *Basics of Thermodynamics and Phase Transitions in Complex Intermetallics*. 2008.

[35] C. Cayron, “One-step model of the face-centred-cubic to body-centred-cubic martensitic transformation,” *Acta Crystallogr. Sect. A*, vol. A69, pp. 498–509, 2013, doi: 10.1107/S0108767313019016.

[36] V. M. Gundyrev, V. I. Zel’dovich, and V. M. Schastlivtsev, “Crystallographic Analysis of the Martensitic Transformation in Medium-Carbon Steel with Packet Martensite,” *Fiz. Met. i Metalloved.*, vol. 117, no. 10, pp. 1052–1062, 2016, doi: 10.1134/S0031918X16100100.

[37] M. J. Starink, “Kinetic equations for diffusion-controlled precipitation reactions,” *J. Mater. Sci.*, vol. 32, no. 15, pp. 4061–4070, Aug. 1997, doi: 10.1023/A:1018649823542.

[38] M. Avrami and M. Vrami, “Kinetics of Phase Change. I: General Theory,” *J. Chem. Phys. 7*, vol. 12, no. 12, pp. 1103–1112, Dec. 1939, doi: 10.1063/1.1750380.

[39] H. Li, K. Gai, L. He, C. Zhang, H. Cui, and M. Li, “Non-isothermal phase-transformation kinetics model for evaluating the austenization of 55CrMo steel based on Johnson-Mehl-Avrami equation,” *Mater. Des.*, vol. 92, pp. 731–741, Feb. 2016, doi:

10.1016/j.matdes.2015.12.110.

[40] J. B. Austin and R. L. Rickett, "Kinetics of the decomposition of austenite at constant temperature," *Trans. Am. lnst. Min. Engrs,* vol. 135, p. 396, 1939.

[41] S. E. Offerman *et al.*, "Grain nucleation and growth during phase transformations," *Science (80-.).*, vol. 298, no. 5595, pp. 1003–1005, Nov. 2002, doi: 10.1126/science.1076681.

[42] E. Erişir, O. G. Bilir, and M. Sezen, "A Study of Microstructure and Phase Transformations of Medium-Carbon Dual-Phase Steels," in *TMS 2015 144th Annual Meeting & Exhibition*, Springer International Publishing, 2015, pp. 1417–1423.

[43] J. E. Garcia-Gonzalez, "Fundamental study of the austenite formation and decomposition in low-Si, Al added trip Steels.," University of Pittsburgh, 2005.

[44] J. W. Cahn, "The kinetics of grain boundary nucleated reactions," *Acta Metall.*, vol. 4, no. 5, pp. 449–459, Sep. 1956, doi: 10.1016/0001-6160(56)90041-4.

[45] T. Fukino and S. Tsurekawa, "In-Situ SEM/EBSD Observation of alpha /gamma Phase Transformation in Fe-Ni Alloy," *Mater. Trans.*, vol. 49, no. 12, pp. 2770–2775, 2008, doi: 10.2320/matertrans.MAW200824.

[46] I. Lischewski, D. M. Kirch, A. Ziemons, and G. Gottstein, "Investigation of the α - γ - α Phase Transformation in Steel: High-Temperature In Situ EBSD Measurements," *Texture, Stress Microstruct.*, vol. 2008, pp. 1–7, 2008, doi: 10.1155/2008/294508.

[47] A. F. Gourgues-Lorenzon, "Application of electron backscatter diffraction to the study of phase transformations," *Int. Mater. Rev.*, vol. 52, no. 2, pp. 65–128, 2007, doi: 10.1179/174328007x160254.

[48] F. L. G. G. Oliveira, M. S. Andrade, and A. B. Cota, "Kinetics of austenite formation during continuous heating in a low carbon steel," *Mater. Charact.*, vol. 58, no. 3, pp. 256–261, Mar. 2007, doi: 10.1016/j.matchar.2006.04.027.

[49] H. Smith and D. R. F. West, "The reversion of martensite to austenite in certain stainless steels," *J. Mater. Sci.*, vol. 8, no. 10, pp. 1413–1420, Oct. 1973, doi: 10.1007/BF00551664.

[50] C. Zhang, L. Zhou, X. Liu, X. Wu, and Y. Liu, "Reverse Transformation from Ferrite/Pearlite to Austenite and Its Influence on Structure Inheritance in Spring Steel 60Si2MnA," *steel Res. Int.*, vol. 85, no. 10, pp. 1453–1458, Oct. 2014, doi: 10.1002/srin.201300386.

[51] H. Farahani, G. Zijlstra, M. G. Mecozzi, V. Ocelík, J. T. M. De Hosson, and S. van der Zwaag, "*In Situ* High-Temperature EBSD and 3D Phase Field Studies of the Austenite–Ferrite Transformation in a Medium Mn Steel," *Microsc. Microanal.*, vol. 25, no. 3, pp. 639–655, Jun. 2019, doi: 10.1017/S143192761900031X.

[52] D. Raabe *et al.*, "Segregation engineering enables nanoscale martensite to austenite phase transformation at grain boundaries: A pathway to ductile martensite," *Acta Mater.*, vol. 61, no. 16, pp. 6132–6152, 2013, doi: 10.1016/j.actamat.2013.06.055.

[53] K. B. Guy, E. P. Butler, and D. R. F. West, "Reversion of bcc alpha' martensite in Fe-Cr-ni austenitic stainless steels," *Met. Sci.*, vol. 17, no. April, pp. 167–176, 1983.

[54] Y. K. Lee, H. C. Shin, D. S. Leem, J. Y. Choi, W. Jin, and C. S. Choi, "Reverse transformation mechanism of martensite to austenite and amount of retained austenite after reverse transformation in Fe - 3Si - 13Cr - 7Ni (wt-%) martensitic stainless steel," *Mater. Sci. Technol.*, vol. 19, no. 3, pp. 393–398, Mar. 2003, doi: 10.1179/026708303225009742.

[55] H. K. Yeddu, T. Lookman, and A. Saxena, "Reverse phase transformation of martensite to austenite in stainless steels: A 3D phase-field study," *J. Mater. Sci.*, vol. 49, no. 10, pp. 3642–3651, May 2014, doi: 10.1007/s10853-014-8067-9.

[56] D. E. Laughlin, “Magnetic Transformations and Phase Diagrams,” *Metall. Mater. Trans. A Phys. Metall. Mater. Sci.*, vol. 50, no. 6, pp. 2555–2569, Jun. 2019, doi: 10.1007/s11661-019-05214-z.

[57] P. Weiss and R. Forrer, “Aimantation et phénomène magnétocalorique du nickel,” *Ann. Phys. (Paris).*, vol. 10, no. 5, pp. 153–213, Apr. 1926, doi: 10.1051/anphys/192610050153.

[58] Encyclopedia Britannica, “Physics: Ferromagnetism.” [Online]. Available: https://www.britannica.com/science/ferromagnetism. [Accessed: 10-May-2019].

[59] G. Jaeger, “The Ehrenfest Classification of Phase Transitions : Introduction and Evolution,” *Arch. Hist. Exact Sci.*, no. May, 1998, doi: 10.1007/s004070050021.

[60] B. Legendre and M. Sghaier, “Curie temperature of nickel,” *J. Therm. Anal. Calorim.*, vol. 105, pp. 141–143, 2011, doi: 10.1007/s10973-011-1448-2.

[61] D. A. . Bradbury and D. M. Edwards, “The temperature dependence of the magnetization of Nickel,” *Phys. Lett.*, vol. 30, no. 5, pp. 301–302, 1969.

[62] P. A. Tipler and G. Mosca, *Physics for scientists and engineers.*, 5th ed. Orlando: Saunders College Publishing, 2003.

[63] C. Y. Jeong, K. J. Kim, H. U. Hong, and S. W. Nam, “Effects of aging temperature and grain size on the formation of serrated grain boundaries in an AISI 316 stainless steel,” *Mater. Chem. Phys.*, vol. 139, no. 1, pp. 27–33, 2013, doi: 10.1016/j.matchemphys.2012.11.021.

[64] S. Illescas, J. Fernández, and J. M. Guilemany, “Kinetic analysis of the austenitic grain growth in HSLA steel with a low carbon content,” *Mater. Lett.*, vol. 62, pp. 3478–3480, 2008, doi: 10.1016/j.matlet.2008.03.001.

[65] D. Burke, J.E. and Turnbull, “Recrystallization and grain growth,” *Prog. Met. Phys.*, pp. 220–292, 1952.

[66] A. Giumelli, “Austenite grain growth kinetics and the grain size distribution,” The university of British Columbia, 1995.

[67] M. P. Anderson, D. J. Srolovitz, G. S. Grest, and P. S. Sahni, “Computer simulation of grain growth-I. Kinetics,” *Acta Metall.*, vol. 32, no. 5, pp. 783–791, May 1984, doi: 10.1016/0001-6160(84)90151-2.

[68] P. Feltham, “Grain growth in metals,” *Acta Metall.*, vol. 5, no. 2, pp. 97–105, Feb. 1957, doi: 10.1016/0001-6160(57)90136-0.

[69] H. V. Atkinson, “Overview no. 65. Theories of normal grain growth in pure single phase systems,” *Acta Metall.*, vol. 36, no. 3, pp. 469–491, 1988, doi: 10.1016/0001-6160(88)90079-X.

[70] D. Dong, F. Chen, and Z. Cui, “Modeling of Austenite Grain Growth During Austenitization in a Low Alloy Steel,” *J. Mater. Eng. Perform.*, vol. 25, no. 1, pp. 152–164, 2016, doi: 10.1007/s11665-015-1810-9.

[71] P. A. Beck, M. L. Holzworth, and H. Hu, “Instantaneous rates of grain growth [15],” *Physical Review*, vol. 73, no. 5. American Physical Society, pp. 526–527, 01-Mar-1948, doi: 10.1103/PhysRev.73.526.

[72] H. Hu and B. B. Rath, “On the time exponent in isothermal grain growth,” *Metall. Trans.*, vol. 1, no. 11, pp. 3181–3184, Nov. 1970, doi: 10.1007/BF03038435.

[73] P. A. Beck, J. C. Kremer, and L. Demer, “Grain growth in high purity aluminum [10],” *Physical Review*, vol. 71, no. 8. American Physical Society, p. 555, 15-Apr-1947, doi: 10.1103/PhysRev.71.555.

[74] F. J. Humphreys and M. Hatherly, *Recrystallization and related annealing phenomena*. Elsevier, 2004.

[75] B. K. Kad and P. M. Hazzledine, "Monte Carlo simulations of grain growth and Zener pinning," *Mater. Sci. Eng. A*, vol. 238, no. 1, pp. 70–77, Oct. 1997, doi: 10.1016/S0921-5093(97)00435-8.

[76] V. Randle and B. Ralph, "Interactions of grain boundaries with coherent precipitates during grain growth," *Acta Metall.*, vol. 34, no. 5, pp. 891–898, May 1986, doi: 10.1016/0001-6160(86)90062-3.

[77] G. Parker, *Encyclopia of Materials: Science and Technology*. Elsevier, 2001.

[78] B. Fernando, A. Lasagni, G. C. Requena, and E. A. Soppa, "In Situ Measurements of Local Strain in Heterogeneous Materials," *Adv. Eng. Mater.*, vol. 10, no. 1, pp. 73–78, 2008, doi: 10.1002/adem.200700250.

[79] K. Shin, D. Chung, and S. Lee, "The Effect of Consolidation Temperature on Microstructure and Mechanical Properties in Powder Metallurgy – Processed 2XXX Aluminum Alloy Composites Reinforced with SiC Particulates," *Metall. Mater. Trans. A*, vol. 28A, no. December, pp. 2625–2636, 1997.

[80] H. Farahani, G. Zijlstra, M. G. Mecozzi, V. Ocelík, J. T. M. De Hosson, and S. Van Der Zwaag, "In Situ High-Temperature EBSD and 3D Phase Field Studies of the Austenite-Ferrite Transformation in a Medium Mn Steel," *Microsc. Microanal.*, no. April, 2019, doi: 10.1017/S143192761900031X.

[81] W. W. Mullins, "Theory of Thermal Grooving," *J. Appl. Phys.*, vol. 333, no. 1957, pp. 333–339, 1986, doi: 10.1063/1.1722742.

[82] O. Akyildiz and T. O. Ogurtani, "Thermal Grooving by Surface Diffusion: a Review of Classical Thermo-Kinetics Approach," *Hittite J. Sci. Eng.*, vol. 4, no. 1, pp. 7–16, 2017, doi: 10.17350/hjse19030000042.

[83] W. . Mullins, "The effect of thermal grooving on grain boundary motion," *Acta Metall.*, vol. 6, no. 6, pp. 414–427, Jun. 1958, doi: 10.1016/0001-6160(58)90020-8.

[84] D.J. Allen, "Thermal Grooving at migrating grain boundaries," *Scr. Metall.*, vol. 16, no. 1, pp. 5–9, 1982.

[85] Y. Zhang, A. Godfrey, and D. Juul Jensen, "Kinetics of thermal grooving during low temperature recrystallization of pure aluminum," *Mater. Sci. Forum*, vol. 753, pp. 117–120, 2013, doi: 10.4028/www.scientific.net/MSF.753.117.

[86] P. Sachenko, J. H. Schneibel, and W. Zhang, "Effect of faceting on the thermal grain-boundary grooving of tungsten," *Philos. Mag. A Phys. Condens. Matter, Struct. Defects Mech. Prop.*, vol. 82, no. 4, pp. 815–829, 2002, doi: 10.1080/01418610208243204.

[87] V. Y. Aristov, V. Y. Fradkov, and L. S. Shvindlerman, "Interaction of moving grain boundary with a crystal surface.," *Phys. Met. Metallogr.*, vol. 45, no. 5, pp. 83–94, 1978.

[88] P. Sachenko, J. H. Schneibel, and W. Zhang, "A Effect of faceting on the thermal grain-boundary grooving of tungsten," *Philos. Mag.*, vol. 82, no. 4, pp. 815–829, 2009, doi: 10.1080/01418610208243204.

[89] R. Strassberg, L. Klinger, Y. Kauffmann, and E. Rabkin, "Grain growth inhibition in thin nanocrystalline Au films by grain boundary diffusion and oxidation of Ti," *Acta Mater.*, vol. 61, no. 2, pp. 529–539, 2013, doi: 10.1016/j.actamat.2012.09.076.

[90] H. D. Merchant, "Oxidation Kinetics of Iron-Carbon Base Alloys," *Oxid. Met.*, vol. 2, no. 2, pp. 145–153, 1970.

[91] N. B. Pilling and R. E. Bedworth, “Oxidation of Copper-Nickel Alloys at High Temperature,” *Ind. Eng. Chem.*, vol. 27, no. 4, pp. 372–376, 1925.

[92] R. Y. Chen and W. Y. D. Yuen, “Review of the high-temperature oxidation of iron and carbon steels in air or oxygen,” *Oxidation of Metals*, vol. 59, no. 5–6. pp. 433–468, Jun-2003, doi: 10.1023/A:1023685905159.

[93] R. Haugsrud, “On the high-temperature oxidation of nickel,” *Corros. Sci.*, vol. 45, no. 1, pp. 211–235, 2003, doi: 10.1016/S0010-938X(02)00085-9.

[94] D. Caplan, R. J. Hussey, G. I. Sproule, and M. J. Graham, “Effect of carbon on cavity formation during the high-temperature oxidation of Ni,” *Oxid. Met.*, vol. 14, no. 4, pp. 279–299, 1980, doi: 10.1007/BF00603786.

[95] J. S. Sheasby, W. E. Boggs, and E. T. Turkdogan, “Scale growth on steels at 1200°C: rationale of rate and morphology,” *Met. Sci.*, vol. 18, no. 3, pp. 1–10, 1984, doi: 10.1179/msc.1984.18.3.127.

[96] R. Griffiths, “The Blistering of Iron Oxide Scales and the Conditions for the Formation of a Non-adherent Scale,” *J. iron steel Inst.*, vol. 130, 1934.

[97] H. Engell and F. Wever, “Über einige grundfragen der bildung und der haftung von zunder auf eisen,” *Acta Metall.*, vol. 5, no. 12, pp. 695–702, Dec. 1957, doi: 10.1016/0001-6160(57)90071-8.

[98] F. Matsuno, “Blistering and Hydraulic Removability of Scale Films of Rimmed Steel At High Temperature.,” *Tetsu To Hagane*, vol. 65, no. 6, pp. 599–607, 1979, doi: 10.2355/tetsutohagane1955.65.6_599.

[99] Y. Kondo, H. Tanei, N. Suzuki, K. Ushioda, and M. Maeda, “Blistering Behavior during Oxide Scale Formation on Steel Surface,” *ISIJ Int.*, vol. 51, no. 10, pp. 1696–1702, 2011.

[100] Bodycote Plc, “Vacuum heat treatment-Technical glossary,” 2019. [Online]. Available: https://www.bodycote.com/technical-glossary/vacuum-heat-treatment/. [Accessed: 29-Apr-2020].

[101] Y. Feng, H. Yu, Z. Luo, G. Xie, and R. Misra, “The Impact of Surface Treatment and Degree of Vacuum on the Interface and Mechanical Properties of Stainless Steel Clad Plate,” *Materials (Basel).*, vol. 11, no. 9, p. 1489, Aug. 2018, doi: 10.3390/ma11091489.

[102] H. Abuluwefa, J. H. Root, R. I. L. Guthrie, and F. Ajersch, “Real-time observations of the oxidation of mild steel at high temperature by neutron diffraction,” *Metall. Mater. Trans. B Process Metall. Mater. Process. Sci.*, vol. 27, no. 6, pp. 993–997, 1996, doi: 10.1007/s11663-996-0014-y.

[103] W. M. Melfo and R. J. Dippenaar, “In situ observations of early oxide formation in steel under hot-rolling conditions,” *J. Microsc.*, vol. 225, no. 2, pp. 147–155, Feb. 2007, doi: 10.1111/j.1365-2818.2007.01726.

[104] M. E. Story and B. A. Webler, “Evolution of Near-Surface Internal and External Oxide Morphology During High-Temperature Selective Oxidation of Steels,” *J. Miner. Met. Mater. Soc.*, vol. 70, no. 7, pp. 1225–1231, Jul. 2018, doi: 10.1007/s11837-018-2885-1.

[105] J. Rydz, A. Šišková, and A. Andicsová Eckstein, “Microscopic Techniques in Materials Science: Current Trends in the Area of Blends, Composites, and Hybrid Materials,” vol. Advances i, 2019, doi: 10.1155/2019/9072958.

[106] C. P. Davis, “Definition of Microscopy,” *Medicine Net*. [Online]. Available: https://www.medicinenet.com/script/main/art.asp?articlekey=13024. [Accessed: 15-Apr-2020].

[107] D. Fields and S. Robertson, “Brief History of Microscopy & Diffraction,” *News Medical*, pp. 1–5, 2019.

[108] L. Cox, “Who Invented the Microscope?,” *Live Science*, 2013. [Online]. Available: https://www.livescience.com/39649-who-invented-the-microscope.html. [Accessed: 19-Oct-2020].

[109] D. Bardell, “The Biologists’ Forum: The invention of the microscope,” *BioOne Complet.*, vol. 75, no. 2, pp. 78–84, May 2004, doi: 10.1893/0005-3155(2004)75<78:tiotm>2.0.co;2.

[110] F. Henderson, “Small Wonders: The invention of microscopy,” *Catalyst*, no. February, pp. 9–12, 2010.

[111] T. G. Rochow, P. A. Tucker, T. G. Rochow, and P. A. Tucker, “A Brief History of Microscopy,” in *Introduction to Microscopy by Means of Light, Electrons, X Rays, or Acoustics*, Springer US, 1994, pp. 1–21.

[112] D. Fields, “What is Transmission Electron Microscopy?,” *News Medical Life Sciences*, 2019. [Online]. Available: https://www.news-medical.net/life-sciences/What-is-Transmission-Electron-Microscopy.aspx. [Accessed: 06-Apr-2021].

[113] M. A. Reina *et al.*, “Electron Microscopy and the Expansion of Regional Anesthesia Knowledge,” *Tech. Reg. Anesth. Pain Manag.*, vol. 6, no. 4, pp. 165–171, Oct. 2002, doi: 10.1053/trap.2002.123512.

[114] M. Z. Knoll, “Aufladen Potentiel und Sekundäremission elektronen bestrahlter Körper,” *Tech. Phys.*, 1935.

[115] M. Z. Von Ardenne, “The scanning electron microscope: Theoretical fundamentals,” *J. Phys.*, 1938.

[116] A. Mohammed and A. Abdullah, “Scanning Electron Microscopy (SEM): a Review,” *Proc. 2018 Int. Conf. Hydraul. Pneum. - HERVEX*, no. January, p. 85, 2018.

[117] V. K. Z. J. H. and R. L. Snyder, “A scanning electron microscope,” *Am. Soc. Test. Mater.*, 1942.

[118] A. N. Broers, “Electron gun using long-life lanthanum hexaboride cathode,” *J. Appl. Phys.*, vol. 38, no. 4, pp. 1991–1992, Mar. 1967, doi: 10.1063/1.1709807.

[119] S. / A. C. publishing Office, “Timeline of SEM development,” *poster*, 2015. [Online]. Available: https://www.sciencemag.org/sites/default/files/custom-publishing/documents/SEM poster_front_0.pdf. [Accessed: 20-Oct-2020].

[120] J. I. Goldstein, D. E. Newbury, J. R. Micahel, N. W. W. Ritchie, J. H. J. Scott, and D. C. Joy, *Scanning Electron Microscopy and X-ray Microanalysis*, Fourth edi. Springer, 2018.

[121] M. I. Szynkowska, *Microscopy Techniques: Scanning Electron Microscopy*, 2nd editio. Elsevier, 2005.

[122] L. Hughes, “Introduction to Biological Electron Microscopy,” *Biological Electron Microscopy*. [Online]. Available: https://www.biologicalelectronmicroscopy.com/introduction-to-biological-electron-microscopy.html. [Accessed: 11-Nov-2020].

[123] “FEG vs. Tungsten source in a scanning electron microscope (SEM): what’s the difference?,” *Lambda News*, 2019. [Online]. Available: https://www.lambdaphoto.co.uk/news/2019/04/26/feg-vs-tungsten-source-in-a-scanning-electron-microscope-sem-whats-the-difference/. [Accessed: 10-Nov-2020].

[124] “Emission stability in SEM thermionic electron sources: CeB6, LaB6 and W filaments,”

Lambda News, 2018. [Online]. Available: https://www.lambdaphoto.co.uk/news/2018/02/22/emission-stability-in-sem-thermionic-electron-sources-ceb6-lab6-and-w-filaments/. [Accessed: 10-Nov-2020].

[125] G. W. Kammlott, "Some aspects of scanning electron microscopy," *Surf. Sci.*, vol. 25, no. 1, pp. 120–146, Mar. 1971, doi: 10.1016/0039-6028(71)90212-3.

[126] AZO Material and Phenom-World BV, "Different Types of SEM Imaging – BSE and Secondary Electron Imaging," *AZO Mater.*, pp. 1–7, 2017.

[127] "Electron Microscopy : Scanning Electron Microscopy," *Thermofisher Scientific*. [Online]. Available: https://www.thermofisher.com/uk/en/home/materials-science/learning-center/applications/sem-electrons.html. [Accessed: 11-Nov-2020].

[128] "How Does EDX Analysis with a Scanning Electron Microscope (SEM) Work?," *AZO Material*, 2018.

[129] S. I. Wright, M. M. Nowell, R. De Kloe, P. Camus, and T. Rampton, "Ultramicroscopy Electron imaging with an EBSD detector," *Ultramicroscopy*, vol. 148, pp. 132–145, 2015, doi: 10.1016/j.ultramic.2014.10.002.

[130] W. Wisniewski and C. Russel, "An experimental viewpoint on the information depth of EBSD;," *Scanning*, vol. 38, pp. 164–171, 2016, doi: 10.1002/sca.21251.

[131] V. H. Bethe, "Bremsformel ffir Elektronen relativistischer Geschwindigkeit," 1932.

[132] K. Kanayat and S. Okayama, "Related content Penetration and energy-loss theory of electrons in solid targets," *J. Phys. D Appl. Phys*, vol. 5, p. 43, 1972.

[133] A. H. Demers, N. Poirier-Demers, A. Réal Couture, D. Joly, M. Guilmain, N. de Jonge and D. Drouin, "Three-dimensional electron microscopy simulation with the CASINO Monte Carlo software.," *Scanning*, vol. 33, no. 3, pp. 135–146, 2011.

[134] D. C. Joy, "Beam interactions, contrast and resolution in the SEM," 1984.

[135] P. Hovington, D. Drouin, and R. Gauvin, "CASINO: A new monte carlo code in C language for electron beam interaction -part I: Description of the program," *Scanning*, vol. 19, no. 1, pp. 1–14, Dec. 1997, doi: 10.1002/sca.4950190101.

[136] F. A. Lukiyanov, E. I. Rau, and R. A. Sennov, "Depth range of primary electrons, electron beam broadening, and spatial resolution in electron-beam studies," *Bull. Russ. Acad. Sci. Phys.*, vol. 73, no. 4, pp. 441–449, 2009, doi: 10.3103/S1062873809040029.

[137] S. Nishikawa and S. Kikuchi, "Diffraction of cathode rays by calcite [4]," *Nature*, vol. 122, no. 3080. Nature Publishing Group, p. 726, 1928, doi: 10.1038/122726a0.

[138] J. A. Venables and C. J. Harland, "Electron back-scattering patterns—a new technique for obtaining crystallographic information in the scanning electron microscope," *Philos. Mag.*, vol. 27, no. 5, pp. 1193–1200, 1973, doi: 10.1080/14786437308225827.

[139] D. J. Dingley, "On-line determination of crystal orientation and texture determination in an SEM," *J. R. Microsc. Soc.*, 1984.

[140] W. Zhou, R. Apkarian, Z. L. Wang, and D. Joy, "Fundamentals of Scanning Electron Microscopy (SEM) Scanning Microscopy for Nanotechnology," in *Scanning Microscopy for Nanotechnology: Techniques and Applications*, Springer New York, 2007, pp. 1–40.

[141] K. Moffat, "Laue diffraction and time-resolved crystallography: a personal history," *Philos. Trans. R. Soc. A Math. Phys. Eng. Sci.*, vol. 377, no. 2147, p. 20180243, Jun. 2019, doi: 10.1098/rsta.2018.0243.

[142] A. J. Schwartz, M. Kumar, B. L. (Brent L. . Adams, D. P. Field, and K. -Lawrence, *Electron Backscatter Diffraction in Materials Science*. Springer, 2009.

[143] A. J. Schwartz, M. Kumar, and B. L. (Brent L. . Adams, *Electron backscatter diffraction in materials science*. Kluwer Academic, 2000.

[144] Oxford Instruments, "About the EBSD Pattern Lecture Series." .

[145] EDAX Report, "Specimen Preparation for Electron Backscatter Diffraction (EBSD) Analysis." .

[146] K. Z. Baba-Kishi, "Scanning reflection electron microscopy of surface topography by diffusely scattered electrons in the scanning electron microscope," *Scanning*, vol. 18, no. 4, pp. 315–321, Dec. 1996, doi: 10.1002/sca.1996.4950180408.

[147] D. P. Schwartz, A.J., Kumar, M., Adams, B.L., Field, *Electron Backscatter Diffraction in Materials Science*. 2009.

[148] S. Aps, "Product Data Sheet," pp. 1–2, 2016.

[149] M. M. Nowell, R. A. Witt, and B. W. True, "EBSD Sample Preparation: Techniques , Tips , and Tricks," *Microsc. Microanal.*, vol. 11, no. S02, pp. 44–48, 2005, doi: 10.1017/S143192760550672X.

[150] E A Fischione Instruments Inc, "Metallic sample preparation for EBSD by mechanical method and argon ion beam milling." pp. 1–5, 2014.

[151] D.-I. Kim, B.-K. Kim, and J.-H. Kim, "Technical Overview on the Electron Backscattered Diffraction Sample Preparation," *Appl. Microsc.*, vol. 45, no. 4, pp. 218–224, 2015, doi: 10.9729/am.2015.45.4.218.

[152] L. Ma, "Comparison of different sample preparation techniques in TEM observation of microstructure of INCONEL alloy 783 subjected to prolonged isothermal exposure," *Micron*, vol. 35, no. 4, pp. 273–279, Jun. 2004, doi: 10.1016/j.micron.2003.10.048.

[153] G. Vander Voort, "Solutions for Materials Preparation, Testing and Analysis Metallographic Preparation for Electron Backscattered Diffraction," 2015.

[154] W. R. B. & N. Hilal, *Atomic Force Microscopy in Process Engineering*. 2009.

[155] L. Koll, P. Tsipouridis, and E. A. Werner, "Preparation of metallic samples for electron backscatter diffraction and its influence on measured misorientation," *J. Microsc.*, vol. 243, no. February, pp. 206–219, 2011, doi: 10.1111/j.1365-2818.2011.03495.x.

[156] A. J. Wilkinson and T. Ben Britton, "Strains , planes , and Electron back scatter diffraction (EBSD) in materials science," *Materialstoday*, vol. 15, no. 9, pp. 366–376, 2012.

[157] T. C. Isabell, P. E. Fischione, C. O'keefe, M. U. Guruz, and V. P. Dravid, "Plasma Cleaning and Its Applications for Electron Microscopy," *Microsc. Microanal.*, vol. 5, pp. 126–135, 1999.

[158] B. Schmid, N. Aas, Ø. Grong, R. Ødegård, Grong, and R. Ødegård, "High-temperature oxidation of nickel and chromium studied with an in-situ environmental scanning electron microscope," *Scanning*, vol. 23, no. 4, pp. 255–266, Dec. 2001, doi: 10.1002/sca.4950230406.

[159] B. Schmid, N. Aas, Ø. Grong, and R. Ødegård, "In situ environmental scanning electron microscope observations of catalytic processes encountered in metal dusting corrosion on iron and nickel," *Appl. Catal. A*, vol. 215, pp. 257–270, 2001.

[160] B. Schmid and N. Aas, "High-Temperature Oxidation of Iron and the Decay ¨ stite Studied with in situ ESEM of Wu," *Oxid. Met.*, vol. 57, no. February, pp. 115–130, 2002.

[161] N. B. C. Kerist, R.E. Loge, S. Jacomet, V. Llorca, "EBSD coupled to SEM in situ annealing for assessing recrystallization and grain growth mechanisms in pure tantalum," *J. Microsc.*, vol. 250, no. 3, pp. 189–199, 2013, doi: 10.1111/jmi.12034.

[162] D. M. Kirch *et al.*, "Laser powered heating stage in a scanning electron microscope for microstructural investigations at elevated temperatures," *Rev. Sci. Instrum.*, vol. 79, no. 4, 2008, doi: 10.1063/1.2908434.

[163] T. Fukino, S. Tsurekawa, and Y. Morizono, "In-situ scanning electron microscopy/electron backscattered diffraction observation of microstructural evolution during α → γ phase transformation in deformed Fe-Ni alloy," *Metall. Mater. Trans. A*, vol. 42, no. 3, pp. 587–593, 2011, doi: 10.1007/s11661-010-0285-4.

[164] H. Marzagui and T. Cutard, "Characterisation of microstructural evolutions in refractory castables by in situ high temperature ESEM," *J. Mater. Process. Technol.*, vol. 156, pp. 1474–1481, 2004, doi: 10.1016/j.jmatprotec.2004.04.365.

[165] G. Zijlstra, M. S. B. Van Daalen, D. I. Vainchtein, V. Ocelík, and J. T. M. De Hosson, "Interphase boundary motion elucidated through in-situ high temperature electron back-scatter diffraction," *Mater. Des.*, vol. 132, pp. 138–147, 2017.

[166] E. Alabort *et al.*, "In - situ high-temperature tensile testing of a polycrystalline nickel-based superalloy," *Mater. High Temp.*, vol. 33, no. 4, pp. 338–345, 2016, doi: 10.1080/09603409.2016.1180857.

[167] H. S. Ubhi, J. Parsons, N. Othen, S. Campbell, R. Poole, and A. Gholinia, "In-situ EBSD Phase Transformation and Recrystallisation," *J. Phys. Conf. Ser.*, vol. 552, 2014, doi: 10.1088/1742-6596/522/1/012011.

[168] W. Wisniewski, C. Bocker, M. Kouli, M. Nagel, and C. Rüssel, "Surface crystallization of fresnoite from a glass studied by hot stage scanning electron microscopy and electron backscatter diffraction," *Cryst. Growth Des.*, vol. 13, no. 8, pp. 3794–3800, 2013, doi: 10.1021/cg4008087.

[169] "gatan website," *https://www.gatan.com/products/sem-specimen-stages*. .

[170] "Kammrath & Weiss," *https://www.kammrath-weiss.com/en/products/*. .

[171] A. Nagy, J. B. Campbell, and D. L. Davidson, "High-temperature, cyclic-loading stage for the scanning electron microscope.," *Rev. Sci. Instrum.*, vol. 55, pp. 778–782, 1984, doi: 10.1109/mspec.1967.5217128.

[172] K. S. Chan, "Fracture and toughening mechanisms in an α2 titanium aluminide alloy," *Metall. Trans. A, Phys. Metall. Mater. Sci.*, vol. 21 A, no. 10, pp. 2687–2699, 1990, doi: 10.1007/BF02646064.

[173] K. S. Chan and Y. W. Kim, "Influence of microstructure on crack-tip micromechanics and fracture behaviors of a two-phase TiAl alloy," *Metall. Trans. A*, vol. 23, no. 6, pp. 1663–1677, 1992, doi: 10.1007/BF02804362.

[174] M. J. Mayo and W. D. Nix, "Direct observation of superplastic flow mechanisms in torsion," *Acta Metall.*, vol. 37, no. 4, pp. 1121–1134, 1989, doi: 10.1016/0001-6160(89)90108-9.

[175] Y. Huang, F. J. Humphreys, and I. Brough, "The application of a hot deformation SEM stage, backscattered electron imaging and EBSD to the study of thermomechanical processing," *J. Microsc.*, vol. 208, no. 1, pp. 18–23, 2002, doi: 10.1046/j.1365-2818.2002.01061.x.

[176] F. J. Humphreys and M. Ferry, "Combined in-situ annealing and EBSD of deformed aluminium alloys," *Mater. Sci. Forum*, vol. 217–222, no. PART 1, pp. 529–534, 1996, doi: 10.4028/www.scientific.net/msf.217-222.529.

[177] R. Muñoz-Moreno, M. T. Pérez-Prado, E. M. Ruiz-Navas, C. J. Boehlert, and J. Llorc, "In situ SEM observations of the tensile-creep deformation behavior and fracture mechanisms of a γ-TiAl intermetallic alloy at low and high stresses," *Mater. Res. Soc. Symp. Proc.*, vol. 1477, pp. 61–66, 2012, doi: 10.1557/opl.2012.

[178] R. Munoz-Moreno, C. J. Boehlert, T. M. Perez-Prado, E. M. Ruiz-Navas, and J. Llorca, "In Situ Observations of the Deformation Behavior and Fracture Mechanisms of Ti-45Al-2Nb-2Mn + 0.8 vol pct TiB2," *Metall. Mater. Trans. A*, vol. 43A, pp. 1198–1208, 2012, doi: 10.1007/s11661-011-1022-3.

[179] "MTI Instruments," *https://mtiinstruments.com/*. .

[180] M. Petrenec, J. Polák, T. Šamořil, J. Dluhoš, and K. Obrtlík, "In-situ study of the mechanisms of high temperature damage in elastic-plastic cyclic loading of nickel superalloy," *Adv. Mater. Res.*, vol. 891–892, pp. 530–535, 2014, doi: 10.4028/www.scientific.net/AMR.891-892.530.

[181] E. Alabort, D. Putman, and R. C. Reed, "Superplasticity in Ti – 6Al – 4V: Characterisation , modelling and applications," *Acta Mater.*, vol. 95, pp. 428–442, 2015.

[182] S. Upadhayay, H. Li, P. Bowen, and A. Rabiei, "A study on tensile properties of Alloy 709 at various temperatures," *Mater. Sci. Eng. A*, vol. 733, pp. 338–349, Aug. 2018, doi: 10.1016/j.msea.2018.06.089.

[183] J. Wang, Y. Zhang, J. Ma, J. Li, and Z. Zhang, "Microcrack Nucleation and Propagation Investigation of Inconel 740H Alloy Under In Situ High Temperature Tensile Test," *Jinshu Xuebao/Acta Metall. Sin.*, vol. 53, no. 12, pp. 1627–1635, 2017, doi: 10.11900/0412.1961.2017.00218.

[184] W. Zhang *et al.*, "In-situ EBSD study of deformation behavior of Inconel 740H alloy at high-temperature tensile loading," *J. Alloys Compd.*, vol. 820, p. 153424, Apr. 2020, doi: 10.1016/j.jallcom.2019.153424.

[185] R. Ullah *et al.*, "In-situ tensile deformation behavior of as-built laser direct metal deposited Ti–6Al–4V alloy at 200 °C," *J. Alloys Compd.*, vol. 817, p. 152781, 2020, doi: 10.1016/j.jallcom.2019.152781.

[186] G. Gregori, H. Kleebe, F. Siegelin, and G. Ziegler, "In situ SEM imaging at temperatures as high as 1450 ° C," *J. Electron Microsc. (Tokyo).*, vol. 51, no. October, pp. 347–352, 2017.

[187] G. Biallas and H. J. Maier, "In-situ fatigue in an environmental scanning electron microscope – Potential and current limitations," *Int. J. Fatigue*, vol. 29, pp. 1413–1425, 2007, doi: 10.1016/j.ijfatigue.2006.11.008.

[188] A. Di Gianfrancesco, "Technologies for chemical analyses, microstructural and inspection investigations," in *Materials for Ultra-Supercritical and Advanced Ultra-Supercritical Power Plants*, Elsevier Inc., 2017, pp. 197–245.

[189] T. Sandle, "Microbiology laboratory techniques," in *Pharmaceutical Microbiology*, Elsevier, 2016, pp. 63–80.

[190] J. Bergström, "Experimental Characterization Techniques," in *Mechanics of Solid Polymers*, Elsevier, 2015, pp. 19–114.

[191] S. V. Baryshev, R. A. Erck, J. F. Moore, A. V. Zinovev, C. E. Tripa, and I. V. Veryovkin, "Characterization of surface modifications by white light interferometry: applications in ion sputtering, laser ablation, and tribology experiments.," *J. Vis. Exp.*, no. 72, 2013, doi: 10.3791/50260.

[192] M. Visscher and K. G. Struik, "Optical profilometry and its application to mechanically inaccessible surfaces Part I: Principles of focus error detection," *Precis. Eng.*, vol. 16, no. 3,

pp. 192–198, Jul. 1994, doi: 10.1016/0141-6359(94)90124-4.

[193] "Optical Profilometry - Nanoscience Instruments." [Online]. Available: https://www.nanoscience.com/techniques/optical-profilometry/. [Accessed: 26-May-2020].

[194] C. Y. Poon and B. Bhushan, "Comparison of surface roughness measurements by stylus profiler, AFM and non-contact optical profiler," *Wear*, vol. 190, no. 1, pp. 76–88, Nov. 1995, doi: 10.1016/0043-1648(95)06697-7.

[195] L. C. Xu and C. A. Siedlecki, *Atomic force microscopy*, vol. 3. 2011.

[196] Park Systems, "Atomic Force Microscope Principle | AFM Scanning | How AFM Works." [Online]. Available: https://parksystems.com/medias/nano-academy/how-afm-works. [Accessed: 26-May-2020].

[197] ASTM International, "Standard Test Methods for Determining Average Grain Size." 2010, doi: 10.1520/E0112-10.

[198] ASTM International, "Standard test methods for tension testing of metallic materials." 2009, doi: 10.1520/E0008.

[199] H. . Exner, "Analysis of Grain- and Particle-Size Distributions in Metallic Materials," *Int. Metall. Rev.*, vol. 17, no. 1, pp. 25–42, 2013, doi: 10.1179/imtlr.1972.17.1.25.

[200] M. Li, D. Wilkinson, and K. Patchigolla, "Comparison of particle size distributions measured using different techniques," *Part. Sci. Technol.*, vol. 23, no. 3, pp. 265–284, 2005, doi: 10.1080/02726350590955912.

[201] Y. Li, A. J. Bushby, and D. J. Dunstan, "The Hall – Petch effect as a manifestation of the general size effect," *Proc. R. Soc.*, vol. A, 2016.

[202] E. O. Hall, "The Deformation and Ageing of Mild Steel: III Discussion of Results," *Proc. Phys. Soc. Sect. B*, vol. 64, no. 9, p. 747, 1951, doi: 10.1088/0370-1301/64/9/303.

[203] N. J. Petch, "The cleavage strength of polycrystals," *J. iron steel Inst.*, 1953.

[204] Z. Yanushkevich, S. V. Dobatkin, A. Belyakov, and R. Kaibyshev, "Hall-Petch relationship for austenitic stainless steels processed by large strain warm rolling," *Acta Mater.*, vol. 136, pp. 39–48, Sep. 2017, doi: 10.1016/j.actamat.2017.06.060.

[205] R. Rodríguez Baracaldo, J. M. Cabrera Marrero, J. Antonio, and B. Páramo, "Studying the Hall-Petch effect regarding sub- garding sub-micrometer steel micrometer steel (0.6% C)," *Ing. E Investig.*, vol. 31, no. 3, pp. 112–120, 2011.

[206] R. Armstrong and F. Zerilli, "Dislocation mechanisms based analysis of material behaviour," *J. Phys. Colloq.*, no. C3, p. 49, 1988, doi: 10.1051/jphyscol:1988374ï.

[207] K. I. Dragnevski, A. Pellegrino, R. Heard, C. R. Siviour, A. M. Mullis, and R. F. Cochrane, "Mechanical behaviour of rapidly solidified copper: effects of undercooling and strain rate," *Mater. Sci. Technol.*, vol. 36, no. 2, pp. 202–209, Jan. 2020, doi: 10.1080/02670836.2019.1691354.

[208] M. Ashby *et al.*, *Engineering Materials and Processes Desk reference*. 2008.

[209] P. Luo, D. T. McDonald, W. Xu, S. Palanisamy, M. S. Dargusch, and K. Xia, "A modified Hall-Petch relationship in ultrafine-grained titanium recycled from chips by equal channel angular pressing," *Scr. Mater.*, vol. 66, no. 10, pp. 785–788, May 2012, doi: 10.1016/j.scriptamat.2012.02.008.

[210] H. Galarraga, R. J. Warren, D. A. Lados, R. R. Dehoff, M. M. Kirka, and P. Nandwana, "Effects of heat treatments on microstructure and properties of Ti-6Al-4V ELI alloy fabricated

by electron beam melting (EBM)," *Mater. Sci. Eng. A*, vol. 685, pp. 417–428, Feb. 2017, doi: 10.1016/j.msea.2017.01.019.

[211] C. A. Schneider, W. S. Rasband, and K. W. Eliceiri, "NIH Image to ImageJ: 25 years of image analysis," *Nature Methods*, vol. 9, no. 7. NIH Public Access, pp. 671–675, Jul-2012, doi: 10.1038/nmeth.2089.

[212] S. Gupta and S. G. Mazumdar, "Sobel Edge Detection Algorithm," *Int. J. Comput. Sci. Manag. Res.*, vol. 2, no. 2, pp. 1578–1583, 2013.

[213] T. Ferreira and W. Rasband, "ImageJ User Guide," 2012.

[214] G. N. Chaple, R. D. Daruwala, and M. S. Gofane, "Comparisions of Robert, Prewitt, Sobel operator based edge detection methods for real time uses on FPGA," in *Proceedings - International Conference on Technologies for Sustainable Development, ICTSD 2015*, 2015, doi: 10.1109/ICTSD.2015.7095920.

[215] J. Canny, "A Computational Approach to Edge Detection," *IEEE Trans. Pattern Anal. Mach. Intell.*, no. December, 1986, doi: 10.1109/TPAMI.1986.4767851.

[216] H. S. Ahmed, H. Zhao, M. Hussain, and J. Wang, "Crystal Dislocation in SEM with Image Processing 1," *Pattern Recognit. Image Anal.*, vol. 27, no. 4, pp. 804–809, 2017, doi: 10.1134/S1054661817040083.

[217] "Edge Detection - MATLAB & Simulink." [Online]. Available: https://www.mathworks.com/help/images/edge-detection.html. [Accessed: 06-Jul-2020].

[218] G. G. . Seward *et al.*, "High-Temperature Electron Backscatter Diffraction and Scanning Electron Microscopy Imaging Techniques : In-situ Investigations of Dynamic Processes," *Scanning*, vol. 24, pp. 232–240, 2002.

[219] A. E. Smith and C. D. Hause, "Fraunhofer Multiple Slit Diffraction Patterns with Finite Sources," *J. Opt. Soc. Am.*, vol. 42, no. 6, p. 426, Jun. 1952, doi: 10.1364/josa.42.000426.

[220] N. Brodusch, H. Demers, R. Gauvin, N. Brodusch, H. Demers, and R. Gauvin, "Imaging with a Commercial Electron Backscatter Diffraction (EBSD) Camera in a Scanning Electron Microscope: A Review," *J. Imaging*, vol. 4, no. 7, p. 88, Jul. 2018, doi: 10.3390/jimaging4070088.

[221] A. M. A. D. EDAX, "OIM Academy Tilburg Manual."

[222] S. Kidder and D. Prior, "Reversed scan direction reduces electron beam damage in EBSD maps," *J. Microsc.*, vol. 255, no. 2, pp. 89–93, 2014, doi: 10.1111/jmi.12140.

[223] D. Maritza, M. Cardona, J. Wongsa-ngam, and T. G. Langdon, "Microstructural evolution and microhardness in a low carbon steel processed by high-pressure torsion ☪," *Integr. Med. Res.*, vol. 3, no. 4, pp. 344–348, 2014, doi: 10.1016/j.jmrt.2014.09.004.

[224] R. Heard, K. I. Dragnevski, and C. R. Siviour, "In-situ SEM observation of grain growth in the austenitic region of carbon steel using thermal etching," *J. Microsc.*, p. jmi.12894, Apr. 2020, doi: 10.1111/jmi.12894.

[225] C. Garcia de Andres, F. G. Caballero, C. Capdevila, and D. San Martin, "Revealing austenite grain boundaries by thermal etching : advantages and disadvantages," *Mater. Charact.*, vol. 49, pp. 121–127, 2003, doi: 10.1016/S1044-5803(03)00002-0.

[226] "Iron-carbon phase diagram [SubsTech]." [Online]. Available: https://www.substech.com/dokuwiki/doku.php?id=iron-carbon_phase_diagram. [Accessed: 04-Jun-2020].

[227] R. Heard, J. E. Huber, C. R. Siviour, G. Edwards, E. Williamson-Brown, and K. Dragnevski,

"An investigation into experimental in-situ SEM imaging at high temperature.," *Rev. Sci. Instrum.*, 2020.

[228] H. Farahani, G. Zijlstra, M. G. Mecozzi, V. Ocelík, J. T. M. De Hosson, and S. Van Der Zwaag, "In Situ High-Temperature EBSD and 3D Phase Field Studies of the Austenite-Ferrite Transformation in a Medium Mn Steel," *Microsc. Microanal.*, pp. 639–655, 2019, doi: 10.1017/S143192761900031X.

[229] A. A. El-Meligi, "Effect of heating rates on the formable oxide scale on a c-steel surface," *J. Mater. Sci. Technol.*, vol. 20, no. 5, 2004.

[230] C. P. Somrerk Chandra-ambhorrn, Thammaporn Thublaor, "Thermodynamics and Kinetics of the High Temperature Oxidation of Stainless Steels," *Solid State Phenom.*, vol. 300, pp. 1–24, 2020.

[231] M. J. Rost, D. A. Quist, and J. W. M. Frenken, "Grains, Growth, and Grooving," *Phys. Rev. Lett.*, vol. 91, no. 2, Jul. 2003, doi: 10.1103/PhysRevLett.91.026101.

[232] M. Fanfoni and M. Tomellini, "The Johnson-Mehl-Avrami-Kolmogorov model: A brief review," *Nuovo Cim. della Soc. Ital. di Fis. D - Condens. Matter, At. Mol. Chem. Physics, Biophys.*, vol. 20, no. 7, pp. 1171–1182, 1998, doi: 10.1007/BF03185527.

[233] A. Walentek, M. Seefeldt, B. Verlinden, E. Aernoudt, and P. Van Houtte, "Electron backscatter diffraction on pearlite structures in steel," *J. Microsc.*, vol. 224, no. 3, pp. 256–263, Dec. 2006, doi: 10.1111/j.1365-2818.2006.01702.x.

[234] M. Avrami, "Kinetics of phase change. II Transformation-time relations for random distribution of nuclei," *J. Chem. Phys.*, vol. 8, no. 2, pp. 212–224, 1940, doi: 10.1063/1.1750631.

[235] M. Avrami, "Granulation, phase change, and microstructure kinetics of phase change. III," *J. Chem. Phys.*, vol. 9, no. 2, pp. 177–184, 1941, doi: 10.1063/1.1750872.

[236] R. Saito, N. Nakada, S. Yabu, and K. Hayashi, "Effects of Initial Structure and Reversion Temperature on Austenite Nucleation Site in Pearlite and Ferrite–Pearlite," *Metall. Mater. Trans. A Phys. Metall. Mater. Sci.*, vol. 49, no. 12, pp. 6001–6009, Dec. 2018, doi: 10.1007/s11661-018-4950-3.

[237] D. Hömberg, F. S. Patacchini, K. Sakamoto, and J. Zimmer, "Revisited Johnson-Mehl-Avrami-Kolmogorov model and the evolution of grain-size distributions in steel," *IMA J. Appl. Math. (Institute Math. Its Appl.*, vol. 82, no. 4, pp. 763–780, 2017, doi: 10.1093/imamat/hxx012.

[238] J. Hou and B. He, "Effect of starting microstructures on the reverse transformation kinetics in low-carbon steel," *Metals (Basel).*, vol. 10, no. 12, pp. 1–12, 2020, doi: 10.3390/met10121601.

[239] J. Meiser and H. M. Urbassek, "Ferrite-to-austenite and austenite-to-martensite phase transformations in the vicinity of a cementite particle: A molecular dynamics approach," *Metals (Basel).*, vol. 8, no. 10, 2018, doi: 10.3390/met8100837.

[240] H. Chen and S. van der Zwaag, "An Overview of the Cyclic Partial Austenite-Ferrite Transformation Concept and Its Potential," *Metall. Mater. Trans. A Phys. Metall. Mater. Sci.*, vol. 48, no. 6, pp. 2720–2729, Jun. 2017, doi: 10.1007/s11661-016-3826-7.

[241] P. Dastur *et al.*, "Martensite Reversion Duality Behavior in a Cold-Rolled High Mn Transformation-Induced Plasticity Steel," *Metall. Mater. Trans. A Phys. Metall. Mater. Sci.*, vol. 50, no. 10, pp. 4550–4560, Oct. 2019, doi: 10.1007/s11661-019-05385-9.

Appendices

Appendix - Chapter 2

Johnson-Mehl-Avrami-Kolmogorov (JMAK) Law Derivation

The JMAK law used to predict diffusion driven kinetics can be derived using the following assumptions [107]:

1. Homogeneous nucleation occurs randomly and, on average, uniformly across the whole untransformed area of the material.
2. The growth rate is independent of the percentage of the phase transformed.
3. The growth rate is isotropic.
4. The nucleation rate and growth rate are constant.

If these conditions are all met, then a transformation from one phase to another will occur in a time interval $0 < \tau < t$ via nucleation and growth across the material volume (V). Nucleation of the new phase occurs at rate N per unit volume, which subsequently grows at a rate G and growth stops when nuclei agglomerate. Therefore, during a time interval $\tau + d\tau$ the number of nuclei (n) which appear within the volume (V) is defined by,

$$n = VNd\tau \qquad \text{Equation A2.1}$$

Since growth rate is isotropic, it can be assumed that each nuclei grows to a sphere of radius $G(t- \tau)$ and so the volume of the second phase present within the first, considering a large extended volume V_b^e, is,

$$dV_b^e = \frac{4\pi}{3}[G(t - \tau)]^3 VNd\tau \qquad \text{Equation A2.2}$$

When Equation A2.2 is integrated between $\tau = 0$ and $\tau = t$ the solution is,

$$V_b^e = \frac{\pi}{3} G^3 V N t^4$$ Equation A2.3

Now consider that the whole volume (V_b^e) has not transformed, but only a portion of it has (V_b). As nucleation occurs randomly, the fraction of the new phase that forms will be proportional to the volume fraction of the original phase (V_a),

$$\frac{dV_b}{dV_b^e} = \frac{V - V_b}{V}$$ Equation A2.4

rearranged,

$$dV_b^e = \left(\frac{1}{1 - \frac{V_b}{V}} \right) dV_b$$ Equation A2.5

And integrated,

$$ln\left(1 - \frac{V_b}{V}\right) = \frac{-V_b^e}{V}$$ Equation A2.6

where *Vb/V* is equal to the volume fraction *f*. Substitution of *f* and Equation A2.3 into Equation A2.6 produces the familiar JMAK equation:

$$f = 1 - e^{-kt^n}$$ Equation A2.7

This equation can be subsequently used to predict the volume fraction of that phase transformed at a given time for a constant temperature, as defined by the temperature dependent constant *k*.

Grain Growth Power Law Derivation

The grain growth power law was originally derived by Burke and Turnbull based on the movement of a boundary via atom transport due to the pressure from surface curvature. Hence, boundary movement is considered to move towards its centre of curvature in order to reduce the boundary area and associated energy. Based on these principles, coupled with reaction rate theory, Burke and Turnbull made the following assumptions:

1. All grains can be modelled as spheres and so the grain boundary radius (r) of curvature is equal on all sides.
2. The grain boundary free energy is the same for all grain boundaries and is independent of grain size and time.
3. The radius of grain boundary curvature (r) is proportional to the mean grain radius $\bar{R}$, related by the constant (C_1),

- $$r = C_1\bar{R} \qquad \text{Equation A2.8}$$

4. The rate of change of grain radius (dR/dt) is proportional to the grain boundary pressure (P), related by a constant (C_2)

- $$\frac{dR}{dt} = C_2P \qquad \text{Equation A2.9}$$

5. The only force acting on a grain boundary is due to surface curvature.

Aside from these assumptions, it should also be noted that the surface curvature pressure is dependent on the grain boundary radius of curvature (r) and the grain boundary free energy (γ), defined as,

$$P = \gamma r \qquad \text{Equation A2.10}$$

Substitution of Equation A2.8 and Equation A2.10 into Equation A2.9 gives,

$$\frac{dR}{dt} = \frac{2C_2\gamma}{C_1 R\_} \qquad \text{Equation A2.11}$$

Assume R= $\bar{R}$ and integrate for R=R_o at t=0 and R=R_t at t=t to get,

$$R_t^2 - R_0^2 = \frac{4C_2\gamma t}{C_1} \qquad \text{Equation A2.12}$$

Since radius is the twice the diameter and everything except time is constant, this rearranges to the familiar power law:

$$d_t^n - d_0^n = kt \qquad \text{Equation A2.13}$$

Where, based on these assumptions, *n=2*. As discussed in the literature, experimental results indicate that n rarely equals 2 owing to the in-homogeneous features within the microstructure, leading to non-spherical grain growth.

Mullins' Stationary Thermal Grooving Principle Derivation

Mullins' principle governing the groove profile of thermal etching was derived based on the following assumptions:

1. The system is closed and contains a metal polycrystal in quasi-equilibrium with its vapour.
2. The properties of an interface are independent of its orientation with respect to the adjacent crystal.
3. The only mechanisms associated with the transport of matter are evaporation-condensation and surface diffusion.
4. Slope angles are assumed to be small.
5. The process of grooving is adequately described by macroscopic concepts as surface curvature and surface free energy.
6. Ignore crystalline imperfections.
7. There is a negligible flow of matter out of the boundary; assume boundary's role is to maintain correct equilibrium angle.

From these assumptions, two key principles were used: the Gibbs-Thomson relationship,

$$\mu = -\gamma_s \Omega \frac{d^2y}{dx^2} \qquad \text{Equation A2.14}$$

which describes the change in chemical potential with respect to curvature, and the Nernst-Einstein relationship,

$$J = vu = \frac{B}{\Omega}\frac{d^3y}{dx^3} \qquad \text{Equation A2.15}$$

which describes the flux (velocity x area) at which atoms move along a given curvature. In both cases, *dy/dx* = gradient of profile and d^2y/dx^2 is the curvature.

By combining the Gibbs-Thompson and Nernst-Einstein relationships, Mullins' forms the differential equation describing the change of profile with time, *t* and displacement, *x.*

$$\frac{dy}{dt} = -B\frac{d^4y}{dx^4} \qquad \text{Equation A2.16}$$

From this, *dy/dt* can subsequently be solved for *y* using the boundary conditions $y(x,0) = 0, y'(0,t) = \tan(\theta) = m, y''(0,t) = 0$ small angle approximation, which produces,

$$y = m(Bt)^{0.25}Z[\frac{x}{(Bt)^{0.25}}] \qquad \text{Equation A2.17}$$

which is the well-known Mullins thermal grooving equation where *m* is an experimental constant, *t* is time, $B = \frac{D_S\gamma_S\Omega^2\nu}{KT}$ and $Z = \sum_0^\infty a\frac{x}{(Bt)^{0.25n}}$ is the summation of atoms in the x-direction as they vary with time and temperature. For $B = \frac{D_S\gamma_S\Omega^2\nu}{KT}$, the parameters are defined as *Ds* is surface diffusion, *K* is Boltzman's constant, *T* is temperature, omega is volume per atom, v is no. of atoms per unit of surface energy, γ is surface tension.

From the y-profile, if we assume that the depth only varies in the y-direction with respect to time, and that the effects of the x-direction are negligible, we can find an approximation with the change in depth with respect to time as,

$$\delta = m(Bt)^{0.25} \qquad \text{Equation A2.18}$$

Derivation of Moving Grain Boundary Motion

Both Mullins [86] and Allen [86] examined different derivations for quantifying how grain boundary motion affects thermal grooving. Here, Allen's approach is examined, which considers that thermal grooving occurs due to a dynamic balance between two processes; capillarity, which acts to reduce the sharp surface curvature and hence leads to thermal grooving and boundary motion which limits the time available for the groove to form before the boundary moves to a new area. From these two dynamic processes the following assumptions are made:

1. The size of a moving thermally grooved boundary (w_l) is limited by the time it takes to move through its own width.
2. The moving groove grows in depth at the same rate as a stationary groove, until the moving groove has moved through its own width at time t_l.
3. At time t_l the moving groove reaches the limiting size (w_l) and stops growing.
4. The thermally grooved boundary velocity (v_o) is constant.

Thus, the final groove size of a moving grain boundary (w_l) is defined as:

$$w_l = v_o t_l \qquad \text{Equation A2.19}$$

From geometry, Mullins was able to relate the distance between the two curves of a stationary groove by,

$$w_l = 4.6(Bt)^{1/4} \qquad \text{Equation A2.20}$$

where B is as defined for stationary grain boundaries, this assumes that thermal grooving occurs in the same way, regardless of whether the boundary is stationary or moving, up to the point at which movement exceeds the width of the boundary at the point $t = t_l$. Combining Equation A2.19 and Equation A2.20 leads to,

$$v_o = B\left(\frac{7.65}{w_l}\right)^3 \qquad \text{Equation A2.21}$$

When compared to Mullins' more rigorous solution based on the movement of a Catenoid, discussed in Section 2.6.2, Allen's simplified derivation shows good agreement. However, it does produce slightly too large a value of w_l owing to the difference in shape of the stationary versus moving grain boundary, as shown in Figure A2.1Fig.

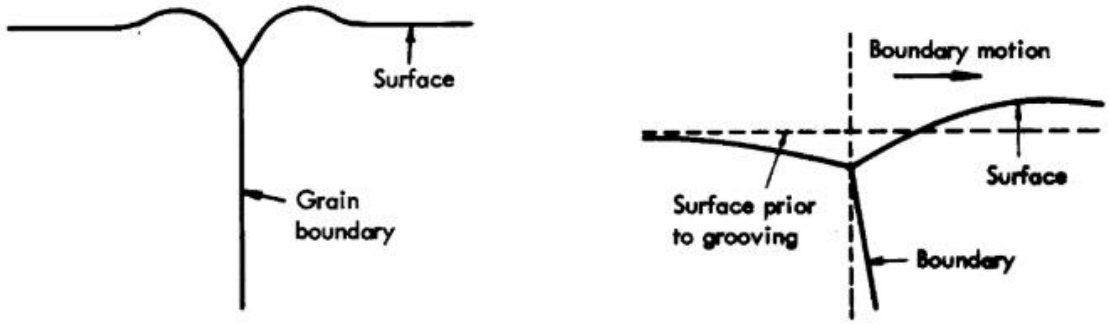

(a) (b)

Figure A2.1: Thermal grooving at (a) stationary grain boundary, and (b) migrating grain boundary, where the vertical is exaggerated by roughly three the distance [86].

Hence, experimental results show variations of the *M* value, shown here to be equal to 7.65 in the derivation to account for this.

Appendix - Chapter 3

Bragg's Law Derivation

The derivation of Bragg's law assumes that two incident beams on a surface coincide at the point when the incident angle and the reflecting angle are equal, shown in Figure A3.1. For this to occur, the incident beams must always be in phase and parallel until the point of interference.

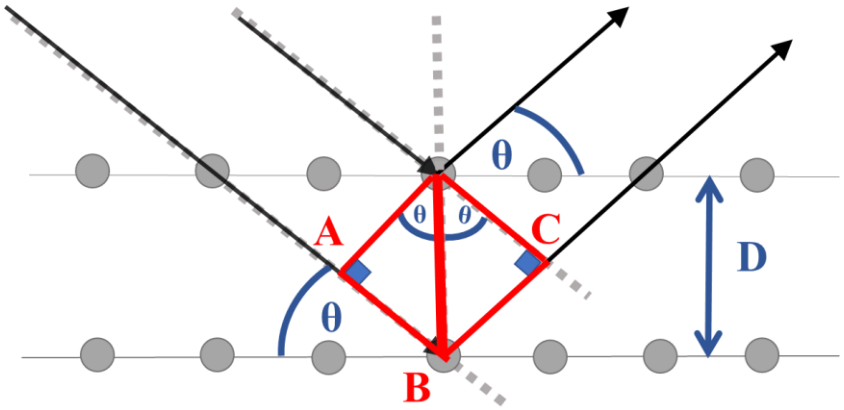

Figure A3.1: Conditions necessary for Bragg's law where two parallel incident beams coincide with a surface with identical incident and reflecting angles.

From this assumption the interaction between the beam and the surface can be defined as follows in order to derive Bragg's law:

1) The first beam strikes the atom in layer Z.
2) The second beam continues to the next layer, where it is scattered by atom B. The extra distance travelled by the second beam compared to the first beam must be AB+BC for the two beams to continue to be in phase and parallel upon scattering.
3) The extra distance (*AB*+*BC*) must be an integer multiple (*n*) of the wavelength (λ) for the phases of the two beams to be the same. Therefore,

- $AB + BC = n\lambda$ Equation A3.1

4) Considering the red triangle defining the reflection geometry from Figure A3.1, shown alone in Figure A3.2, enables the definition of the lattice spacing D and the length AB as the hypotenuse and opposite sides of the triangle respectively.

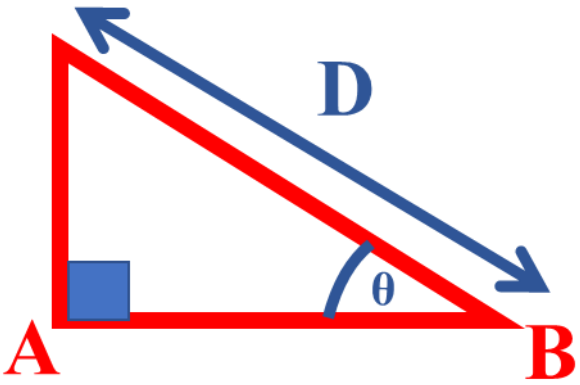

Figure A3.2: Reflection geometry of two incident beams.

5) The use of trigonometry allows *AB* to be defined with respect to the lattice spacing *D* as,

- $AB = Dsin\theta$ Equation A3.2

6) Since *AB* is equal to *BC*, Equation A3.1 can be converted to,

- $2AB = n\lambda$ Equation A3.3

7) Substitution of Equation A3.2 into Equation A3.3 results in Bragg's law,

- $2Dsin\theta = n\lambda$ Equation A3.4

Appendix - Chapter 4

Thermo-Mechanical Stage Design

This appendix details the design and testing of a combined thermo-mechanical *in situ* stage; an extension of the current novel heat stage developed in collaboration with Deben UK Ltd. Development focused on the clamping mechanisms, specimens design and load cell calibration to ensure accurate data are obtained *in situ*. It is anticipated that this *in situ* stage will provide the ability to further investigate the high-temperature mechanical response of the alloys detailed in this thesis, and the effect of applied loads on structural evolution.

Clamp & Specimen Specifications

Clamping and specimen design are fundamental to ensuring that accurate stress and strain data are produced during mechanical testing, allowing properties to be calculated that are representative of the bulk material. A selection of stage design specifications, which in turn provide criteria for the clamp design, were developed in collaboration with Deben UK Ltd.

- The stage dimensions are fixed at maximum size of 204 x 135 x 50 mm (L x W x H) limited by the size of the smallest SEM chamber manufactured by Zeiss. This corresponds to a maximum clamp length and face diameter of 33 mm and 24 mm respectively.
- The clamps must not yield when the specimen is loaded at a maximum load of 5 kN.
- The stage must be able to image specimens with electron backscatter diffraction (EBSD), secondary electron (SE) and backscattered electron (BSE) imaging, which will require rotation of clamps at angles of 0º, 70º, 180º and 290º for EBSD detectors on both sides of the chamber and to examine the back of the specimen.
- Specimens must meet ASTM standards for tensile testing.

- Specimens must be easily mounted within the clamps to ensure the polished surface, required for EBSD imaging, is not damaged during handling.

Specimen Design

Literature investigations were conducted into the geometry of samples required to provide accurate stress and strain results on this scale. The preliminary clamp geometry was set based on the ASTM specimen geometry and then developed to meet the imaging capacity of the SEM and the stage constraints including stage geometry, load cell capacity (5 kN) and heating module contact and compared against current literature geometries. The specimen shape most commonly used in the literature survey was the dog-bone shape. Hence, a dog-bone specimen geometry (Figure A4.1) was defined by the clamp separation distance of 30-50 mm and the heat stage width (fixed by the stage dimensions at 19 mm), which in turn dictated the minimum gauge length to be 40 mm. It was noted that the minimum gauge length assumed a 5 mm shoulder length within the clamp, as this should be significantly larger than the specimen width, thus reducing the tested gauge length not in the clamp to 30 mm and the maximum overall gauge length to 50 mm.

A double gauge length notched specimen was also considered for the combined thermo-mechanical testing so that the clamps were away from the imaged area. This was to improve working distance and to keep the section of specimen that was heated away from the clamps, which minimises the need for extensive cooling. The specimen is shown in Figure A4.2.

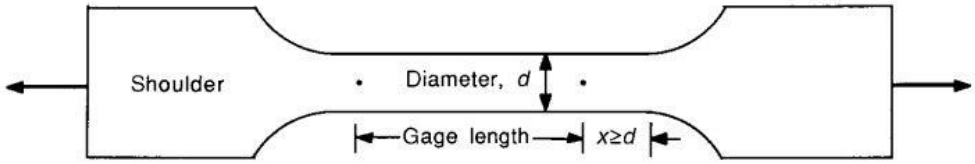

Figure A4.1: Single gauge length specimen with a gauge width (diameter) of 2 mm, max gauge length of 30 mm and shoulder length (x) of 5 mm. Shoulder geometry is to be defined by clamp type.

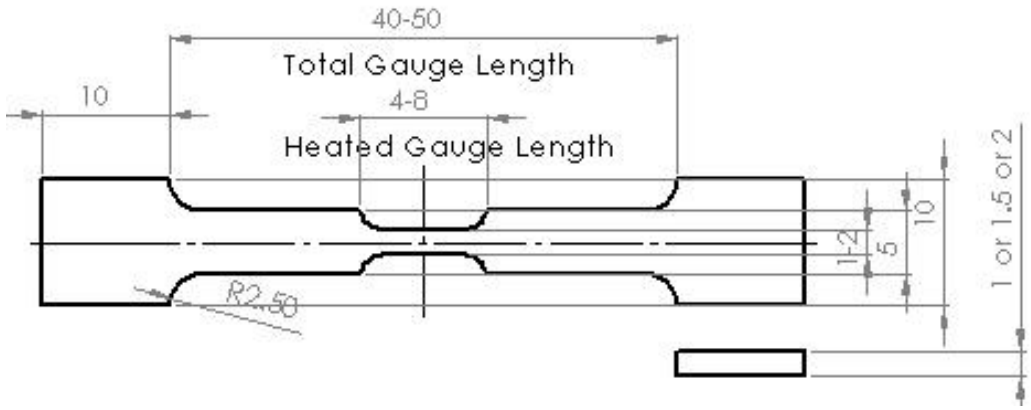

Figure A4.2: Double gauge length notched specimen with final dimensions.

Clamp Design

Clamping mechanisms vary depending on the load frame and can affect the triaxiality or strain rate in the specimen. As such, clamps ranging from those on micro-test stages to those on large-scale experimental systems were examined, to identify the most appropriate and effective clamping mechanism. The two main clamping principles most commonly used for tensile metal specimens are mechanical wedge-action and split-collet grips. Wedge action grips have a variety of flat and grooved faces, which provide a gripping mechanism on the specimen. However, grooved clamp faces may cause damage to the specimen surface, as well as some initial specimen slippage post-clamping. Split-collet tensile grips, often used for 3D dog-bone test specimens, enable uniform gripping around the shoulders of the specimen, but may spread under a heavy load. Hence, split-collet grips are often more suited to weaker

specimens. If stronger specimens are required, a constraint ring is used to mitigate against failure or ‘pull-out’ at the grips.

A modified version of the split-collet grip design was chosen as the foundation for clamp design to eliminate slippage within the clamps and prevent specimen end deformation. After qualitative analysis and discussions with Deben UK Ltd about the issues that may arise during manufacturing, sample preparation, and specimen mounting, a preliminary cut-out design was tested (Figure A4.3) to ensure that specimens within the clamps produced the expected results. The geometry of the cut out and resulting specimen, including the gripped length and width and the shoulder length and width were set to meet ASTM standards and tested experimentally. After identifying an appropriate geometry to hold the specimen, three materials that Deben UK Ltd had available for the manufacture of the clamps were investigated (Table A4-1).

Out of the three material’s available, inconel 718 was chosen based on its high strength to density ratio compared to steel 316 and its high operating temperature compared to Liquidmetal. Both of these were requirements of a stage operating at temperatures up to 1000 °C and under loads of 5 kN.

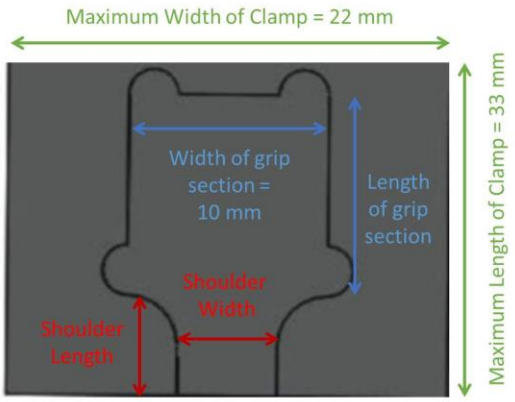

Figure A4.3: The cut out geometry designed to hold the specimen within the clamps.

Properties	Steel 316	Liquidmetal (Amorphous Zirconium Alloy)	inconel 718 (Nickel)
Tolerance (μm)	5-20 (wire-cutting)	20	Comparable to steel
Ultimate Tensile Strength (MPa)	515	1524	1375
Density (g/cm^3)	8	6.57	8.19
Elastic modulus (GPa)	193	86.5	208
Max Operating Temperature (°C)	538	250	1200
Magnetic Field	paramagnetic – can be magnetised over time	mildly diamagnetic – cannot be magnetised over time	minimal
Corrosion Resistance	Ph13 and Seawater	HCL, H3SO4, pH13, Seawater	yes

Table A4-1: Materials and their properties considered for clamp design.

Clamp Testing

Clamp testing involved preliminary experiments using a prototype brass clamp and then a final round of experiments using clamps made from inconel 718. Prototypes of the clamps and corresponding specimens were tested in an *ex situ* rig to determine the feasibility of the design and subsequent material choice.

The testing rig, shown in Figure A4.4, used a clamp containing the cut-out geometry, which could be attached to a commercial clamp system wedge grip within an Instron Universal Testing System (Instron). The rig tested dog-bone specimens, in the proposed geometry, were made of aluminium alloy for the brass clamps and titanium alloy (Ti-64) for the inconel clamps. The aluminium specimens were loaded, using the Instron, in tension at a rate of 20 μm/s until specimen failure. Specimens were tested both in the designed clamps and for a comparison in the Instron clamps to determine the reliability of the designed prototype clamps. The testing was repeated for the final prototype clamp made from inconel 718 with titanium specimens in the required geometry to ensure the shoulder widths could withstand the maximum loading of 5 kN without deformation.

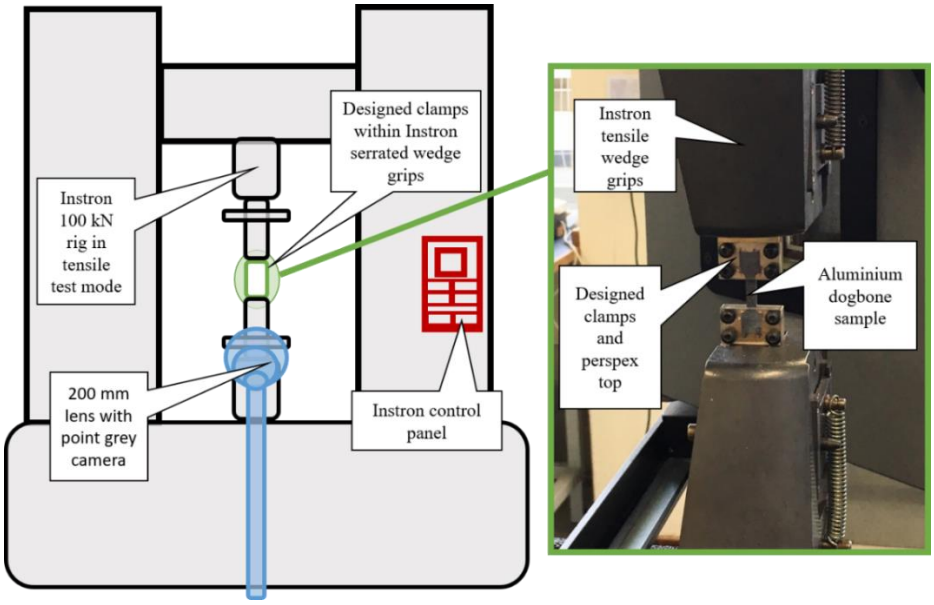

Figure A4.4: A schematic of the Instron set-up and a photograph of the prototype clamp.

The stress-strain graph, presented in Figure A4.5, identifies the Young's modulus of the aluminium specimen as 68 GPa, which is comparable to the ASTM standards literature value for Al1060 (the alloy tested) of 69 GPa. To confirm the effectiveness of the prototype clamps, the data were compared against the specimen clamped in the Instron clamps.

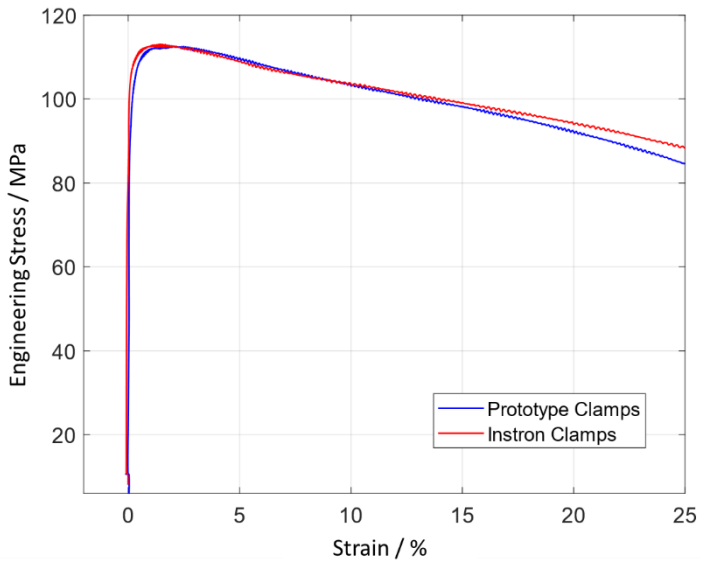

Figure A4.5: Stress-strain graph of brass prototype clamps (blue) versus Instron clamps (red), showing good agreement.

Upon confirmation that the clamps had minimum slippage and produced good stress-strain results, the testing was repeated for the inconel 718 clamp. A comparison of force-time data obtained using the inconel clamps and Instron wedge grips is shown in Figure 4.6. The data indicate that significantly greater slippage occurred within the Instron serrated wedge grips than in the prototype clamps. This difference was not observed when testing the aluminium specimens, and it is likely to be a result of the harder titanium specimens being initially less firmly gripped. Due to the limited travel distance of a micro-tensile stage and restricted imaging field, it is important to minimise this slippage, making the prototype clamp design well suited to the novel thermo-mechanical micro-stage.

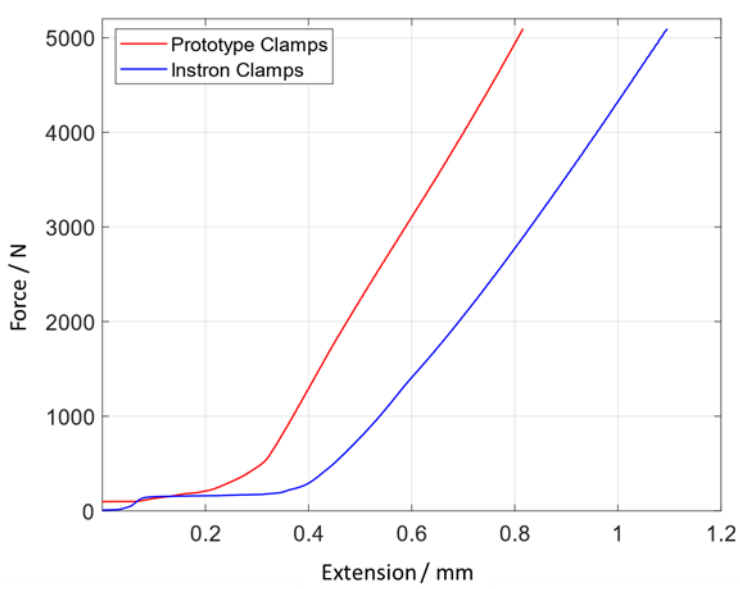

Figure A4.6: Force versus extension graph of both inconel designed prototype clamps (red) and Instron clamps (blue).

Testing of the titanium specimens using the double notched specimen format (Figure A4.2) enabled confirmation of accurate stress-strain data as this specimen geometry resulted in Ti-64 yielding at approximately 4.5 kN [24]; just below the stage's required maximum load; the results of which are presented in Figure A4.7, indicating an appropriate yield strength and failure value.

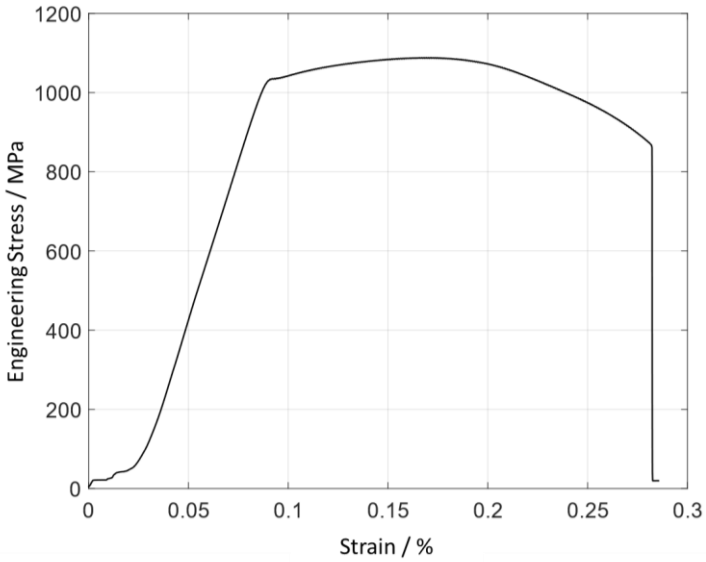

Figure A4.7: Stress versus strain results for double notch titanium dog-bone specimen to failure.

The above design for the clamps and the specific material were selected by Deben UK Ltd for the new micro-tensile stage. This was based on its accurate stress-strain results and lack of slippage, as well as the corresponding specimen design suited for both heating and mechanical testing on a micro imaging scale.

Load Cell Calibration

Load cells were designed by Deben UK Ltd and were manufactured out of grade 5 titanium alloy. Load cell calibration was conducted at the Deben UK Ltd testing facility to ensure there was minimal drift in the load cell up to temperatures up to 100 °C and loads of 5 kN.

The load cell was tested using a purpose built calibration rig in both tension and compression. The results of the load cell hysteresis, shown in Figure A4.8a, confirm that it is stable at room temperature and calibrated to within 1% accuracy. The results of the load cell hysteresis at elevated temperature confirmed that it is calibrated to within 3% accuracy, as shown in Figure A4.8b.

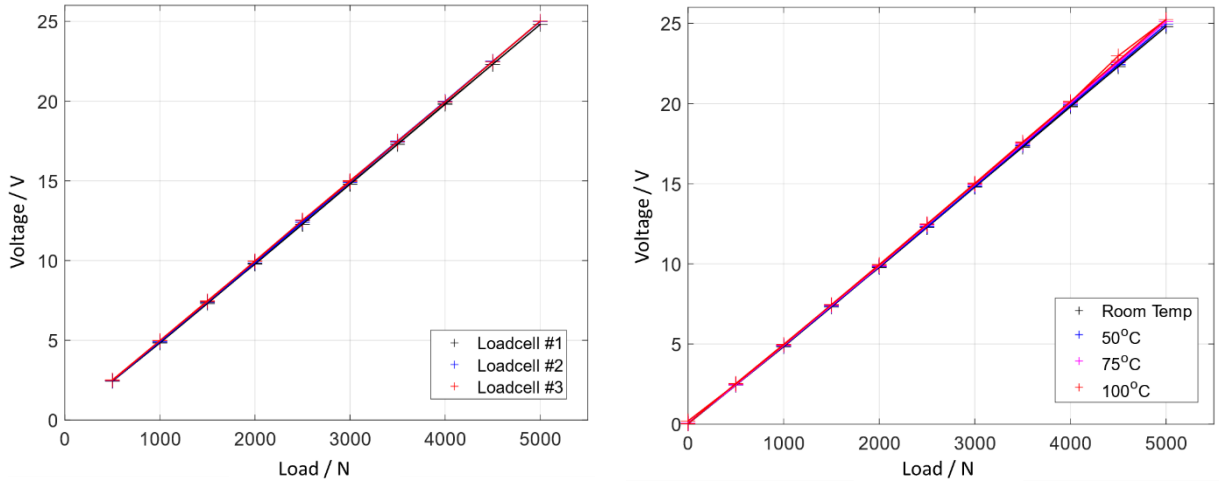

Figure A4.8: Hysteresis of (a) room temperature, and (b) elevated temperature results indicating good linearity and confirming load cell calibration.

The overall loading discrepancies observed both at room temperature and at elevated temperature can be accounted for by compliance in the screws, variation in CaliBruce (loading apparatus) and material tolerances of the load cell. The load cell drift is less than 3%, which is required as part of Deben's micro-stage accuracy guarantee and so is acceptable. Hence, the load cell was well calibrated and will be used within the micro-stage.

Casino Simulation Results

Unprocessed interaction volume simulations produced using CASINO.

keV	Steel	Nickel
5	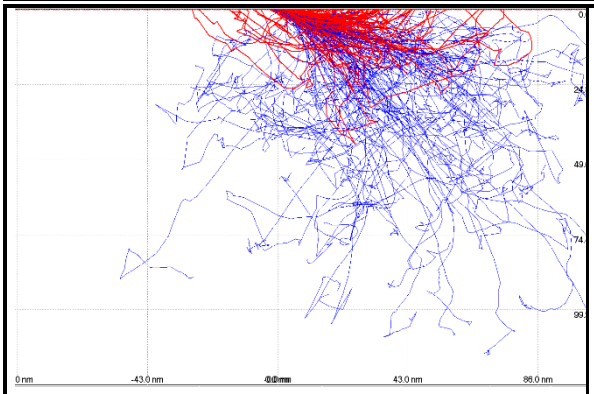	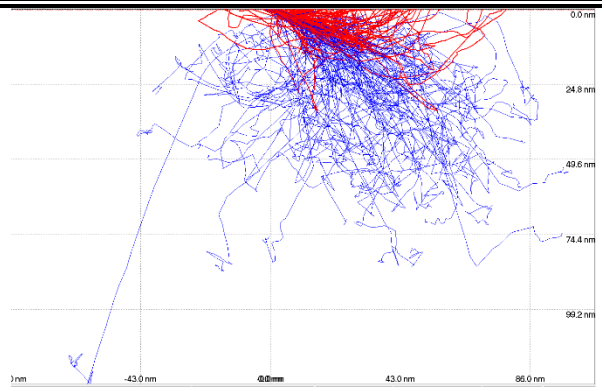
10	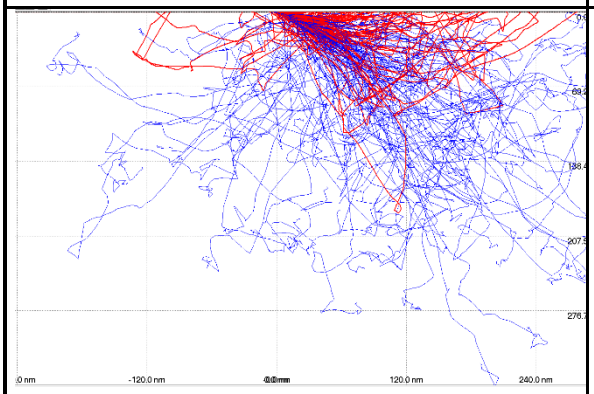	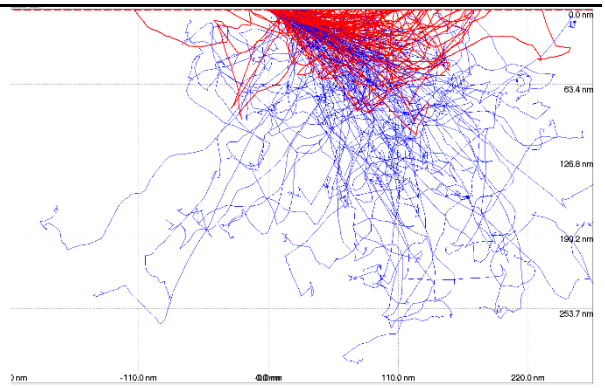
15	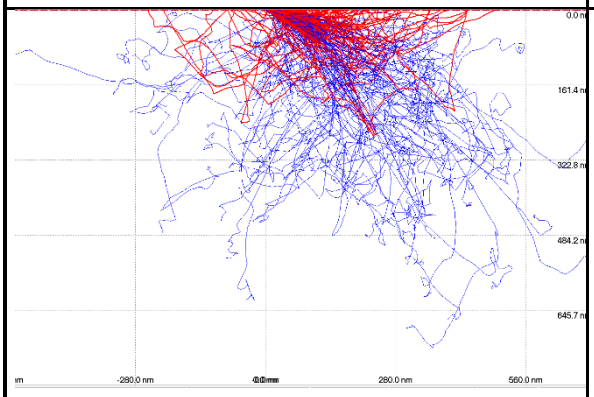	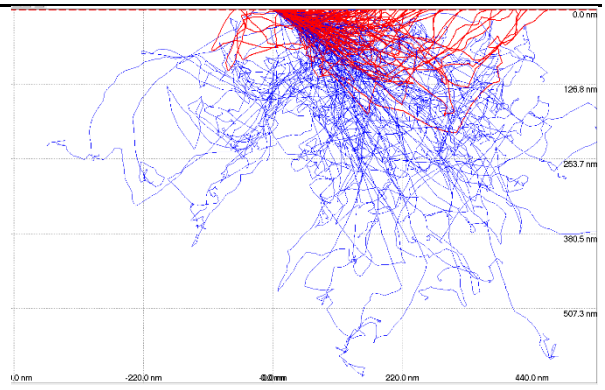

20	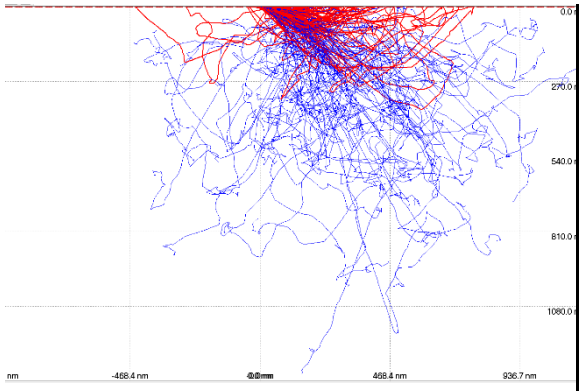	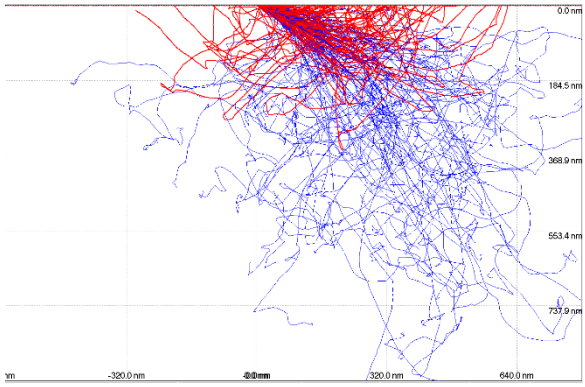
25	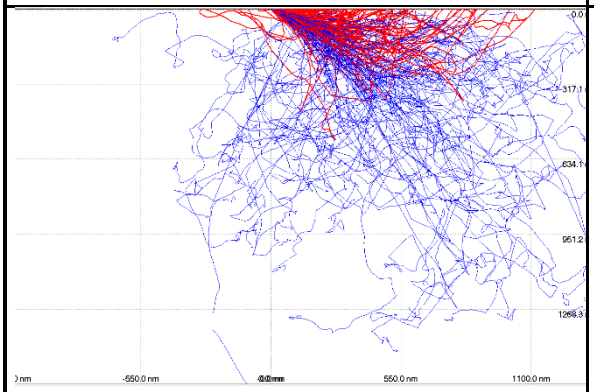	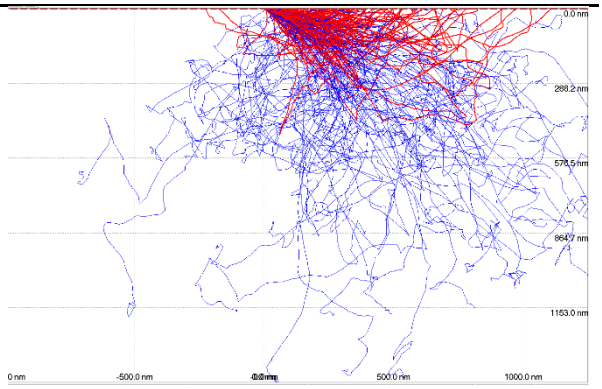
30	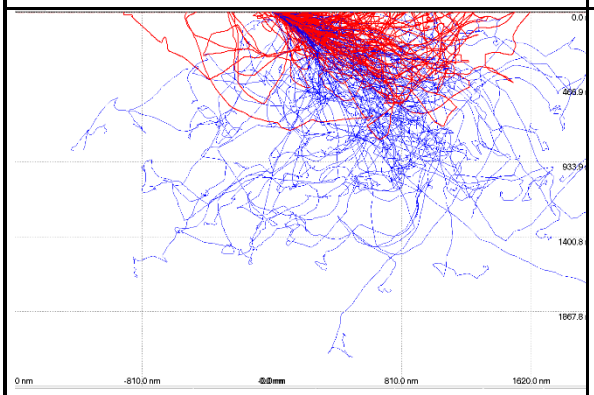	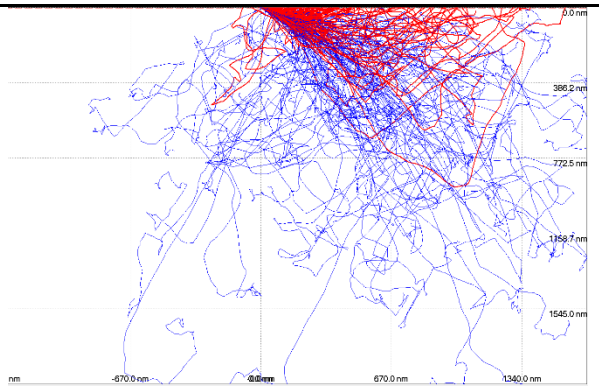

Table A4-2: CASINO simulation results showing the interaction volumes of nickel and steel at voltages of 5-30 keV.

Appendix - Chapter 5

Optical Images

Optical images pre- and post-heat treatment at 20× magnification.

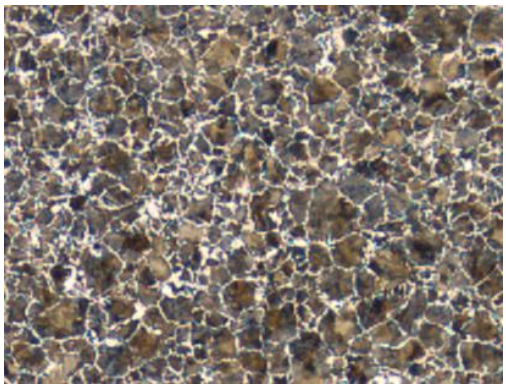

(a) Pre-heat treatment

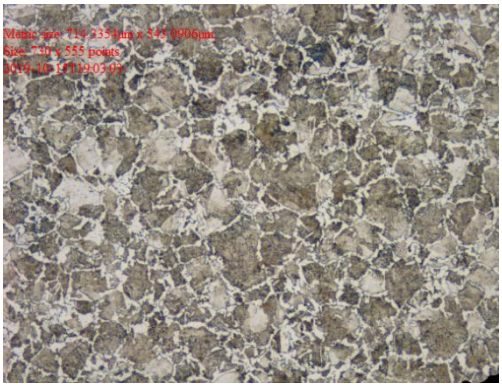

(b) 800 °C 1 hour surface

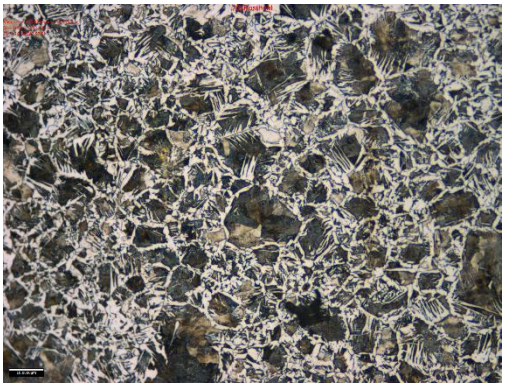

(c) 800 °C 1 hour bulk

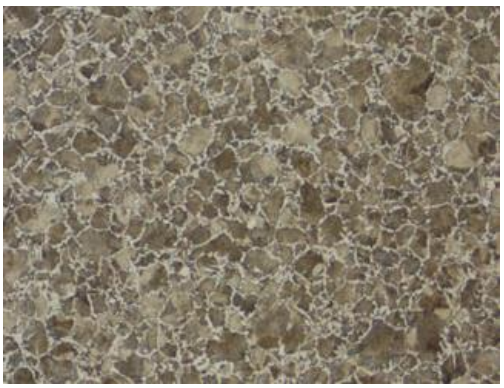

(d) 800 °C 4 hour surface

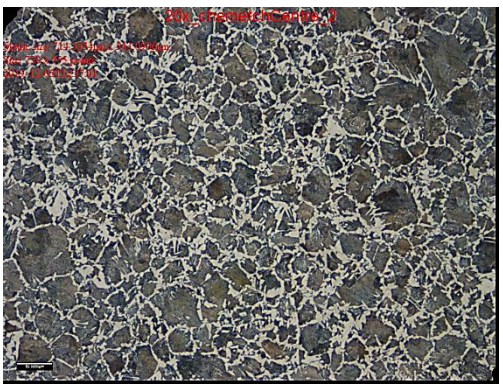

(e) 800 °C 4 hour bulk

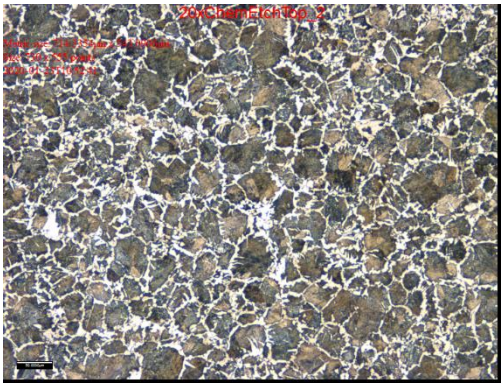

(f) 850 °C 1 hour surface

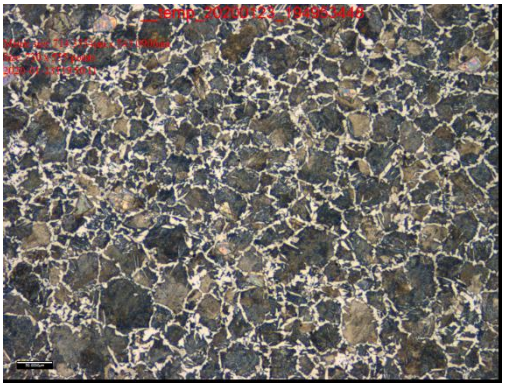

(g) 850 °C 1 hour bulk

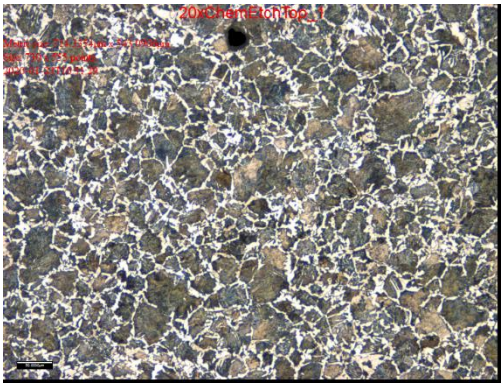

(h) 850 °C 4 hour surface

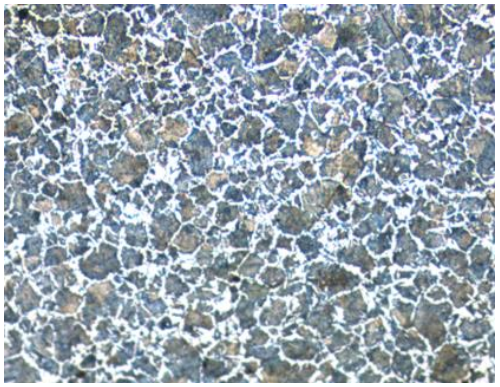

(i) 850 °C 4 hour bulk

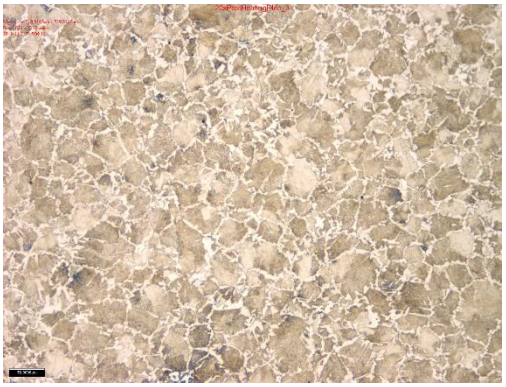

(j) 850 °C 4 hour surface (no polish)

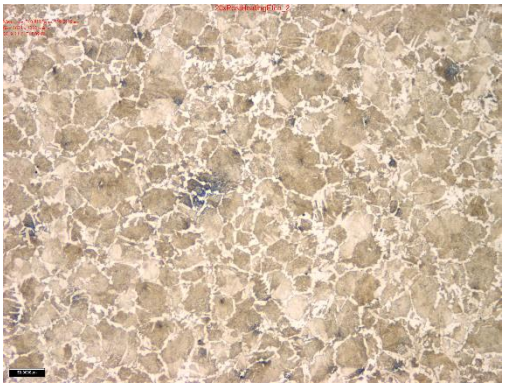

(k) 850 °C 4 hour bulk (no polish)

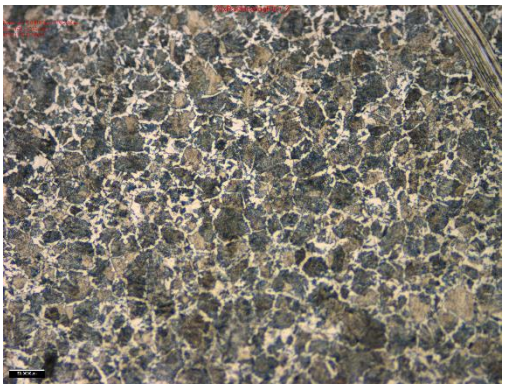

(l) 920 °C 4 hour surface

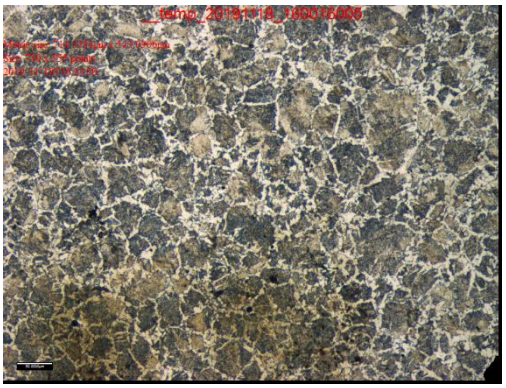

(m) 920 °C 4 hour bulk

Figure A5.1: Optical images of 0.4 wt.% carbon steel pre- and post-heat treatment.

Solving the Power Law Equation for Bulk Grain Growth

The Burke and Turnbul power law equation was converted to a logarithmic form,

$$ln(d^n - {d_o}^n) = ln(t) - \frac{Q}{RT} + ln\,(k_o) \qquad \text{Equation A5.1}$$

which was then iterated to find the optimal activation energy (Q) based on the polyfit function. Given that Q would be expected to be in the range of 1-500 kJ, these values were iterated for at a step size of 0.01 kJ. The most appropriate value of Q was then chosen based on the minimum standard error between the polyfitted equation and the raw data. The standard error from the polyfit was plotted against each value of Q. This polyfit was applied for multiple *n* values, which were then subsequently plotted. However, unfortunately, there was insufficient data to be able to iterate exactly for n but the results indicated that Q for *n=1:8* were between 100 kJ and 120 kJ, which is in the appropriate range. The results of the multiple iterations are presented in Figure A5.2.

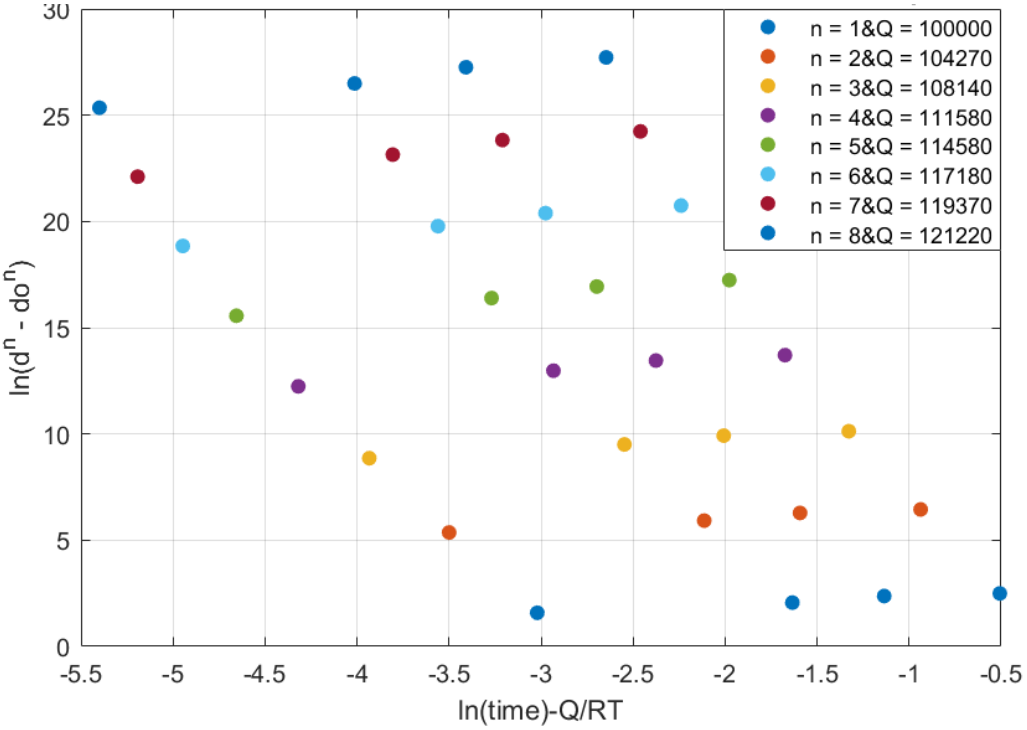

Figure A5.2: Values of Q for multiple values of n for the power law equation iteration.

The MATLAB script for the power law equation showing the Q polyfit iteration for multiple values of n is presented below.

```
%% LINEAR FIT ITERATION to find Q for grain growth%%

clear All
%% Grain Diameters
diameter_0=[19.46, 19.83, 19.57, 19.95];
%diameter=[800C 1hrs    800C 4hrs    850 4hrs  920 4hrs
diameter=[    24.330427,  27.681, 30.295,    32.0634 ];
logDiameter=[log(diameter(1)-diameter_0(1)) log(diameter(2)-
diameter_0(2)) log(diameter(3)-diameter_0(3)) log(diameter(4)-
diameter_0(4))];
%% other parameters

Q=111*10^3;
R=8.314;
T=[800+273 850+273 920+273];
t=[60*60 240*60];

%% for loop for linear regression of Q

for Q=1*10^3:10:500*10^3

    logtimeQRTReal=[log(t(1))-Q/(R*T(1)) log(t(2))-Q/(R*T(1))
log(t(2))-Q/(R*T(2)) log(t(2))-Q/(R*T(3))];
    logDiameter;
        [p, S]=polyfit(logtimeQRTReal,logDiameter,1);  %finds fit for
linearity

    x1 = logtimeQRTReal;
    [y_fit,delta] = polyval(p,x1,S);   %delta provides the standard
error of linear regression against data points

    mean_delta=mean(delta);  %finds mean standard error against all
points
    A(Q)=mean_delta;
    B(Q)=p(1); %combine all gradients of equations into one matrix
    C(Q)=p(2); %combine all intercepts of equations into one matrix
end

%% finding minimum standard error to get Q
%find proper Detla matrix
Delta_Column=nonzeros(A);  %matrix of mean detlas but in column format
Delta_Row=Delta_Column.';   %Convert matrix of mean deltas to row format
same as Q

 %A(A==0) = []   %%alternative all average standard error values in
positions corresponding to Q values

 Q_final=1*10^3:10:500*10^3;  %% All Q values
 [Min_stderror,Location]=min(Delta_Row(2:end));
   Q_minError=Q_final(Location); %find Q min

  %Normalised_stderror=Min_stderror/abs(mean_mass)*100;
  normalized_y = (logtimeQRTReal-mean(logDiameter))/Min_stderror

 %% finding equation of line for Q_min error
```

```
  gradient1=nonzeros(B); %find proper gradient matrix
gradient=gradient1.';

%find proper intercept matrix
intercept1=nonzeros(C);
intercept=intercept1.';
 gradient_minError=gradient(Location); %find gradient
 intercept_minError=intercept(Location); %find intercept


 % definig equation
 x = -4:0.1:2;
 y=gradient_minError.*x+intercept_minError;

% checking for minium point
  figure
 plot(Q_final./1000,Delta_Row(2:end))
 grid on
    box on
    xlabel('Activation Energy (Q / kJ)')
    ylabel('Standard Error for Burke & Turnbull Fit')
    title('Optimisaton for Activation Energy from Bulk Grain Growth
Data')

%%Burke & turnbull comparison of grain growth values for different n's

R=8.314; %% defining parameters
T=[800+273 850+273 920+273];
t=[60*60 240*60];

i=8; %n numer
Q=[100000 104270 108140 111580 114580 117180 119370 121220];
%Activation energy when n=1 in Joules

 for n=1:i
    logtimeQRTMinError=[log(t(1))-Q(n)/(R*T(1)) log(t(2))-Q(n)/(R*T(1))
log(t(2))-Q(n)/(R*T(2)) log(t(2))-Q(n)/(R*T(3))];
    logDiameter=[log((diameter(1)).^n-(diameter_0(1)).^n)
log((diameter(2)).^n-(diameter_0(2)).^n) log((diameter(3)).^n-
(diameter_0(3)).^n) log((diameter(4)).^n-(diameter_0(4)).^n)];

     hold on
    scatter(logtimeQRTMinError,logDiameter,'filled')
    legend(['n = ' num2str(1) '&Q = ' num2str(Q(1))],['n = ' num2str(2)
'&Q = ' num2str(Q(2))], ['n = ' num2str(3) '&Q = ' num2str(Q(3))],['n =
' num2str(4) '&Q = ' num2str(Q(4))],['n = ' num2str(5) '&Q = '
num2str(Q(5))],['n = ' num2str(6) '&Q = ' num2str(Q(6))],['n = '
num2str(7) '&Q = ' num2str(Q(7))],['n = ' num2str(8) '&Q = '
num2str(Q(8))])

    grid on
    box on
    ylabel('ln(d^n - do^n)')
    xlabel('ln(time)-Q/RT')
    title('Grain Growth of Carbon Steel Fitted to Burke & Turnbull Eqn')
end
```

Figure A5.3: Summary of MATLAB code for optimising Q in the power law equation.

EDX Oxidation Compositional Results

A summary of the oxidation results for each of the heat treatment temperatures and their corresponding EDX spectra.

Summary of Data Composition

Temp	**Time**	**Composition (%)**				
		Fe	**C**	**Si**	**Mn**	**O**
800 °C	1 hour	92.78	1.42	0.55	0.42	4.83
850 °C	1 hour	89.28	1.6	0.61	0.31	8.20
800 °C	4 hours	84.57	1.21	0.47	0.22	13.53
850 °C	4 hours	81.66	1.20	0.60	0.28	16.26
920 °C	4 hours	72.26	1.52	0.66	0.24	25.33
885 °C at 25 minutes	Eqv. 800 °C 1 hour	91.52	1.97	0.68	0.31	5.52
885 °C at 42 minutes	Eqv. 850 °C 1 hour	89.21	1.42	0.61	0.35	8.41
885 °C at 100 minutes	Eqv. 800 °C 4 hours	83.28	1.66	0.61	0.32	14.13

Table A5-1: EDX results post-heat treatment of 0.4 wt.% carbon steel.

EDX Spectra

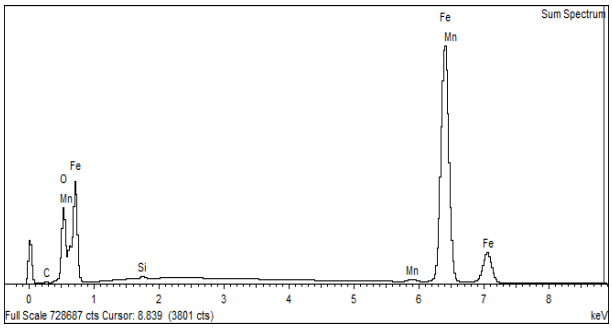

(a) 1 hr @ 800 °C

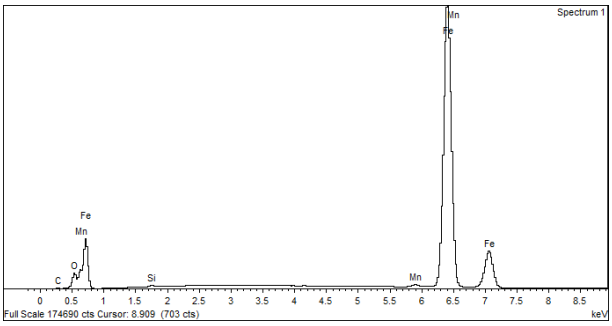

(b) 25 mins @ 885 °C

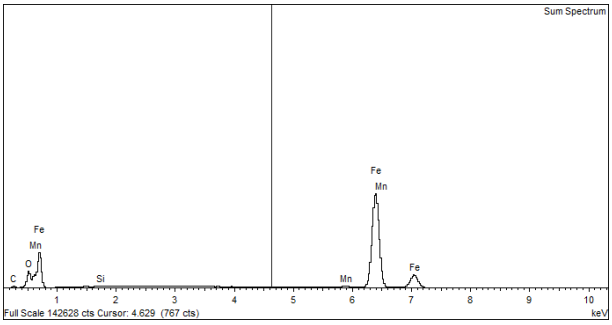

(c) 1 hr @ 850 °C

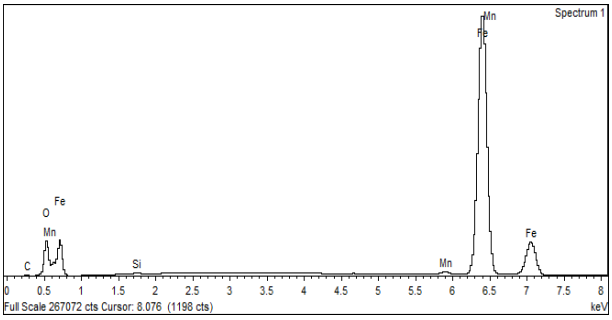

(d) 42 mins @ 885 °C

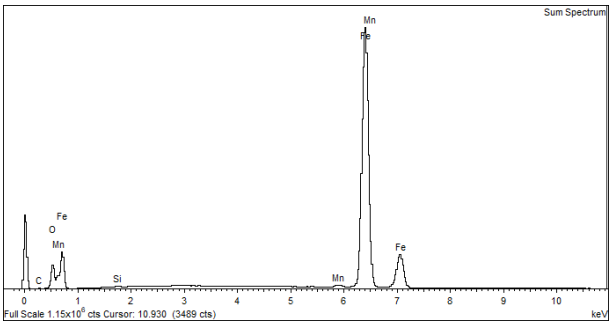

(e) 4 hr @ 800 °C

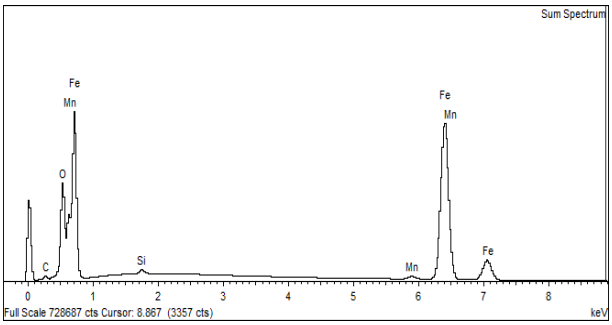

(f) 100 mins @ 885 °C

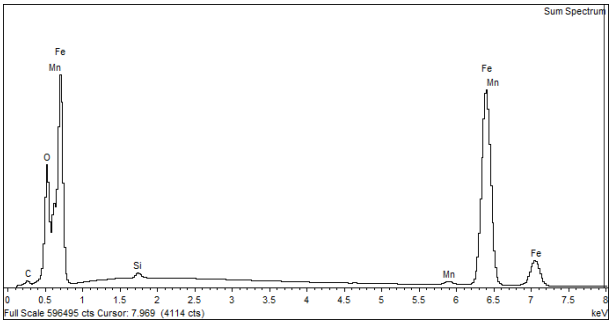

(g) 4hr @ 850 °C

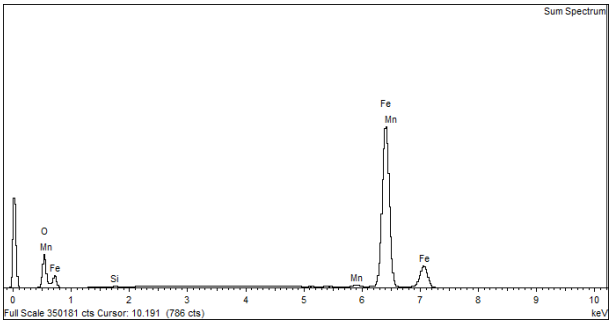

(h) 4hr @ 920 °C

Figure A5.4: Summary of EDX spectra post heat treatment of 0.4 wt.% carbon steel.

Solving for the Pilling-Bedworth Equation

For finding the correlation between time and oxidation the Pilling – Bedworth equation, in its log form, was considered,

$$log(w^2 - {w_0}^2) = log(t) + [log(k_0) - \frac{Q}{RT}] \qquad \text{Equation A5.2}$$

which was then iterated to find the optimal activation energy (Q) based on the polyfit function. Given that Q would be expected to be in the range of 1-500 kJ, these values were iterated for at a step size of 0.01 kJ. The most appropriate value of Q was then chosen based on the minimum standard error between the polyfit equation and the raw data. The standard error from the polyfit was plotted against each value of Q, shown in Figure A5.5. Based on the minimum error, the ideal value of Q was 105 kJ, which is in expected range of 100-250 kJ.

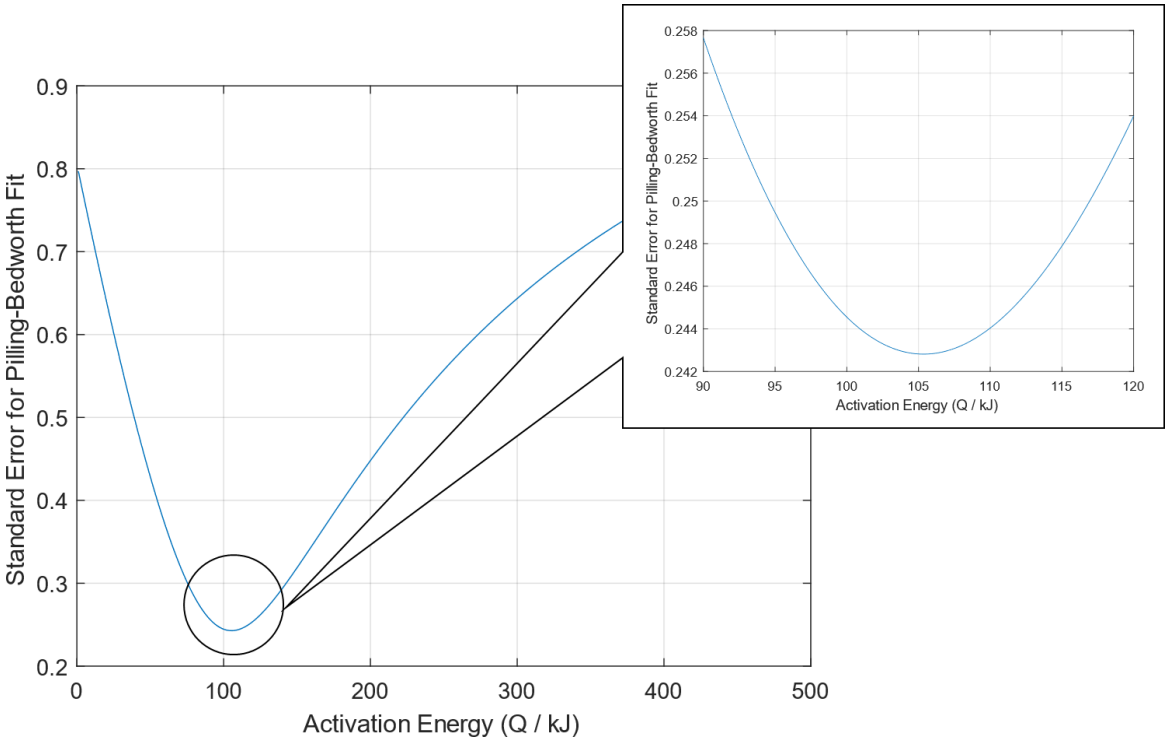

Figure A5.5: Optimisation for activation energy (Q) from oxidation data.

The MATLAB script for the Pilling-Bedworth Q polyfit iteration is presented below.

```
%% LINEAR FIT ITERATION %%
 clear All

%% find mass

 p=7.870;  %density of 1045 med carbon steel from AZO Materials g/cm^3
d=1.87*10^-7; %depth EDS penetrates from CASINO simulation
A=0.0001*0.0001;  %area from EDX scans in m

V=d*A;
W=V*p;

PercentFour=[13.53 16.26 25.33]; %oxidation % after four hours
PercentOne= [4.83 8.2 ]; %oxidation % after 1 hour
Percent25=[0 0 0 5.52];
Percent42=[0 0 0 8.41];
Percent100=[0 0 0 14.13];

%mass
m_800=[(PercentOne(1)*W/100) (PercentFour(1)*W/100)];
m_850=[(PercentOne(2)*W/100) (PercentFour(2)*W/100)];
m_920=PercentFour(3)*W/100;
m_885=[(Percent100(4)*W/100) (Percent25(4)*W/100) (Percent42(4)*W/100)];


R=8.314;
T=[800+273 850+273 920+273 885+273];
t=[60*60 240*60 25*60 42*60 100*60];

%% for loop for linear regression of Q
  for Q=1*10^3:10:500*10^3
          logtimeQRTReal=[log(t(1))-Q/(R*T(1)) log(t(2))-Q/(R*T(1))
log(t(1))-Q/(R*T(2)) log(t(2))-Q/(R*T(2)) log(t(2))-Q/(R*T(3)) ];
%log(t(5))-Q/R*T(4)  log(t(4))-Q/R*T(4)log(t(3))-Q/R*T(4)
    logmass2R=[log(m_800(1).^2) log(m_800(2).^2) log(m_850(1).^2)
log(m_850(2).^2) log(m_920.^2) ]; % log(m_885(1).^2) log(m_885(3).^2)
log(m_885(3).^2)
     [p, S]=polyfit(logtimeQRTReal,logmass2R,1);  %finds fit for
linearity
    %disp(['Equation is y = ' num2str(p(1)) '*x + ' num2str(p(2))]);

    x1 = logtimeQRTReal;
    [y_fit,delta] = polyval(p,x1,S);   %delta provides the standard error
of linear regression against data points

    mean_delta=mean(delta);  %finds mean standard error all points
    A(Q)=mean_delta;
    B(Q)=p(1); %combine all gradients of equations into one matrix
    C(Q)=p(2); %combine all intercepts of equations into one matrix
 end

%% finding minium standard error to get Q
%find proper Detla matrix
Delta_Column=nonzeros(A);  %matrix of mean detlas but in column format
Delta_Row=Delta_Column.';   %Convert matrix of mean deltas to row format
same as Q

  Q_final=1*10^3:10:500*10^3;  %% All Q values
```

```
 [Min_stderror,Location]=min(Delta_Row(2:end));

 Q_minError=Q_final(Location); %find Q min

 normalized_y = (logtimeQRTReal-mean(logmass2R))/Min_stderror

 %% finding equation of line for Q_min error

 %find proper gradient matrix
gradient1=nonzeros(B);
gradient=gradient1.';

%find proper intercept matrix
intercept1=nonzeros(C);
intercept=intercept1.';
 gradient_minError=gradient(Location); %find gradient
 intercept_minError=intercept(Location); %find intercept

 %% Plotting for minimum Q point

 figure
 plot(Q_final./1000,Delta_Row(2:end))
 grid on
    box on
    xlabel('Activation Energy (Q / kJ)')
    ylabel('Standard Error for Pilling-Bedworth Fit')
```

Figure A5.6: MATLAB code for optimisation of Q for Pilling-Bedworth equation.

Appendix - Chapter 6

Histogram and SE Image Data

A summary of SE images and corresponding histogram breakdown for ferrite / pearlite to austenite phase transformation quantified for Area 1. The images capture the 1-hour heat treatment of 0.4 wt.% carbon steel at 800 °C. Areas 2 & 3 were analysed similarly.

Time	Image	Histogram
1 min	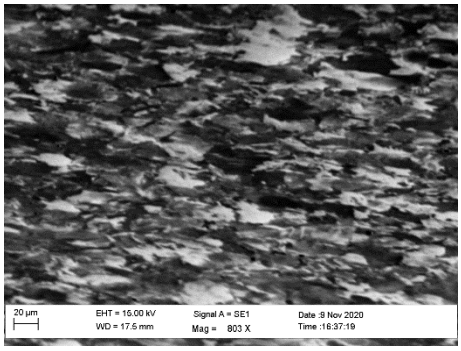	 Count: 786432 Mean: 97.772 StdDev: 70.168 Min: 0 Max: 255 Mode: 255 (71486)
3 mins	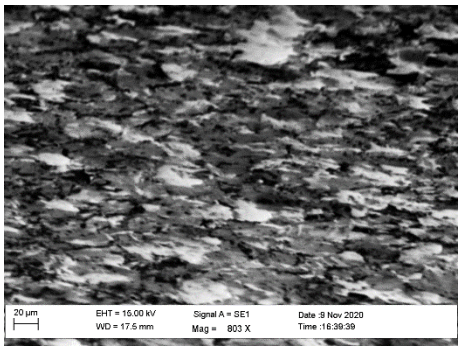	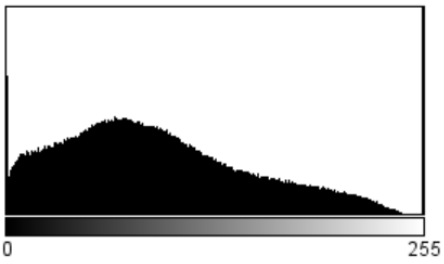 Count: 786432 Mean: 105.982 StdDev: 71.465 Min: 0 Max: 255 Mode: 255 (71431)
6 mins	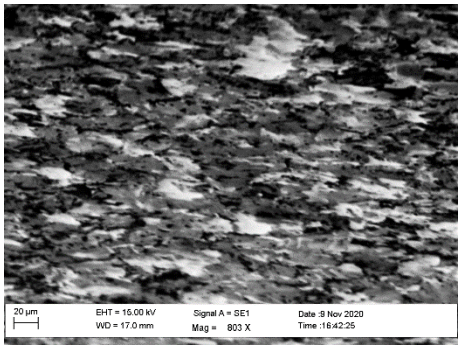	 Count: 786432 Mean: 105.635 StdDev: 73.238 Min: 0 Max: 255 Mode: 255 (71457)

12 mins

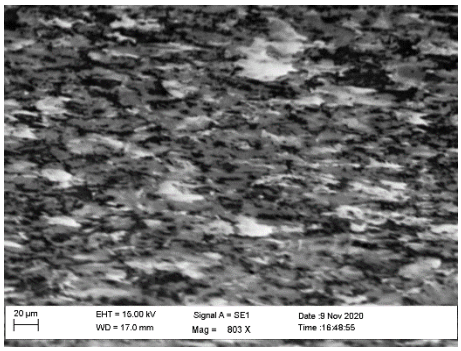

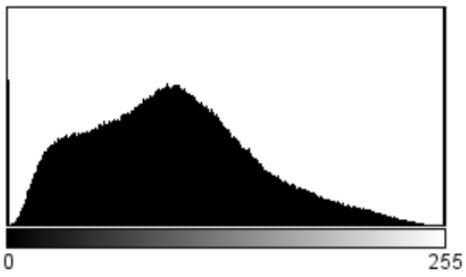

Count: 786432 Min: 0
Mean: 109.354 Max: 255
StdDev: 65.504 Mode: 255 (71428)

16 mins

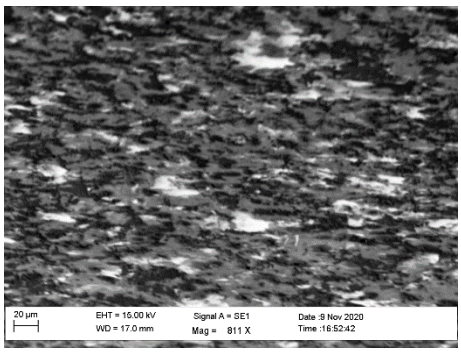

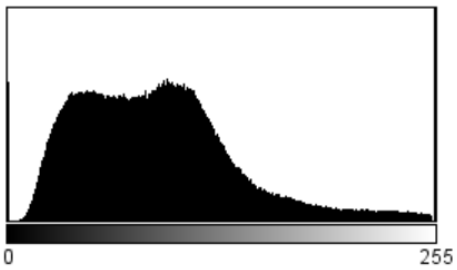

Count: 786432 Min: 0
Mean: 103.671 Max: 255
StdDev: 66.043 Mode: 255 (71513)

20 mins

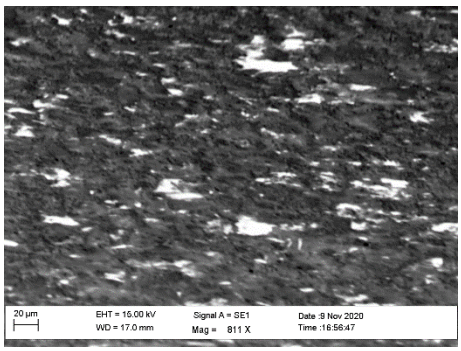

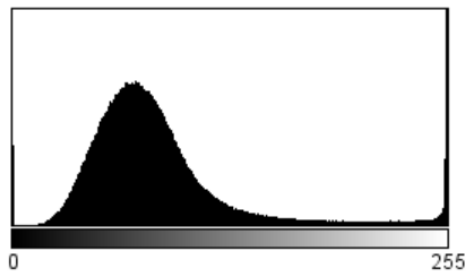

Count: 786432 Min: 0
Mean: 99.712 Max: 255
StdDev: 64.064 Mode: 255 (71515)

24 mins

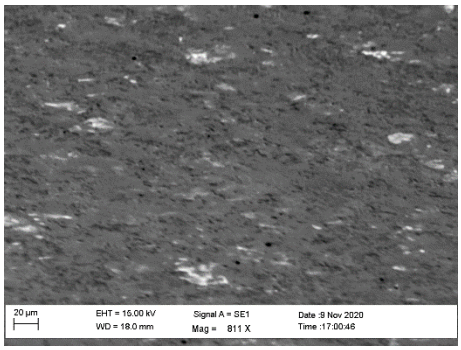

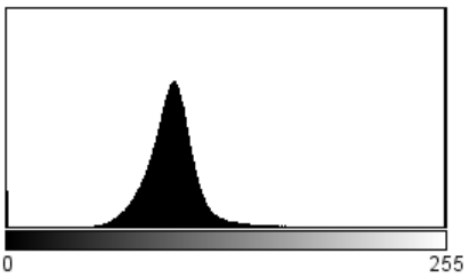

Count: 786432 Min: 0
Mean: 110.523 Max: 255
StdDev: 49.650 Mode: 255 (71484)

32 mins

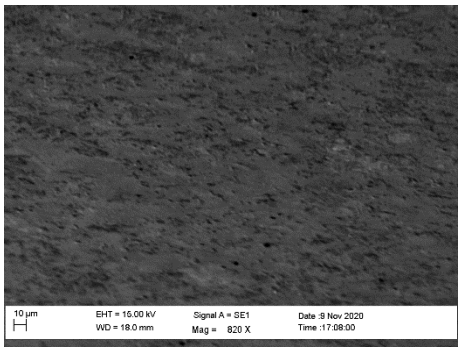

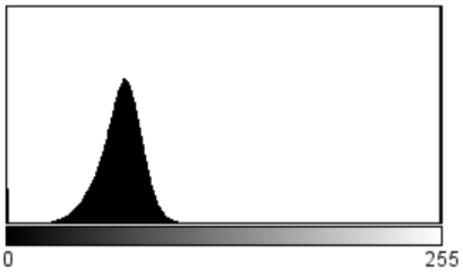

Count: 786432 Min: 0
Mean: 83.152 Max: 255
StdDev: 55.913 Mode: 255 (71494)

36 mins

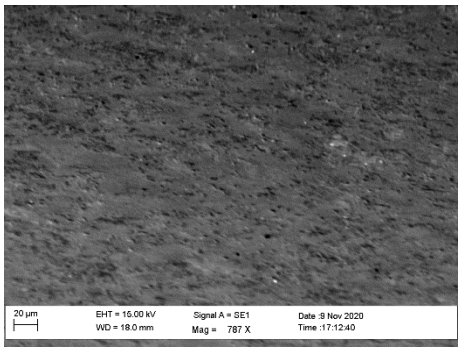

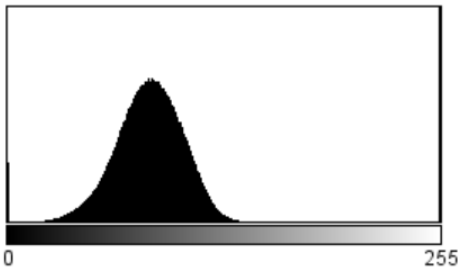

Count: 786432 Min: 0
Mean: 98.454 Max: 255
StdDev: 53.377 Mode: 255 (71516)

39 mins

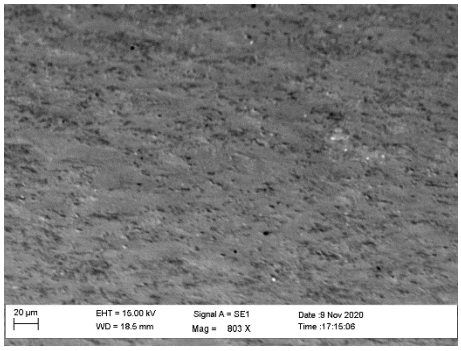

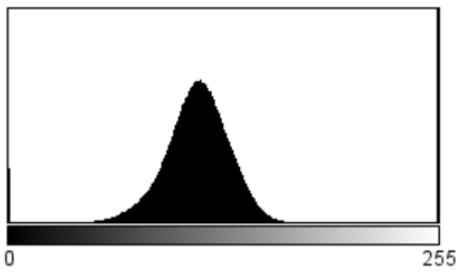

Count: 786432 Min: 0
Mean: 124.102 Max: 255
StdDev: 46.129 Mode: 255 (71450)

48 mins

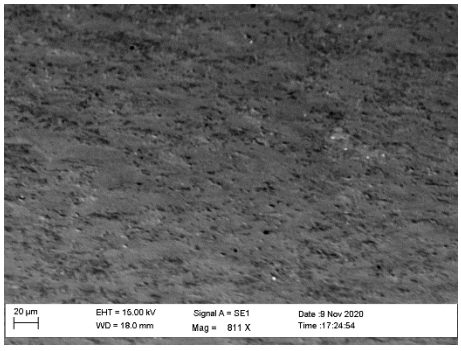

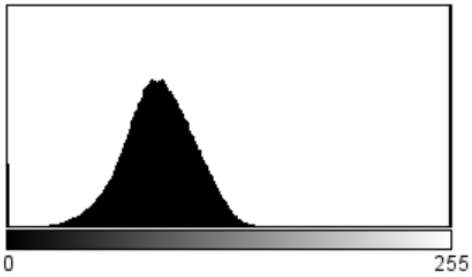

Count: 786432 Min: 0
Mean: 101.715 Max: 255
StdDev: 52.715 Mode: 255 (71506)

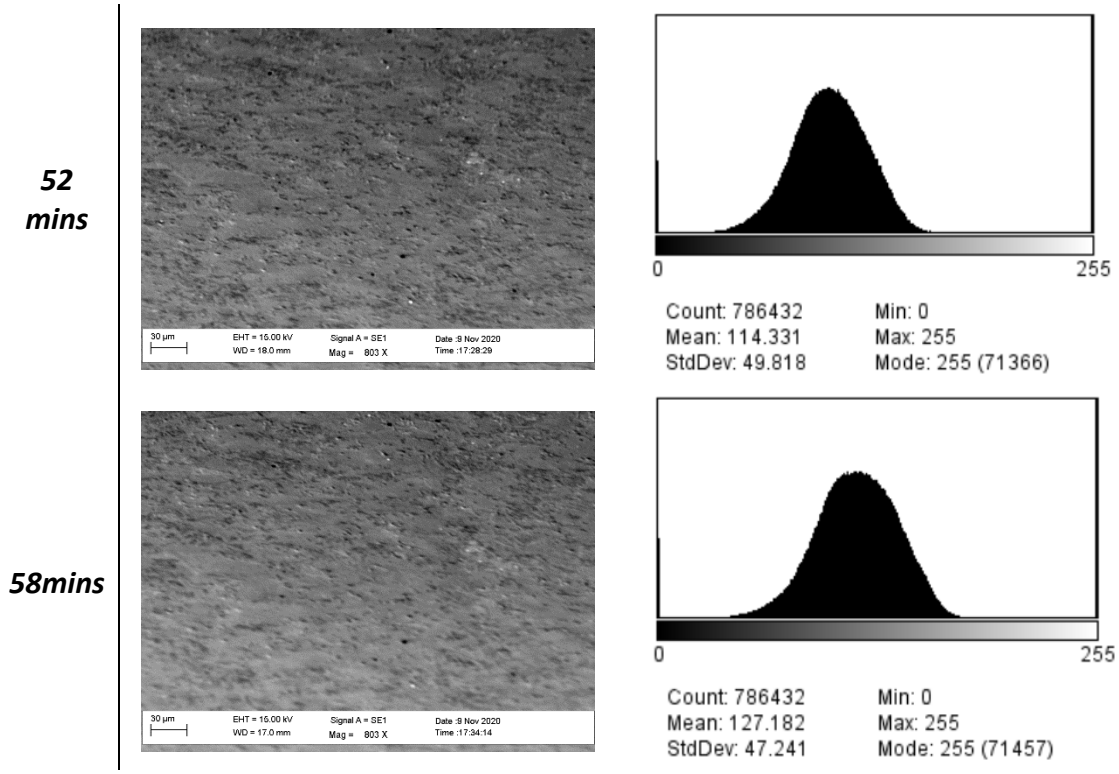

Table A6-1: SE and corresponding histogram data for one hour 0.4 wt.% C Steel heat treatment at 800 °C.

Summary of Histogram Raw Data

The histogram was segmented into 0-39 for dark areas (pearlite), 40-129 for mid areas (austenite) and 130-255 for light areas (ferrite). Table A5-2 summaries the percentages for each of the phases.

image no. 1	**time (minutes)**	dark %	med %	light %
2	1	23.32	60.12	16.56
5	3	18.95	60.82	20.24
8	6	21.3	58.23	20.47
13	12	13.42	69.25	17.33
16	16	13.94	73.92	12.14
19	20	5.19	86.45	8.36
22	24	0.09	97.32	2.59
32	32	2.3	97.7	0
34	36	1.6	98.24	0.16
46	48	1.19	98.58	0.23
48	52	0.34	97.25	2.41

Table A6-2: Dark (pearlite), medium (austenite) and light (ferrite) phase quantities.